SYNTHESIS AND DENSITY FUNCTIONAL THEORY STUDY OF IRIDIUM(III) COMPLEXES WITH PYRIDINYLFORMIMIDAMIDE ANCILLARY LIGAND FOR EFFICIENT BLUE PHOSPHORESCENT

NURUL HUSNA AS SAEDAH BINTI BAIN

UNIVERSITI PENDIDIKAN SULTAN IDRIS

2025

SYNTHESIS AND DENSITY FUNCTIONAL THEORY STUDY OF IRIDIUM(III) COMPLEXES WITH PYRIDINYLFORMIMIDAMIDE ANCILLARY LIGAND FOR EFFICIENT BLUE PHOSPHORESCENT

NURUL HUSNA AS SAEDAH BT BAIN

THESIS PRESENTED TO QUALIFY FOR A DOCTOR OF PHILOSOPHY

FACULTY OF SCIENCE AND MATHEMATICS
UNIVERSITI PENDIDIKAN SULTAN IDRIS

2025

UNIVERSITI PENDIDIKAN SULTAN IDRIS
SULTAN IDRIS EDUCATION UNIVERSITY

Please tick (√)
Project Paper
Masters by Research
Master by Mixed Mode
PhD

/

INSTITUTE OF GRADUATE STUDIES

DECLARATION OF ORIGINAL WORK

This declaration is made on the ……5……..day of….AUG…..20…25

i. Student's Declaration:

I, Nurul Husna As Saedah Bt Bain, P20202001246, Faculty of Sciences & Mathematics (PLEASE INDICATE STUDENT'S NAME, MATRIC NO. AND FACULTY) hereby declare that the work entitled Synthesis and Density Functional Theory Study of Iridium(III) Complexes with Pyridinylformimidamide Ancillary Ligand for Efficient Blue Phosphorescent is my original work. I have not copied from any other students' work or from any other sources except where due reference or acknowledgement is made explicitly in the text, nor has any part been written for me by another person.

Signature of the student

ii. Supervisor's Declaration:

I Assoc. Prof. ChM. Dr. Noorshida Mohd Ali (SUPERVISOR'S NAME) hereby certifies that the work entitled Synthesis and Density Functional Theory Study of Iridium(III) Complexes with Pyridinylformimidamide Ancillary Ligand for Efficient Blue Phosphorescent (TITLE) was prepared by the above named student, and was submitted to the Institute of Graduate Studies as a * ~~partial~~/full fulfillment for the conferment of Doctor of Philosophy (Chemistry) (PLEASE INDICATE THE DEGREE), and the aforementioned work, to the best of my knowledge, is the said student's work.

5 - 8 -2025
Date

Signature of the Supervisor

UNIVERSITI PENDIDIKAN SULTAN IDRIS
SULTAN IDRIS EDUCATION UNIVERSITY

INSTITUT PENGAJIAN SISWAZAH /
INSTITUTE OF GRADUATE STUDIES

BORANG PENGESAHAN PENYERAHAN TESIS/DISERTASI/LAPORAN KERTAS PROJEK
DECLARATION OF THESIS/DISSERTATION/PROJECT PAPER FORM

Tajuk / *Title*: Synthesis and Density Functional Theory Study of Iridium(III) Complexes with Pyridinylformimidamide Ancillary Ligand for Efficient Blue Phosphorescent

No. Matrik /*Matric's No.*: P20202001246

Saya / *I* : Nurul Husna As Saedah Bt Bain

(Nama pelajar / *Student's Name*)

mengaku membenarkan Tesis/Disertasi/Laporan Kertas Projek (Kedoktoran/Sarjana)* ini disimpan di Universiti Pendidikan Sultan Idris (Perpustakaan Tuanku Bainun) dengan syarat-syarat kegunaan seperti berikut:-
acknowledged that Universiti Pendidikan Sultan Idris (Tuanku Bainun Library) reserves the right as follows:-

1. Tesis/Disertasi/Laporan Kertas Projek ini adalah hak milik UPSI.
   The thesis is the property of Universiti Pendidikan Sultan Idris
2. Perpustakaan Tuanku Bainun dibenarkan membuat salinan untuk tujuan rujukan dan penyelidikan.
   Tuanku Bainun Library has the right to make copies for the purpose of reference and research.
3. Perpustakaan dibenarkan membuat salinan Tesis/Disertasi ini sebagai bahan pertukaran antara Institusi Pengajian Tinggi.
   The Library has the right to make copies of the thesis for academic exchange.
4. Sila tandakan (√) bagi pilihan kategori di bawah */ Please tick (√) for category below:-*

☐	**SULIT/*CONFIDENTIAL***	Mengandungi maklumat yang berdarjah keselamatan atau kepentingan Malaysia seperti yang termaktub dalam Akta Rahsia Rasmi 1972. / *Contains confidential information under the Official Secret Act 1972*
☐	**TERHAD/*RESTRICTED***	Mengandungi maklumat terhad yang telah ditentukan oleh organisasi/badan di mana penyelidikan ini dijalankan. / *Contains restircted information as specified by the organization where research was done.*
☑	**TIDAK TERHAD / *OPEN ACCESS***	

(Tandatangan Pelajar/ Signature)

(Tandatangan Penyelia / *Signature of Supervisor*)
& (Nama & Cop Rasmi / *Name & Official Stamp*)

Tarikh: 5-8-2025

PROF. MADYA CHM. DR. NOORSHIDA MOHD ALI
Timbalan Dekan (Penyelidikan & Inovasi)
Fakulti Sains dan Matematik
Universiti Pendidikan Sultan Idris

Catatan: Jika Tesis/Disertasi ini **SULIT** @ **TERHAD**, sila lampirkan surat daripada pihak berkuasa/organisasi berkenaan dengan menyatakan sekali sebab dan tempoh laporan ini perlu dikelaskan sebagai **SULIT** dan **TERHAD**.

Notes: If the thesis is CONFIDENTAL or RESTRICTED, please attach with the letter from the organization with period and reasons for confidentiality or restriction.

ACKNOWLEDGEMENT

First and foremost, I want to express my sincere gratitude to Allah S.W.T. for all of His favours, which made it possible for me to finish this thesis. I would especially like to remember my late father, Hj Bain bin Ijap; may Allah reward him abundantly and provide him *berkah*. I want to express my sincere appreciation to my supervisor, Associate Professor ChM Dr. Noorshida Mohd Ali and Dr. Yusnita Juahir, for their invaluable support, advice, and patience. Her guidance has been essential in shaping my research and academic development. I also thank Emeritus Professor Bohari Yamin, Professor Muhammad Kassim, and Mr. Fadzlee Ngatiman from Universiti Kebangsaan Malaysia for their contributions to the crystallographic single-crystal analysis. To Dr. Fazira Ilyana Abdul Razak and Dr. Suhaila Sapari from Universiti Teknologi Malaysia, Dr. Elhassane Anour from Prince Sattam University, Saudi Arabia, and Dr. David Robinson from Nottingham Trent University, United Kingdom, I am deeply grateful for the guidance on computational DFT analysis. Thank you also to Dr. Didi Erwandi from Universiti Malaya for the extensive mass-spec crash courses and LCMS sample analysis.

My appreciation also goes to my family, especially my beloved mother, Mrs. Hamisah Arshat, for the unconditional love, faith, and constant prayers for me. I am eternally grateful to my dear siblings for their unyielding belief in me. To all my nieces and nephews, thank you for adding a special kind of joy to my life, especially when I was going through the challenging parts of this doctorate journey. They always reminded me to laugh, to stay resilient, and to find balance amidst the chaos. A special note of appreciation also goes to my PhD "partner in crime," Ili Syuhada, who shared countless late-night conversations despite the 7-hours time difference between Malaysia and New Zealand. We've got through it all together, from laughing at our difficulties with writing to talking about opportunities and expressing our worries about the future. I hope we both succeed in crossing the finishing line! To Hajar, Bidd, Mika, Nadh MK and Nad, your endless support, warm hugs, hot coffee, and life gossip have always kept me going when things felt overwhelming. Thank you for always being with me and making the hard days bearable. Finally, I also extend my thankful to the Faculty of Science and Mathematics, Universiti Pendidikan Sultan Idris, for providing access to the facilities and instruments essential to my research. Special thanks to Mr. Hazim, Mrs. Johanna, Mrs. Radiah, and Mr. Zureen for their technical support and guidance. May Allah bless all of you for your kindness and support throughout this journey.

ABSTRACT

This study aims to synthesise and characterise new blue phosphorescent iridium(III) complexes and investigate their structural and photophysical properties through experimental techniques and theoretical calculations. Complexes of bis(phenylpyridine)(2,6- difluorobenzylpyridinylformimidamide) iridium(III) (**IR1**), bis(2,4- difluorophenylpyridine)(2,6-difluorobenzylpyridinylformimidamide)iridium(III) (**IR2**), bis(phenylpyridine)(4-methylbenzylpyridinylformimidamide)iridium(III) (**IR3**) and bis(2,4-difluorophenylpyridine)(4- methylbenzylpyridinylformimidamide)iridium(III) (**IR4**) were synthesised by reaction between dichloro-bridged iridium(III) dimers with the respective triazolium salts. Characterisation was conducted using carbon, hydrogen and nitrogen (CHN) elemental analyser and spectroscopic techniques: nuclear magnetic resonance (NMR), Fourier transform-infrared (FT-IR) and liquid chromatography-mass spectrometry (LC-MS). Photophysical properties were examined using ultraviolet-visible (UV-Vis), fluorescence and photoluminescence (PL) spectroscopy. Density functional theory (DFT) and time-dependent DFT (TD-DFT) calculations with the B3LYP functional and LanL2DZ basis set were used to evaluate ground state geometries and electronic transitions. IR spectra showed strong ν(C≡N) stretching bands between 2220−2224 cm^{-1} for all complexes. In ^{1}H NMR spectra, the disappearance of singlet protons from triazolium salts confirmed complex formation, while ^{13}C NMR displayed nitrile carbon peaks between 116.7−118.6 ppm. X-ray crystallographic study verified the iridium was coordinated to two phenylpyridine ligands and one pyridinylformimidamide ancillary ligand in a distorted octahedral geometry. Emission spectra showed that **IR2** (λ_{em}=463 nm) and **IR4** (λ_{em}=464 nm) resulted slightly blue emission in dichloromethane solution compared to the green emission of **IR1** and **IR3** (λ_{em}= 518 nm). **IR3** displayed the highest phosphorescence quantum yield (49%) and the longest lifetime (τ = 78.82 ns). DFT calculations showed that **IR4** has the largest band gap (3.88 eV), consistent with the experimental NMR chemical shifts and IR vibrational modes. In conclusion, new blue phosphorescent iridium(III) complexes were successfully synthesised and characterised using both experimental techniques and theoretical calculations. **IR4** exhibited a notable, blue-shifted emission and the largest band gap. As implication, **IR4** has a high potential for application in blue organic light-emitting diode (OLED) devices.

SINTESIS DAN KAJIAN TEORI FUNGSIAN KETUMPATAN BAGI KOMPLEKS IRIDIUM(III) DENGAN LIGAN ANSILARI PIRIDINILFORMIMIDAMIDA UNTUK BERPENDARFOSFOR BIRU YANG EFISIEN

ABSTRAK

Kajian ini bertujuan untuk mensintesis dan mencirikan kompleks iridium(III) berpendarfosfor biru yang baharu serta mengkaji sifat struktur dan fotofizikalnya melalui teknik eksperimen dan pengiraan teori. Kompleks bis(fenilpiridina)(2,6-diflorobenzilpiridinilformimidamida)iridium(III) (**IR1**), kompleks bis(2,4-diflorofenilpiridina)(2,6-diflorobenzilpiridinilformimidamida)iridium(III) (**IR2**), kompleks bis(fenilpiridina)(4-metilbezilpiridinilformimidamida)iridium(III) (**IR3**) dan bis(2,4-diflorofenilpiridina)(4-metilbenzilpiridinilformimidamida) iridium(III) (**IR4**) disintesis melalui tindak balas antara dimer iridium(III) titian-dikloro dengan garam triazolium sepadan. Pencirian telah dijalankan menggunakan penganalisis unsur karbon, hidrogen dan nitrogen (CHN) serta teknik spektroskopi: resonans magnet nukleus (NMR), inframerah-transformasi Fourier (FT-IR) dan kromatografi cecair-spektrometri jisim (LC-MS). Sifat fotofizikal dikaji menggunakan spektroskopi ultralembayung boleh nampak (UV-Vis), pendar fluor dan foto pendarcahaya (PL). Pengiraan teori fungsian ketumpatan (DFT) dan DFT bersandarkan masa (TD-DFT) dengan fungsian B3LYP dan set asas LanL2DZ digunakan untuk menilai geometri keadaan asas dan peralihan elektronik. Spektrum IR menunjukkan jalur regangan ν(C≡N) yang kuat antara 2220–2224 cm^{-1} untuk semua kompleks. Dalam spektrum ^{1}H NMR, kehilangan proton singlet daripada garam triazolium mengesahkan pembentukan kompleks, manakala spektrum ^{13}C NMR menunjukkan puncak karbon nitril antara 116.7–118.6 ppm. Kajian kristalografi sinar-X mengesahkan iridium berkoordinasi dengan dua ligan fenilpiridina dan satu ligan ansilari piridinaformimidamida dalam geometri oktahedral terherot. Spektrum pancaran menunjukkan bahawa **IR2** (λ_{em}= 463 nm) dan **IR4** (λ_{em}= 464 nm) menghasilkan pancaran sedikit biru dalam larutan diklorometana berbanding pancaran hijau oleh **IR1** dan **IR3** (λ_{em}= 518 nm). **IR3** menunjukkan hasil kuantum pendarfosfor tertinggi (49%) dan jangka hayat terpanjang (τ = 78.82 ns). Pengiraan DFT menunjukkan bahawa **IR4** mempunyai jurang jalur terbesar (3.88 eV), selari dengan anjakan kimia NMR dan mod getaran IR eksperimen. Kesimpulannya, kompleks iridium(III) berpendarfosfor biru yang baharu telah berjaya disintesis dan dicirikan menggunakan kedua-dua teknik eksperimen dan pengiraan teori. **IR4** memperlihatkan pancaran beranjak biru yang ketara dan jurang jalur terbesar. Implikasinya, **IR4** berpotensi tinggi untuk diaplikasikan dalam peranti diod pemancar cahaya organik (OLED) biru.

TABLE OF CONTENTS

CHAPTER 4 RESULTS AND DISCUSSIONS

LIST OF TABLES

LIST OF SCHEMES

LIST OF FIGURES

LIST OF ABBREVIATIONS

Å	equal to one-tenth of a millimicron
Abs	absorbance
acac	acetylacetonate
ADC	acyclic diamino carbene
ATR	attenuated total reflectance
Au	gold
C	degree Celsius
C^N	cyclometallating ligand
CC	column chromatography
CD_2Cl_2-d_2	deutrated methylene chloride
CIE	commission internationale de l'eclairage
cm	centimetre
CNF_2bpyfa	(E)-N-cyano-N-(2,6-diflurobenzyl)-N'-(pyridin-2-yl)formimidamide
CNMbpyfa	(E)-N-cyano-N-(methylbenzyl)-N'-(pyridin-2-yl)formimidamide
CT	charge transfer
d	duplet
def2-SVP	double-zeta plus polarization
DFT	density functional theory
DMSO-d_6	deuterated dimethyl sulfoxide
dpbic	1-phenyl-3-phenyl-benzimidazolin-2-ylidene
e	molar absorption coefficient
Ea	activation energy
ECL	electrochemiluminescence
EDG	electron-donating group
EL	electroluminescence
ESI	electrospray ionisation
ESMS	electrospray ionisation mass spectrometry

ESP	electronic potential surface
EWG	electron-withdrawing group
Fac	facial
F_2bpyta	(2-(2,6-difluorobenzyl)-1h-1,2,4-triazol-1-yl)pyridine ligand
FIrPic	Iridium(III)bis[2-(4,6-difluorophenyl)pyridyl-N,C2']picolinate
FMO	frontier molecular orbital
fppz	acidic pyrazolyl-pyridine
FT-IR	fourier transform-infrared
g	gram
HF	Hartree-Fock
HPC	high-performances computer
Hz	hertz
IEF-PCM	integral equation formalism, polarisable continuum model
Ir	iridium
ISC	intersystem crossing
ITU	International Telecommunication Union
kJ	kilojoule
Knr	non-radiative rate
Kr	radiative rate
LC	ligand centred
LC-MS	liquid chromatography mass spectrometry
LCD	liquid crystal display
LMCT	ligand to metal charge transfer
m	multiplet
m/z	mass-to-charge-ratio
MBCT	metal to boron charge transfer
MBpyta	2-(4-methylbenzyl)-(1,2,4-triazol-1-yl)pyridine ligand
MC	metal centred
mer	meridional
mg	milligram
MHz	megahertz

mL	millilitre
MLCT	metal to ligand charge transfer
mmol	millimole
MO	molecular orbital
mol	mole
NHC	N-heterocyclic carbene
NMR	nuclear magnetic resonance
NR	non-radiative
ns	nanosecond
OLED	organic light-emitting diode
Os	osmium
Pd	paladdium
pic	picolinate acid
PL	photoluminescence
PLQY	photoluminescence quantum yield
ppy	phenylpyridine
Pt	platinum
PTLC	prep thin layer chromatography
pyta	2-(1,2,4-triazol-1-yl)pyridine ligand
QE	quantum efficiencies
Ru	ruthenium
ROS	reactive oxygen species
s	second
s	singlet
SCF	self-consistent field
S_0	ground state
SC-XRD	single crystal- x ray diffraction
SMD	solvation model based on density
SOC	spin-orbit coupling
SST	solid state technology
t	triplet

τ	lifetime
TADF	thermally activated delayed fluorescence
TD-DFT	time-dependent density functional theory
TLC	thin layer chromatography
TVCF	thermal vibration correlation function
UV	ultraviolet
μs	microsecond
UV-Vis	ultraviolet-visible
XC	exchange-correlation
XPS	X-ray Photoelectron Spectrometry
ZORA	zero-order relativistic approximation

CHAPTER 1

INTRODUCTION

The introduction begins with the history of organic light-emitting diode (OLED) and how phosphorescent materials are being utilised in this OLED. Hence, the introduction continues to describe several luminescent transition metal complexes that have been reported to be used as OLED emitters. This chapter includes the problem statement, research objectives, hypothesis, and scope of study.

1.1 Background of Study

1.1.1 The History of Organic Light-Emitting Diode

Organic light-emitting diodes (OLEDs) are light sources used in displays of smartphones, television screens, and many OLED devices, as well as in panels for lighting applications. Over the past 40 years, the research and development of OLEDs has become a rapidly expanding field in academia and industry. OLED offers a new, efficient, and sustainable method for lighting and display technologies; hence, it is rising to supersede the previous technologies on the market. In industry, OLEDs have moved into focus in recent years as these displays offer some features that grant them superior properties over well-established technologies like liquid crystal displays (LCDs). In the instrumentation aspects, OLED devices do not require a backlight system compared to LCDs (Hsiang et al., 2021). This property is not only energy-efficient, as an inactive OLED element does not produce light or consume power, but also allows for thinner and lighter display devices (Yafei Wang et al., 2016). The result of this behaviour has made OLED displays show improvements in resolution, wider viewing angles, high contrast colours, faster response time, and the possibility of realising transparent displays. Moreover, the development of flexible OLED displays can be twisted and rolled up like a poster, and expanding the options for display design is another significant factor in how OLED was chosen over other solid-state technologies (Hong et al., 2021).

The instrumentation of OLED is shown in **Figure 1.1**, where it is typically a thin multilayer devices that consist of layers of organic semiconductors (Hong et al., 2021). In short, the charge carriers, electrons and holes, are obtained at the cathode and

anode, respectively, when the external voltage is applied. Subsequently, the charge carriers are injected into the electron and hole injection layers. Next, the electrons and holes migrate through the electron and hole transport layers into the emissive layer (EML), where the recombination of the charge carriers and the formation of excitons occur. Electroluminescence (EL) occurs as these excitons relax radiatively from the excited state to the ground state. Therefore, there was a crucial need in the rational design of the materials for the emissive layer that holds the dopant emitter system, as it is the most critical factor in achieving high efficiencies of OLED devices (Hong et al., 2021).

Figure 1.1

Schematic depiction of a stacked device structure of an organic light-emitting diode

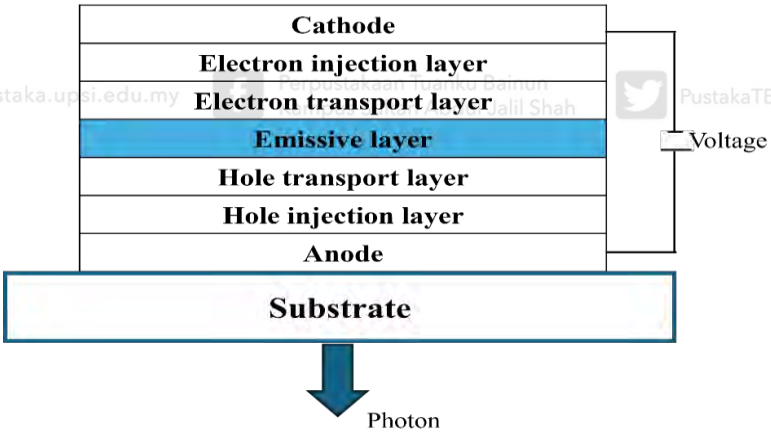

Over the past decades, the design and development of OLED emissive materials have been structured according to various “generations” of OLED, which are based on the emission mechanism used to emit light. With this, the term “generation” is closely approximated to the chronological order of the development of OLED. The first generation of OLED used fluorescent emitters. In contrast, the second generation is based on phosphorescent. The third generation relies on thermally activated delayed

fluorescence (TADF) as the light-emitting pathway (Hsiang et al., 2021). The first three generations are subdivided into green, orange-red, and blue emitters, as green OLED emitters were introduced before red and red before blue. These three red, green, and blue colours are crucial for the colour saturation of OLED devices. In short, the emitter materials must have a remarkable emission that is tunable over the whole of the visible region from the blue to the red region of the spectrum, as shown in **Figure 1.2,** and this is the crucial property for OLED emitters.

Figure 1.2

The electromagnetic spectrum

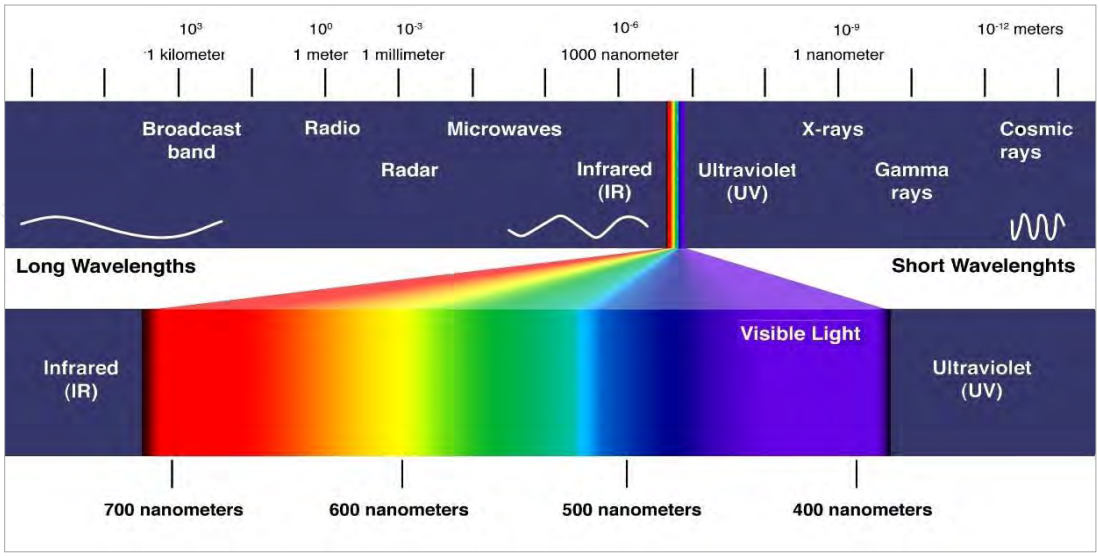

Over the decades, a lot of fundamental research has been developed to explore the high efficiencies of emissive materials for emissive layers (EML), as shown in **Figure 1.1**. In significance, the synthesis of various types of transition metal complexes that comply with the mechanisms of fluorescence or phosphorescence has been highly explored since then. Transition metal complexes are known to have facile chemical modifications depending on the metal or the ligand used for various applications that

are not limited only to OLED but also other Solid-State Technology (SST) applications. To best explain the role of transition metal complexes in enhancing the emissive layer of OLED devices, it is crucial to have a brief introduction to the fundamentals of "luminescence".

1.1.2 Luminescence

Luminescence is the emission of light from any substance and occurs from an electronically excited state. Significantly, the explanation of luminescence involves the mechanism of absorption, charge transfer transition, and emission in the form of fluorescence and phosphorescence (Stanitska et al., 2024).

1.1.2.1 Absorption

The luminescence process begins with the absorption of light by a molecule in the visible or ultraviolet regions, forming excited electronic states in the molecule. Each excited state has its characteristic energy relative to the ground state. Atoms in their absorption spectra show very sharp lines, each related to a transition to a different electronic state. In the case of polyatomic molecules, we can observe that absorption spectra manifest the transitions involved with a different appearance as a broad band because of vibrational and rotational energy in every electronic state (Brulatti, 2010), as shown in **Figure 1.3**. This can be explained considering the Franck-Condon principle, which states that in the classical form of the molecule, since absorption is "instantaneous," a molecule is formed in its excited state with the size and shape of its ground state and therefore has vibrational excitation (Brulatti, 2010). Since the nuclei

are much heavier compared to the electrons, the electronic transition is much faster than the possible response of the nuclei. In general terms, absorption is defined by the Beer-Lambert law, which can be written as:

$$\mathbf{Abs = \log_{10}(I_0/I_t) = \varepsilon cl}$$

Abs is the absorbance, I is the light path length through the absorbent material, c is the concentration of the absorbent, and I_0 and I_t are, respectively, incident and transmitted light intensities. The molar extinction coefficient is referred to as the molar absorptivity, a function of incident light. In absorption, extinction coefficients are related to the nature of the transition. If the transition is forbidden by the principles of quantum mechanics, the extinction coefficient will be small. On the other hand, if the transition is allowed, the extinction coefficient is larger. The integrated extinction coefficient for one band in the absorption spectrum is related to the transition probability from the lower ground state to the upper excited state. The reciprocal of the transition probability is the lifetime of the upper state before it spontaneously reverts to the ground state by emitting a photon (Brulatti, 2010).

Figure 1.3

Franck-Condon effect for absorption and emission for excited and ground states of the same geometry and size

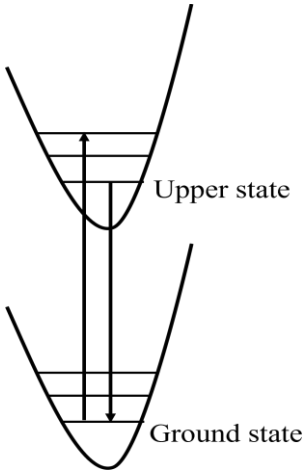

1.1.2.2 Emission

To observe emission by a molecule, excitation must occur in the first place, in other words, the excited state needs to be populated, and if the energy required comes from absorbed light, then the subsequent emission of a photon by a molecular system is referred to as luminescence. Upon absorption of a photon of light of a suitable wavelength, an electron is promoted to a higher energy orbital, producing a singlet excited electronic state ($S_1/S_2/S_3$) (Stanitska et al., 2024). The way in which emissions occur from $S_1/S_2/S_3$ can be visualised by the Jablonski diagram in **Figure 1.4**.

Figure 1.4

The Jablonski diagram shows the excitation and decay processes

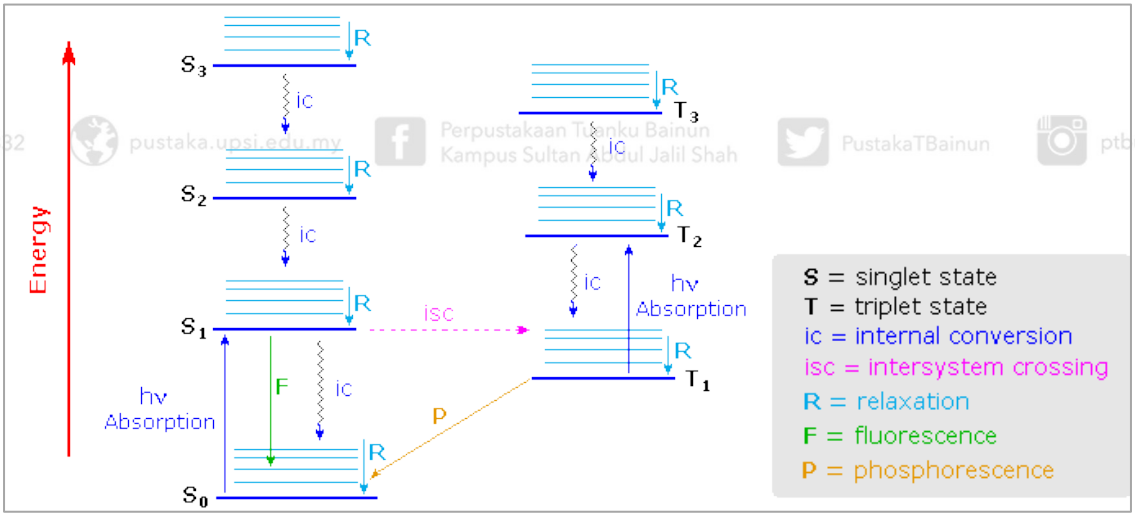

In this diagram, as a result of absorption, the electron occupies the S_1 orbital, and sometimes higher absorption energy can make the electron occupy higher orbits, such as S_2 and S_3. Once an electron is excited, there are many ways that energy may be dissipated. The ways the excited state decays to the ground state can be any of these three ways: (i) photochemistry, which is the decomposition of the original molecule, (ii) luminescence, which is radiative decay by the emission of photons and (iii) non-

radiative decay by the loss of the thermal energy (Lee & Han, 2020; Stanitska et al., 2024).

The non-radiative decay process is through vibrational relaxation, labelled as **R** in **Figure 1.4**; it occurs between vibrational levels, so generally, electrons will not change from one electronic level to another through this method. Each electron energy level (S_0, S_2, T_1) has a set of vibrational levels. Vibrational relaxation causes the electron to occupy the ground vibrational state of the electronic state. However, suppose vibrational energy levels strongly overlap with electronic energy levels. In that case, the excited electron can move from a vibrational level in one electronic state to a higher vibrational level in a lower electronic state. This process is called internal conversion (IC), as shown in the diagram, showing the electron switching from S_2 to S_1. No energy is emitted, and the electron now occupies an excited vibrational level of S_1 (Lee & Han, 2020; Stanitska et al., 2024).

Next is luminescence, which is divided into two types depending on the nature of the excited state, which are fluorescence and phosphorescence, discussed in detail as follows:-

a) Fluorescence

After the internal conversion occurs from the $S_2 \rightarrow S_1$, the electron can spontaneously move to the ground state of S_0 and hence revert spontaneously to the ground state, and this process is called the fluorescence mechanism. Theoretically, fluorescence involves the excited singlet state of the electron, which is the excited orbital paired by opposite spin to the second electron in the ground state orbital. Then, returning to the ground

state is a spin-allowed transition that occurs rapidly by the emission of a photon. The emission rates of fluorescence are typically 10^8 s^{-1} or faster without a change in multiplicity and a large energy difference between the ground state and the first excited state (typically $S_1 \rightarrow S_2$ transition. Previous studies have shown that much fluorescence happens at lower frequencies than exciting radiation because the emissive transition occurs after the energy is partially dispersed to the environment as vibrational energy. Many fluorescent materials absorb in the UV and blue region and emit in the visible region as green or orange light (Lee & Han, 2020; Stanitska et al., 2024; Yin et al., 2022).

b) Phosphorescence

The other way of luminescence to the ground singlet state, $S_{0,}$ is by phosphorescence, which is caused by an intersystem crossing (ISC), sometimes called spin-orbit coupling (SOC). The difference is that the electron transitions from a singlet to a triplet state. The relaxation is from an excited triplet state T_1 to the ground singlet state, $S_{0,}$ shown in **Figure 1.4**. The spontaneous crossing from the initially formed excited state (S_1) to a triplet excited state (T_1) of different spin occurs, a process named intersystem crossing. Intersystem crossing occurs when the energy curve of the singlet and triplet excited states cross each other, therefore, conversion from ↑↓ to ↑↑ of the electronic spins is possible, and the molecule enters an excited triplet state, followed by phosphorescence to occur (Lee & Han, 2020). Being spin-forbidden, phosphorescence is commonly characterised by a longer natural lifetime, whilst non-radiative processes are much faster at room temperature (Omar et al., 2018). Triplet-singlet transitions become more favoured when the spin-orbit coupling is relatively strong, for example, in heavy metal

complexes. Here, the process is accelerated by the strong spin-orbit coupling of the metal atoms that promotes the triplet-to-singlet transition by introducing a mixed character of singlet and triplet states and provoking a breakdown of the selection rules. In this situation, the spin quantum number thus becomes an inaccurate description of the system, and promotion of the spin-forbidden triplet-to-singlet radiative pathway increases the rate constant of phosphorescence to the point that it becomes competitive with the spin-allowed processes. Since the triplet excited states are always lower in energy than the singlet excited states according to Hund's rules, phosphorescent emission is lower in energy than the corresponding fluorescent emission.

1.1.2.3 Luminescence Quantum Yield

Quantum yield in terms of fluorescence or phosphorescence quantum yield is an important parameter to quantify OLED efficiencies. The efficiency with which a compound emits light can be quantified, which is the number of photons that are emitted per photon absorbed by the system. A transition metal complex in an excited state can also lead to a wide range of photochemical reactions due to the change in the electronic distribution caused by absorption. Thus, a different reactivity characterised the excited molecule compared to that of the ground state situation, and a large number of processes caused by molecular excitation are known. Significant, high spin-orbit coupling needs to occur for the phosphorescence process to be held; thus, the quantum yield will increase, and a relatively short phosphorescence lifetime will further increase the performance of a phosphorescent material over a fluorescence material (Na & Teets, 2018; Sarada et al., 2018).

1.1.3 Charge Transfer Transition

Metal complexes are susceptible to the absorption of light, which in some cases may lead to the transfer of an electron from the ligand to the *d* orbitals or vice versa. This transition is called charge transfer in which electrons move over a notable distance within the molecule. Since metal complexes have complicated electronic structures, the presence of both metal and ligand orbitals leads to a wide range of available excited states (Alsaeedi, 2023), as shown in **Figure 1.5**. Molecular orbitals (MOs) comprise several atomic orbitals. They can be described as predominantly metal or ligand character, depending upon which atomic orbitals have the most similar energy to the MO of interest. When radiation is absorbed, an electronic transition between two molecular orbitals occurs, and the resulting excited state can be characterised approximately by the molecular orbitals involved, as shown in **Figure 1.5**. Charge transfer involves displacement of the electronic charge from the ligands to the metal or vice versa and can be of several types. In metal complexes, the transitions that occur in absorption can often be classified as first approximation, as charge transfer, intraligand, or metal-centred. For example, metal-to-ligand charge transfer (MLCT) is an appropriate description when an electron is promoted from a d orbital of the metal to a π^* orbital of the ligand, or LMCT when the charge transfer can be regarded as an electronic transition from an orbital of the ligand to an orbital of the metal (Qu et al., 2014).

Similarly, electronic transitions can take place by promoting an electron between two orbitals localised on the ligand, such as $\pi \rightarrow \pi^*$ transitions (LC, ligand-centred, or intraligand transitions) (Qu et al., 2014). Also, metal-centred transitions (MC) may be observed in which the participating MOs are localised predominantly on

the metal centre and involve electron promotion between two orbitals of the metal (Qu et al., 2014). The transitions localised on the central metal ion are of the *d→d* type, usually observed in fluid solutions and relatively weak (Qu et al., 2014).

Figure 1.5

*Schematic energy-level diagram showing electronic transitions that happened during the absorption process for an octahedral transition metal complex (**MC**: Metal-centred Transfer, **LMCT**: Ligand to Metal Charge Transfer, **MLCT**: Metal to Ligand Charge Transfer, **LC**: Ligand-centred Transfer)*

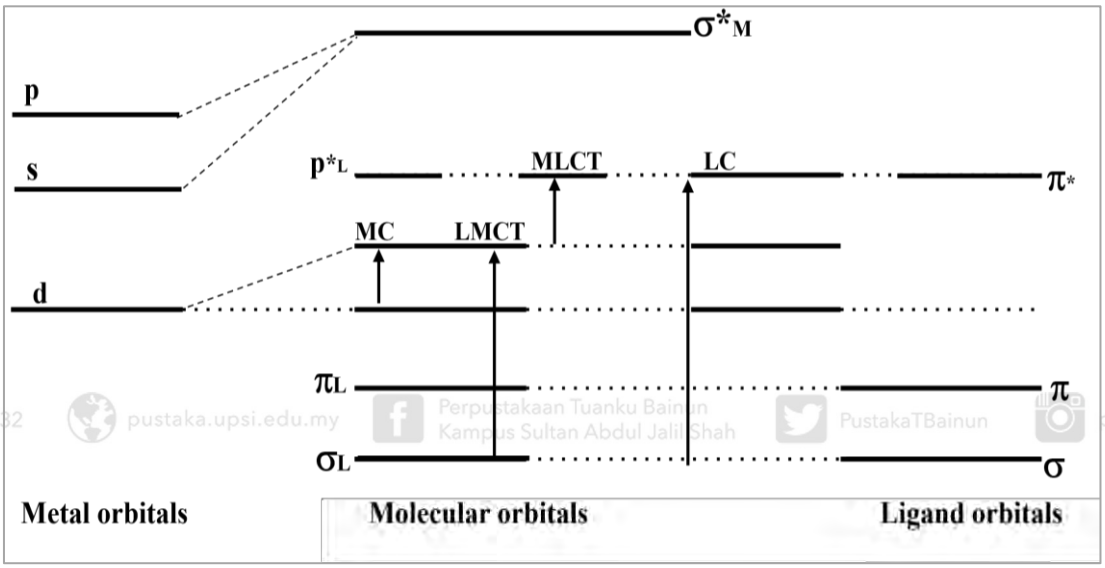

In conclusion, the charge transition is greatly affected by the luminescence properties and is one of the critical parameters to be dealt with in designing high-efficiency emissive materials for OLEDs.

1.1.4 Transition Metal Complexes Used for OLED Emissive Layer

Due to their photoluminescence properties, the studies of the luminescence complex of transition metal ions have become very interesting in solid-state technology. Transition metal complexes are coordination compounds formed by coordinating transition metal

ions with several ligands. The arrangement of ligands around the central metal ion is known as coordination geometry, and it often exhibits vivid colours due to the absorption of specific wavelengths of light corresponding to electronic transitions within the complex. In significance, a complex's absorption and emission colour depends on factors such as the identity of the transition metal ion, the oxidation state, the nature of the ligands, and the coordination geometry. Nowadays, great attention is currently focused on the synthesis of transition metal complexes and the study of their photophysical and electrochemical properties. Previous research has reported on various transition metals with d^6 or d^8 electronic configuration, such as platinum (Guijie et al., 2020; Omidyan et al., 2019; Sicilia et al., 2020), iridium (Han et al., 2022; Ryu et al., 2021; Sarada et al., 2018), ruthenium (Haghighatbin et al., 2018; Lakshmanan et al., 2018), and osmium (Buil et al., 2021; Omar et al., 2018) that have been utilised to form phosphorescent OLED emitters due to their efficient luminescence properties. Previously, they had shown that several families of these compounds are very interesting from the electrochemical and photophysical views.

1.1.4.1 Ruthenium-based Metal Complexes

Historically, ruthenium complexes were the first family of triplet emitters to be tested as light-emitting materials for solid-state devices. In 2008, the first ruthenium complexes exhibiting near-infrared emission were reported in **Figure 1.6** (Xun et al., 2008). By varying the ligands in these complexes, researchers were able to obtain a red shift of the photoluminescence (PL) emission from 650 nm to 1040 nm. The turn-on time for the different ruthenium complexes varied from a few seconds to a few hundred seconds, depending on the applied voltage (Ibrahim-Ouali & Dumur, 2019). These

complexes' emission and Photoluminescence Quantum Yield (PLQY) characteristics can be fine-tuned by varying the cyclometallating and ancillary ligands used (Ibrahim-Ouali & Dumur, 2019). However, more research is needed to fully understand the performance of ruthenium complexes in various device configurations, as numerous quenching processes happen during the excited state decay lifetime, making ruthenium complexes quickly replaced by iridium complexes nowadays (Haghighatbin et al., 2018).

Figure 1.6

Several ruthenium complexes were reported with near-infrared emission (Xun et al., 2008)

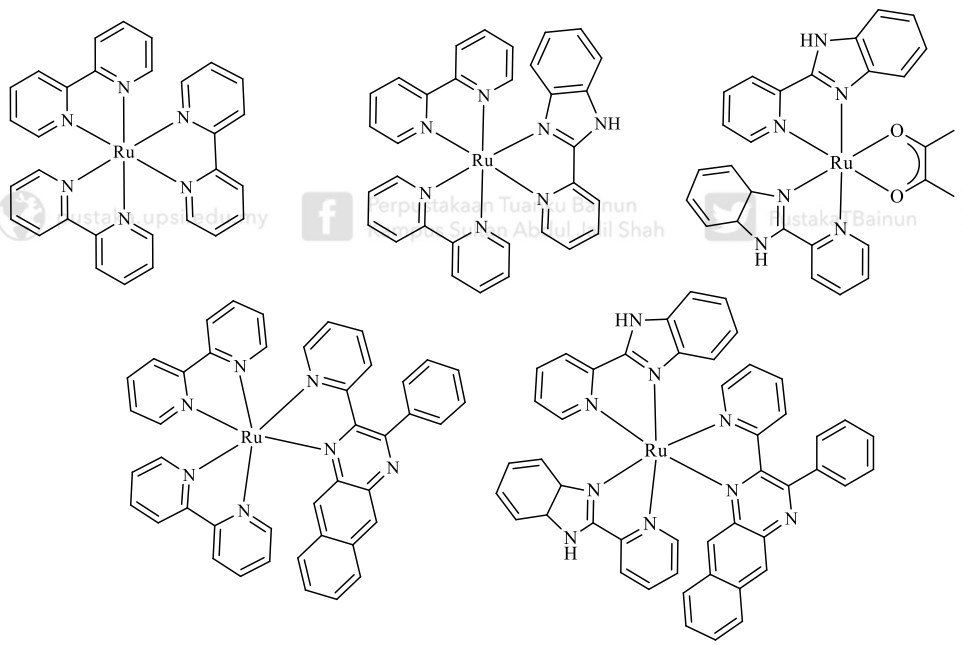

1.1.4.2 Platinum-based Metal Complexes

On the other note, various platinum complexes have been investigated to explore their suitability in OLED instrumentation. Recently, Pt(II) complexes have also demonstrated their potential in this type of application. Among them, complexes bearing bidentate or tridentate cyclometallated N-heterocyclic carbenes have been

shown as promising, efficient and stable blue-phosphorescent emitters (Sicilia et al., 2020). In these compounds, the strong metal-carbon bonds raise the energy of the MC states, hindering their photothermal population and then increasing the emission quantum yield and avoiding degradation via bond-breaking processes (Fuertes et al., 2017). The use of bidentate cyclometallated carbenes, as **Figure 1.7,** allows for tuning the emission properties by changing the nature of both the cyclometallated and the ancillary ligands. In this field, blue-emitters have been reported, but they were still limited in particular, particularly for solution-processable OLEDs

Figure 1.7

Several bidentate cyclometallated carbene ligands coordinate to platinum complexes (Fuertes et al., 2017; Sicilia et al., 2020)

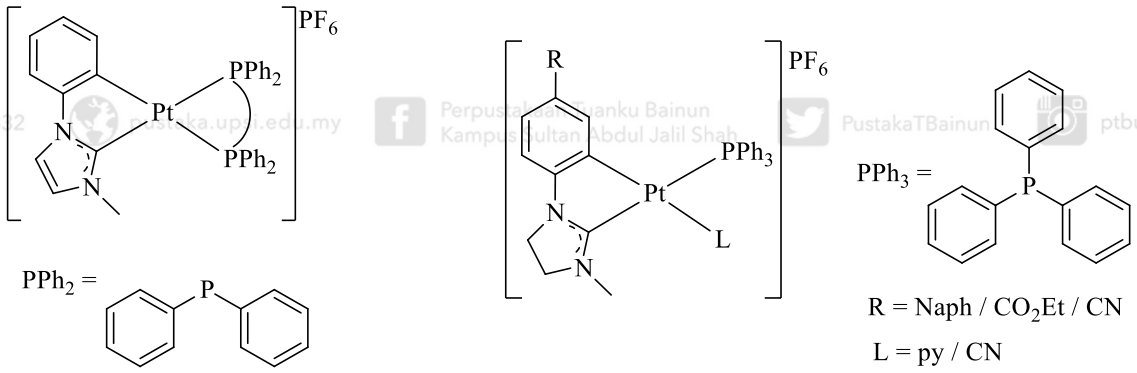

1.1.4.3 Gold-based Metal Complexes

The other significant transition metal complex is based on gold ions as shown in **Figure 1.8**, which are among the promising enhancers of photophysical and electroluminescent properties. Over the past 15 years, the development of gold(III) complexes as emissive dopants has been rapidly evolving. Highly efficient solution-processed and vacuum-deposited gold(III)-based OLEDs with sky blue, green, yellow, orange, red, and white

emission colours have been achieved. However, further investigations are needed to improve the colour gamut of the devices to satisfy the standard recommended by the International Telecommunication Union (ITU), in which the CIE coordinates for blue, green, and red emissions are (0.131, 0.046), (0.170, 0.797), and (0.708, 0.292), respectively. In the case of gold, research has lagged behind, probably because of the low-lying *d-d* states that result in a facile population of the $dx^2–y^2$ orbital and effective non-radiative decay by thermal equilibration (Tang et al., 2021).

Figure 1.8

Gold(III)-based complexes emitters with pincer template ligand (tridenttate behaviour) and extended π-conjugation within both the ancillary ligand (Beucher et al., 2020)

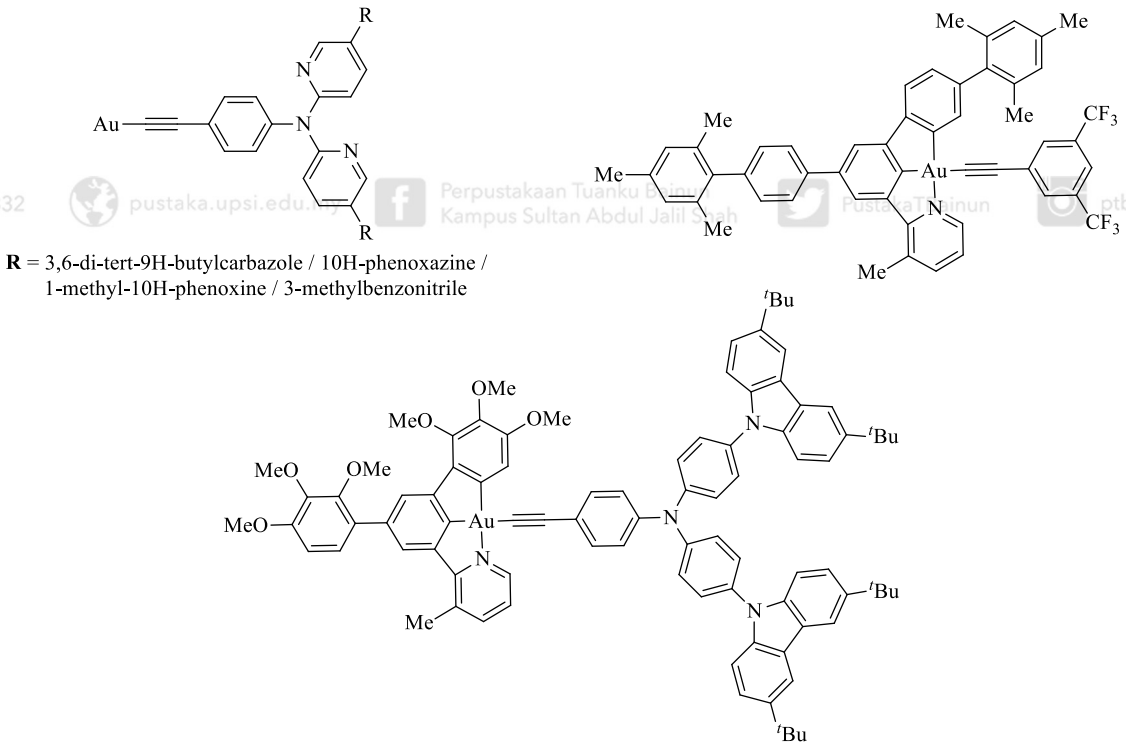

R = 3,6-di-tert-9H-butylcarbazole / 10H-phenoxazine / 1-methyl-10H-phenoxine / 3-methylbenzonitrile

In some cases, the susceptibility of gold(III) complexes to decomposition via reductive elimination has been a key limitation (Tang et al., 2016). This challenge can be mitigated by employing cyclometalation to enhance the stability of the gold(III) centre. Furthermore, systematic modulation of electron density, steric hindrance, and π-

conjugation within both the ancillary ligand and the pincer template behaviour (tridentate ligand behaviour) has been demonstrated to effectively tune emission colour across the visible spectrum, from blue to red, thereby enabling the development of high-performance devices (Beucher et al., 2020). As a result, highly efficient gold(III)-based emitters are under extensive investigation for use in both solution-processed and vacuum-deposited OLEDs, as shown in **Figure 1.8**, with increasing attention to improving device operational stability. Ongoing studies also aim to elucidate the molecular orientation of gold(III) complexes in doped films.

1.1.5 Choice of Ligand for Iridium Complexes

In general, the phosphorescent properties of iridium(III) complexes strongly depend on the coordinating ligands' abilities to act as electron donors or acceptors (Ahn et al., 2011). In particular, to achieve a blue shift in the emission wavelength, the energy gap between the highest occupied molecular orbital (HOMO) and the lowest unoccupied molecular orbital (LUMO) must be increased by stabilising the HOMO and/or destabilising the LUMO energy levels. This can be accomplished through strategic ligand design. The HOMO energy can be lowered by introducing electron-withdrawing groups, which reduce electron density at the metal centre through inductive effects, or by employing strong π-acceptor ligands. Conversely, the LUMO energy can be raised by incorporating electron-donating groups, which increase electron density through inductive or resonance effects, or by modifying the ancillary ligand to reduce orbital overlap and π-back bonding (Adeloye et al., 2017; Yafei Wang et al., 2016). These electronic modifications effectively widen the HOMO–LUMO energy gap, resulting in a blue-shifted emission and promoting efficient blue phosphorescence. Thus, the proper

choice of ligand is critical to achieving the desired electronic tuning for high-performance blue-emitting iridium(III) complexes.

1.1.5.1 Phenylpyridine Cyclometallating Ligand

This study employed phenylpyridine ligand in the cyclometallating moiety of the iridium(III) complexes, as phenylpyridine has been proven to be a potent ligand for blue emitters. Tamayo et al were the first researchers to report the modification of phenylpyridine ligands to enhance the emission energy of iridium(III) complexes (Tamayo et al., 2013). Their approach focused on methods to decrease the HOMO energy while keeping the LUMO energy relatively unchanged by adding electron-withdrawing groups such as fluoride on phenylpyridine ligands, resulting in a blue-shift emission of complex *fac*-Ir(phenylpyridine)$_3$ **(Figure 1.9)**.

Figure 1.9

Molecular structure of complex fac-Ir(phenylpyridine)$_3$

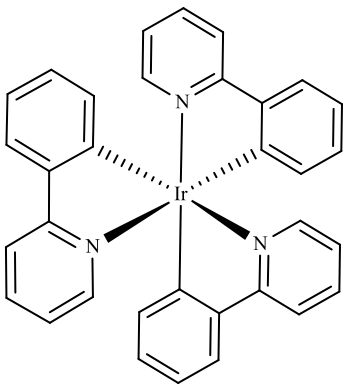

fac-Ir(phenylpyridine)$_3$

1.1.5.2 2-(1,2,4-triazol-1-yl)pyridine Ancillary ligand

At the same time, N-heterocyclic carbene of 1,2,4-triazole ligand was selected for the ancillary moiety of the complexes synthesised in this study. 1,2,4-triazole became the area of interest in this study due to the facile modification and high potential to achieve good photophysical properties (Flifel & Hlail, 2017). 1,2,4-triazoles have a pair of isomeric chemical compounds with molecular formula $C_2H_3N_3$, other than 1,2,3-triazole, which has a five-membered ring of two carbon atoms and three nitrogen atoms azole ring. These properties made triazole readily bind with different substituents via diverse non-covalent interactions, thus displaying versatile chemical activities. Compared to imidazole and pyrazole, triazoles are expected to have a more facile modification in achieving a wide range of ligands to alter the photophysical properties of the desired iridium(III) complexes. In addition, the newly synthesised complexes with carbene complexes have proven to have excellent quantum yields and good thermal stability (Ryu et al., 2021). Tailoring 1,2,4-triazole with a different substituent, such as 4-methylbenzyl and 2,6-difluorobenzyl, alters the HOMO-LUMO energy gap by destabilising the LUMO energy level. The stronger the electron-withdrawing ability of the substituent, the higher the HOMO-LUMO energy gap was, resulting in higher blue shifting (Cortés-Arriagada et al., 2015).

1.1.6 Computational Perspective in the Studies of Metal Complexes

A computational perspective of molecular modelling is an insightful method for discussing material properties at the atomistic level and guiding the synthesis of new materials through molecular designs. A density functional theory (DFT) is an effective

method that has been widely utilised in photofunctional complexes. In the simplest definition, DFT is the use of a computer to solve the equations of a model or theory for the properties of chemical systems. DFT is a well-known technique that can provide information on molecules and reactions that are impossible to observe experimentally due to the short-lived, unstable, and complex nature of the transition state. In designing phosphorescent iridium(III) complexes, DFT can help in the structural studies as a preliminary screening for synthesising organometallic ligands, confirming model approximation and lastly, as conformational studies, especially for the molecular orbitals studies (Mitani et al., 2020).

An exchange-correlation (XC) of hybrid functionals, which usually determines the calculation accuracy, has been primarily used in chemistry, such as B3LYP, PBE, PBE0, M06L, and M11L. Nowadays, the time-dependent functional theory (TD-DFT) has become the favoured method for accurately predicting photophysical properties in organic and inorganic molecules, specifically for excited-state properties (Hopmann, 2016). TD-DFT can efficiently simulate the absorption spectrum from the ground state geometry and search for the geometries of the excited state. As a result, the predicted emission spectra and the excited-state dynamics method can be obtained. Besides that, the lowest excited states of iridium complexes are usually triplet states. Thus, the DFT calculation can achieve an approximation of triplet excited state geometries such as ^{3}MLCT and ^{3}MC excited states, making this a valuable method for calculating the excited state geometries. The disadvantage of the TD-DFT method is that it may take a longer time than the DFT method. Typically, the solvation effect is included in the TD-DFT method calculation for closely modelling actual experiments (X. Zhang et al., 2019).

There are two models for simulating solvents: explicit and implicit models. The explicit model is a simulation of solvent molecules, and it has a limitation in that it can only be applied to medium-sized solutes. Meanwhile, the implicit model is performed as a dielectric medium without a solvent structure, and the solvent is limited within a cavity determined by the molecular structure. Another substantial effect for the metal complexes is a relativistic effect, which is occasionally utilised for ground and excited-state properties. To calculate the relativistic effect, including the SOC effect, the four-component Dirac equations are reduced to two-component procedures such as the Zero Order Regular Approximation (ZORA) (Smith et al., 2016).

In the case of iridium(III) complexes, the geometry used in a calculation is essential for predicting the emission energy and lifetime. Previous studies have reported the phosphorescent properties using optimised triplet geometry reasoning from the exciton population on the T_1 manifold. On the other hand, some reports show that the emission properties obtained from optimised singlet geometry were in good agreement with the experiment (Li et al., 2011; Minaev et al., 2009). A better correlation with the experimental calculation was found by calculating emission energies from both singlet and triplet geometries. These observations can be described by the vibrational mode relating to the change between the singlet and triplet geometries. The triplet state displays a shallow and anharmonic potential, so the maximum wave function is located between the singlet and triplet equilibrium geometries. Reliable calculations of phosphorescent lifetimes were performed using the Quadratic Response (QR) approximation associated with the TD-DFT method for different iridium(III) complexes. To sum up, DFT and TD-DFT computational methods were among the insightful techniques in discussing material properties at the atomistic level and guiding

the synthesis of high-emission energy of blue phosphorescent iridium(III) complexes (Hopmann, 2016).

In conclusion, computational chemistry is a powerful method to enhance the study of the photophysical and electrochemical properties of metal complexes. Significantly, the theoretical study of metal complexes analysis strongly needs the role of computational chemistry, especially the DFT and TD-DFT analysis, to develop phosphorescent transition metal complexes suited to the OLED application.

1.2 Problem Statement

Phosphorescent iridium(III) complexes have been extensively studied and have been the focus for decades due to their potential application in OLED, particularly for flat panel displays and lighting devices. Between the three primary colours in displaying white OLED, such as blue, green and red, phosphorescent red and green emitters are well established with excellent device lifetimes. In contrast, the design and development of highly efficient, long-lived blue emitters is still an ongoing challenge (Fu et al., 2023). In this regard, the design and synthesis of deep-blue-emitting phosphorescent iridium(III) complexes are particularly difficult. The main challenges in developing deep-blue-emissive iridium(III) complexes are that they lack sufficient colour purity for the ideal Commission Internationale de L'Eclairage (CIE) coordinates of (0.14, 0.09) and have low emission efficiency (Fu et al., 2023). Although high quantum efficiencies (QE) exceeding 30% have been achieved for green and red OLED devices, high QE for deep-blue OLED devices have rarely been reported (D. Wang et

al., 2020). These difficulties are related to the properties of blue phosphors that have faster decomposition due to their highly energetic excited states.

In addition, the material used to produce blue light OLED degrades more rapidly than the other two colours, which eventually throws off the colour balance and reduces the overall brightness of the display or lighting devices (Fu et al., 2023; Yao et al., 2023). Improving photostability refers to enhancing the resistance of the complex to degradation or breakdown when exposed to light over extended periods, which is essential for maintaining emission efficiency and device lifespan. This not only increases production time and cost but also reduces the reproducibility of the final product, which is one of the essential factors for industrial scalability. Hence, even iridium(III) complexes show deep blue emission, but they will show poorer efficiencies compared to their red- and green-emitting counterparts previously (Fu et al., 2023). Moreover, there are only a few reports concerning the design and preparation of pure and intense blue phosphorescent materials at room temperature. Thus, the design and development of blue-light-emitting iridium(III) complexes is highly desirable and has become an area of significant interest nowadays to answer the problem of lacking high efficiencies in blue phosphorescence emitters, especially for OLEDs.

In addition to the photophysical and stability challenges, a significant problem that persists during the synthesis stage of blue-emitting iridium(III) complexes is the limited availability of suitable ligands that can be easily synthesised, purified, and reliably coordinated to the iridium centre. Many ligand frameworks used to achieve high triplet energies or improve photostability are synthetically complex, requiring multi-step procedures with low overall yields and sensitivity to air or moisture (Lee & Han, 2020). Moreover, the control of regioselectivity and ligand geometry during

complex formation is crucial, as even slight structural differences can significantly alter the electronic and emissive properties of the final complex (Buil et al., 2021). Addressing these synthetic challenges requires a careful balance between molecular design, synthetic accessibility, and performance, highlighting the need for new ligand systems that are both functionally robust and synthetically practical.

Additionally, the difficulty in precisely controlling the stoichiometry and purity of the final complex is another significant issue. Iridium(III) complexes are highly sensitive to slight deviations in the ligand-to-metal ratio, and any imbalance can result in defective products with suboptimal photophysical properties (Zhu et al., 2023). The precise preparation of homogeneous complexes with well-defined stoichiometry often requires tedious purification steps and is prone to contamination by unwanted side-products, leading to further complications during synthesis (Lee & Han, 2020; Zhu et al., 2023). Overcoming this challenge is critical for scaling up the synthesis of high-performance blue-emitting iridium(III) complexes and achieving consistent material properties for OLED applications.

While the scientific and technical rationale for developing these complexes is compelling, it is also important to consider their potential industrial impact, particularly regarding production costs and scalability (Fan et al., 2023). Iridium is a rare and costly metal, and the synthesis of its complexes often involves multiple steps, low yields, and sophisticated purification techniques, all of which contribute to high manufacturing costs (Fan et al., 2023). For real-world applications, these challenges must be addressed through process optimisation, more efficient ligand synthesis, and scalable methods, such as continuous flow chemistry or greener reaction conditions.

Despite these limitations, the exceptional photophysical properties of Ir(III) complexes, particularly their ability to achieve triplet harvesting and high emission efficiency, make them valuable candidates for high-end OLED technologies, where performance may justify higher material costs. Improvements in device lifetime, colour accuracy, and brightness can offset the initial investment, especially in premium markets such as smartphones, TVs, and specialised lighting. Therefore, the development of efficient blue phosphorescent materials is not only a scientific challenge but also a critical step toward the broader commercial viability of full-colour phosphorescent OLED displays. Up to now, most strategies to tune the photophysical efficiencies of iridium(III) complexes have been by substitutions of donor or acceptor moieties on the pyridine or the phenyl groups of the phenylpyridine ligand moiety. Therefore, appropriate substituents on the phenylpyridine ligands or the bipyridine cause a shifting of the light emission from the red to the almost blue region of the visible spectrum.

1.3 Research Objectives

Below are the objectives designed to answer all the research problems highlighted before: -

a) To synthesis blue phosphorescent iridium(III) complexes and characterise the chemical properties using spectroscopic techniques and elemental analyser instrumentation.

b) To study the structural properties of the synthesised iridium(III) complexes using X-ray crystallography analysis and Density Functional Theory (DFT) investigation.

c) To investigate the photophysical properties of the synthesised iridium(III) complexes using spectroscopic techniques: Ultraviolet-Visible (UV-Vis), fluorescence and photoluminescence (PL).

d) To analyse the effect of electron-withdrawing (EWG) or donating capabilities (EDG) of ancillary ligands on the ground states of the synthesised iridium(III) complexes using the DFT and TD-DFT calculations.

1.4 Hypotheses

a) New phosphorescent iridium(III) complexes bearing N-heterocyclic Carbene (NHC) ligand will be synthesised from the reflux reaction of dichloro-bridged iridium(III) dimer complex with the triazolium-based ligand.

b) The experimental structural properties of single-crystals will be aligned to their respective theoretical DFT data, confirming the successful synthesised of all the complexes.

c) Blue emission with significant phosphorescence efficiencies of iridium(III) complexes will be characterised in this study.

d) The frontier molecular orbital (FMO) studies of the synthesised iridium(III) complexes will show the HOMO-LUMO band gap increment due to the ancillary ligand modification. For instance, ancillary ligands with electron-withdrawing substituents will destabilise the LUMO energy. At the same time, the one with an electron-donating effect will stabilise the LUMO energy.

1.5 Scope of Study

Since most OLEDs aim for high colour purity of the three primary colours, blue, green, and red, it is vital to modify the molecular structure of iridium(III) complexes to achieve the most promising high colour purity phosphors. Hence, this research focused on altering the ancillary ligands of phosphorescent heteroleptic iridium(III) complexes with several carbene-based ligands differing by their EWG or EDG properties to achieve high blue purity phosphors. Specifically, novel ancillary ligands were employed with and without fluorine cyclometallating ligands to study their effect on the phosphorescence efficiencies, decay-lifetime process, and purity of blue emission. In addition, the ground state was optimised using DFT to analyse structural properties, frontier molecular orbitals, and quantum efficiency. The TD-DFT methods and solvation effect were also explored for a reliable calculation protocol.

In particular, all the analyses in this thesis were explicitly designed to achieve the excellent parameter of high-energy blue phosphorescent iridium(III) complexes for OLED application. The overview structure of this thesis is simplified as follows:-

Chapter 1 comprehensively introduces the history of OLEDs and explains several transition metal complexes utilised as the emitters of OLEDs. This chapter includes the problem statement, research objectives, hypotheses, and scope of study.

Chapter 2 described a comprehensive literature review of the synthesis of iridium(III) complexes and their photophysical properties. A brief comparison of preliminary work on decay lifetime and photoluminescence quantum yield was

discussed. In addition, some previous work from our laboratory was included to provide a chronological experimental history of this research.

Chapter 3 described the detailed experimental, instrumentation, and methodologies to synthesise phosphorescent iridium(III) complexes with novel ancillary ligands that can improve the intensity of blue emission and efficiency of OLED devices.

Chapter 4 discussed the spectroscopic and photophysical aspects of the synthesised iridium(III) complexes that bear new formimidamide-based ancillary ligands experimentally and computationally. The DFT and TD-DFT calculations described all the mechanisms, including spectroscopic calculations, efficiency calculations, and band gap analyses.

Chapter 5 describes the conclusion and recommendations of this study. Finally, all the supporting documents were included in the appendices section.

CHAPTER 2

LITERATURE REVIEW

This chapter will detail the preliminary studies of iridium(III) complexes designed for blue-efficient phosphorescence. The first part of this literature study will explain the concept of designing blue efficient iridium(III) complexes through ligand molecular design. Next, the previous significant report on blue efficient phosphorescent iridium(III) complexes was analysed in this literature review. Finally, the significant reports on the DFT and TD-DFT analysis related to the design strategy of highly efficient iridium(III) complexes used for OLED applications were discussed.

2.1 Significance of Iridium(III) Complexes over other Metal Complexes

Considering the price and scarcity of iridium, it may seem counterintuitive that iridium-based complexes are extensively used as emissive materials in OLEDs. However, their exceptional photophysical properties justify their prominence. Iridium is a well-known heavy metal with a $5d^6$ electronic configuration that enables strong spin-orbit coupling, a key factor in enhancing phosphorescence efficiency. This coupling allows for efficient mixing between singlet and triplet excited states, thereby relaxing spin-forbidden transitions and enabling intense phosphorescence even at room temperature, with quantum yields often approaching unity (Chan et al., 2017; Zhou et al., 2016). In addition, most iridium(III) complexes adopt a low-spin configuration, which is favoured due to the strong ligand field typically generated by cyclometalating and ancillary ligands. This low-spin state helps maintain a large energy gap between the t_{2g} and e_g orbitals, contributing to their photostability and controlled excited-state dynamics (Monti et al., 2021). Furthermore, the emission lifetimes of these complexes typically range from hundreds of nanoseconds to several microseconds, offering a balance between brightness and lifetime (Alsaeedi, 2023). These features collectively make iridium(III) complexes highly attractive despite their high cost and rarity.

In most cases, it can be seen that the emission lifetime of iridium(III) complexes is more extended with intense phosphorescence at room temperature than those of Platinum(II), Osmium(II), and Ruthenium(II) complexes. In general, multi-colour display applications require efficient and stable blue, green, and red OLED emitters. Iridium cyclometallates, as mentioned earlier, exhibit favourable photophysical properties for OLEDs, including longer excited-state lifetimes, high quantum efficiencies, and good stability (Henwood & Zysman-Colman, 2017; Omar et al., 2018;

Yafei Wang et al., 2016). The emission colour can be readily tuned from blue to red by judicious modification of the cyclometallating ligands and/or ancillary ligands (Henwood & Zysman-Colman, 2017).

The fact that the iridium(III) complex has easy emission colour tunability makes it possible to obtain luminescence colours from blue to red, spanning the whole visible region, which meets the need for red, green, and blue emitters of OLED. As the related uses of the iridium(III) complexes strongly depend on the characteristics of their ground and excited states, it is crucial to have a deep investigation regarding the interactions between these states and thus come up with a systematic strategy to alter the photophysical properties by modifying their molecular structure making the study about iridium become the central area of interest nowadays (Henwood & Zysman-Colman, 2016; You et al., 2021).

For OLED applications, phosphorescent materials are preferred over fluorescent materials as they can retain their excited state for a relatively extended period before emitting light due to the intersystem crossing of the heavy metal effect (Monti et al., 2021). The fact that iridium has proven to be a phosphorescent emitter that can emit light from both singlet and triplet excited states gives this metal a longer phosphorescent lifetime than other fluorescent materials that typically only occur from singlet states. In purely organic fluorescent materials, the excited electron returns to the ground state from the lowest singlet excited state ($S_1 \rightarrow S_0$) through a spin-allowed transition. Triplet states (T_1), which are spin-forbidden, are typically non-emissive or decay through non-radiative processes, leading to energy losses. In contrast, iridium(III) complexes exhibit phosphorescence because the heavy metal centre

induces strong spin-orbit coupling, which facilitates intersystem crossing from singlet to triplet excited states and partially allows radiative decay from the triplet state ($T_1 \rightarrow S_0$). This makes spin-forbidden transitions partially allowed, enabling efficient emission from the triplet state hallmark behaviour of phosphorescent materials. The population of singlet and triplet states can be quantified using time-resolved photoluminescence spectroscopy, where fluorescence (from singlet states) typically appears within nanoseconds, while phosphorescence (from triplet states) is observed on microsecond to millisecond timescales (Mohd Yusoff et al., 2017; Q. Zhang et al., 2014). Therefore, using the phosphorescent iridium complex in OLEDs offers advantages in terms of efficiency, brightness, and colour quality compared to fluorescent materials. Thus, iridium is the most compatible heavy metal that can play an essential role in providing a heavy metal effect, enhancing phosphorescence efficiencies, and providing a vibrant display for OLED devices.

2.2 Critical Need for Efficient Blue Phosphorescent Emitters

Blue, green, and red are the primary colours behind the white OLED displays. Between these three primary colours, phosphorescent red and green emitters have been commercialised with well-established properties, such as having excellent OLED device lifetimes. In contrast, designing and developing highly efficient, long-lived lifetime blue emitters is still challenging (Baranoff & Curchod, 2015; Fu et al., 2023; Stanitska et al., 2024). The detailed problems regarding blue phosphors have been discussed in the problem statement in **Chapter 1**. Hence, the design and development of blue-light-emitting iridium(III) complexes is highly desirable and has become an

area of significant interest nowadays to answer the problem of lacking high efficiencies in blue phosphorescence emitters.

2.3 Strategies for Saturated Blue Iridium(III) Complexes

The strategies to achieve blue emission iridium complexes are summarised in **Figure 2.1,** and each of the strategies is discussed in detail in this subtopic.

Figure 2.1

Summary of factors that affect the efficiency of blue phosphorescent emitter iridium complexes

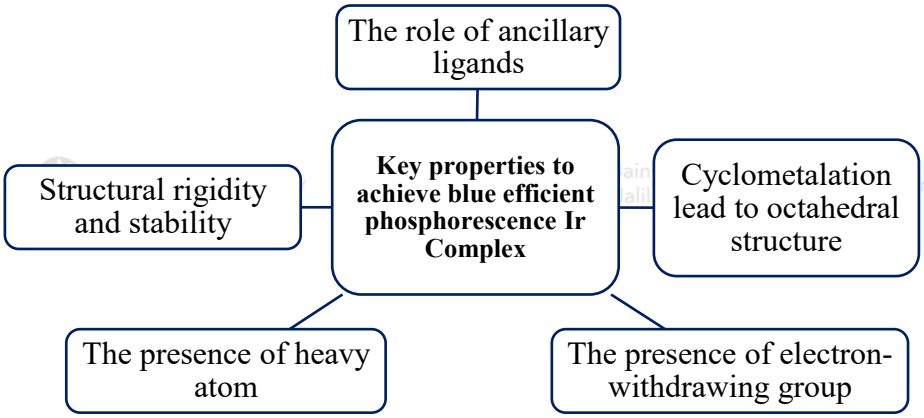

2.3.1 Cyclometalation

The feature of cyclometalated ligands (shown in **Figure 2.2**), where the ligands form a stable five-membered ring with the iridium centre, contributes to the cyclometallation properties. This five-membered ring strongly influences the emission energy of the synthesised complex as it affects the radiative and non-radiative constants of the complexes (Lee & Han, 2020). The deactivation of non-radiative can be inhibited to a

significant extent, thereby facilitating high energy emission and resulting in the desired blue colour emission required for OLED applications (Lee & Han, 2020).

Figure 2.2

Cyclometalated ligands are marked with blue, while the ancillary ligand moiety is marked with red, forming the cyclometallation behaviour of the complex

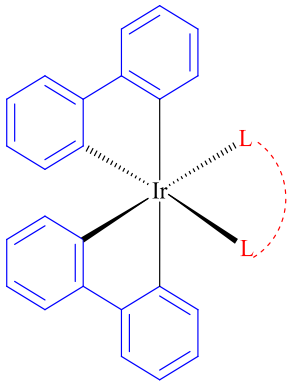

2.3.2 Ligand Engineering

In the case of iridium(III) complexes designed for blue phosphorescence, potent and strong field ligands are often used to increase the ligand-field splitting, leading to blue-shifted emission (Omae, 2016). Ligands must be engineered to stabilise the complex's excited states and optimise energy transfer (Cho et al., 2017). The ligand field's strength will depend on the ligand's ability to split the *d*-orbitals in the metal centre. Potent field ligands cause a more excellent splitting of the *d*-orbitals, influencing the energy difference between the metal-centred and ligand-centred orbitals, thus altering the band gap (Omae, 2016). For example, ancillary ligands with strong field strengths, such as those containing nitrogen or phosphorus donor atoms, can increase the metal-ligand bonding interaction, which raises the energy levels of the non-bonding *d*-orbitals of

iridium and can contribute to a more significant energy gap, favouring blue emission. The choice of ligand is significant for achieving deep-blue emission with the specific Commission Internationale de l'Éclairage (CIE) coordinates.

On the other hand, tailoring ligands to widen the band gap between the Highest Occupied Molecular Orbital (HOMO) and Lowest Unoccupied Molecular Orbital (LUMO) is another approach to achieve blue phosphorescence emission (Gökce et al., 2014; Kajjam & Vaidyanathan, 2018; Omae, 2016). The HOMO-LUMO band gap is a fundamental parameter that dictates the energy difference between the highest occupied molecular orbital and the lowest unoccupied molecular orbital. This gap determines the energy required to excite an electron from the HOMO to the LUMO, which in turn affects the wavelength of light emitted when the electron returns to the ground state. In practice, the HOMO–LUMO band gap in iridium(III) complexes can typically be widened by approximately 0.2 to 1.0 eV through ligand modification (Lee & Han, 2020; G. Li et al., 2018). For example, introducing strong electron-withdrawing groups such as $–CF_3$ or –CN on the cyclometalating ligands can lower the HOMO energy, while using rigid or less π-conjugated ancillary ligands can raise the LUMO energy (Sanner et al., 2016; Thomassen et al., 2020). Such adjustments can shift emission from orange (~580 nm, ~2.1 eV) to blue (~460 nm, ~3.0 eV), demonstrating the effectiveness of ligand engineering in achieving higher-energy phosphorescence suitable for blue OLED applications.

In the typical case of cyclometallated $[Ir(ppy)_2(bpy)]^+$ where ppy is phenylpyridine and bpy is bipyridine, HOMO was localised in the cyclometallated while LUMO is mainly in the ancillary ligand of bipyridine, as shown in **Figure 2.3** (Wang et al., 2019). Several approaches to increase its emission energy were focused

on methods to decrease the HOMO energy while keeping the LUMO energy relatively unchanged (Omae, 2016). Theoretically, increasing the emission energy means widening the energy gap between the HOMO and LUMO, which results in shorter wavelength (bluer) emission. Lowering the HOMO energy shifts its level further from the LUMO, effectively increasing the band gap without altering the excited state configuration significantly. The addition of electron-withdrawing groups to the phenyl ring has been used as one way to achieve the goal of blue-shifted emission energy (Omae, 2016), and the most common electron-withdrawing group used for this purpose is fluorine. The typical example of blue shifting is seen for *fac*-Ir(F_2ppy)$_3$ when compared to Ir(ppy)$_3$ in which stabilisation of HOMO occurred to broaden the HOMO-LUMO band gap energy (Parker, 2019). For instance, the use of ancillary ligands with LUMO destabilisation effects, such as carbene (Wu et al., 2020) and picolinate (Cho et al., 2017), can lower the energy of the LUMO more than that of the HOMO, increasing the energy gap and shifting the emission towards the blue region. Hence, the emission colour can be finely tuned by varying the ligand structure and the substituents.

Figure 2.3

a) Typical position of the frontier orbitals archetypal iridium complex [Ir(ppy)$_2$(bpy)]$^+$, b) Electron density contours of their HOMO and LUMO (Wang et al., 2019)

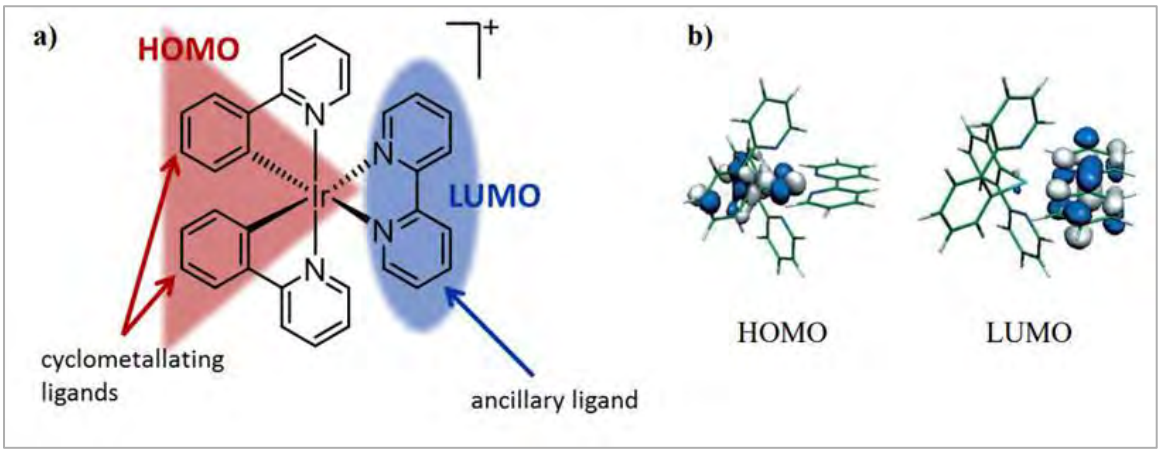

2.3.3 The Presence of Electron-Withdrawing Groups and Electron-Donating Groups

Many blue phosphorescent iridium complexes often include electron-withdrawing groups (EWG) such as fluorine, trifluoromethyl, or sulfonyl, either in the cyclometallated or ancillary moiety. The most outstanding EWG was fluorine, which has been proven as the HOMO stabiliser, increasing the energy gap and shifting the emission towards the blue region. However, the presence of fluorine has been reported to result in low photoluminescence quantum yield, which is crucial for OLED applications (Baranoff et al., 2012; Li et al., 2018). In contrast, electron-donating groups (EDG) such as alkyl groups and amino groups can increase the energy of the HOMO, making EDG more suitable to be utilised as the ancillary ligand so that LUMO destabilisation can be experienced to achieve blue emission (He et al., 2016).

2.3.4 Heavy Atom Effect

The presence of the iridium atom itself is essential to achieve blue phosphors of iridium(III) complexes. Iridium is a heavy atom, as a critical factor as it promotes strong spin-orbit coupling. The spin-orbit coupling is the interaction between the electron's spin and its orbital motion around the nucleus. In heavy atoms like iridium, the nucleus has many protons, which creates a stronger electric field around the atom. This field affects the electron's motion, causing a greater interaction between the electron's spin and its orbit. As a result, the singlet and triplet excited states, which are typically "spin-forbidden" (meaning they do not easily interconvert), become mixed (Maroń & Małecki, 2014; Zulkifli et al., 2023). For iridium, this spin-orbit coupling is strong

enough to allow intersystem crossing, a process where the molecule transitions between singlet and triplet states. This transition between states is what makes phosphorescence possible, as it enables the system to emit light even after the electron moves to a lower energy state, which is key for long-lasting emission typical in phosphorescent materials. This effect facilitates intersystem crossing from the singlet to the triplet state, which is essential for phosphorescence (Chan et al., 2017; Omar et al., 2018).

2.3.5 Structural Rigidity and Stability

Blue efficient phosphorescent iridium complexes often have a rigid ligand framework, which helps reduce non-radiative decay processes and enhances the photoluminescence quantum yield (PLQY). In addition, the complexes showed excellent stability under operational conditions and had a lengthy lifespan for the OLED devices. The example of the ligand with structural rigidity included a combination of both cyclometalated and strongly σ-donating ligands such as carbene compounds (Omae, 2016). The extent of conjugation within the ligand strongly affects the electronic distribution and, consequently, the band gap. Conjugated systems often lower the band gap by extending the π-system, while rigid, non-conjugated ligands can maintain or increase the band gap (Han et al., 2022; He et al., 2016). For saturated blue phosphorescence, ligands with minimal conjugation or those designed to restrict π-conjugation are preferred to achieve a higher band gap and blue emission (He et al., 2016).

Chiu et al. found that the solid-state PLQY can be increased by more than one order compared to that in solution (Chiu et al., 2009). This result suggests that a cyclometalated iridium(III) complex with rigid conformation can suppress motional

relaxations and increase photoluminescence quantum yield. The structural origin of these behaviours can be understood by considering the temperature-independent decay process and the vibronic-coupled non-radiative (NR) decay process. Therefore, cyclometallated iridium(III) complexes with rigid structures have been extensively studied to restrict intramolecular motions and minimise NR decay. The increments of PLQY with blue efficient phosphorescence are often observed in solid-state complexes, such as frozen solutions and doped polymer films.

2.3.6 Coordination Geometry

The geometry of the iridium complex, which is influenced by the ligand's coordination, has also impacted the synthesis complex's electronic properties. Ligands that enforce a particular geometry, such as octahedral or square planar, can influence the overlap between the metal's *d*-orbitals and the ligands' *p*-orbitals, affecting the band gap (Chan et al., 2017). Precise geometry control through ligand design helps in tuning the emission properties; hence, the octahedral iridium(III) complex will be the choice to aim for blue phosphorescence properties.

2.4 Overview of Ligands Used for Enhancing Blue Phosphorescence in Iridium Complexes

After carefully analysing the strategies for achieving saturated blue iridium complexes in the previous subtopic of 2.3, it can be seen that all factors are strongly related to the choice and design of ligands. Since cyclometallating and auxiliary ligands have been reported to affect the HOMO-LUMO band gap significantly, it is crucial to conduct a

preliminary study on the choice of ligand that has been utilised to fabricate a blue efficient phosphorescent iridium complex needed for OLED.

2.4.1 Phenylpyridine-Based Ligand

Phenylpyridine (ppy) is derived as C^N ligands when attached bidentately to iridium metal. Generally, all C^N ligands are considered to be derived from the archetypal ligand phenylpyridine in iridium(III) complex $Ir(ppy)_3$. Previously, ppy was among the monoanionic C^N chelating ligands utilised in the homoleptic iridium(III) complex. As shown in **Figure 2.4**, a complex of $Ir(ppy)_3$ exists as two different isomers, namely facial (*fac*) or meridional (*mer*) configurations (Sanner et al., 2016).

Figure 2.4

The mer and fac isomers in $Ir(C^N)_3$ (where C^N = cyclometallating ligand of phenylpyridine) complexes (Sanner et al., 2016)

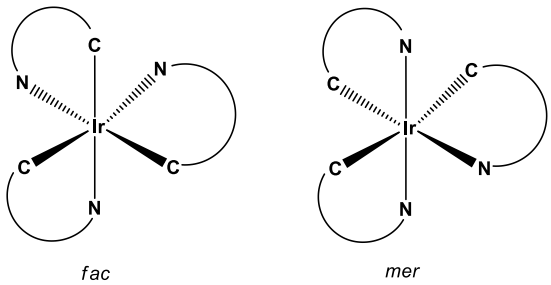

The two isomers show different structural properties, considering that the *fac* isomer Ir–C and Ir–N bonds are nearly the same length. On the other hand, for the *mer* isomer, the bond situated in a *trans* position to the Ir–C bond is longer than those *trans* to an Ir–N bond. The two isomers can thus manifest different behaviour in terms of electrochemical and photophysical properties (Suzuri et al., 2014). Besides that, these

two isomers show negligible differences in emission energy, specifically in the green region of the spectrum with λ_{max} presented in **Table 2.1**. The emission originates from a state primarily of ^{3}MLCT character due to the higher energy of the ^{3}LC state (ppy phosphorescence λ_{max} = 460 nm). Due to the strong field cyclometallating ligands, the ^{3}MC state is thermally inaccessible at temperatures of up to at least 398 K. Consequently, at room temperature, $Ir(ppy)_3$ displays a relatively broad and featureless emission spectrum. DFT calculations agree with the assigned MLCT character in which the HOMO orbital is primarily localised on the iridium centre and the cyclometallating phenyl groups. In contrast, the LUMO orbital is localised mainly on the pyridyl moieties. Thus, this orbital pattern is typical for cyclometallated Ir complexes based on ppy ligands.

In addition, the photoluminescence quantum yields (PLQYs) of the *mer* isomers and their emission lifetimes are significantly lower than those of the *fac* isomers. These significant differences between the quantum efficiencies of the mer and fac isomers are due to an efficient bond-breaking process in the mer excited state, which acts as an effective quenching path leading to the isomerisation of the *fac* type (Omae, 2016).

Table 2.1

Photophysical and Electrochemical Properties of Fac- and Mer-$(ppy)_3Ir$

Complexes	**λem (nm)**	**τ (μs)**	**PLQYs (%)**
fac-$(ppy)_3Ir$	510	1.9	40
mer-$(ppy)_3Ir$	512	0.15	3.6

Source: (Tamayo et al., 2013)

To tune the emission colour by changing the C^N ligand structure, there are three widely used ligand engineering strategies: (i) extending aromatic conjugation, (ii) using heterocyclic rings, and (iii) peripheral substituents of the ligand core. Theoretical investigation suggests that these modifications alter both the energy of the highest occupied molecular orbitals (HOMO) and the lowest unoccupied molecular orbitals (LUMO), as well as the nature of emissive triplet states.

Further modification on the ppy ligand has been done by the Tamayo group by utilising an electron-donating methyl group ($Ir(tpy)_3$) and electron-withdrawing group fluorine atoms ($Ir(4,6\text{-}dfppy)_3$) as shown in **Figure 2.5.** The emission data of these complexes, shown in **Table 2.2,** significantly reveal that $Ir(4,6\text{-}dfppy)_3$ with fluorine atoms exhibits a blue shift. The emission in the *mer* isomers is broad and red-shifted compared to the *fac* forms. Besides, the PLQY and the emission lifetime of the *mer* isomers are significantly lower than the *fac* isomers of the identical cyclometallating ligands (Omae, 2016). Besides, a complex of *tris*[2-[3-(dimesitylboryl)phenyl]pyridinato]iridium $Ir(Bppy)_3$ exhibited bright green phosphorescence with an emission lifetime and PLQY of 1.0–1.4 μs and nearly 100%, respectively, in nonpolar or polar solvents at 298 K (**Table 2.2**).

Figure 2.5

From left shown $(tpy)_3Ir$, $(4,6\text{-}dfppy)_3Ir$ and $Ir(Bppy)_3$

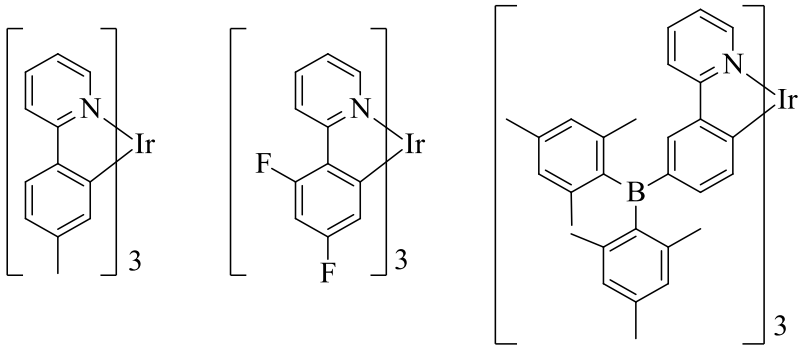

The HOMO of $Ir(Bppy)_3$ is localised on the iridium centre atom and the cyclometallating phenyl rings in the ppy groups, which are similar to those of $Ir(ppy)_3$. In contrast, the LUMO of the complex is best characterised by the electron densities on the boron atoms. Thus, the lowest-energy absorption transition in $Ir(Bppy)_3$ is assigned to metal-to-boron charge transfer (MBCT). According to DFT calculation, the emission state compound is considered a metal-boron charge transfer (MBCT) excited state in which an excited electron occupies the vacant p-orbital on the boron atom. Introducing arylborane charge transfer units to a ligand in a transition metal compound has enhanced the absorption and emission efficiencies through MBCT interactions (Ito et al., 2011). Overall, the complex $Ir(Bppy)_3$ is in the range of weak lifetime calculation for blue materials, so further modifications to the molecular design still need to be investigated.

Table 2.2

Summary of Photophysical and Electrochemical Properties of Fac- and Mer-$(ppy)_3Ir$, $(tpy)_3Ir$ and $(4,6\text{-}dfppy)_3Ir$

Complexes	λ_{em} (nm)	τ (μs)	PLQYs (%)
fac-$(tpy)_3Ir$	510	2.0	50
mer-$(tpy)_3Ir$	550	0.26	5.1
fac-$(4,6\text{-}dfppy)_3Ir$	468	1.6	43
mer-$(4,6\text{-}dfppy)_3Ir$	482	0.21	5.3
$Ir(Bppy)_3$	494	1.4	100

2.4.2 Ancillary ligand engineering

Ancillary ligands are ligands that do not have significant contributions to the emissive triplet states. Usually, they possess very high triplet states that cannot be easily populated, thus having a minor impact on energy emissions. Common ancillary ligands include picolinate acid (pic) (Baranoff et al., 2011; Cho, Kim, et al., 2017; Omidyan et al., 2019); acetylacetone (acac) (Altinolcek et al., 2020); and triazole-pyridine derivatives (Bain et al., 2020; Walden et al., 2019). Although ancillary ligands are non-chromophoric and are not able to emit light, the ^{3}LC energy will remain invariant upon changing ancillary ligands. It has already been reported that changing ancillary ligands may alter the energy of ^{1}MLCT states. The composition of MLCT in the T_1 state was found to decrease when the complex has deeper HOMO levels, resulting in a longer excited state lifetime (Monti et al., 2021).

2.4.2.1 Piconate ancillary ligand

Picolinate is a ligand derived from picolinic acid, a pyridine derivative. The chemical structure of picolinic acid includes a pyridine ring with a carboxylate group (-COO^{-}) attached to the 2-position (adjacent to the nitrogen atom). As a ligand, picolinate coordinates to metal centres through the pyridine ring's nitrogen atom and the carboxylate group's oxygen atom, making it a bidentate ligand. This coordination forms a stable five-membered chelate ring with metal ions. When picolinate ligands are incorporated into iridium complexes, picolinate ligands form stable chelate rings with the iridium centre, enhancing the complex's overall stability. This stabilisation is crucial

for achieving desirable photophysical properties in iridium complexes. In addition, the bidentate coordination of picolinate to iridium affects the electron density around the metal centre. The nitrogen and oxygen donor atoms provide different electronic contributions, which can modify the complex's metal-to-ligand charge transfer (MLCT) properties.

Figure 2.6 shows a series of iridium complexes coordinated with picolinate ancillary ligands. Complex 1 is (*Fac*-Iridium(III) Bis(4,6-difluorophenyl)pyridinato-N,C^2) Picolinate), FIrPic, which is a commercial blue-emitting iridium complex used in OLEDs, known for its high quantum efficiency, long excited-state lifetime, and stable emission, making it photophysically excellent for optoelectronic applications with $\lambda_{emission}$ = 468 nm. Complex 2–9 in **Figure 2.6** shows the blue phosphorescence of iridium complexes that coordinate with picolinate ligand but have modification on their cyclometallated moieties by adding electron-deficient N atoms on the phenyl ring. Adding more F on the phenyl ring does not necessarily raise emission energy and adding electron-donating substituents on the neutral N part (pyridine). Overall, all the complexes 1–9 share the similarities of having picolinate ancillary ligands, and they successfully achieved blue emission colour (Cho et al., 2017; Liu et al., 2021; Omidyan et al., 2019; Tao et al., 2017).

Figure 2.6

Representative blue iridium(III) complexes incorporating picolinate ancillary ligand with their respective emission energy (Z. Liu et al., 2021)

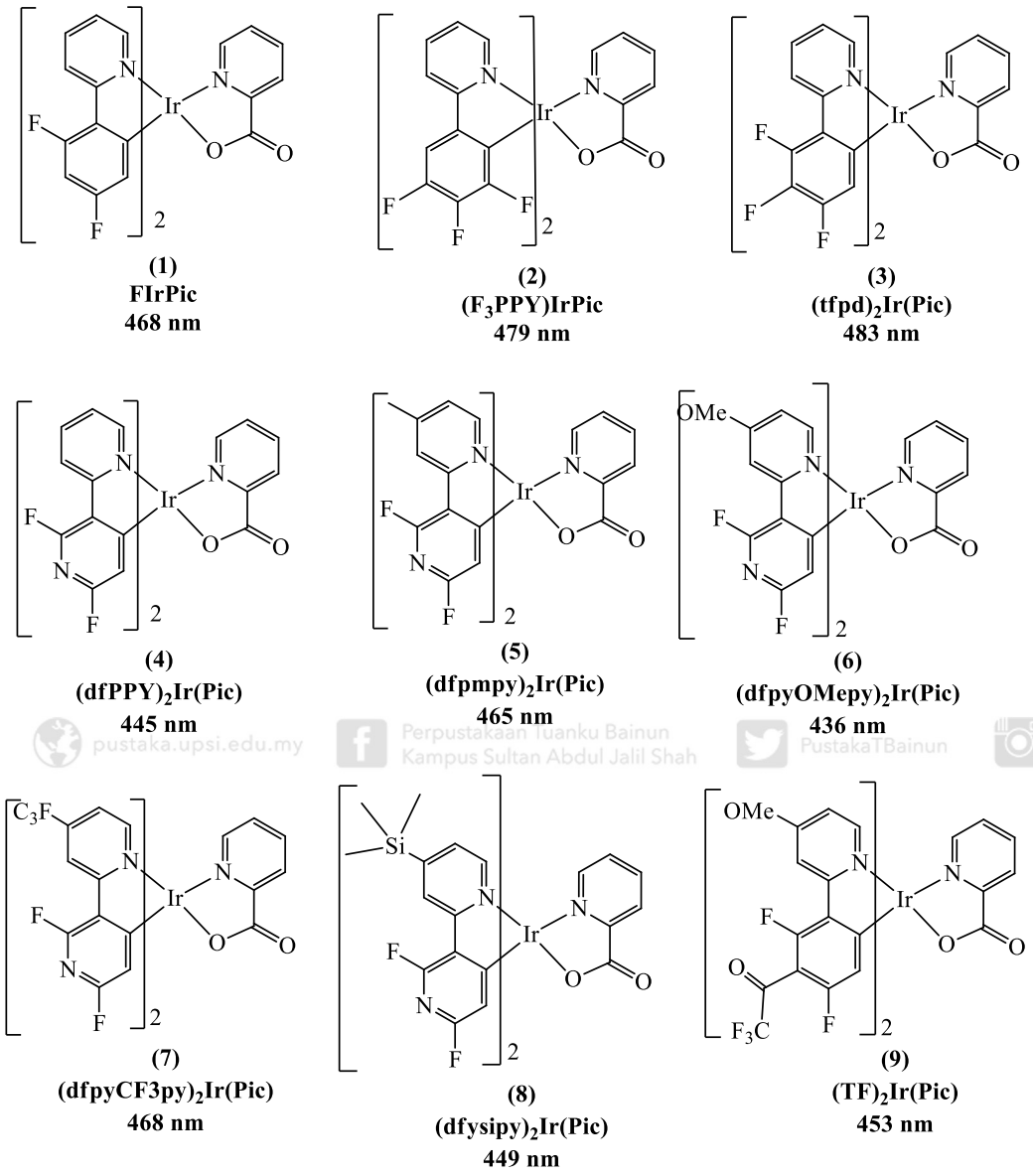

2.4.2.2 Triazole-based ancillary ligand

Triazole-based ancillary ligands were reported to be suitable for achieving higher emission energy of iridium complex due to their higher triplet state of the N-heterocyclic five-membered ring (Complex 10, **Figure 2.7**). Adding peripheral

substituents (Complex 11 and 12, **Figure 2.7**) and adding N atoms with tetrazole (Complex 13) do not significantly impact the emission energy. In recent years, iridium(III) complexes bearing bis-NHC ligands have proved their advantages in tuning blue emissions. The high triplet energy of NHC coordination and strong σ donating nitrile (C≡N) group as monodentate ligand contributes to the blue emission of dfpypyCN (Complex 14, 436 nm), in comparison with $(dfpypy)_2Ir(pic)$, 445 nm (Complex 4, **Figure 2.6**) and $Ir(dfpypy)_3$ (Complex 15, 438 nm). Recent reports state that the chemical modification of triazole-derived ancillaries may result in different emitting dipole orientations. **Figure 2.7** shows the ancillary ligand engineering strategy for heteroleptic complexes.

Figure 2.7

Representative blue iridium(III) complexes incorporating ancillary ligand engineering with their respective emission energy

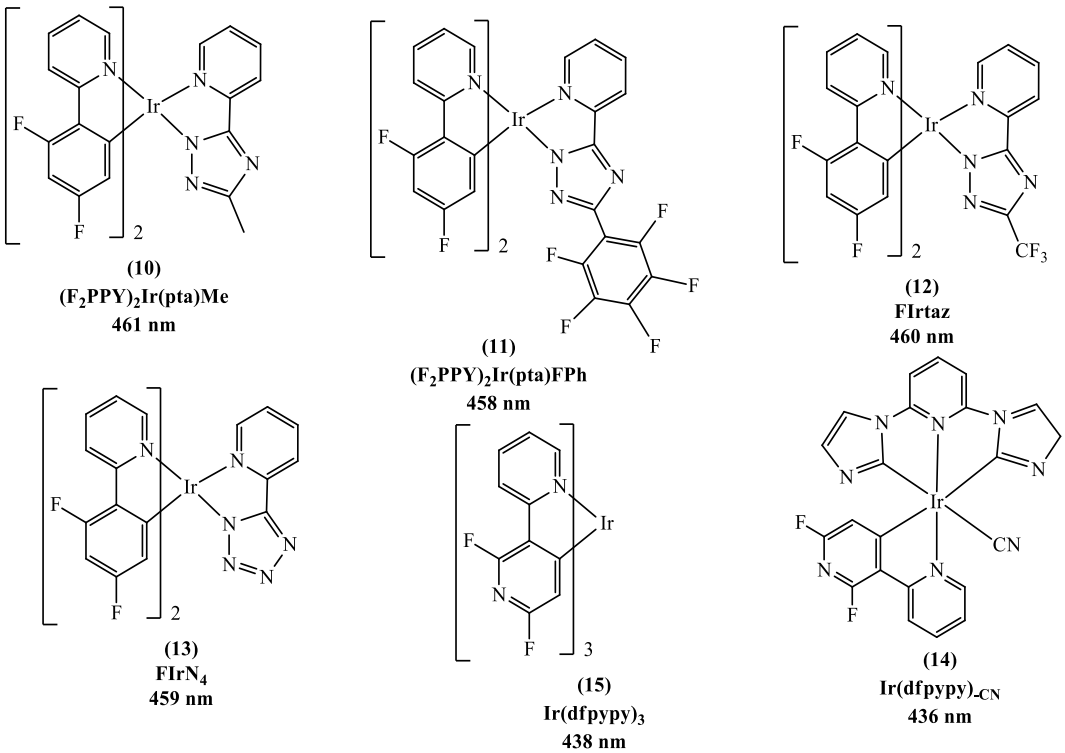

2.4.2.3 Acyclic Diamino Carbene (ADC) base ligand

Acyclic Diaminocarbene (ADC) ligands are characterised by their planar structure, where the carbene carbon atom is bonded to two nitrogen atoms in a sp^2 hybridised state. As shown in **Figure 2.8**, ADC ligands were marked in blue, and it clearly shows that the C−N bonds in these ligands are intermediate between single and double bonds, reflecting the resonance between the lone pair on nitrogen and the carbene centre. This resonance contributes to the strong electron-donating ability of the ADC ligands, which will enhance the LUMO destabilisation and lead to efficient blue emission energy. The ligands also exhibit a degree of rotational flexibility around the N−C bond, which allows them to adapt to different coordination environments when bound to metal centres (Kinzhalov et al., 2019). Due to the strong electron-donating properties, steric control, and rotational flexibility, complex 15–16 has vibronic emission energy with a blue and green colour emission (Eremina et al., 2020). To summarise, ADC-based iridium complexes have enormous potential in OLED applications, even though the invention of this complex is still new compared to other commercial ligands.

Figure 2.8

Various cyclometallated iridium(III) complexes bearing different ADC ancillary ligands, with their respective emission energy

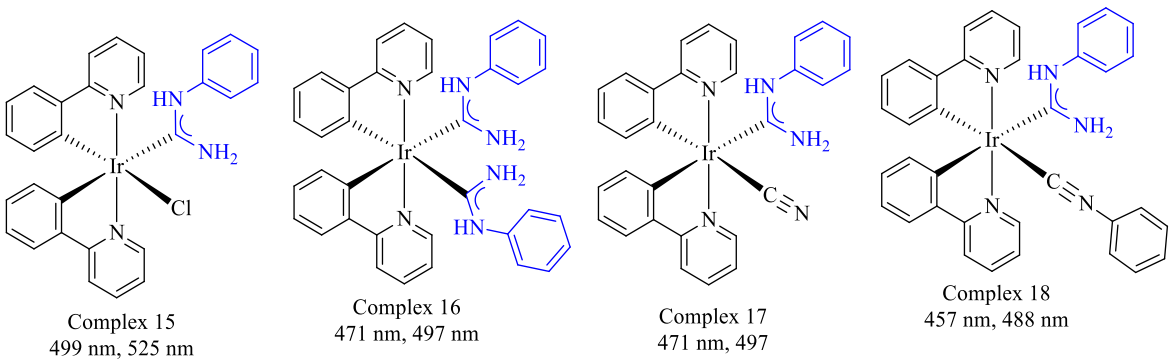

2.4.2.4 N-heterocyclic Carbene (NHC) Ancillary Ligand

N-heterocyclic carbenes (NHCs) are cyclic compounds containing a divalent carbon atom bound to at least one nitrogen atom within the heterocycle. **Figure 2.9** shows some of the most commonly applied types of NHCs (Schuster et al., 2009). They have attracted particular attention as ancillary ligands because of their donating properties, steric hindrance, and stabilising properties (Ferreira et al., 2013), similar to the ADC ligand.

Figure 2.9

Different Types of Carbene Compounds (Schuster et al., 2009)

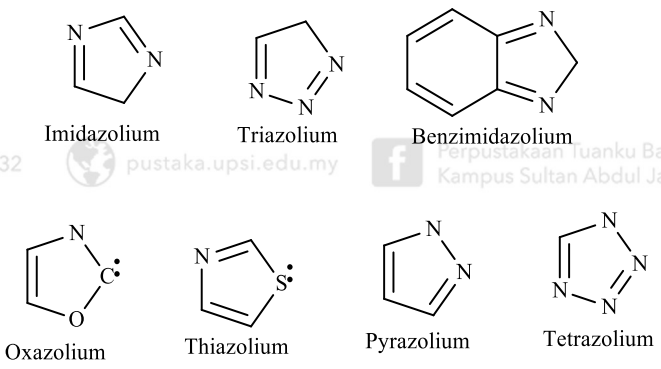

Their ability to act as donors and the resulting stable bonds to most transition metals make them excellent ligands in coordination chemistry (Hopkinson et al., 2014). These exclusive characteristics of NHCs have been utilised to produce ligands for OLED phosphors. In particular, the carbene ligand has a stronger field than traditional N-heterocycle-based ligands, as they can increase the Ir-carbene bond strength and remarkably destabilise the LUMO levels. In addition, this strong Ir-carbene bond retards the ^{3}MC state generation. Thus, the thermal and photostabilities of these complexes are impressively high, as shown in **Figure 2.10**.

Figure 2.10

Effect of NHC ligand on destabilisation of non-emissive state (^{3}MC) on iridium(III) complex

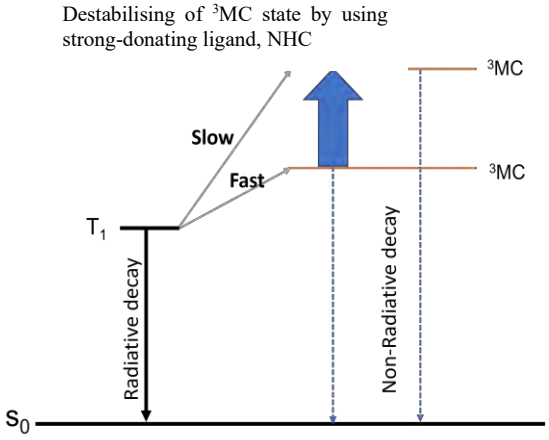

The most outstanding iridium(III) carbene complex reported was utilising an imidazolium-based ancillary ligand, and one of them is Ir(dFppy)$_2$(1-(2-trifluoromethyl)phenyl-3-methylimidazole), which utilised a trifluoromethyl substituent on the phenyl moiety of carbene ligand shown in **Figure 2.11** (Li et al., 2015). The HOMO-LUMO gaps were increased by modifying the phenyl moiety in the NHCs with electron-withdrawing substituents of trifluoromethyl, and the emissions were blue-shifted accordingly in good performance of the OLED device.

Figure 2.11

Chemical structure of iridium(III) carbene complexes of Ir(dFppy)$_2$(1-(2-trifluoromethyl)phenyl-3-methyl imidazole) (Li et al., 2015)

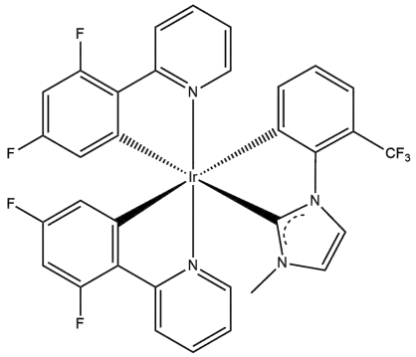

Crystal structure analysis of Ir(dFppy)$_2$(1-(2-trifluoromethyl)phenyl-3-methyl imidazole) (**Figure 2.11**) showed that the average Ir-$C_{carbene}$ distance (2.026 Å) is significantly shorter than the average Ir-C_{phenyl} distance, indicating that the carbene moiety is more strongly bound to the Ir than the phenyl ligand. A shorter bond distance concluded that the ligand is a strong-field ligand. Accordingly, strong-field carbene ligands destabilise thermally accessible non-emissive states, and carbene-based iridium(III) complexes exhibit higher photoluminescence quantum yields than other iridium(III) complexes, making them well suited to the OLED application.

2.5 Overview of the Recent Development of Blue Phosphorescence Iridium(III) Complexes and Their Efficiencies

The past 10 years have significantly developed blue efficient phosphorescent iridium(III) complexes in various modifications of ligands. This subtopic highlights some aspects related to the homoleptic and heteroleptic species, especially those with highly efficient phosphorescence properties. As the introduction, such octahedral cyclometallated iridium(III) complexes can be divided into two basic categories (Li et al., 2018), which are:

a. Homoleptic complexes which feature identical ligands (usually three monoanionic C^N chelates)
b. Heteroleptic complexes that feature non-identical ligands (usually two identical monoanionic C^N chelates and a third non-identical chelate).

2.5.1 Homoleptic Species Iridium(III) Complex

The most common strategy for achieving blue-shifted emission of cyclometalated iridium(III) complexes may be introducing electron-withdrawing groups (EWGs) to the phenyl ring of a cyclometalated ligand. The computational investigation of complex $Ir(ppy)_3$ revealed that the HOMO is mainly localised at the Ir *d*-orbital and phenyl moiety. The LUMO is localised at the pyridyl moiety, as shown in **Figure 2.12** (Smith et al., 2016). Therefore, introducing EWGs to the phenyl ring allows stabilisation of the HOMO energy level. Furthermore, decoration of the pyridyl unit with an electron-donating group can heighten the LUMO energy level. For example, in **Figure 2.6**, Thompson et al. reported that the introduction of F atoms at positions 4– and 6– on the $Ir(ppy)_3$, with the resultant complex being named *fac*-$Ir(dfppy)_3$, significantly shifts the emission from 510 to 468 nm, with similar PLQY = 0.43 and emission lifetime (τ_{em} = 1.6 μs) (Sajoto et al., 2009).

Figure 2.12

(a) The absorption spectrum of $Ir(ppy)_3$ in 10 μM solution of dichloromethane (inset: chemical structure) and (b) orbital contributions of their HOMO and LUMO

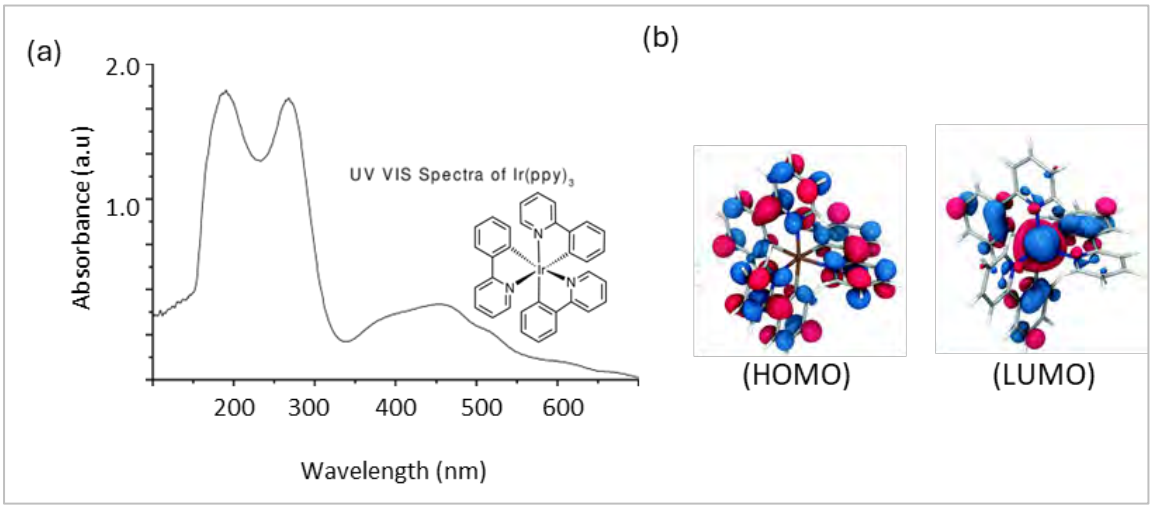

Figure extracted from the work by Lee & Han, 2020.

Another exploration of the number of F atoms in the same molecular architecture has been studied (Lee & Han, 2020). Complex 19 utilised one more F atom that is substituted at the 3-position of the phenyl ring, and the emission shows a hypsochromic shift to 459 nm (**Figure 2.13)**. On the other perspective, the emission of the tetrafluorinated complex 20 (**Figure 2.13)** shifts to lower energy at 468 nm. De Cola et al. suggested that the lower emission energy of complex 20 is due to the more positive reduction potential caused by the presence of more F atoms. Note that these two complexes have different emission quantum yields, which are 0.30 and 0.53 for complexes 19 and 20, respectively. Their respective emission lifetime was found to be τ_{em} =1600 ns and τ_{em} = 2300 ns at room temperature. Different stabilities for devices fabricated with the *fac*- and *mer*-isomers were also observed when OLED was fabricated using complexes 19 and 20.

Further theoretical studies performed by the Tian group revealed that the differences between complexes 19 and 20 are due to the different transition dipole moments (Li et al., 2011). The same effects were also observed for cationic iridium(III) complexes. De Angelis et al. reported a combined experimental and theoretical study comparing complex 23:dfppy-based complex and complex 24: a ppy-based complex (**Figure 2.13)** (De Angelis et al., 2007). Those authors controlled the phosphorescent emission wavelength and improved the photoluminescence quantum yields by modulating the electronic structures of the cyclometalated iridium(III) complexes through F functionalisation. The F-functionalised complex 24 showed blue-shifted emission at 463 nm with a higher PLQY = 0.85 than complex 23 (λ_{max} = 491 nm, PLQY = 0.80) in acetonitrile solution. Different emission energy was related to a dramatic decrease in the NR deactivation rate constant, which agrees with the 'Energy-Gap Law'.

The lifetime emission values were also found to increase from complex 23 (τ_{em} = 2.4 μs) to complex 24 (τ_{em} = 4.1 μs), yielding an overall reduction in the k_r; this suggests increasing π–π* character in the emitting excited states. DFT and TD-DFT calculations with solvent effects were conducted to characterise the lowest triplet excited states and revealed that the extensive mixing of the ^{3}MLCT and π–π* contributions agrees with the lifetime emission increment for complex 24 compared to complex 23. Summary of the photophysical properties of Complexes 19–20 and 23–24 tabulated in **Table 2.3.**

Figure 2.13

Chemical structure for homoleptic blue emission iridium(III) complexes 19-24

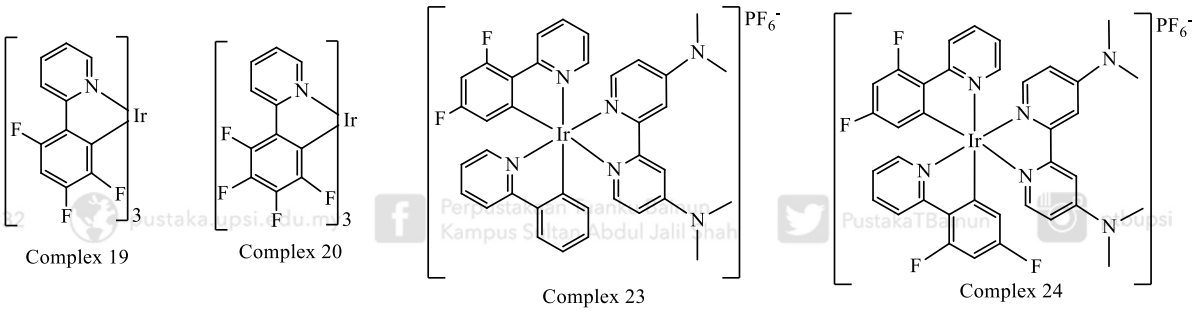

Table 2.3

Summary of Photophysical Properties of Complexes 19,20,23 and 24

Complex	Photophysical properties					Oxidative (V)
	λ_{em} (nm)	τ_{em} (μs)	PLQY	K_r (10^5 s^{-1})	K_{nr} (10^5 s^{-1})	
19	459, 486	0.1	0.03	1.9	4.4	-
20	468, 497	0.1	0.03	2.3	2.0	-
23	491, 520	2.4	0.80	3.3	0.8	0.72
24	463, 493	4.1	0.85	2.1	0.4	1.00

Other modifications were made by replacing phenyl pyridine ligands with phenyl heterocyclic ring systems, such as imidazole, pyrazole, and triazole. Note that imidazole-based homoleptic iridium(III) complexes have been used as blue dopants because the imidazole group can heighten the LUMO energy level, enlarging the energy gap and increasing the T_1 energy level. Kitamura group reported homoleptic and heteroleptic Ir(III)*tris*-phenylimidazolinate complexes (Karatsu et al., 2013). Upon replacement of the pyridyl ring with the imidazolyl ring, the LUMO mainly populates the phenyl ring; this is quite different from the LUMOs of ppy-based iridium(III) complexes. Accordingly, substituting an F atom into the phenyl ring in complex 25 **(Figure 2.14)** yields the bluest emission of 453 nm at room temperature (PLQY = 0.60) and a value of 446 nm at 77 K.

Kang's group studied imidazole-based iridium(III) complexes 26–28, as shown in **Figure 2.14**. However, with a bulky terphenyl unit on the N atom of the imidazoyl ring (Cho et al., 2016). Those researchers concluded that a complex 26 with a *ter*-phenyl ligand without alkyl chains is advantageous in terms of lifetime. In contrast, complexes 27 and 28 coordinated to the *ter*-phenyl with alkyl chains are efficient regarding PLQY. These results explained that the high PLQYs of complexes 27 and 28 assisted the triplet emission of the blue devices by effectively harvesting triplet excitons when employed in OLED devices.

In 2018, Lee's group had a significant report on complexes 29 and 30 utilising diisopropylphenyl-functionalised phenylimidazole-based ligand in the iridium(III) complexes, as shown in **Figure 2.14**. Compared to the ter-phenyl ligand, complexes 29 and 30 showed more blue-shifted emission at 454 nm (Kwon et al., 2018). Even though

the diisopropylphenyl group has less bulkiness than the terphenyl ring, this group still efficiently limits intermolecular aggregation and prevents the different self-quenching processes. On the other hand, the substitution of CN at the 5th position of phenyl carbon forming complex 30, as shown in **Figure 2.14,** and this complex was found to affect the device lifetime significantly, exceeding 550 h at 200 cd m^{-2} was obtained when instrumented in OLED.

Figure 2.14

Chemical structure of Chemical structure for homoleptic blue emission iridium(III) complexes 25–30

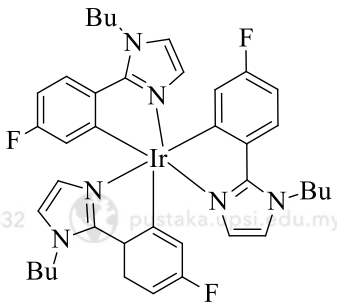

Complex 25

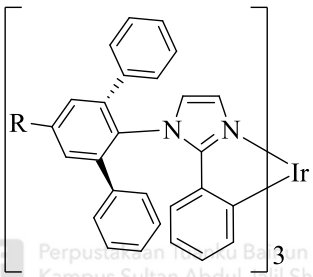

Complex 26: R = H
Complex 27: R =CH_3
Complex 28: R = Prophyl

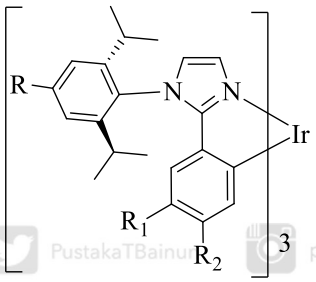

Complex 29: R_1 = H, R_2 = F
Complex 30: R_1 = CN, R_2 = H

Table 2.4

Summary of Photophysical Properties of Complexes 25–30

Complex	Photophysical properties				
	λ_{em} (nm)	τ_{em} (μs)	PLQY	K_r (10^5 s^{-1})	K_{nr} (10^5 s^{-1})
25	453, 482	3.4	0.60	1.7	1.2
26	461, 492	3.3	0.53	1.6	1.4
27	459, 487	-	0.45	-	-
28	462, 487	-	0.50	-	-
29	454, 484	1.1	0.87	7.9	1.2
30	462, 494	1.8	0.99	5.5	0.5

Homoleptic iridium(III) complexes with pyrazolyl-based ligands also had blue emission phosphorescence, shown in **Figure 2.15**. For example, Thompson et al. reported that the MLCT transitions of the pyrazolyl-based iridium(III) complexes of 31–33 are hypsochromically shifted relative to pyridyl-based complexes of complexes 34–35 (**Figure 2.15**) due to the higher triplet energy of phenylpyrazole at 3.28 eV compared to ppy at 2.88 eV. F substitution effectively shifts the emission further to the blue region, up to 21 nm. Notably, the phosphorescence of complex 32 was observed at 390 nm, which has rarely been reported. However, these homoleptic pyrazolyl-based complexes are not emissive at room temperature, which is unsuitable for an OLED emitter.

Figure 2.15

Chemical structure for homoleptic blue emission iridium(III) complexes utilised different behaviour of fluorine atoms 31–35

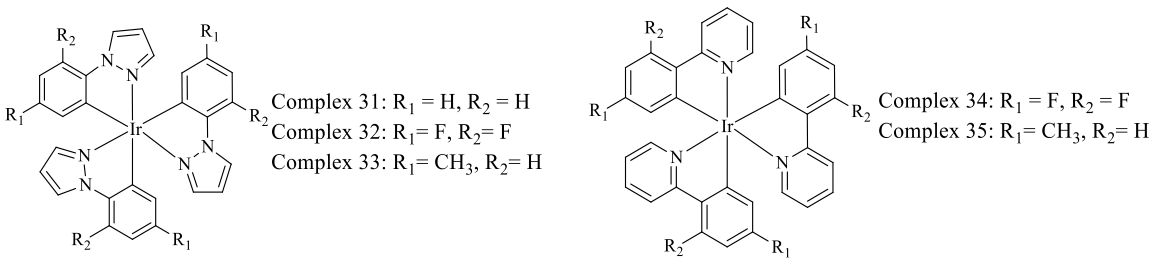

Table 2.5

Summary of Photophysical Properties of Complexes 31–35

Complex	Photophysical properties					Oxidative (V)
	λ_{em} (nm)	τ_{em} (μs)	PLQY	K_r (10^5 s^{-1})	K_{nr} (10^5 s^{-1})	
31	414	14	-	-	-	0.39
32	390	27	-	-	-	0.80
33	428	0.05	-	-	-	0.73
34	468	1.6	0.05	2.7	3.6	0.78
35	510	2.0	0.50	2.5	2.5	0.3

Powell et al. theoretically studied the effects of fluorination on the role of metal-ligand bond fission in the NR decay of excited states in cylcometallated iridium(III) complexes (Smith et al., 2012; Zhou et al., 2016). The calculated activation barrier to the ^{3}MC state shows a clear correlation with the experimentally obtained NR decay rate for a series of iridium(III) complexes. As ^{3}MC state formation requires breaking an Ir–N bond, Powell et al. compared Ir–N bond distances in the ^{3}MC states of cylcometallated iridium(III) complexes. For complexes 36 and 37 in (**Figure 2.16**), the Ir–N bond length changes in the ^{3}MC state relative to the ground-state structure are much more minor than those of complexes 38 and 39 (**Figure 2.16)**. Accordingly, the activation barrier to the ^{3}MC state is lower for complexes 38 and 39, which yields low PLQY.

Figure 2.16

Chemical structure for homoleptic blue emission iridium(III) complexes of 36–39 utilises 1,2,4-triazole-based ligands

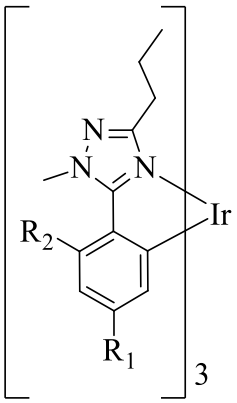

Complex 36: R_1 = H, R_2 = H
Complex 37: R_1 = F, R_2 = H
Complex 38: R_1 = H, R_2 = F
Complex 39: R_1 = F, R_2 = F

Table 2.6

Summary of Photophysical Properties of Complexes 36–39

Complex	Photophysical properties					Oxidative
	λ_{em} (nm)	τ_{em} (μs)	PLQY	K_r (10^5 s^{-1})	K_{nr} (10^5 s^{-1})	(V)
36	449	1.08	0.66	6.1	3.1	0.28
37	443	0.15	0.06	4.0	6.3	0.50
38	428	1.25	0.27	2.2	5.8	0.5
39	425	0.15	0.03	2.0	6.5	0.72

Samuel et al. extended their work to dendronised triazole-based iridium (III) complexes to attain a solution-processable material (Lo et al., 2008; Yang Wang et al., 2016). F-attached dendrimers 40–43 **(Figure 2.17)** show phosphorescence emissions at approximately 441 nm; however, these materials are unsuitable for device applications because of their low triplet energy and vibrational quenching, which yield luminescence quenching or low thermal properties (Lee & Han, 2020; Yang et al., 2016) To solve this problem, dendrons were later modified to have a twisted geometry and successfully utilised in a blue PHOLED device as complex 41. Complex 41, shown in **Figure 2.17**, is highly emissive, with PLQY = 0.94 and 0.6, and τ_{em} of 3.6 and 2.8 μs, in solution and neat film, respectively. Their high emissivity is attributed to the dendron rigidifying effect, which reduces the geometry change in the excited state (Yang et al., 2016). The summary of complexes 40–43 photophysical properties is tabulated in **Table 2.7**.

Figure 2.17

Chemical structure for homoleptic blue emission iridium(III) complexes 40–43

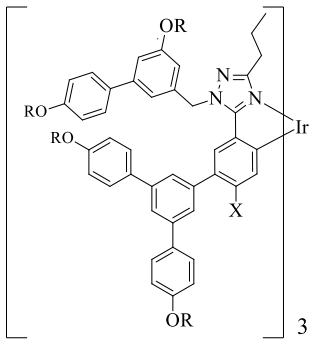

Complex 40: R = 2-ethylhexyl, X = H
Complex 41: R = 2-ethylhexyl, X = F

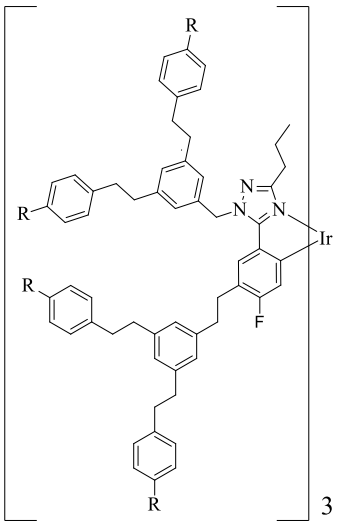

Complex 42: R = H
Complex 43: R = 2-ethylhexyl

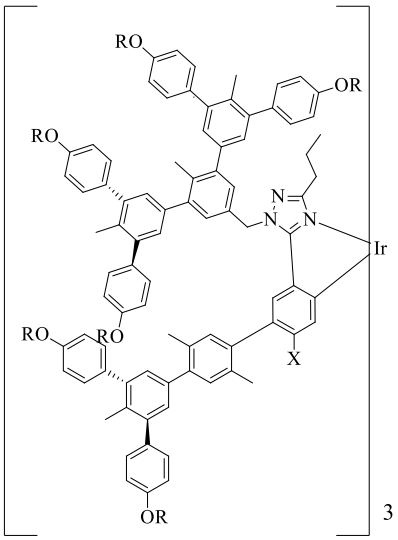

Complex 43

Table 2.7

Summary of Photophysical Properties of Complexes 41–44

Complex	Photophysical properties					Oxidative
	λ_{em} (nm)	τ_{em} (μs)	PLQY	K_r (10^5 s^{-1})	K_{nr} (10^5 s^{-1})	(V)
40	441, 468	22.0	0.59	0.3	0.2	0.53
41	441,468	1.7	0.46	-	-	0.47
42	441, 470	1.7	0.45	2.7	3.3	0.45
43	435,465	3.6	0.94	2.6	1.7	0.61

2.5.1.1 Conclusion for the Trend of Blue Emission Homoleptic Iridium(III) Complexes

All complexes exhibited blue emission phosphorescence, but not all emit saturated pure blue emission in ultraviolet lamps. The bluest emission observed at complex 32 with a pyrazolyl-based ligand shows the most blue-shifted emission at λ_{em} = 390 nm, the shortest wavelength observed among the complexes discussed. However, it is unsuitable for OLED applications due to low PLQY and lack of room-temperature emissivity. Complex 30 has an emission at λ_{em} = 462 nm, slightly less blue-shifted than Complexes 25 (λ_{em} = 453 nm) and 29 (λ_{em} = 454 nm). However, its high PLQY and efficiency make it a strong candidate. While Complex 30 is not the bluest Complex 32 is, its emission at 462 nm still falls within the blue range suitable for high-performance OLEDs.

In terms of efficiency, Complex 30 exhibits the highest PLQY, a very high radiative decay rate (K_r), and a relatively low non-radiative decay rate (K_{nr}). This combination indicates it has the highest efficiency in converting absorbed light into emitted light and minimising losses through non-radiative processes. In addition, when evaluating the suitability of phosphorescent materials for OLEDs, the lifetime emission, $\tau_{em,}$ is an essential factor as it affects the device's performance and stability. A longer lifetime emission in OLED applications generally suggests more stable and efficient performance. Complex 24, with the longest lifetime emission of 4.1 μs, might be advantageous for stability and longevity, but its lower PLQY (0.85) and moderate K_r and K_{nr} mean it might not be the most efficient light output. On the other hand, complex 30 has a shorter lifetime emission (1.8 μs). However, it excels in PLQY (0.99) and

efficiency, making it more effective for OLED applications where high brightness and efficiency are prioritised.

2.5.2 Heteroleptic Species Iridium(III) Complex

The previous discussion on homoleptic iridium complexes shows that despite achieving great blue emission energy, it still shows low lifetime and PLQY. The previous discussion in homoleptic complexes revealed that fluorine atoms play an excellent role in contributing to the enlarged energy gap, leading to blue-shifted complexes. This phenomenon is related to decreasing HOMO energy while keeping the LUMO energy relatively unchanged. However, fluorine substituents can introduce intrinsic drawbacks because the reactive C–F bonds are thermally and electrochemically unstable (He et al., 2016). In addition, other electron-withdrawing group substituents resulted in a modest blue shift in the emission energy of homoleptic complexes compared to fluorine substituents, which exhibited a more pronounced efficiency enhancement. Therefore, many groups have improved using non-identical ligands, usually two identical monoanionic C^N chelates and a third non-identical chelate called an ancillary ligand, L^X (**Figure 2.18**).

Figure 2.18

General chemical structure of heteroleptic iridium(III) complex

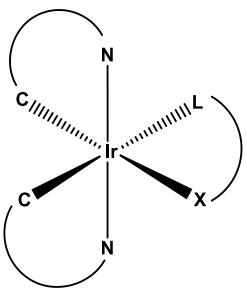

Recently, many studies have found that electron-rich or non-conjugated ancillary ligands remarkably shift the emission toward blue due to the significant enhancement of LUMO levels. The most well-known blue-emissive heteroleptic iridium(III) is a bis[2-(4,6-difluorophenyl)pyridinato-C2, N](picolinato)iridium(III), commonly known as FIrpic (Baranoff & Curchod, 2015). **Figure 2.19** shows the typical emission spectra of FIrpic at room temperature and 77 K. The room temperature emission spectrum exhibits blue phosphorescence peaks at 468 and 495 nm with fine vibronic structures, which are virtually independent of the solvent polarity. At a low temperature of 77 K, the emission spectrum of FIrpic shows narrower and highly structured emission bands at 455 and 485 nm, indicating the increment of ^{3}LC character at this temperature. However, FIrpic is not authentic blue; it is greenish-blue in both wavelength energy and emission colour. Moreover, it has a CIE of 0.17 and 0.34, corresponding to sky blue, which is far from the requirement of a full-colour display. Thus, many refinements have been implemented to develop a deeper blue-emissive cyclometalated iridium(III) complex.

Figure 2.19

Absorption (black), emission at room temperature (green), and emission at 77 K (blue) of FIrpic in $CHCl_2$ (Lee & Han, 2020)

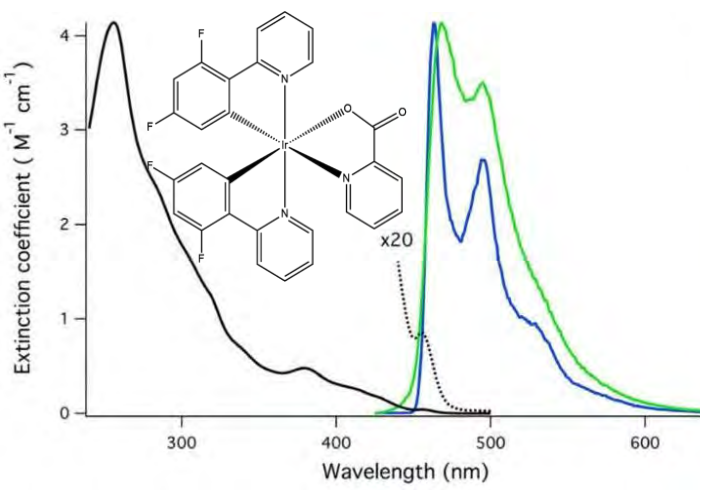

The two picolinate-based ligands of Complexes 44 and 45 also emit blue emission by using a phosphoryl/sulfonyl modified difluorophenylpyridine main ligand, as shown in **Figure 2.20** (Bai et al., 2020; Fan et al., 2012). The P=O and S=O units are believed to stabilise the HOMOs. At the same time, the LUMO keeps destabilising by the influence of the picolinate, resulting in broadened energy band gaps. They present almost identical emission spectra in DCM, indicating a similar electron-withdrawing ability of the phosphoryl and sulfonyl groups. The structured emission band has prominent peaks at 459 nm with shoulder peaks around 487 nm. The PLQY found was 0.49 and 0.55 for Complexes 44 and 45, respectively.

Figure 2.20

Chemical structure for heteroleptic complexes 44 and 45

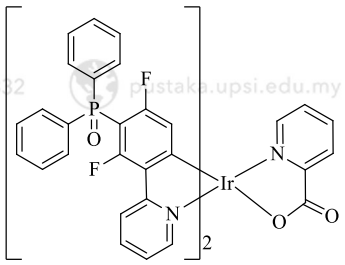

Complex 44

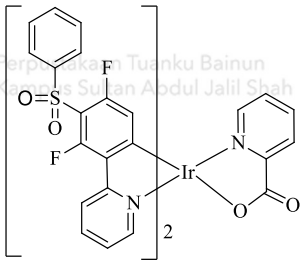

Complex 45

Another modification has been reported: changing the picolinate ligand into phosphine (**Figure 2.21**), successfully enhancing energy emission (Sanner et al., 2016). The absorption energy suggests that the ^{1}MLCT state lies at 413 nm and 409 nm, while the ^{3}MLCT state lies at 441 nm or 437 nm for complexes 46 and 47, respectively. These bands exhibit poor relative absorption and reveal higher-lying T_1 states for these complexes than the 455 nm band of FIrpic due to substituting the picolinate ligand with the more substantial field phosphine and phosphite ligands. In addition, the phosphite causes a slightly more significant blue shift than the phosphine. However, the PLQY found only about 0.60 for Complexes 46 and 47.

Figure 2.21

The chemical formula for iridium(III) complexes 46 and 47 incorporates phosphine and phosphate ligands

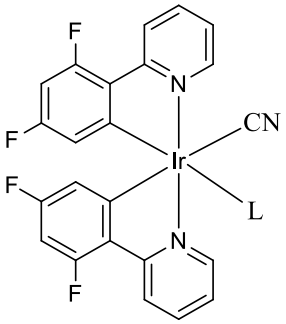

Complex 46: L = PPh_3
Complex 47: L = $P(OPh)_3$

Thompson et al. published the first carbene-based iridium(III) complexes for blue OLEDs in 2005, as shown in **Figure 2.22**. To destabilise the ^{3}MC state, they used high-field-strength carbene ligands of 1-phenyl-3-methylimidazolin-2-ylidene (Complex 48) and 1-phenyl-3-methylbenzimidazolin-2-ylidene (Complex 49) to build new forms of iridium complexes. Hence, increments in the blue phosphorescent quantum yields were obtained. The average Ir–$C_{carbene}$ bond distance (2.026 Å) in complex 49 is much less than the average Ir–N distance (2.124 Å) in complex 50, indicating that the carbene moiety is more strongly bound to the Ir than the pyrazolyl-based ligand. Accordingly, strong-field carbene ligands destabilise thermally accessible non-emissive states and exhibit higher PLQY than pyrazolyl-based complexes.

The efficient, potent field ligand of complexes 48−50 has opened a study of another modification using a carbene ligand to apply to heteroleptic complexes. Complex 51 was invented utilising a trifluoromethyl substituent on the phenyl moiety of the carbene ligand, as shown in **Figure 2.23** (Li et al., 2015). The HOMO-LUMO gaps were increased by modifying the phenyl moiety in the NHCs with electron-withdrawing substituents of trifluoromethyl, and the emissions were blue-shifted

accordingly in good performance of the OLED device. Other significant carbene complexes have been studied by Stringer et al., which also utilised imidazole ancillary carbene ligand systems. They reported the luminescence properties of five iridium(III) complexes containing a 2,4-disubstituted phenylimidazoylidene NHC ancillary ligand (**Figure 2.23**). The inclusion of electron-withdrawing halogen substituents on the phenyl ring of the carbene imidazole ligand on its own changed the emission maxima from 532 nm to 504 nm (Cl) or 490 nm (F), which was credited predominantly to their stabilising inductive impacts on the substantially metal-based HOMO, as appeared differently to the ppy-based LUMO.

Figure 2.22

Chemical structure of homoleptic iridium(III) carbene complexes of complex 48–50. (Sajoto et al., 2005)

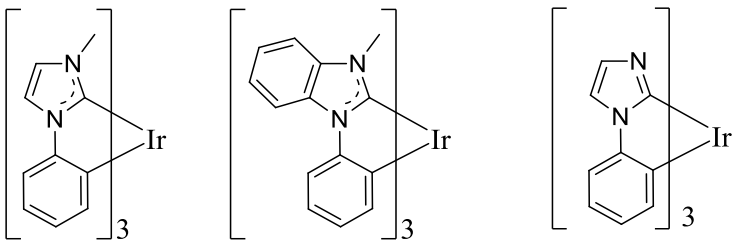

Complex 48 Complex 49 Complex 50

Figure 2.23

Chemical structure of iridium(III) carbene complexes 51–56

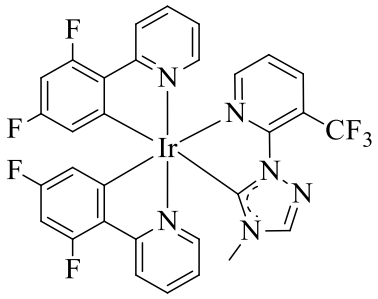

Complex 51

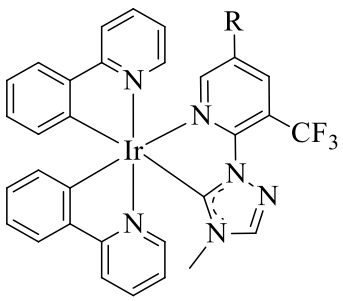

Complex 52: R= H
Complex 53: R= Me
Complex 54: R= OMe
Complex 55: R= Cl
Complex 56: R= F

Table 2.8 summarises heteroleptic Iridium complexes FIrpic and 44–56 photophysical properties. In the quest for highly efficient blue phosphorescence in OLED applications, FIrpic emerges as the most notable choice. Despite its slightly greenish-blue emission and lifetime of 1.70 μs, FIrpic achieves a robust photoluminescence quantum yield (PLQY) of 0.80, making it a strong candidate due to its balanced emission characteristics and efficiency. Although other complexes, such as those with trifluoromethyl substituents and phosphine/phosphite ligands, exhibit promising blue shifts and improvements in emission efficiency, FIrpic's superior PLQY and well-established performance underscore its practicality and effectiveness for blue OLEDs. Its combination of high quantum yield and reliable blue emission positions FIrpic as a leading choice for achieving efficient blue phosphorescence.

Table 2.8

Summary of Photophysical Properties for Iridium Complexes 44–56

Complexes	**Photophysical properties**		
	λ_{max}/nm	$\tau_{emission}$	PLQY
FIrpic	468, 485	1.70	0.80
44	459, 487	-	0.15
45	456, 487	-	0.71
46	413, 441	2.30	0.49
47	409, 437	1.90	0.55
48	380	0.40	0.02
49	389	0.22	0.04
50	414	14.00	-
51	488	1.80	0.69
52	529	1.98	0.49
53	532	1.59	0.42
54	525	1.97	0.62
55	504	2.03	0.68
56	490	2.06	0.53

In another review, the series of N-heterocyclic carbene iridium(III) complexes of 57–64, having dfppy as the main ligand and NHCs as ancillary ligands, were systematically studied (Li et al., 2015, 2018) shown in **Figure 2.24**. The HOMO-LUMO gaps were increased by replacing the phenyl ring with N-heteroaromatic rings, and the emissions were blue-shifted accordingly. Among this series of carbene-based iridium complexes, complex 82, with excellent blue phosphorescent properties, exhibits good performance, with an EQE of 10.3%. More recently, heteroleptic iridium(III) complexes with NHC and acidic pyrazolyl-pyridine (fppz) moieties as ancillary ligands, 65 and 66 as shown in **Figure 2.24,** were synthesised (Chen et al., 2020). These ancillary ligands successfully maintained the relatively high LUMO energy levels because the LUMOs of these complexes are almost entirely located on the antibonding π^* orbital of the pyridyl ring of the primary ligand, F_4ppy. Thus, sky-blue emissions at a wavelength of around 465 nm with PLQYs of over 0.60 were achieved.

Figure 2.24

Chemical structure of iridium(III) carbene complexes of 57–65 and iridium with pyrazole ancillary ligand 67

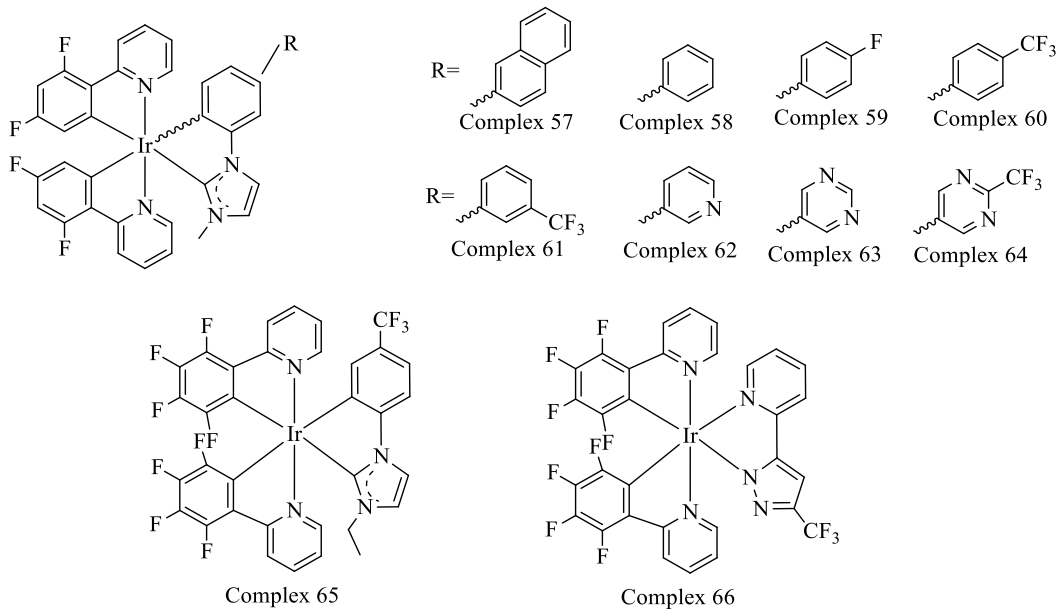

Later, two new iridium compounds based on high field strength bis-carbene cyclometalated ligands and triazolepyridine complex 67 and 68 **(Figure 2.25)** exhibited bright greenish-blue phosphorescence (max ~490 nm) with PLQYs of approximately 50%, excellent electrochemical as well as good thermal properties (Li et al., 2014). On the other hand, bis(1-(methyl- or fluorophenyl)-3-methylimidazolium)iridium complexes 69 and 70 **(Figure 2.25)** emit pure blue emission at 455 and 466 nm, respectively. All the physical properties are summarised in **Table 2.9**.

Figure 2.25

Chemical structure of iridium(III) carbene complexes 67-70

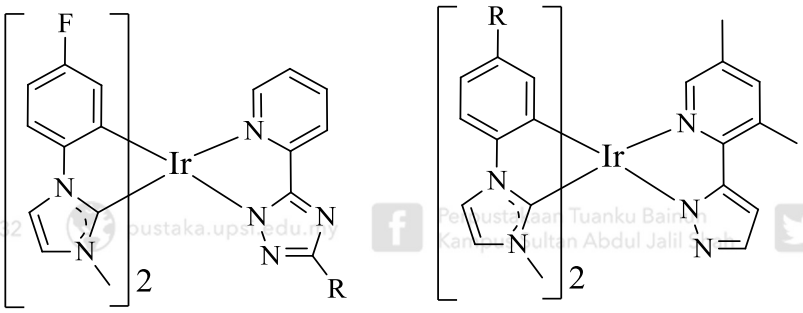

Complex 67: R = CH_3
Complex 68: R = Phenyl

Complex 69: R = F
Complex 70: R = CH_3

Complexes 71–74 show that the ancillary moiety was modified using different substituents on the pyridinyl imidazole ligand, as shown in **Figure 2.26**. All investigated complexes are bright blue emitters in the solid state at room temperature with PLQYs of 0.20–0.80. No significant difference exists in the emission energy of complexes 72–74. In particular, ancillary bis-carbene ligands in complex 75 exhibit much larger PLQYs, as shown in **Table 2.9** (Omae, 2016; Scattolin & Nolan, 2020).

Figure 2.26

Chemical structure of phenylpyridine carbene iridium complexes of 71–75

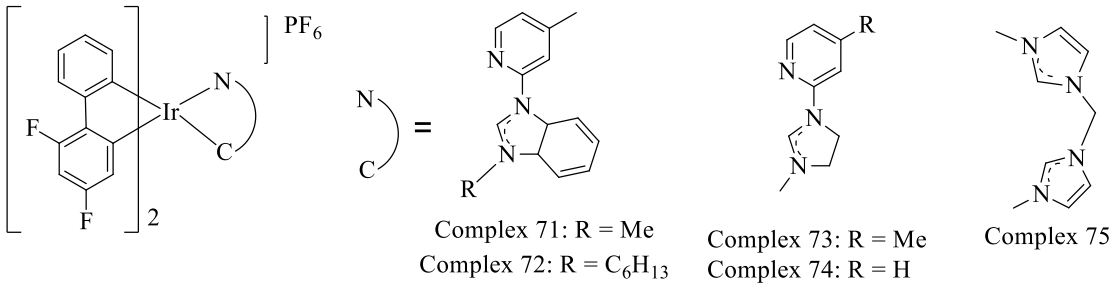

Complex 71: R = Me
Complex 72: R = C_6H_{13}

Complex 73: R = Me
Complex 74: R = H

Complex 75

Table 2.9

Summary of Photophysical Properties of Heteroleptic Iridium(III) Complexes with Carbene Ligand

Complexes	Photophysical properties		
	λ_{max}/nm	$\tau_{emission}$ (μs)	PLQY
57	483	2.1	0.14
58	483	1.8	0.65
59	473	1.8	0.73
60	469	1.9	0.57
61	469	1.8	0.69
62	473, 498	1.8	0.61
63	471, 497	1.7	0.33
64	455, 479	1.9	0.32
65	455, 479	17.6	0.60
66	469, 472	16.6	0.68
67	478, 486	0.13	0.51
68	480, 490	0.18	0.46
69	455	1.84	0.58
70	466	2.24	0.42
71	450, 480	3.40	0.34
72	452, 480	3.80	0.44
73	452, 480	3.00	0.36
74	452, 480	3.10	0.26
75	454, 481	3.20	0.58

From **Table 2.9,** Complex 59 with a fluorine substituent on the ancillary ligand stands out with the highest PLQY of 0.73 and an emission lifetime of 1.8 µs among the blue-emitting complexes. This combination of high quantum yield and reasonable lifetime indicates it is highly efficient for blue phosphorescence in OLED applications. However, Complex 66, with the presence of CF_3 substituent on the ancillary ligand and four fluorine atoms on the cyclometallating ligand, also has a high PLQY of 0.68 and a significantly longer lifetime of 16.6 µs, which is considerably longer than the others. Even though its emission wavelength (469 nm) is slightly less blue than Complex 59 (473 nm), it's very long lifetime and high PLQY make it potentially even more efficient in terms of phosphorescence characteristics. In summary, from the review of imidazole-based ancillary ligands, Complex 59 is the best in terms of a balance between blue emission and high PLQY. In contrast, Complex 66 could be considered the most efficient overall due to its long lifetime and high PLQY, though with slightly less blue emission.

2.5.2.1 Heteroleptic Complexes Bearing Triazole-based Ancillary Ligands

As many previous studies have shown loopholes in electronic properties and the quantum yield efficiency related to the imidazole class of iridium(III)-carbene complexes, enhancing this study by utilising a triazole type of NHCs becomes crucial. Therefore, numerous strategies have been developed to alter the emission of iridium(III) carbene complexes using the triazole class of NHCs (Flifel & Hlail, 2017; Li et al., 2014). Compared to imidazole and pyrazole, triazoles are expected to have a more facile modification in achieving wide ranges of ligands to alter the photophysical properties of the desired iridium(III) complexes.

De Cola et al. investigated triazole ancillary ligand systems using 1,2,4- triazole ancillary ligands with various substituents and dfppy as the primary ligand, as shown in **Figure 2.27**. Their findings show that complexes 78 and 79 have lower PLQY in this series (Mydlak et al,. 2010). This could be related to the torsional angle formed by F atoms in the ortho position between the phenyl and triazole rings. The lowest MLCT states are shifted from pyridyl-triazole to ppy. Besides, complex 78 exhibited the most extended lifetime, highest emission energy, and PLQY among all the synthesised complexes 76–81 due to the 2,6-difluorobenzyl substituent that significantly shifted the emission towards blue. However, there is no comprehensive report on the DFT calculations related to the Frontier Molecular Orbital (FMO) studies of these complexes, leading to loopholes in the relationship between the effect of the number of fluorine substituents towards the HOMO-LUMO energy gap. However, it can be hypothesised that by increasing the electron-withdrawing ability, the HOMO energy level is lowered, and consequently, the HOMO-LUMO gap is widened, leading to blue-shift emission with narrower full width at half maximum (Srivastava & Joshi, 2014).

Figure 2.27

Chemical structure of iridium(III) complexes 76–81 utilising pyridinyltriazole-based ancillary ligand differed by the substituent attached to the triazole ring

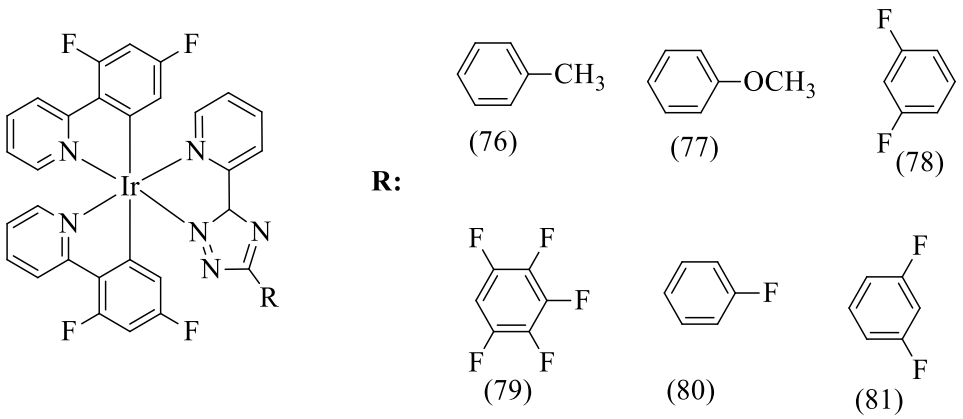

Other cationic blue-emitting iridium(III) complexes were reported using a 1,2,3-triazole-based ancillary ligand; complexes 82–84 were reported with reasonable photophysical properties drawn in **Figure 2.28** (Karmis et al., 2019). Attachment of different environments of the aromatic group does not significantly affect the emission energy, but in some cases, slightly modifies the excited-state lifetimes and PLQY. The summary of the photophysical properties is shown in **Table 2.10**.

Figure 2.28

Chemical structure of blue emitters of cationic iridium(III) complexes 82–84 that utilise 1,2,3-triazole pyridyl-based ancillary ligand

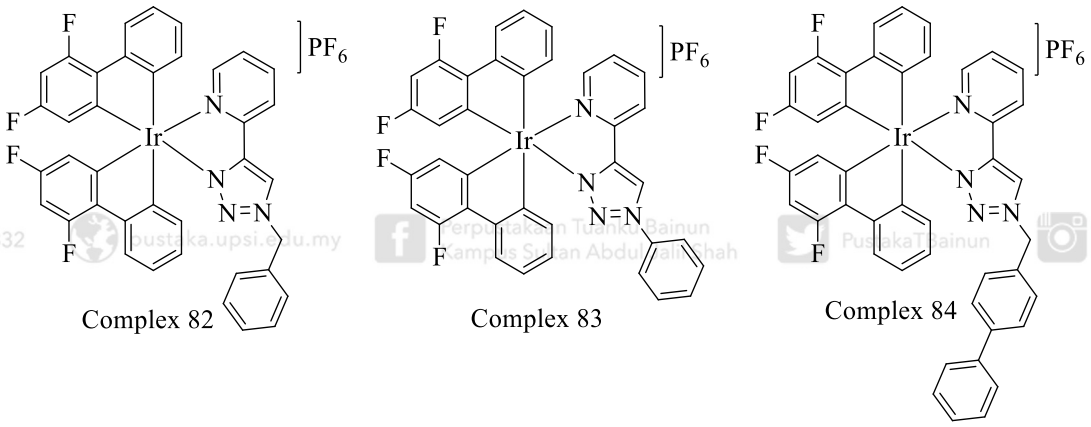

Table 2.10

Summary of Photophysical Properties of Blue Emitter Heteroleptic Iridium(III) Complexes of 76–85 that Utilise the Triazole Class of NHCs

Complexes	Photophysical Properties		
	Emission λ_{max}/nm	Lifetime τ/μs	PLQY
76	463, 492	0.1	0.03
77	464, 492	0.1	0.01
78	458, 487	0.2	0.04
79	460, 490	0.1	0.04
80	459, 489	0.1	0.03

Complexes	Photophysical Properties		
	Emission λ_{max}/nm	Lifetime τ/μs	PLQY
81	459, 488	0.2	0.04
82	452, 483	0.73	0.15
83	453, 483	0.87	0.24
84	452, 482	2.24	0.11
85	496	-	0.01
86	475	46.81	0.57
87	475	43.12	0.50
88	485	32.44	0.08

Complexes 76–84 utilising 1,2,3-triazole and 1,2,4 triazole-based ligands significantly show reasonable greenish blue emission energy with reasonable lifetime and PLQY. Hence, the first blue phosphorescent triazole carbene complex of iridium(III) has been done by Nazeeruddin et al. by alternating the triazole-based ligand into a carbene ligand, consuming the carbanionic of the triazole ring, cleaving with the central metal of iridium(III) **(Figure 2.29)**. This complex achieved $\lambda_{emission}$: 496 nm, but the PLQY is much lower than related triazole-based complexes. This unusual condition is due to the quenching by isomeric impurities or non-radiative processes. In addition, the extremely low PLQY also hindered the complex's lifetime measurement (Nazeeruddin et al., 2016). Since complex 85 did not show satisfying values of photophysical properties for the iridium(III) carbene complex, several researchers have done further modifications on the ancillary ligand. Adding imidazole to the nitrogen ring of triazole and revising the imidazole moiety with methyl and phenyl substituents has blue-shifted the emission energy and improved the PLQY values. The photoluminescence quantum yields for the complexes 86 and 87 showed the highest

importance. These achievements can be credited to the presence of a methyl group in the N3 position of the 1,2,3-triazoles, which influences their abilities to destabilise thermally accessible metal-centred non-emissive states. The lower quantum yield value obtained for complex 88 (0.08) can be attributed to the iodide counter ion, which is well-known for its propensity to quench luminescent emission efficiently (Karmis et al., 2019). The summary of the photophysical properties is shown in **Table 2.10**.

Figure 2.29

Chemical structure of blue emitter heteroleptic iridium(III) carbene complexes that utilise 1,2,4-triazole and imidazole in the ancillary moiety as ligands

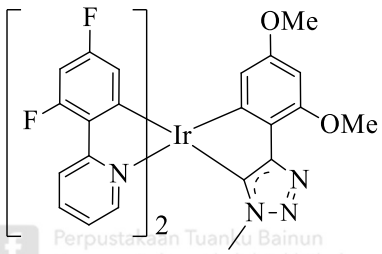

Complex 85

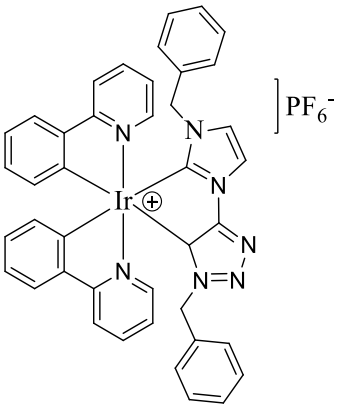

Complex 86

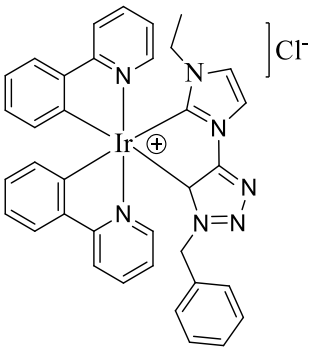

Complex 87

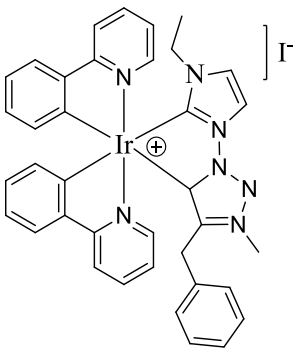

Complex 88

2.5.2.2 Conclusion for the Trend of Blue Emission Heteroleptic Iridium(III) Complexes

Research into blue-emissive iridium(III) complexes highlights significant advancements and challenges. Complexes like FIrpic, despite their high PLQY of 0.80 and blue emission (455–485 nm), exhibit a greenish-blue hue, making them less ideal for applications requiring pure blue. To improve performance, heteroleptic complexes with modified ligands have been explored. Phosphoryl/sulfonyl substituents in complexes 44 and 45 and phosphine/phosphite ligands in complexes 46 and 47 show enhanced emission and PLQY but still face limitations. Carbene-based complexes, such as 48–50, offer high quantum yields due to their ability to stabilise emissive states, while triazole-based ligands in complexes 76–87 show promise in achieving blue-shifted emission with improved photophysical properties. Notably, complexes 82–87 with imidazole and triazole combinations exhibit high PLQYs and long lifetimes. Future efforts should focus on optimising ligand systems for better stability and efficiency, addressing thermal and chemical stability concerns, and evaluating these complexes in OLED devices for practical applications. In conclusion, while FIrpic remains a leading choice, ongoing research continues to refine blue-emissive iridium(III) complexes for enhanced OLED performances.

2.6 Synthetic Routes to Iridium(III) Complexes

Several synthetic routes have been reported by various research groups, typically categorised based on the method of complexation to achieve efficient, scalable and sustainable synthetic routes to iridium(III) complexes. Common synthetic approaches include:

2.6.1 Free Carbene Route

The free carbene route involves the deprotonation of an imidazolium salt (or any related azolium class) using a strong, non-nucleophilic base such as potassium *ter*t-butoxide (Herrmann, 2015), sodium hydride (NaH) (Lu et al., 2019), or potassium bis(trimethylsilyl)amide (Kinzhalov & Luzyanin, 2019) as shown in **Scheme 2.1**. This generates a free N-heterocyclic carbene, which is a highly nucleophilic species that can coordinate directly with an electrophilic iridium precursor, forming a strong Ir–C(NHC) bond. The coordination typically occurs immediately after carbene generation, minimising the time for free carbene remains uncoordinated. The resulting Ir(III)–NHC ligand complexes benefit from the strong σ-donating character and stability imparted by the NHC ligand (Scattolin & Nolan, 2020).

Scheme 2.1

General schematic drawing of free carbene routes of synthesising metal complex with carbene ligand

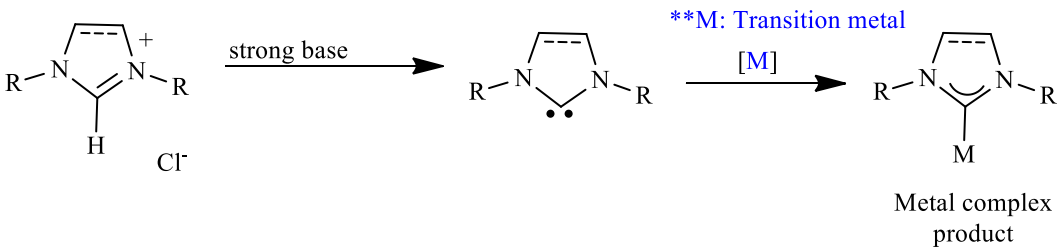

Despite its effectiveness, the free-carbene route presents several practical challenges. Most notably, the free NHC intermediates are extremely sensitive to moisture and air, reacting rapidly with water to regenerate the imidazolium salt or with oxygen to form undesirable by-products (Scattolin & Nolan, 2020). As such, this method requires stringent inert atmosphere techniques, including the use of Schlenk lines or gloveboxes, to exclude air and moisture throughout the reaction. Additionally, the process typically involves stoichiometric quantities of a strong base, generating inorganic salts as waste and reducing the overall percentage yield (Fan et al., 2023). These limitations have led to the development of alternative methods such as silver-mediated transmetalation or in situ deprotonation under milder conditions that aim to preserve the advantages of NHC coordination while improving experimental practicality and scalability.

2.6.2 Weak base route

The second and most recent strategy is the weak base route, in which the metal precursor and imidazolium salt react directly in the presence of a mild base, such as potassium carbonate. This method avoids the need to isolate sensitive intermediates, operates under milder conditions, and offers better compatibility with functionalized ligands, making it a more sustainable and scalable option for synthesizing metal–NHC complexes (Martynova et al., 2021). In the case of iridium–NHC complexes, the weak base route provides a mild, scalable, and user-friendly approach (Martynova et al., 2021) as shown in **Scheme 2.2**. The reaction proceeds under gentle heating to yield well-defined Ir–NHC complexes. Compared to traditional methods that require strong bases or strictly inert conditions, the weak base route offers improved environmental

and operational compatibility. Some mechanistic studies suggest the initial formation of hydroxo intermediates or metallate species, which subsequently convert into the desired complex upon base addition.

Scheme 2.2

General schematic drawing of weak base routes of synthesising metal complex with carbene ligand

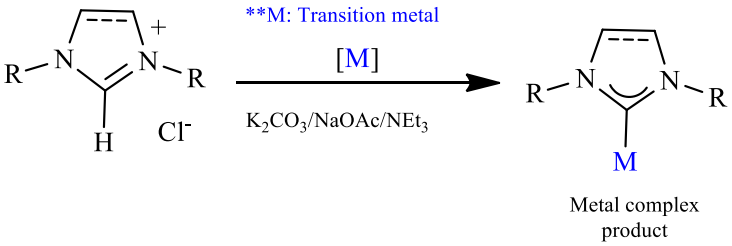

2.6.3 Transmetallation Route

The transmetalation route involves the initial formation of silver–NHC complex intermediates, which are subsequently used to transfer the carbene ligand to a target metal centre as shown in **Scheme 2.3**. This method offers improved handling and stability of the carbene species; however, it typically requires an additional synthetic step and relies on expensive silver salts, which can limit its practicality and scalability.

Scheme 2.3

General schematic drawing of transmetallation routes of synthesising metal complex with carbene ligand using silver oxide

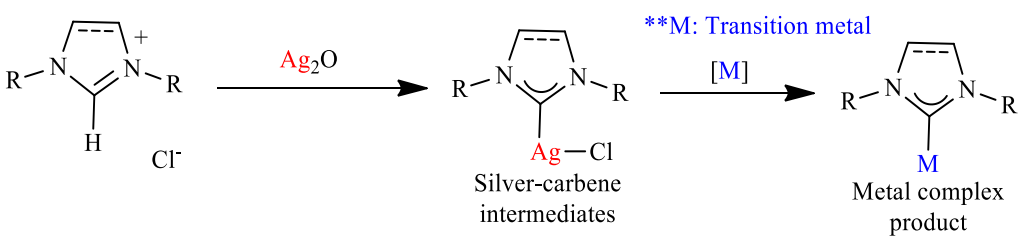

Liu et al. (2011) reported unsuccessful attempts to synthesize *tris*-cyclometallated Ir(III) complexes via traditional silver-mediated transmetalation, using conditions such as $AgPF_6$ in acetonitrile at 100 °C for 48 hours (condition a), and in refluxing 2-ethoxyethanol at 140 °C for 24 hours (condition b) (Szafrański et al., 2015) (S. Liu et al., 2011). As shown in **Scheme 2.4**, despite employing C^N-bound triazole ligands like 2-(*1H*-[1,2,3]triazol-4-yl)pyridine, these approaches failed to yield the desired *tris*-cyclometallated product. Instead, only N^N-chelating iridium complexes were isolated under both conditions, indicating the limitations of these conventional methods in achieving full cyclometalation of triazole-based ligands. To address these challenges, the authors developed a copper(I)-mediated click–transmetalation strategy (S. Liu et al., 2011). This method involved the in situ generation of Cu(I) triazolide intermediates, which effectively transferred the carbene ligand to the iridium centre, leading to the successful formation of the target *tris*-cyclometallated Ir(III) complex under significantly milder conditions.

Scheme 2.4

*The success and failed attempts to synthesise tris-cyclometallated Ir(III) complexes. ** (a) $AgPF_6$, MeCN, 100 °C, 48 h; (b) $AgPF_6$, 2-ethoxyethanol, 140 °C, 24 h*

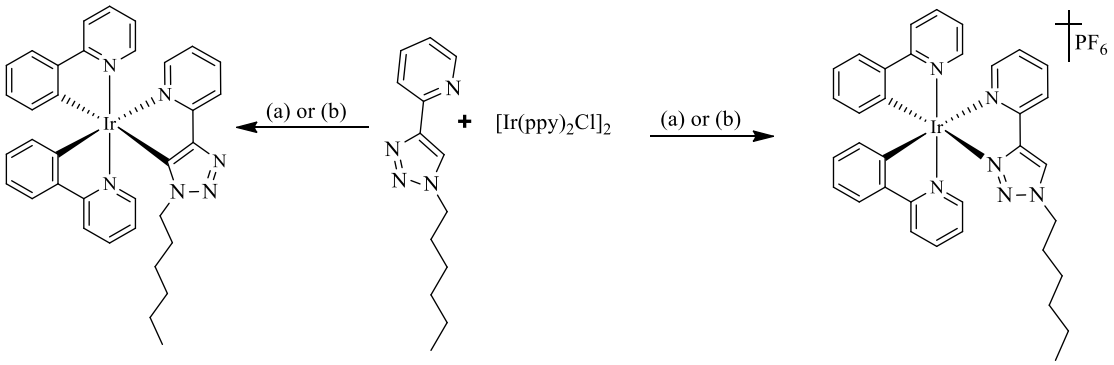

2.6.4 One-pot synthesis

The one-pot synthesis strategy offers a streamlined and efficient method for preparing Iridium(III) complexes. In this approach, $IrCl_3 \cdot nH_2O$ is reacted directly with both C^N cyclometalating ligands and ancillary ligands (e.g., N-heterocyclic carbenes, bipyridines, or triazole derivatives) in a single step, bypassing the need to isolate the chloro-bridged dimeric intermediate $[Ir(C^N)_2Cl]_2$ (Cheng et al., 2021; Cho et al., 2016). This method improves operational simplicity, reduces purification steps, and minimises solvent and reagent use, aligning with green chemistry principles. It also enhances overall yield and reproducibility, particularly when intermediates are unstable or poorly soluble (Cheng et al., 2021).

Nevertheless, precise control over reaction conditions such as ligand ratios, temperature, and solvent is essential to avoid undesired byproducts and ensure efficient complex formation (Savka & Plenio, 2014). While the one-pot method has been successfully used to synthesise Ir(III) complexes for photophysical applications like OLEDs and sensors, it may be less effective for ligand systems that require stepwise activation (e.g., NHCs) (Savka & Plenio, 2014).

2.6.5 Optimising Percentage Yield Recovery of Synthesised Complexes

The efficient synthesis of iridium(III) complexes remains a key objective in both academic research and industrial catalysis due to their broad utility in materials chemistry, photophysics, and catalysis. To maximise product yields and minimise by-product formation, several synthetic variables must be carefully optimised.

One critical factor is the regulation of reaction temperature and time. Elevated temperatures or prolonged reflux can lead to the thermal degradation of sensitive ligands or trigger competing side reactions, ultimately lowering the yield of the desired complex (Sajoto et al., 2009). The selection of an appropriate solvent is equally important. High-boiling, polar solvents such as 2-ethoxyethanol and glycerol have demonstrated superior performance in facilitating the formation of key intermediates, namely, chloro-bridged iridium dimer, which are commonly used precursors in the construction of heteroleptic complexes (Cho, Kim, et al., 2017). Stoichiometric control is also essential, such as utilising a slight excess of the cyclometalating ligand can drive the reaction equilibrium toward the desired product while reducing the presence of unreacted metal precursors (Savka & Plenio, 2014). Moreover, the purity of reagents and the choice of base or halide-scavenging additive such as $AgPF_6$, K_2CO_3, or NaOAc can have a pronounced impact on both the yield and stability of the resulting complexes (Martynova et al., 2021; Park et al., 2013; Savka & Plenio, 2014).

Additionally, reaction setup plays a pivotal role. Degassing solvents and maintaining an inert atmosphere during the reaction can help prevent the oxidation and hydrolysis of iridium intermediates, both of which are known to compromise yield and purity (Altinolcek et al., 2020). Together, these strategies demonstrate the importance of integrating careful reaction design with thoughtful ligand and reagent selection to achieve high-efficiency synthesis of iridium(III) complexes.

2.7 Recent Trends in Phosphorescence Analysis Using DFT

This subtopic will highlight several outstanding DFT and TD-DFT calculations applied in the chemical analysis of iridium(III) complexes. The previous research has drawn insightful predictions for emission properties of OLED materials based on the iridium complex, providing a strong link between theoretical predictions and experimental material development.

Strassner et al. reported that DFT was used to analyse the phosphorescence wavelengths of various metal complexes, including those of osmium, iridium, and platinum. They were accurately predicted with results within a 5% error relative to experimental data. The emission wavelengths were calculated based on the energy difference between the lowest triplet state and the ground state using the optimised T_1 geometry. This approach offers significant advantages over the TD-DFT method, which is known to encounter charge-transfer issues in excited states. The double-zeta polarisation with a 6-31G* basis set was adequate for simulating the electronic structure of the T_1 state. However, the deviations between calculated and experimental wavelengths were larger for charged complexes than for neutral ones. In conclusion, Strassner et al. have shown that the method reported accurate predictions for the emission wavelengths related to the series of N-heterocyclic carbene complexes (Strassner et al., 2013).

Xu et al. performed calculations of emission energies at optimised T_1 geometries using TD-DFT, employing various exchange-correlation functionals with differing percentages of Hartree-Fock (HF) exchange. The study revealed a strong dependency of the calculated emission energies on the HF exchange percentage; the higher HF

exchange led to increased emission energies. The predicted emission energies averaged across different functionals exhibited a linear correlation with experimental values, underscoring the method's predictive reliability. The commonly used Self-Consistent Field (SCF) protocol for emission energy calculation was compared with the TD-DFT method. While the ΔSCF approach agreed well with experimental data, the TD-DFT method offered a superior linear correlation, indicating enhanced accuracy for modelling emission properties in complex systems. To summarise, Xu et al. highlighted that TDDFT's utilisation has successfully and accurately predicted photophysical behaviour in advanced materials (Xu et al., 2015).

Peng et al. studied the emission spectra and the radiative and non-radiative decay processes of green and deep blue emitting iridium(III) complexes by applying thermal vibration correlation function (TVCF) in the DFT and TD-DFT methods. TVCF simulates how molecular vibrations at different temperatures influence reaction rates, particularly non-radiative decay processes, by correlating vibrational energy levels with electronic states, enhancing the prediction of photophysical properties. Their investigation revealed a positive correlation between radiative decay rates and the MLCT character in the emissive triplet state. Additionally, they determined that non-radiative decay rates are primarily influenced by intramolecular reorganisation energy, mainly due to the vibrations of chromophore ligands. Consequently, achieving high phosphorescent efficiency in blue-emitting complexes requires significant MLCT character and low reorganisation energy (Peng et al., 2016).

Next, Jansson et al. investigated the phosphorescence mechanisms of $Ir(ppy)_3$ using TDDFT quadratic response methods. Their findings indicated that the emission

transitions from T_1 to S_0 are predominantly governed by MLCT character. The intense emission observed in $Ir(ppy)_3$ is significant due to the high intensity of S_2–S_5 transitions, attributed to the large spin-orbit coupling (SOC) constants between the T_1 state and the higher singlet states (S_2–S_5). The phosphorescence lifetime calculated at the S_0 geometry (2 μs) aligns more closely with the experimentally observed lifetime in acetonitrile (1.9 μs) compared to the lifetime calculated at the T_1 geometry. The transition moments for S_0 to T_1 at the T_1 geometry are significantly smaller, leading to a longer calculated lifetime at the T_1 geometry. This discrepancy arises because the T_1 state exhibits a highly anharmonic potential near the shallow minimum concerning metal-ligand displacement. Therefore, the S_0 to T_1 transition moments should be calculated at the S_0 geometry for accurate phosphorescence lifetime predictions (Jansson et al., 2007).

Next, Younker et al. conducted an in-depth computational study to accurately predict the emission properties of various cyclometalated iridium(III) complexes using the TDDFT method in conjunction with the zero-order relativistic approximation (ZORA) (Younker & Dobbs, 2013). Their research demonstrated that when calculated at the S_0 geometry, vertical excitation energies exhibit a stronger correlation with experimental emission energies than those calculated at the T_1 geometry. This finding suggests that the S_0 geometry is more appropriate for modelling such properties. For instance, the S_0 geometry was also employed to calculate radiative rates, which agreed well with experimental results. This outcome reinforces the conclusions of the previous works reported by the Jansson group (Jansson et al., 2007), who similarly found that using the S_0 geometry effectively predicts phosphorescence properties. Younker et al. further explored the influence of solvent effects by considering structural optimisations

under these conditions and found that the emission energies and radiative rate constants, calculated using geometries optimised in the gas phase or solvent, were nearly identical. This result implies that geometry optimisation in the gas phase is sufficient for accurately predicting phosphorescent properties without additional solvent considerations (Younker & Dobbs, 2013).

The other outstanding report on DFT work was from the Haneder group. They highlighted the critical role of singlet-triplet splitting in regulating the emission radiative rate of phosphorescent N-heterocyclic carbene complexes that emit in the deep-blue region. Their study, which involved DFT calculations on the $Ir(dpbic)_3$ complex [dpbic = 1-phenyl-3-phenyl-benzimidazolin-2-ylidene-C, C2′)], revealed that ΔEST is a critical factor in determining the efficiency of the emission process. They also noted that increasing the π-conjugation in the ligands could modulate the ΔEST, thereby affecting the emission characteristics (Haneder et al., 2008).

Sajoto et al. investigated the temperature-dependent behaviour of high-energy phosphorescent tris-cyclometalated iridium complexes. Their study revealed that the decrease in phosphorescent efficiency at elevated temperatures is primarily due to the thermal activation of non-radiative decay channels. This deactivation process occurs via forming five-coordinate intermediates, which result from the cleavage of one metal-ligand bond. These intermediates are characterised by an electronic structure akin to a triplet metal-centered (^{3}MC) state. To mitigate this bond cleavage and thus preserve phosphorescent efficiency, the researchers suggested restricting the degrees of freedom necessary for metal-ligand bond dissociation. This can be effectively achieved by

incorporating rigid ligands, such as benzoquinoline, limiting the structural flexibility and inhibiting the formation of such deactivating intermediates (Sajoto et al., 2009).

Zhou et al. studied how metal-ligand bond changes affect the transition from emissive (^{3}MLCT) to non-radiative (^{3}MC) states in blue phosphorescent iridium(III) complexes. They found that simple molecular orbital analysis is insufficient to predict non-radiative states accurately. Instead, they used DFT and TD-DFT calculations with spin-orbit coupling analysis to explore the potential energy surfaces of these states. Their findings showed that non-radiative decay rates are significantly slower in the ^{3}MC state compared to the ^{3}MLCT state, and the energy barrier between these states aligns with observed non-radiative rates. This indicates that the thermal population of the ^{3}MC state is a major non-radiative process at room temperature (Zhou et al., 2016).

In 2016, Escudero et al. introduced a pioneering method for quantitatively predicting the phosphorescence quantum yields of blue and green-emitting iridium(III) complexes. This approach involves calculating the emissive triplet state's radiative rate and analysing the potential energy surface of thermal deactivation pathways to determine the quantum yields accurately. To ensure the accuracy of the quantum yield predictions for other complexes, the method first required the calculations to be validated using $Ir(ppy)_3$ as a reference compound. This approach is a valuable tool for pre-screening the quantum yields of unknown blue and green iridium(III) complexes, offering a predictive framework to streamline the development of new materials. However, it is essential to note that this method is unsuitable for red-emitting iridium(III) complexes. The limitation arises because the approach overlooks

temperature-independent non-radiative processes, which play a significant role in the quantum yield calculations for red-emitting complexes (Escudero, 2016).

Among the latest articles reported on DFT and TD-DFT were those by Alsaeedi in 2023. The paper reports on iridium complexes' phosphorescence quantum efficiency and emission spectra with phenyl triazole-type cyclometallated ligands. The computational methods used include the B3LYP functional, CAM-B3LYP, PBEPBE, and MPW1PW91 functionals to ensure accurate theoretical predictions to optimise the ground and excited states, predicting electronic structures, absorption properties, and emission characteristics. Key findings highlight identifying the lowest-lying singlet absorption energies and the characterisation of emissions as a mixture of triplet ligand-to-ligand charge transfer (^{3}LLCT) and metal-to-ligand charge transfer (^{3}MLCT) states. The study demonstrates how DFT can provide information on the strategic ligand modifications that can significantly influence the performance of iridium(III) complexes, guiding the synthesis of new compounds with enhanced photophysical characteristics (Alsaeedi, 2023).

DFT has also been used to study the reaction mechanism primarily related to novel iridium complexes to have an insightful discussion on the synthesis stage of the complexes. Zhang et al. report a detailed DFT investigation, explicitly employing the M06-2X functional, to elucidate the reaction mechanism for synthesising novel cyclometalated iridium(III) complexes with acyclic diaminocarbene (ADC) ligands (X. Zhang et al., 2019). The study focuses on the reaction pathway involving the $Ir(F_2ppy)_2(CNAr)(Cl)$ complex, which reacts with n-propylamine in dichloromethane solvent. The SMD solvation model was applied to model the solvent effects accurately.

The low value of calculated activation-free energies for the reaction mechanism indicates that the reaction can occur under relatively mild conditions, as typically used in experimental setups. This low activation barrier suggests the reaction is thermodynamically favourable and can proceed efficiently in the laboratory. This work provides a comprehensive mechanistic understanding of synthesising iridium(III) complexes with ADC ligands, bridging the gap between computational predictions and experimental observations. The insights gained from this research could be instrumental in designing more efficient synthetic routes and developing new materials with desirable properties for various applications (X. Zhang et al., 2019).

2.8 Conclusion of Literature Review

This chapter has reviewed the reported studies on the design, modification, and synthesis of iridium(III) complexes, especially those aimed at blue phosphorescent applications. Previous research has shown that the photophysical properties of these complexes, such as emission colour, brightness, and lifetime are strongly influenced by the choice of ligands and the way they coordinate to the metal centre. For instance, homoleptic complexes like $Ir(ppy)_3$ and its fluorinated derivatives have been widely studied due to their good emission efficiency. However, they often face limitations such as poor colour purity and reduced stability in device settings. In contrast, heteroleptic complexes, especially those with N-heterocyclic carbene (NHC) or triazole-type ligands, offer better control over the electronic structure, higher thermal stability, and improved emission suitable for blue light-emitting devices.

Significantly, modifying the ligands by adding electron-donating or withdrawing groups has been a useful way to fine-tune the emission properties. Rigid and electron-rich ligands help achieve blue-shifted emissions and better light output. However, improving colour and brightness often comes at the cost of stability, making it difficult to achieve both in a single complex.

Despite the choice of ligands, the methods used to synthesise these complexes also play an important role. Techniques such as the free carbene route, silver-mediated transmetalation, weak base-assisted reactions, and one-pot syntheses each have their strengths and limitations. Some are simpler and more compatible with different ligands, while others offer better control or yields. Despite these advances, many of these methods still face challenges such as sensitivity to air, difficulty in scaling up, or the need for controlled conditions.

Considering the insights drawn from existing research, it is evident that further investigation is required to bridge the gap between photophysical performance and synthetic feasibility. The identification of ligand frameworks that simultaneously enhance emission efficiency, structural rigidity, and environmental stability remains an open area of study. The findings of this literature review underscore the importance of adopting a holistic approach that integrates ligand design with practical synthetic techniques. These considerations provide a strong foundation for the present study, which aims to explore novel NHC-based iridium(III) complexes with improved blue phosphorescence and synthetic accessibility.

CHAPTER 3

METHODOLOGY

This chapter describes the research design, the inventory of chemicals and solvents, the general specifications of the instruments utilised, and the detailed steps of the experiments for accomplishing all the objectives outlined in **Chapter 1**. The experimental parts discussed in detail throughout this chapter were:

a. The synthesis of the dichloro-bridged iridium(III) dimers complex differed by the presence of fluorine.
b. The synthesis stage of the ancillary ligand pyridinyltriazole and its derivatives.
c. The synthesis of bis(phenylpyridine) iridium(III) complexes bearing a novel pyridinylformimidamide-based ancillary ligand.

3.1 Chemicals and Solvents

The chemicals in this research were purchased from various suppliers as listed in **Table 3.1**. All chemicals were used without further purification unless stated.

Table 3.1

List of Chemicals

Item	Name and Priority	Molecular Formula	Sources	Purity (%)
1	Iridium(III) Chloride Hydrate	$IrCl_3 \cdot xH_2O$	Sigma	99.9
2	2-Phenylpyridine	$C_{11}H_9N$	Sigma	98.0
3	2-Ethoxyethanol	$C_4H_{10}O_2$	Sigma	99.0
4	2-(2,4-Difluorophenyl)pyridine	$C_{11}H_7F_2N$	Sigma	97.0
5	Acetone	CH_3COCH_3	R&M	99.0
6	Ethyl Acetate	$CH_3COOC_2H_5$	R&M	99.8
7	Hexane	C_6H_{14}	R&M	99.0
8	Potassium *tert*-butoxide	$K(CH_3)_3CO$	Sigma	98.0
9	Copper(I) iodide	CuI	Sigma	99.0
10	Sodium chloride	NaCl	Sigma	99.0
11	Silver(I) oxide *ReagentPlus*,	Ag_2O	Sigma	99.0
12	Benzotriazole Reagent*Plus*	$C_6H_5N_3$	Sigma	99.0
13	Sodium Chloride	NaCl	Sigma	99.0
14	4-Methylbenzylbromide	C_8H_9Br	Sigma	99.0
15	2,6-Difluorobenzylbromide	$F_2C_6H_3CH_2Br$	Sigma	98.0
16	1,2,4-Triazole	$C_2H_3N_3$	Sigma	98.0
17	2-Bromopyridine	C_5H_4BrN	Sigma	99.0

Item	Name and Priority	Molecular Formula	Sources	Purity (%)
18	Dimethyl Sulfoxide (d_6- DMSO)	$(CH_3)_2SO$	R&M	99.0
19	Sodium Sulphate	Na_2O_4S	Sigma	99.0
20	Dichloromethane (DCM)	CH_2Cl_2	R&M	99.0
21	Methanol	CH_3OH	R&M	99.0
22	1,2-dichloroethane	$C_2H_4Cl_2$	R&M	99.0
23	Celite 545 0.02-0.1mm	SiO_2	Merck	–
24	Deutrated Methylene Chloride	CD_2Cl_2-d_2	Merck	–
25	Acetonitrile	CH_3CN	R&M	99.0
26	Molecular sieves	–	Merck	–
27	Silica gel 60 H	–	Merck	–

3.2 Experimental

All the reflux reactions were carried out under an inert atmosphere of nitrogen unless otherwise mentioned, though all preparation and post-reflux process work-up was carried out in air. Liquid solvents used for the reflux process were stored over molecular sieves before being used. The dimers precursor of $(ppy)_2IrCl_2Ir(ppy)_2$, and $(F_2ppy)_2IrCl_2Ir(F_2ppy)_2$ were modified according to the literature methods (Wong et al., 2015). The ligand derivatives procedures were referred from previous research by our group as a continuity study.

3.2.1 Synthesis Ligand

3.2.1.1 2-(1,2,4-triazol-1-yl)pyridine ligand, (pyta)

2-(1,2,4-triazol-1-yl)pyridine ligand, (pyta), was prepared referring to the previous literature procedure (Barbante et al., 2013) and shown in **Scheme 3.1**. A mixture of 1,2,4-triazole (7.41 g, 100 mmol), 2-bromopyridine (17.03 g, 100 mmol), potassium *tert*-butoxide (16.87 g, 150 mmol), CuI (1.03 g, 5 mmol) and benzotriazole (1.28 g, 10 mmol) in dimethylsulphoxide (80 mL) was heated at 110 °C for 15 hours under nitrogen atmosphere. Thin-layer chromatography (TLC) with dichloromethane/methanol (93:7 v/v) was performed to monitor the reaction progress and ensure optimal reaction conditions were achieved. 50 mL of deionised water was added, and the mixture was extracted with 150 mL of ethyl acetate three times. The organic extracts were washed with brine (100 mL) and dried with Na_2SO_4, and the solvent was removed under reduced pressure. After purification using column chromatography with dichloromethane/methanol (93:7 v/v) as the eluent, the product was obtained as a pale brown crystalline solid. Yield: 7.55 g, 48%.

Scheme 3.1

Schematic pathway for the synthesis of the 2-(1,2,4-triazol-1-yl)pyridine ligand as the starting material for the synthesis of all other ligands

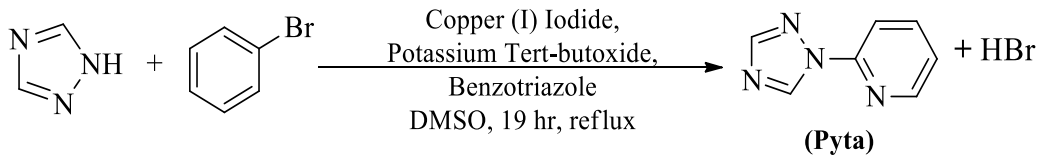

(Pyta)

3.2.1.2 (2-(2,6-difluorobenzyl)-*1H*-1,2,4-triazol-1-yl)pyridine ligand, (F_2bpyta)

F_2bpyta was prepared from **pyta** that was used as previously synthesised (0.610 g, 0.004 mol) and 2,6-difluorobenzylbromide (1.860 g, 0.009 mol) and shown in **Scheme 3.2**. The mixture was refluxed at a mole ratio equivalent to 1:2.1 respectively, for 19 hours under a nitrogen atmosphere in 80 mL of acetonitrile. Thin-layer chromatography (TLC) with dichloromethane/ethyl acetate (93:7 v/v) was performed to monitor the reaction progress and ensure optimal reaction conditions were achieved at 19 hours. The brown oil crude was washed using a non-polar hexane solvent following a modified method from the literature (Barbante et al., 2015). Yield: 1.01 g, 89%.

Scheme 3.2

*Schematic pathway for the synthesis of the **F_2bpyta** ligand as the starting material for the synthesis of complexes **IR1** and **IR2***

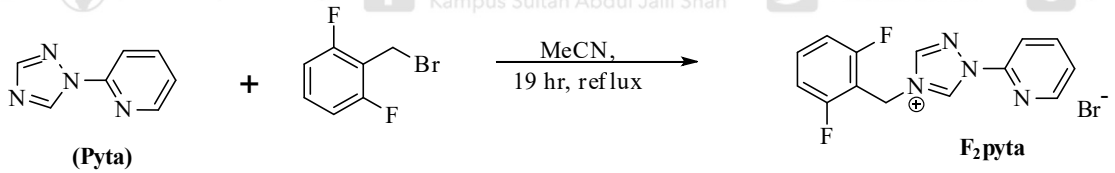

(Pyta) F_2pyta

3.2.1.3 2-(4-methylbenzyl)-(1,2,4-triazol-1-yl)pyridine ligand, (Mbpyta)

Mbpyta was prepared from **pyta** that was used as previously synthesised (0.530 g, 0.003 mol) and 4-methylbenzyl bromide (0.630 g, 0.003 mmol) and visualised in **Scheme 3.3**. The mixture was refluxed at a mole ratio equivalent to 1:2.1 respectively, for 19 hours under a nitrogen atmosphere in 80 mL of acetonitrile. Thin-layer chromatography (TLC) with dichloromethane/ethyl acetate (93:7 v/v) was performed to monitor the reaction progress and ensure optimal reaction conditions were achieved at 19 hours. The brown oil crude was washed using a non-polar hexane solvent

following a modified method from the literature (Barbante et al., 2015). Yield: 0.80 g, 94%.

Scheme 3.3

*Schematic pathway for the synthesis of the **Mbpyta** ligand as the starting material for the synthesis of complexes **IR3** and **IR4***

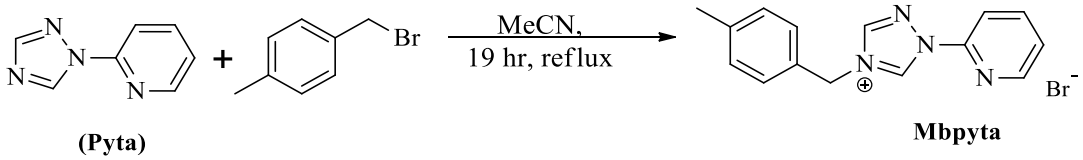

(Pyta) **Mbpyta**

3.2.2 Synthesis of Iridium(III) Dimer Complexes

3.2.2.1 Bis(phenylpyridine)iridium(III)-μ-dichlorobis(phenylpyridine)iridium(III), $(ppy)_2IrCl_2Ir(ppy)_2$, D1

In 60 mL of a 3:1 ethoxyethanol-water mixture, iridium trichloride hydrate (0.093 g, 0.311 mol, 1.0 equiv) and 2-phenylpyridine (0.116 g, 0.748 mmol, 2.4 equiv) were prepared. **Scheme 3.4** visualises the schematic pathway for the synthesis of the Dimer complex **D1**. The mixture was refluxed at 110 °C for 16 hours while being exposed to a nitrogen atmosphere and darkness. The yellow precipitate was employed in the next step to synthesis the iridium(III) complex without additional purification after the mixture had cooled to room temperature and was thoroughly washed with distilled water and chloroform. Yield: 0.297 g, 89%.

Scheme 3.4

*Schematic pathway for the synthesis of the Dimer complex **D1** as the starting material for the synthesis of complexes **IR1** and **IR3***

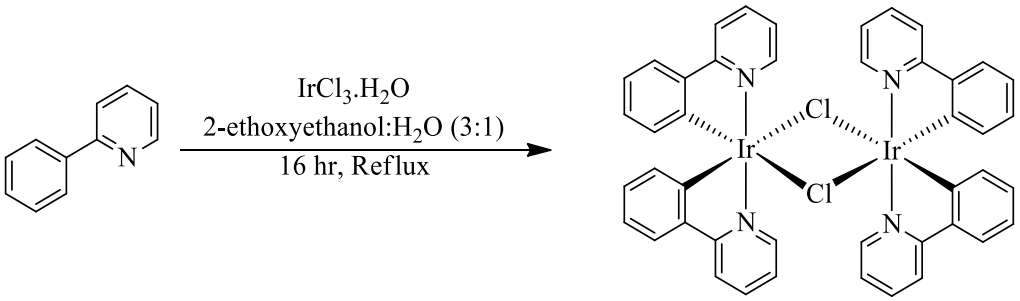

3.2.2.2 Bis(2,4-difluorophenylpyridine)iridium(III)-μ-dichlorobis(2,4-difluorophenylpyridine)iridium(III), $(F_2ppy)_2IrCl_2Ir(F_2ppy)_2$, D2

In 60 mL of a 3:1 ethoxyethanol-water mixture, iridium trichloride hydrate (0.075 g, 0.251 mmol, 1.0 equiv) and 2-(2,4-difluorophenyl)pyridine (0.115 g, 0.603 mmol, 2.4 equiv) were prepared. **Scheme 3.5** visualised the schematic pathway for the synthesis of the Dimer complex **D2**. The mixture was refluxed at 110 °C for 16 hours while being exposed to nitrogen atmosphere and darkness. The yellow precipitate was employed in the next step to synthesis the iridium(III) complex without additional purification after the mixture had cooled to room temperature and was thoroughly washed with distilled water and chloroform. Yield: 0.305 g, 83%.

Scheme 3.5

*Schematic pathway for the synthesis of the Dimer complex **D2** as the starting material for the synthesis of complexes **IR2** and **IR4***

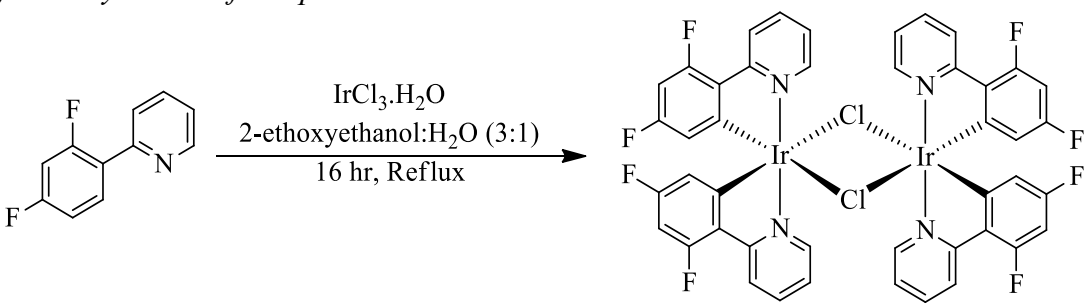

3.2.3 Synthesis Designated Complexes of Iridium

3.2.3.1 $Ir(ppy)_2(CNF_2bpyfa)$ complex, IR1

In 40 mL of 1,2-dichloroethane, F_2Bpyta (0.0955 g, 0.25 mmol equiv.) was reacted with $(ppy)_2IrCl_2Ir(ppy)_2$ (0.1500 g, 0.10 mmol equiv.) with the addition of Ag_2O (0.0681 g, 0.21 mmol equiv.). **Scheme 3.6** visualises the schematic pathway for the synthesis of the complex **IR1.** The mixture was refluxed under continuous nitrogen gas for 24 hours. Thin-layer chromatography (TLC) with $CH_2Cl_2/(CH_3)_2CO$ (4.5:0.5) was performed to monitor the reaction progress and ensure optimal reaction conditions were achieved at 24 hours. Celite was used to filter the reaction mixture, and the filtrate was then evaporated until it was scorched. After dissolving the crude material in 50/50 mL of deionised water and methanol, the mixture was stirred for 1 hour at room temperature. The crude organic layer was collected via extraction and was dried over Na_2SO_4. The crude was purified using column chromatography with $CH_2Cl_2/(CH_3)_2CO$ (4.5:0.5) as the eluent.

Scheme 3.6

*Schematic pathway for the synthesis of the $Ir(ppy)_2(CNF_2bpyfa)$ complex, **IR1**, from the previously synthesised **D1** and **F_2bpyta***

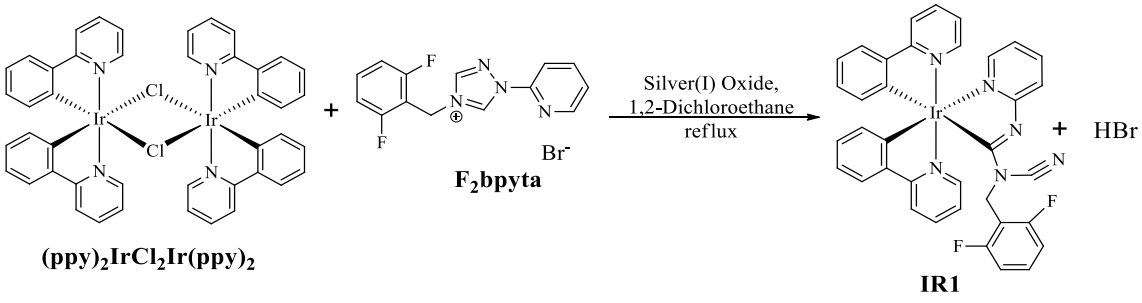

$(ppy)_2IrCl_2Ir(ppy)_2$ **F_2bpyta** **IR1**

3.2.3.2 Ir(F_2ppy)$_2$(CNF_2bpyfa) complex, IR2

In 40 mL of 1,2-dichloroethane, F_2Bpyta (0.0578 g, 0.25 mmol equiv.) was reacted with (F_2ppy)$_2$IrCl_2Ir(F_2ppy)$_2$ (0.1030 g, 0.1 mmol equiv.) with the addition of Ag_2O (0.0412 g, 0.21 mmol equiv.). **Scheme 3.7** visualises the schematic pathway for the synthesis of the complex **IR2.** The mixture was refluxed under continuous nitrogen gas for 24 hours. Thin-layer chromatography with CH_2Cl_2/$(CH_3)_2CO$ (4.5:0.5) was performed to monitor the reaction progress and ensure optimal reaction conditions were achieved at 24 hours. Celite was used to filter the reaction mixture, and the filtrate was then evaporated until it was completely dry. After dissolving the crude material in 50/50 mL of deionised water and methanol, the mixture was stirred for 1 hour at room temperature. The crude organic layer was collected via extraction and was dried over Na_2SO_4. The crude was purified using column chromatography with CH_2Cl_2/$(CH_3)_2CO$ (4.5:0.5) as the eluent.

Scheme 3.7

Schematic pathway for the synthesis of the Ir(F_2ppy)$_2$(CNF_2bpyfa) complex, ***IR2****, from the previously synthesised* ***D2*** *and* ***F_2bpyta***

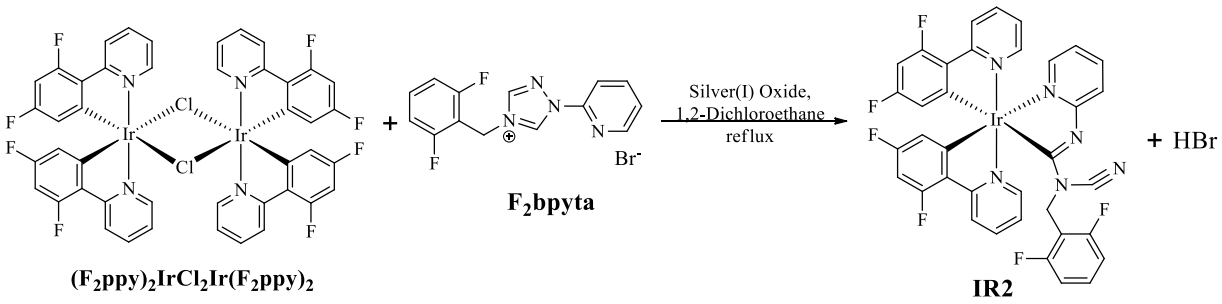

(F_2ppy)$_2$IrCl_2Ir(F_2ppy)$_2$ **F_2bpyta** **IR2**

3.2.3.3 $Ir(ppy)_2(CNMbpyfa)$ complex, IR3

In 40 mL of 1,2-dichloroethane, MBpyta (0.0878 g, 0.25 mmol equiv.) was reacted with $(ppy)_2IrCl_2Ir(ppy)_2$ (0.150 g, 0.1 mmol equiv.) with the addition of Ag_2O (0.0680 g, 0.21 mmol equiv.). **Scheme 3.8** visualises the schematic pathway for the synthesis of the complex **IR3.** The mixture was refluxed under continuous nitrogen gas for 24 hours. Thin-layer chromatography with $CH_2Cl_2/(CH_3)_2CO$ (4.5:0.5) was performed to monitor the reaction progress and ensure optimal reaction conditions were achieved at 24 hours. Celite was used to filter the reaction mixture, and the filtrate was then evaporated until it was completely dry. After dissolving the crude material in 50/50 mL of deionised water and methanol, the mixture was stirred for 1 hour at room temperature. The crude organic layer was collected via extraction and was dried over Na_2SO_4. The crude was purified using column chromatography with $CH_2Cl_2/(CH_3)_2CO$ (4.5:0.5) as the eluent.

Scheme 3.8

*Schematic pathway for the synthesis of the $Ir(ppy)_2(CNMBbpyfa)$ complex, **IR3**, from the previously synthesised **D1** and **Mbpyta***

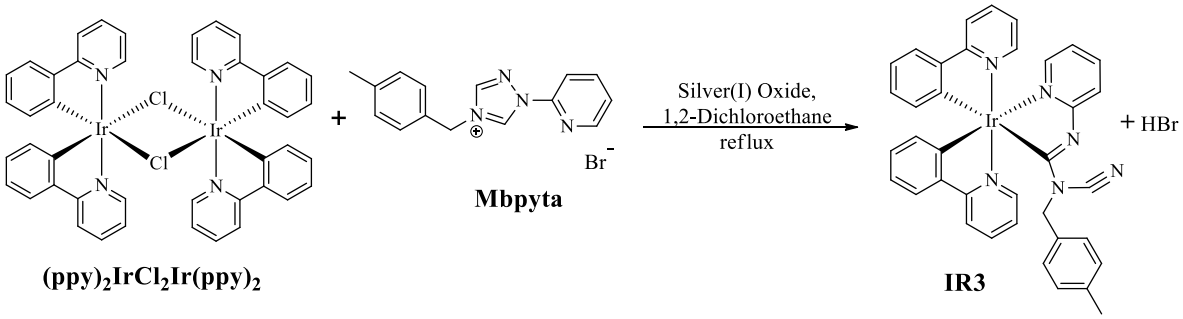

3.2.3.4 Ir(F_2ppy)$_2$(CNMbpyfa) complex, IR4

In 40 mL of 1,2-dichloroethane, MBpyta (0.0504 g, 0.25 mmol equiv.) was reacted with $(F_2ppy)_2IrCl_2Ir(F_2ppy)_2$ (0.0976 g, 0.1 mmol equiv.) with the addition of Ag_2O (0.0391 g, 0.21 mmol equiv.). **Scheme 3.9** visualises the schematic pathway for the synthesis of the complex **IR4.** The mixture was refluxed under continuous nitrogen gas for 24 hours. Thin-layer chromatography with CH_2Cl_2/$(CH_3)_2CO$ (4.5:0.5) was performed to monitor the reaction progress and ensure optimal reaction conditions were achieved at 24 hours. Celite was used to filter the reaction mixture, and the filtrate was then evaporated until it was completely dry. After dissolving the crude material in 50/50 mL of deionised water and methanol, the mixture was stirred for 1 hour at room temperature. The crude organic layer was collected via extraction and was dried over Na_2SO_4. The crude was purified using column chromatography with CH_2Cl_2/$(CH_3)_2CO$ (4.5:0.5) as the eluent.

Scheme 3.9

Schematic pathway for the synthesis of the Ir(F_2ppy)$_2$(CNMBbpyfa) complex, ***IR4****, from the previously synthesised* ***D2*** *and* ***Mbpyta***

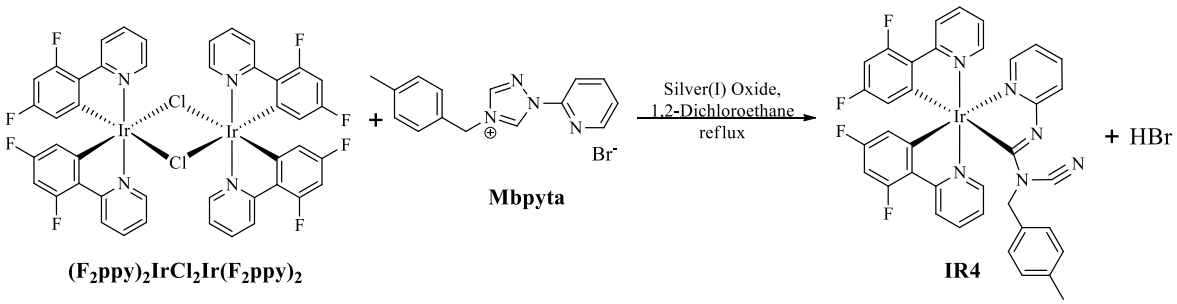

$(F_2ppy)_2IrCl_2Ir(F_2ppy)_2$

3.2.4 Isolation and Purification Techniques

To get a pure species of iridium(III) complexes **IR1**–**IR4**, proper chromatography techniques were performed in the ligand and complex purifications. In this experimental stage, thin-layer chromatography (TLC) and column chromatography (CC) were employed. Conceptually, the chromatography method was used to separate and isolate targeted compounds based on their level of polarity.

At the very beginning of the chromatography process, TLC was performed using the silica gel 60 PF MERCK, Darmstadt, pre-coated aluminium-backed sheets to select an appropriate solvent system and count the number of compounds in the crude samples. For complex purification **IR1**–**IR4**, a solvent system with a ratio of 4.5:0.5 for dichloromethane: acetone (CH_2Cl_2/$(CH_3)_2CO$) was chosen to be employed after several trials of TLC had been done. Two spots of the compound were produced from the TLC results and all the compounds that appeared were justified by calculating their retardation factor (R_f) values (ratio of the solute's distance travelled to the solvent's distance travelled) (Shan, 2016). The values of R_f were spotted as not being close to each other, so we got the most optimum solvent system to be employed in the following column chromatography. The spot was assigned to be pure complex by comparing its R_f value with the R_f values of its starting dimer and ligand, in which the R_f value was not the same as the R_f value of its starting dimer and ligand. To help visualise the spots on TLC, a handheld UV lamp model UVGL-58 under ultraviolet light 254 nm and 365 nm was applied. The data of the potential spot is then referenced for use in the next stage of extensive column chromatography.

Column chromatography was prepared by employing the solvent system that had been optimised in the previous stage of TLC. The absorbents utilised in this study were silica gel 60 (70-230) mesh ASTM MERCK 7734 and sometimes changed into (230-440) mesh ASTM MERCK 9385, while the mobile phase used was 4.5:0.5 of dichloromethane/acetone for complexes **IR1**–**IR4** and 93:7 of dichloromethane/methanol for ligand pyta. The silica gel slurry was placed into the glass column and the column was packed, resulting in a well-packed column that exhibited no cracks or patches. Before being loaded onto the adsorbent bed in the packed column, the crude sample was dissolved completely in an appropriate solvent to fully dissolve the sample in a minimum volume. The separation was observed with the help of UV light (**Figure 3.1**), and each fractional separation was collected in small test tubes and separated according to their fractional polarity.

Figure 3.1

The column chromatography fractional separation for complex $Ir(F_2ppy)_2(CNF_2bpyfa)$, ***IR2***

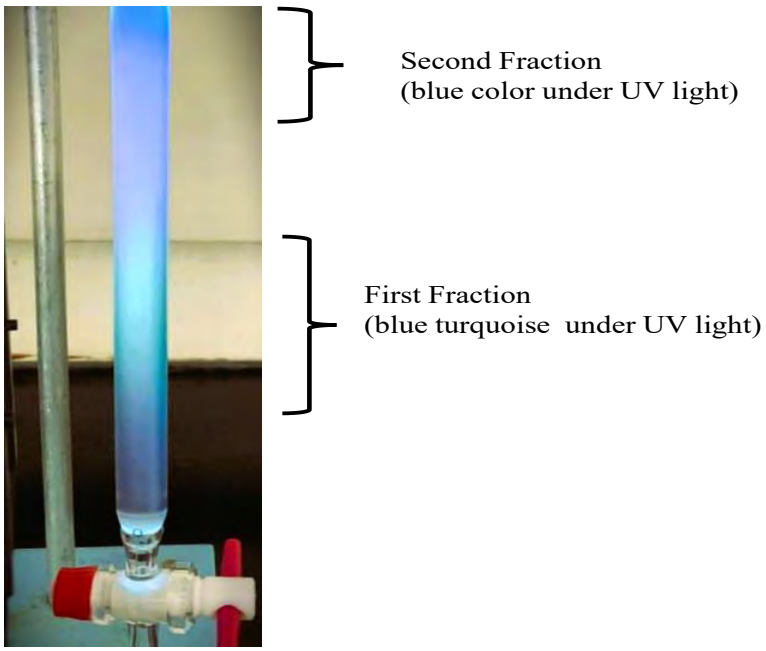

To confirm the identity of the product, each fraction was spotted on a TLC plate at intervals, and fractions containing the same value of R_f were combined with subsequent washing of test tubes using the same solvent system. Next, the R_f value of each fraction was calculated again and the compound with the same R_f value as targeted in the very beginning was combined, concentrated under reduced pressure, and checked for the ^{1}H NMR spectroscopy analysis (Shan, 2016). The well-resolved signal and clean spectra of ^{1}H NMR spectroscopy were used to decide the purity of the synthesised compound. If the compound is not purified enough, TLC and CC procedures will be repeated to obtain the best-purified samples. However, Prep Thin layer chromatography (PTLC) was also introduced to the purification approaches when working with extremely tiny amounts of compounds, where the principles of TLC were employed in the larger sizes of chromatography plates. The compound separation was directly observed in the plate with the help of a UV lamp. Each band of interest was scraped off with a spatula or blade, with options for retrieval, including washing the silica gel in a polar solvent or following with filtration and concentration of the purified compound. Finally, the purified compounds were determined once again as a single spot on the TLC analysis.

To conclude, chromatography techniques for the isolation and purification of crude samples can be lengthy and challenging to be done. Several precautions and steps need to be taken to have a high percentage yield of products, however, this method has proved to be the most promising procedure to have a good isolated purified compound in bulky species (Dong et al., 2019)

3.3 Instruments

The instruments utilised in this study were categorised to achieve four primary characterisation objectives: spectroscopic analysis, purification identification, structural studies, and photophysical analysis. All the instruments were analysed in Universiti Pendidikan Sultan Idris unless otherwise stated. Below are thorough explanations of each instrument used: -

3.3.1 Fourier Transform-Infrared Spectrometer

Fourier Transform-Infrared spectra were measured using the Thermo Nicolet Nexus spectrometer in the 4000–600 cm^{-1} regions to determine the presence of functional groups and bond stretching in all the synthesised compounds. Since the products analysed were in powder, the samples of approximately 5 mg were analysed directly with a diamond as an attenuated total reflectance (ATR) accessory. In definition, the ATR method involves pressing the sample against a high-refractive-index prism and measuring the infrared spectrum using infrared light that is internally reflected in the prism (Werle et al., 2017). All the band stretching was detected using the same software provided by the FT-IR spectrophotometer model and visualised using the spectra analysis conducted in Origin Pro version 8.5.

3.3.2 Nuclear Magnetic Resonance Spectrometer

Nuclear Magnetic Resonance (NMR) analysis of synthesised NHC ligands, dichloro-bridged iridium(III) dimers, and iridium(III) complexes was obtained by using a JEOL, JNM-ECX-500 NMR spectrometer, and the spectra were analysed using DELTA NMR

Spectra version 5.3.1 by JEOL. The spectra were used to confirm the structure of the designed compound by detecting protons, carbon, and some 3D analysis. Approximately 5 mg of each sample was diluted by a minimum amount of specific deuterated solvent for NMR analysis and was put into the NMR tube. The solvent used is either deuterated dimethyl sulfoxide-d_6 (DMSO-d_6), Chloroform-d ($CDCl_3$), or methylene chloride-d_2 (CD_2Cl_2-d_2), depending on the sample that needs to be characterised. The peak of solvents was used as the point of reference, which is 2.49 ppm for DMSO-d_6, 7.25 ppm for $CDCl_3$, and 5.45 ppm for CD_2Cl_2-d_2 to normalise the spectra (Fulmer et al., 2010). For all NMR, the NMR J-coupling or nuclear spin-spin coupling has been analysed to show indirect interaction of the nuclear magnetic moments mediated by the bonding electron, or in simple terms; J-coupling contains information about relative bond distances and angles. Recently, relativistic effects have been included in the NMR processing software to consider the effect of the heavy metal and heavy atoms that can promote a stronger coupling effect (Green & Yates, 2014).

Iridium(III) complexes can be effectively analysed using NMR spectroscopy because they are generally diamagnetic in nature due to their low-spin d^6 electronic configuration in an octahedral geometry which results in all electrons being paired (Green & Yates, 2014). Diamagnetic species do not possess unpaired electrons, allowing them to produce sharp, well-resolved NMR signals without significant broadening or shifting. However, the paramagnetic effect of iridium(III) complexes still can be analysed using NMR with some limitations, such as they often exhibit broadened peaks and poor resolution in NMR spectra due to magnetic interactions (Novotny et al., 2024). Paramagnetism of iridium(III) complexes usually happens when the ligands create a weak ligand field, which does not strongly split the *d*-orbitals. As a result,

electrons may spread out into higher energy orbitals instead of pairing up in lower ones. This leads to unpaired electrons, making the complex paramagnetic (Novotny et al., 2024). However, in most common Ir(III) complexes, especially with strong-field ligands like bipyridine or phenylpyridine, the electrons tend to pair up, making them diamagnetic instead. But if the ligands are weak field or the geometry is distorted, iridium(III) could show paramagnetic behaviour.

3.3.3 Liquid Chromatography–Mass Spectrometry System

Mass spectra of the synthesised iridium(III) complexes were recorded using a Bruker Esquire Liquid Chromatography Mass Spectrometry (LC-MS) 6000 fitted with an Agilent electrospray (ESI) ion source in the INFRA Laboratory at Universiti Malaya (UM). All samples were filtered using a micro-scale membrane to remove detergents and to reduce the complexity of the samples when focusing on specific known identification or quantitation (Wiśniewski, 2019). The samples were converted into ions so that the ions were sorted and separated according to their mass-to-charge (m/z) ratios and relative abundances (Kaklamanos et al., 2015; Nakorchevsky & Yates, 2012). The instrument consists of three major components: the ion source for producing gaseous ions from the substance being studied, the mass analyser for resolving the ions into their characteristic mass components according to their m/z ratio, and the detector system for detecting the ions and recording the relative abundance of each of the resolved ionic species (Kaklamanos et al., 2015). The results of separated ions are finally displayed according to their retention time. Significantly, the mass spectrometer is one of the important instruments in supporting the successful characterisation of new compounds.

3.3.4 Carbon, Hydrogen, and Nitrogen Elemental Analyser

Carbon, Hydrogen, and Nitrogen (CHN) elemental analysis were carried out to measure the purities of synthesised complexes in bulky species by using Thermo Scientific Flash EA 1112 Elemental Analyser. The analysis was conducted by combustion of the samples in an oxygen-rich atmosphere and measurement of the resulting gases, which are H_2O, CO_2, and N_2. The samples of synthesised iridium(III) complexes were weighed in milligrams, subsequently put in the loading chamber, and then held until a dose of oxygen was released. The sample was then dropped into the furnace, and at the same time, the oxygen arrived and combusted in the heated oxygen-rich environment. The final integrated signal was adjusted for blank, calibration, and weights, and the result was displayed as the weight percentage of carbon, nitrogen, and hydrogen (Thompson, 2008). Usually, the measured values have to fit the gold standard of ± 0.40% of the calculated values to guarantee sufficient purity according to some guidelines from international journal publishers (Kandioller et al., 2022). In contrast to the single crystallographic X-ray diffractometer (SC-XRD) equipment, which only provided the purities in a single spot of compound species, the findings from this instrument will demonstrate the purity of the species under bulky circumstances (Kandioller et al., 2022).

3.3.5 Single Crystal X-ray Diffraction (SC-XRD)

The single crystal X-ray crystallography study was performed using a Bruker D8 QUEST with a photon CCD area-detector diffractometer (Bruker, AXS Inc., Madison, WI, USA) and graphite monochromated Mo-Kα radiation (λ = 0.71073 Å) from I-CRIM Laboratory at Universiti Kebangsaan Malaysia. The data collected were reduced

using the SAINT program, and empirical absorption correction was carried out using SADABS (Lynch, 1987). The structure was solved by direct methods and refined via the SHELXL software package using a full matrix least-squares approach (Bahron et al., 2019). The molecular graphics were created using SHELXTL and MERCURY software. All hydrogen atoms were assigned by assuming idealised geometries with d(C–H) = 0.93 and 0.96 Å for aromatic and aliphatic carbon atoms, respectively, with Uiso(H) = 1.2 Ueq(C). All non-hydrogen atoms were refined anisotropically. The PLATON program was used for molecular structure calculation.

3.3.6 UV-Visible spectrometer

Steady-state absorption spectra of the synthesised iridium(III) complexes were recorded by using a Cary 60 Agilent Technologies types of UV-Visible spectrophotometer. The samples were prepared in dichloromethane solutions at room temperature in a 1 cm path-length quartz cell. UV-Vis spectrophotometer uses visible light and ultraviolet light to analyse the chemical structure of a substance, such as to measure the intensity of light, and the intensity is proportional to the wavelength. When the ultraviolet light projects onto various organic complexes, these complexes will absorb it. Thus, the absorption of a compound is obtained by the result (Rocha et al., 2018). Although the UV wavelength ranges from 100–380 nm and the visible component goes up to 800 nm, most of the spectrophotometers have a working wavelength range between 200–1100 nm (Glory et al., 2015; Rocha et al., 2018). The spectra were then analysed using Microsoft Excel and OriginPro 8.5 software to study the electronic transition properties of the synthesised iridium(III) complexes. In addition, the molar absorption coefficient (ε) was then calculated according to the Beer-Lambert Law formula:

$$A=\varepsilon c\iota,$$

Where A: absorbance from the Uv-Vis spectrum, c: concentration of the sample (mol/L), and ι: sample path length (usually 1 cm path length).

3.3.7 Fluorescence Spectrometer

Steady-state emission spectra of the sample were recorded using an Agilent Cary Eclipse Fluorescence Spectrophotometer at room temperature by using air-equilibrated dichloromethane, CH_2Cl_2, and determined with a microsecond xenon flashlamp. Fluorescence spectroscopy is a spectroscopy method used to analyse the fluorescence properties of a sample by determining the concentration of an analyte in a sample. In fluorescence spectroscopy, a beam with a wavelength varying between 180 and ~800 nm passes through a solution in a cuvette, and the light that is emitted by the sample is measured. In fluorescence spectrometry, both an excitation spectrum (the light that is absorbed by the sample) and/or an emission spectrum (the light emitted by the sample) can be measured. The concentration of the analyte is directly proportional to the intensity of the emission. The absolute quantum yields in fluid solutions have been measured using a more reliable method than those previously reported. By integrating the excited wavelength data from the UV-Vis spectroscopy into the featured instrument, the steady state of the emission spectra was calculated at the ranges 400 nm to 600 nm. The spectra were then analysed using Microsoft Excel and OriginPro 8.5 software.

3.3.8 Photoluminescence Spectrometer

Photoluminescence Spectrometer (PL), Edinburgh Instrument, FLS920 model from I-CRIM Laboratory at Universiti Kebangsaan Malaysia was used to study the decay lifetime and photoluminescence quantum yield (PLQY) in the excited state. The PLQY was measured using the relative method using Ir(phenylpyridine)3 in dichloromethane, with CH_2Cl_2 solution as the standard. The equation $\Phi_s = \Phi_r(I_s/I_r)(A_r/A_s)(\eta_s^2/\eta_r^2)$ was used to calculate the quantum yields, where Φ_s = quantum yield of the sample, Φ_r = quantum yield of the reference, I_s = area of the emission fluorescence spectrum of the sample, I_r = area of the emission fluorescence spectrum of the reference, A_s = absorbance of the sample, A_r = absorbance of the reference, η_s = refractive index of the solvent for the sample, η_r = refractive index of the solvent for the reference.

3.4 Computational Methods of DFT and TD-DFT Analysis

DFT and TD-DFT analyses for all the synthesised iridium(III) complexes were calculated using Gaussian 16 and visualised using GaussView 6.0, performed using High Performance Computer (HPC) at Universiti Teknologi Malaysia and Prince Sattam bin Abdulaziz University, Al-Kharj, Saudi Arabia. Geometry optimisation, NMR analysis, and frequency vibration calculations of the synthesised iridium(III) complexes were performed at Becke's three-parameter functional and the Lee-Yang-Parr functional (B3LYP) with the basis set LANL2DZ as implemented in Gaussian 16 software. The Electrostatic Potential Surface (ESP), Frontier Molecular Orbital (FMO) specifically transition contribution, and HOMO-LUMO analysis were obtained at the ground state level. The absorption spectra were predicted using the TD-DFT method at

the same level of theory. The solute-solvent effects were considered implicitly using the integral equation formalism polarizable continuum model (IEF-PCM).

A theoretical mechanistic study was analysed using the Avicenna High-Performance Computing cluster at Nottingham Trent University (NTU). Density functional theory (DFT) was employed to provide a theoretical mechanistic study of the role of silver oxide, Ag_2O, in the synthesis pathway of the complex. All the calculations were performed using the ωB97X-D3 functional and def2-SVP (double-zeta plus polarisation) basis set. The ωB97X-D3 functional was chosen as it excels in various chemical phenomena, including barrier heights. Solvation was accounted for using the C-PCM solvation model with a dielectric constant of 10.36, corresponding to ethylene dichloride, as implemented in the Q-Chem 5.4 package. The CiF file generated from the single crystal of complex $Ir(F_2ppy)_2$(CNMBpyfa) was used as the starting coordinates, which were optimised using the functional and basis set above.

3.4.1 Geometrical Designs and Optimisation of S_0 Geometries in Density Functional Theory

The DFT calculation for the synthesised iridium(III) complexes **IR1–IR4** began by optimising the molecular structure. Since the complexes **IR1–IR4** bear the novel types of ancillary ligands, we draw the structure using GaussView 6.0 rather than the experimental CiF file from SC-XRD to better compare the theoretical and experimental analysis. This approach was intentionally chosen to enable a clearer and more consistent comparison between the theoretical (DFT-optimised) and experimental (SC-XRD) structures. By starting from an idealised, manually constructed geometry, we ensured that any structural deviations observed during optimisation could be directly attributed

to the theoretical modelling, rather than being biased by the experimental input. This strategy is particularly important for these complexes, as they feature novel types of ancillary ligands whose flexibility and coordination behaviour may not be fully captured in a crystal environment. The full comparative discussion of the theoretical versus experimental geometries is presented in **Chapter 4, subtopic 4.6**. Geometries of all iridium(III) complexes in the ground state (S_0) were optimised by restricted and unrestricted density functional theory without any symmetry constraints. The absorption energies of singlet-singlet transitions were calculated by using the TD-DFT associated with the polarised continuum model (PCM) in dichloromethane (CH_2Cl_2) media based on the optimised ground-state equilibrium structures (Alsaeedi, 2023). However, to deal with the time-consuming problems, the solvation effect of PCM was disregarded in the theoretical vibrational and NMR analysis. The Natural Bond Analysis was calculated at the same level of theory and the percentage of charge contribution together with Frontier Molecular Orbital Studies, the Natural Bond Analysis was computed at the same theoretical level and the percentage of charge contribution was determined. Together with Frontier Molecular Orbital Studies, the Molecular Orbitals (MO) contribution analysis was computed at the same theoretical level and the percentage of charge contribution was determined.

CHAPTER 4

RESULTS & DISCUSSION

4.1 Synthesis of a New Class of Heteroleptic Iridium(III) Complexes

Heteroleptic cyclometallated iridium complexes have attracted considerable interest, where one bidentate or two monodentate ancillary ligands occupy the remaining two coordination sites. The ancillary ligand offers another means of controlling the photophysical properties, motivating studies to aim for long-lived blue-emitting Organic Light Emitting Diodes (OLEDs) that are critically needed in addition to their green and red-emitting counterparts (Adeloye et al., 2017; Omae, 2016).

In this study, four new species of octahedral heteroleptic iridium(III) complexes bearing one bidentate ancillary ligand moiety were successfully synthesised and characterised with spectroscopic and chemical analysis. The general formula of the synthesised complexes was $Ir(ppy)_2(pyfa)$, where ppy is a phenylpyridine ligand that occupied the cyclometallating moieties, while pyfa is a pyridinylformimidamide-based ligand that occupied the ancillary moiety of iridium(III) complexes. The chemical analysis, including the spectroscopic studies, has confirmed the molecular structure of the synthesised complexes. The synthetic procedure leading to the synthesised complexes is described in three experimental stages as follows:

The first stage was the synthesis of precursors dichloro-bridged iridium(III) dimer complexes, $(ppy)_2IrCl_2Ir(ppy)_2$, **D1** and $F_2(ppy)_2IrCl_2Ir(F_2ppy)_2$, **D2**. The dimer precursors of **D1** and **D2** were synthesised by using modifications of the previously reported literature (Wong et al., 2015). The substituents on the 2- and 4 4-positions of the phenylpyridine (ppy) varied by the presence of fluorine (**D2**) or hydrogen (**D1**) atoms. Previous studies have reported that the 2,4-difluorophenylpyridine is one of the promising ligands to achieve blue emission iridium(III) complex (Henwood et al., 2016; Na & Teets, 2018). Introducing fluorine into the ligand was among the promising factors to achieve HOMO stabilisation and hence contributed to blue emission luminescences complexes (He et al., 2016; Lee & Han, 2020). However, most of these synthesised complexes with fluorine substituents experienced low-efficiency phosphorescence due to the heavy atom effect triggered by the fluorine atom that introduces intrinsic drawbacks because the reactive C–F bonds are thermally and electrochemically unstable (He et al., 2016). Significantly, electrochemical instability will eventually lead to a short emission lifetime that strongly affects the

phosphorescence efficiencies. Hence, the design of the dimer with and without fluorine substituents attached to phenylpyridine, as shown in **Scheme 4.1,** can provide an insightful comparison discussion about this issue. The physical properties of the synthesised dichloro-bridged iridium(III) dimer are reported in **Table 4.1,** with good percentages of yield recorded exceeding 80%. These dimer precursor products were stored in a dark cupboard to avoid direct exposure to light and were used as synthesised in stage 3 without any further purification methods.

Scheme 4.1

The synthesis of dichloro-bridged iridium(III) dimer complexes precursor with and without fluorine substituents

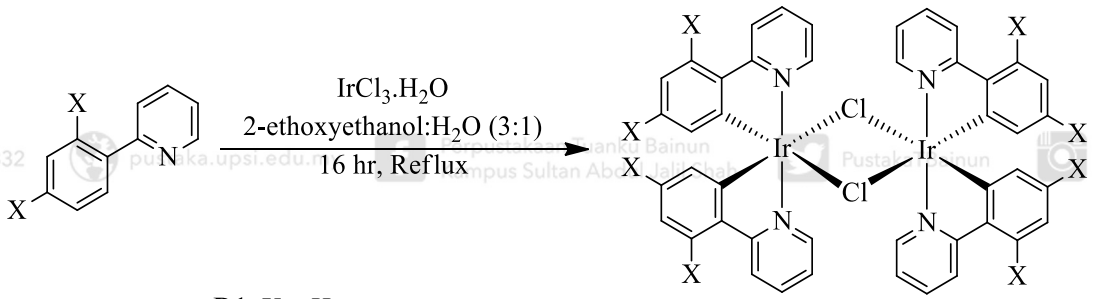

D1: X = H
D2: X = F

Table 4.1

Physical Properties of the Dichloro-Bridged Iridium(III) Dimer Complexes

Compound	Colour	Yield (%)
$(ppy)_2IrCl_2Ir(ppy)_2$, **(D1)**	Yellow	89
$(F_2ppy)_2IrCl_2Ir(F_2ppy)_2$, **(D2)**	Yellow	83

The dichloro-bridged iridium(III) dimer precursors of **D1** and **D2** were successfully characterised using ^{1}H NMR spectroscopy. The detailed proton assignment of **D1** and **D2** is shown in **Figure 4.1,** with the solvent residual peaks marked with an asterisk. The ^{1}H NMR spectrum of dimer **D1** displayed 8 well-resolved proton signals in the aromatic region between 10.00 and 5.00 ppm that were assigned to phenylpyridine proton (Wong et al., 2015), while the spectrum of dimer **D2** displayed 6 well-resolved signals in the same aromatic region. Both dimers consider C_2 symmetry.

Figure 4.1

*^{1}H NMR spectra of dichloro-bridged iridium(III) dimer precursors of **D1** and **D2***

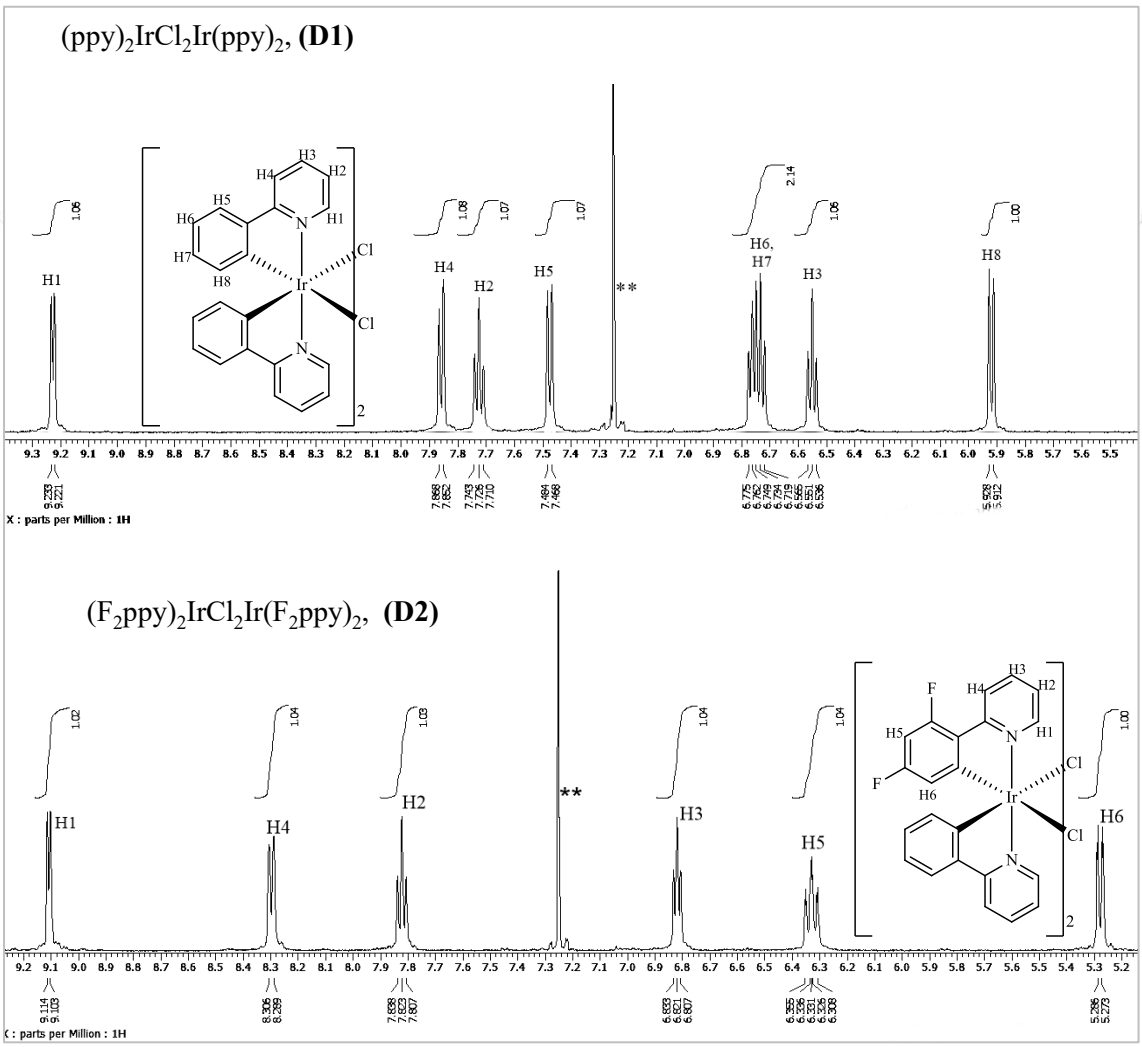

It can be seen clearly in **Figure 4.2** that the proton signals of H5 in the spectrum of dimer **D2** [6.35 ppm (*m*, J = 24.5 Hz)] and H6 [5.35 ppm (*d*, J = 21.5 Hz)] are split into triplet (2*n*+1) and duplet (*n*+1) respectively due to the coupling of two fluorine nuclei instead of having singlet multiplicity. In addition, the large value of the coupling constant for triplet H5 and H6 proved the splitting of the proton (Balci, 2005). To conclude, the dichloro-bridged iridium(III) dimer of **D1** and **D2** was successfully synthesised and characterised to be used as precursors for the complex synthesis.

Figure 4.2

Zoom images for proton H5 and H6 in the dimer $(F_2ppy)_2IrCl_2Ir(F_2ppy)_2$, ***D2****, instead of having singlet multiplicity, these protons split into triplets and duplets caused by the neighbouring fluorine atom's strong coupling*

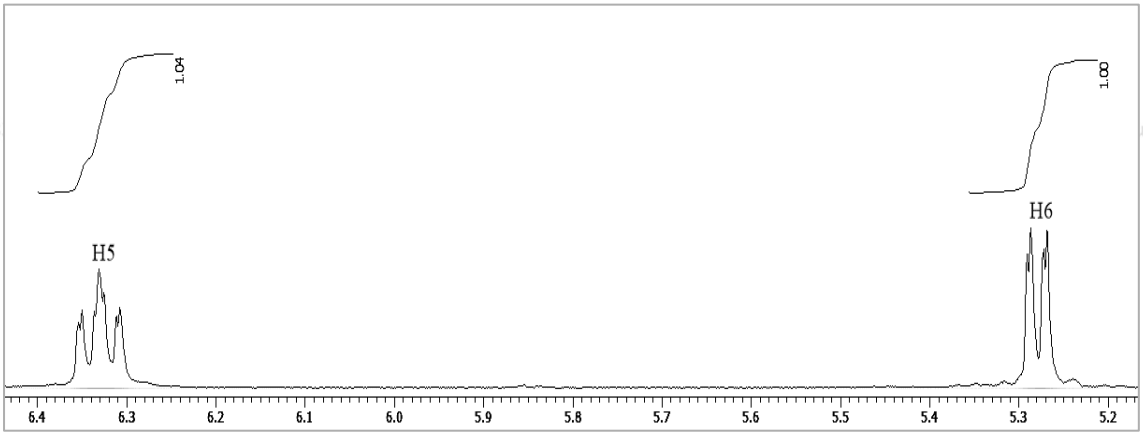

The second stage of the experimental part was the synthesis of the desired ligand triazolium salt analogues with different substituents to be used as the ancillary ligand in the complexes. The schematic pathway leading to the ligands **F_2bpyta** and **Mbpyta** was depicted in **Scheme 4.2**. The synthesised procedure of the ligands began with the synthesised of 2-(*1H*-1,2,4-triazol-1-yl)pyridine, **pyta,** by arylation of 1,2,4-triazole with 2-bromopyridine and copper(I) iodide was used as the catalyst. N1 arylation usually dominates due to the greater nucleophilicity of the N–N linkage in comparison

with that of N4. Further reaction of pyta with the appropriate alkyl halide (2.1 equivalent of 4-methylbenzyl bromide, 2.1 equivalent of 2,6-difluorobenzylbromide) in acetonitrile gave triazolium salts of 2-(4-methylbenzyl)-1,2,4-triazol-1-yl)pyridine **Mbpyta**, and 2-(2,6-difluorobenzyl)-1,2,4-triazol-1-yl)pyridine **F_2bpyta**, respectively. **Table 4.2** summarises the physical properties of the synthesised triazole-based ligands. The ligands **F_2bpyta** and **Mbpyta** were used as synthesised in stage 3.

Scheme 4.2

*Synthesis of pyridinyltriazole (**pyta**) and its derivatives, **F_2bpyta** and **Mbpyta** ligands*

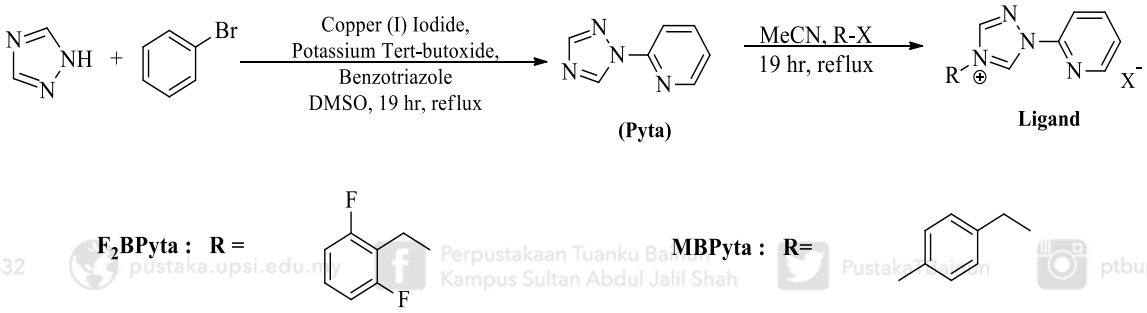

Table 4.2

Physical Properties of the Desired Ligand Triazolium Salt Analogues with Different Substituents

Compound	Colour	Yield (%)
2-(*1H*-1,2,4-triazol-1-yl)pyridine **(Pyta)**	Pale brown Crystalline	48
2-(2,6-difluorobenzyl)-(1,2,4-triazol-1-yl)pyridine **(F_2bpyta)**	Pale brown powder	89
2-(4-methylbenzyl)-(1,2,4-triazol-1-yl)pyridine **(Mbpyta)**	Pale brown powder	94

The ligands **F$_2$bpyta** and **Mbpyta** were selected for use in this study because the triazole ring is a class of N-heterocyclic carbene (NHC) group with electron-rich properties. These triazole rings will act as electron donors, resulting in stable bonds with metal, hence improving the decay lifetime and increasing the luminescence quantum yield of the synthesised complexes (Hopkinson et al., 2014). In addition, the ligands **F$_2$bpyta** and **Mbpyta** differed by the presence of 2,6-difluoro and methyl substituents. 2,6-difluoro substituents were chosen to give electron-withdrawing group properties. In contrast, methyl substituents were chosen to give electron-donating group properties to the ancillary ligand (Cortés-Arriagada et al., 2015). The stronger the electron-withdrawing ability of the substituent, the higher the LUMO destabilisation, hence the higher the HOMO-LUMO energy gap, resulting in higher emission energy of the synthesised complexes (Henwood & Zysman, 2016; Mohd Yusoff et al., 2017).

The ^{1}H NMR of the synthesised ligand **pyta** and its derivatives of **F$_2$bpyta** and **Mbpyta** are shown in **Figure 4.3 (A)–(C).** The proton in ^{1}H NMR spectra for ligand derivatives **F$_2$bpyta** and **Mbpyta** were assigned by comparing them with the spectrum of ligand **pyta**. As for the synthesised ligands, all the ^{1}H NMR spectra displayed well-resolved signals and similar patterns to each other in the aromatic region between 10.00 and 5.00 ppm, that assigned to proton correlation with phenylpyridine (Tao et al., 2017; Zulkifli et al., 2023) and pyridyltriazole (Qu et al., 2014). Additionally, there is a slightly different pattern in the aliphatic region due to the addition of different substituents referring to the 2-6-difluorobenzyl group and methylbenzyl group that successfully attached to the N4 of the triazole ring (You et al., 2021).

Figure 4.3 (A)

*The [1]H NMR spectrum for the **pyta** ligand precursor with its labelling scheme*

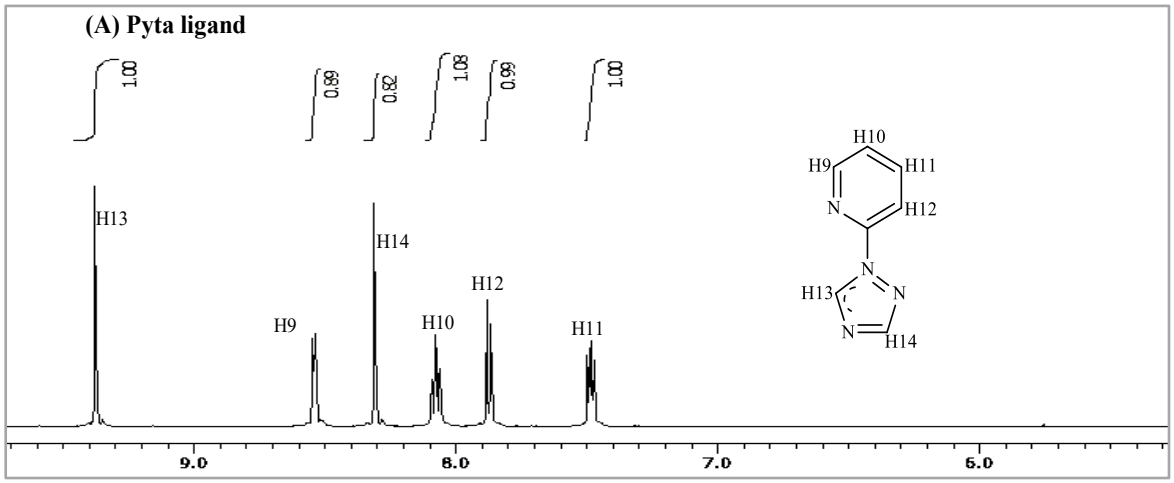

^{1}H NMR (500 MHz, DMSO-d_6) δ 9.38 (s, 1H), 8.54 (d, J = 4.0 Hz, 1H), 8.31 (s, 1H), 8.08 (t, J = 8.6 Hz, 1H), 7.88 (d, J = 7.4 Hz, 1H), 7.50–7.47 (m, 1H)

Figure 4.3 (B)

*The [1]H NMR spectra for the **F_2bpyta** ligand with its labelling scheme, H_2O residual peak is marked with ** and DMSO-d_6 residual is marked with ****

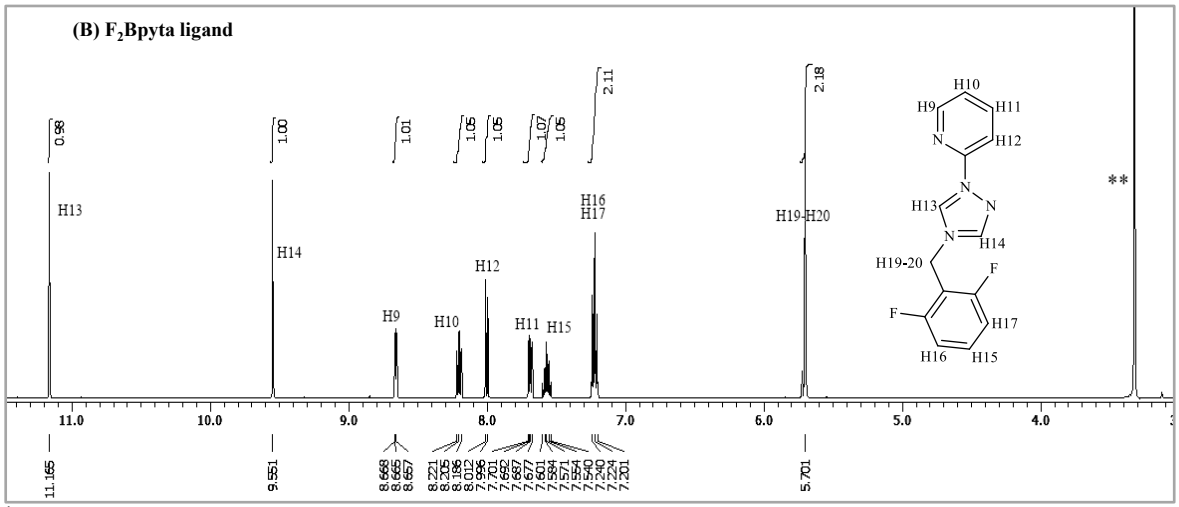

^{1}H NMR (500 MHz, DMSO-d_6) δ 11.16 (s, 1H), 9.55 (s, 1H), 8.66 (d, J = 4.6 Hz, 1H), 8.21 (t, J = 8.0 Hz, 1H), 8.00 (d, J = 8.0 Hz, 1H), 7.70-7.68 (m, 1H), 7.60–7.54 (m, 1H), 7.22 (t, J = 8.0 Hz, 2H), 5.70 (s, 2H)

Figure 4.3 (C)

*The [1]H NMR spectra for the **Mbpyta** ligand with its labelling scheme, H_2O residual peak, is marked with ** and the DMSO-d_6 residual is marked with ****

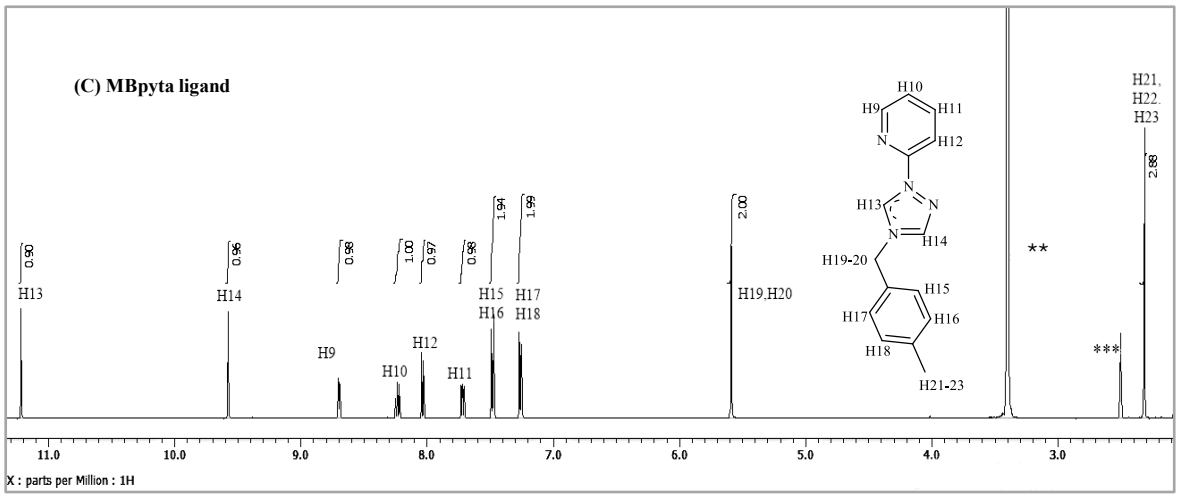

^{1}H NMR (500 MHz, DMSO-d_6) δ 11.22 (s, 1H), 9.58 (s, 1H), 8.70 (d, J = 4.3 Hz, 1H), 8.25–8.22 (m, 1H), 8.04 (d, J = 8.0 Hz, 1H), 7.72 (dd, J = 8.0, 5.2 Hz, 1H), 7.48 (d, J = 8.0 Hz, 2H), 7.26 (d, J = 8.0 Hz, 2H), 5.59 (s, 2H), 2.32 (s, 3H)

For all spectra of **Figure 4.3 (A)–(C)**, H13 and H14 proton singlets are highly deshielded and, hence, are a reference peak in many studies. This singlet proton in triazole appeared highly deshielded in the ^{1}H NMR spectrum (δ ~8–10 ppm or more), due to the strong electron-withdrawing effects of the three nitrogen atoms in the ring (Ji Ram et al., 2019; Omae, 2016). These electronegative atoms pull electron density away from the proton, reducing its shielding. Additionally, triazole is an aromatic heterocyclic compound, and the induced ring currents under an external magnetic field further deshield the proton by reinforcing the magnetic field experienced by it. In some cases, hydrogen bonding involving the triazole proton can also contribute to this deshielding effect by further lowering the local electron density (Ji Ram et al., 2019; Omae, 2016). These combined factors result in the triazole proton experiencing a stronger magnetic field, causing it to resonate at a higher chemical shift than 8.0 ppm.

For the comparative analysis of the ^{1}H NMR chemical shifts for **Pyta**, **F₂bpyta**, and **Mbpyta** ligands presented in **Table 4.3,** which demonstrates clear trends influenced by the electronic nature of the substituents. In **F₂bpyta**, the introduction of two strongly electron-withdrawing fluorine atoms on the phenyl ring induces a downfield shift of nearby protons, particularly H13 and H14 on the triazole ring, which resonate at δ 11.16 and 9.55 ppm, respectively. These values were significantly higher than in the unsubstituted **Pyta** ligand. Conversely, the presence of a methyl group in **Mbpyta**, an electron-donating substituent, leads to a slight upfield shift of the same protons, observed at δ 11.22 and 9.58 ppm. In addition, the pyridine ring protons (H9–H12) also show minor shifts consistent with these electronic effects. Additionally, the methylene bridge, H19–H20 experiences a slight deshielding in **F₂bpyta** (δ 5.70) compared to **Mbpyta** (δ 5.59), further supporting the influence of substituents on the ligand's electronic environment. These variations are primarily attributed to the electronic effects of the substituents, which either withdraw or donate electron density through inductive or resonance mechanisms (Navarro et al., 2017; Z. Wang et al., 2015). In **F₂bpyta**, the electronegative fluorine atoms act as electron-withdrawing groups, reducing electron density in the adjacent aromatic and heterocyclic systems (Tatarin et al., 2021). These result in deshielding of nearby protons, causing them to resonate downfield. In contrast, the methyl group in **Mbpyta** acts as an electron-donating group, increasing local electron density and leading to shielding of surrounding protons, which shifts their signals upfield (Tatarin et al., 2021). In summary, the substituents significantly influence the NMR chemical shifts by altering the electron distribution throughout the ligand framework. These systematic changes not only confirm successful structural modifications but also reflect how electronic effects can propagate through conjugated systems to affect distant protons within the ligand’s compound.

Table 4.3

*Comparative Analysis of ^1H NMR Spectra for ligands **Pyta**, **F_2bpyta** and **Mbpyta***

Proton Group	Pyta (ppm)	F_2Bpyta (ppm)	Mbpyta (ppm)
H13 (Triazole)	9.38	11.16	11.22
H14 (Triazole)	8.31	9.55	9.58
H9 (Pyridine)	8.54	8.66	8.70
H10	8.08	8.21	8.25–8.22
H11	7.88	8.00	8.04
H12	7.50–7.47	7.70–7.68	7.72
H15–H18 (Aromatic ring substituent)	–	7.60–7.22	7.48–7.26
H19–H20 (CH_2 linker)	–	5.70	5.59
H21–H23 (CH_3 in methyl)	–	–	2.32

The third stage is the final stage to synthesise a new class of heteroleptic bis(phenylpyridine) iridium(III) complexes using the dimer precursor and triazole-based ligand that have been synthesised in the first and second stages of the experimental flow previously. Subsequently, series of bis(phenylpyridine)(pyridinylformimidamide)iridium(III) complexes were successfully synthesised by reacting the dichloro-bridged iridium(III) dimer, in 1,2-dichloroethane solvent in the presence of silver(I) oxide (Ag_2O) with ligands F_2Bpyta and Mbpyta respectively, which gave bis(phenylpyridine)[(E)-N-cyano-N-(2,6-diflurobenzyl)-N'-(pyridin-2-yl)formimidamide]iridium(III); $Ir(ppy)_2(CNF_2pyfa)$, (**IR1**), bis(2,4-difluorophenylpyridine)[(E)-N-cyano-N-(2,6-diflurobenzyl)-N'-(pyridin-2-yl)formimidamide]iridium(III); $Ir(F_2ppy)_2(CNF_2pyfa)$, (**IR2**), bis(phenylpyridine)[(E)-N-cyano-N-(methylbenzyl)-N'-(pyridin-2-yl)formimidamide]iridium(III); $Ir(ppy)_2(CNMBpyfa)$, (**IR3**),

and bis(2,4-difluorophenylpyridine) (E)-N-cyano-N-(methylbenzyl)-N'-(pyridin-2-yl)formimidamide] iridium(III); $Ir(F_2ppy)_2(CNMBpyfa)$, (**IR4**). The schematic pathway leading to the complexes (**IR1**–**IR4**) was depicted in **Scheme 4.3**.

Scheme 4.3

*Synthesis of Bis(phenylpyridine)(pyridinylformimidamide)iridium(III) Complexes **IR1–IR4***

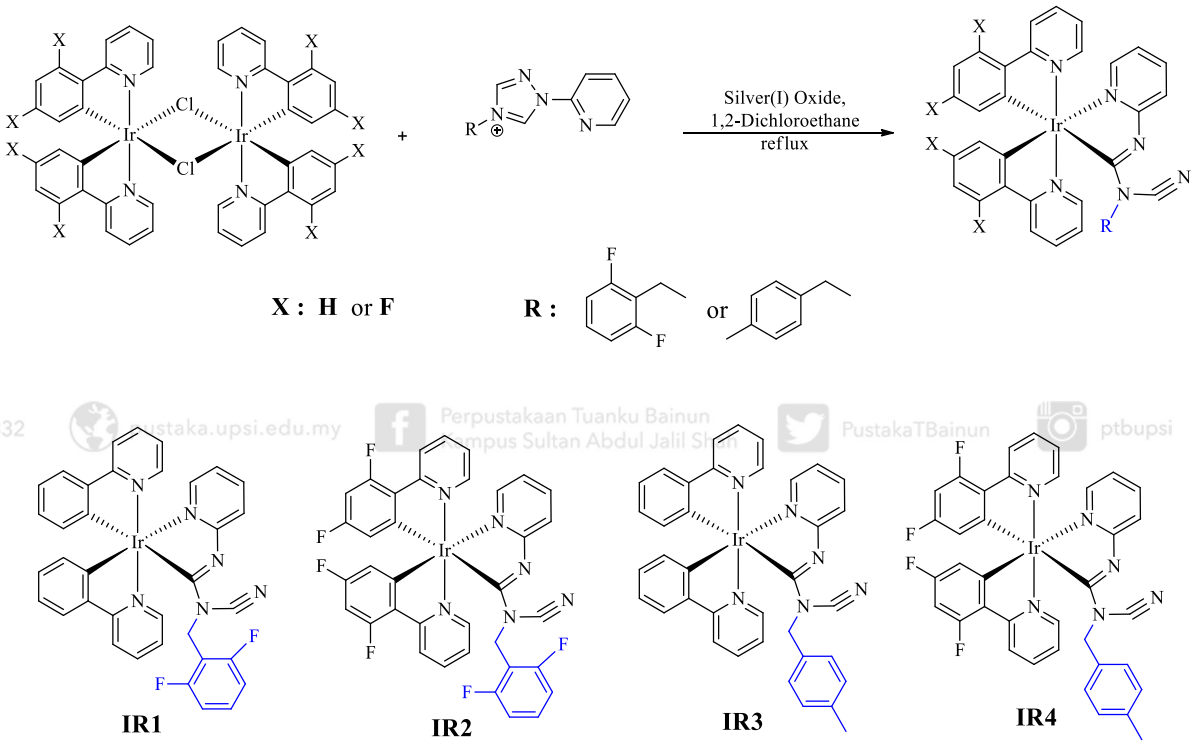

We have explained in **Chapter 2** that our complexes **IR1**–**IR4** were designed to meet the criteria of having high-emission energy with blue-efficient phosphorescence properties. These properties are related to the HOMO-LUMO molecular orbital contributed by the cyclometallated and ancillary ligand of the complexes. Significantly, different types of ligands will alter the HOMO-LUMO properties of each synthesised complex due to the different substituents in each ligand. Based on **Scheme 4.3**, an interesting finding has been revealed in this research where the starting cyclic triazole-

based ligand of **F_2bpyta** and **Mbpyta** has converted into acyclic formimidamide-based ligand of CNF_2bpyfa; (E)-N-cyano-N-(2,6-difluorobenzyl)-N'-(pyridin-2-yl)formimidamide and CNMbpyfa; (E)-N-cyano-N-(methylbenzyl)-N'-(pyridin-2-yl)formimidamide, respectively, when undergoing complexation with the iridium atom in a bidentate manner. This result was contradicted by the hypothesis of having a product of iridium(III) carbene complexes reported to have a high probability of blue efficient phosphorescence properties. After several trials of experimental procedure repeated with different molar ratios of starting ligand and dimers, the results of acyclic ancillary ligands still appeared. Hence, this result has opened a new discussion on the reaction mechanism of how the complexation process between iridium(III) dimer precursor with the triazole-based ligand took place in which the presence of silver(I) oxide and refluxed heating in an inert condition with the schlenk technique has became the important parameters to be discussed in the mechanism. A detailed investigation of the reaction mechanism and structural properties behind the formation of acyclic formimidamide ancillary ligands will be discussed in the final part of this chapter. In a nutshell, we have successfully synthesised four species of iridium(III) complexes bearing novel pyridinylformimidamide-based ligands in the auxiliary moiety to study their photoluminescence properties.

4.2 Characterisation of the Synthesised Iridium(III) complexes Bearing Pyridinylformimidamide Ancillary Ligand

The summary of physical and elemental analysis of all the synthesised bis(phenylpyridine)(pyridinylformimidamide)iridium(III) complexes **IR1**–**IR4** is shown in **Tables 4.4** and **4.5,** respectively. The yield for all the synthesised complexes was acceptable, approximately in the range of 50%. Achieving yields above 80% in coordination complex synthesis is often challenging due to the multiple reaction steps involved and the difficulty in removing by-products and impurities during purification, especially when using column chromatography. Similar moderate yields have been reported in previous studies involving the synthesis of iridium(III) complexes with bidentate ligands, where product isolation and purification constraints led to yields typically ranging between 40–70% (Fan et al., 2023; Han et al., 2022). The presence of closely related side products and incomplete reactions often results in product loss during separation, further reducing the overall yield. Notably, a study by Mingxing et al. (2021) reported a particularly low yield of 17% for similar iridium(III) complexes (Mingxing et al., 2021). However, despite having a low recovery, the resulting complexes exhibited high photophysical efficiencies, demonstrating that lower yields do not necessarily correlate with poor performance in application. In significance, all these findings support the current results and highlight that the obtained yields are within an acceptable and expected range for this type of complex.

Table 4.4

*Physical Properties of the Synthesised Complexes **IR1**–**IR4***

Complex	Colour	Percentage yields (%)
IR1	Yellow powder	54
IR2	Yellow powder	69
IR3	Yellow powder	56
IR4	Yellow powder	47

The elemental analysis of carbon, hydrogen, and nitrogen investigation was consistent with the expected molecular formula for all the synthesised complexes that meet the ranges of ±1.0% percentage differences. The range of ±1.0% indicates that the products have a high degree of homogeneity and purity in bulky species (Kandioller et al., 2022). Although many high-impact publications recently highlighted that the maximum deviation between found species and theoretical value was only 0.4%, a value of 1.0% can still be considered acceptable (Kandioller et al., 2022; Thompson, 2008). **Table 4.5** shows some big deviations for the element carbon in complex **IR3** and element nitrogen in complex **IR4,** where the maximum difference calculated between the theory and found species exceeded 1.0%. As the CHNS Elemental analyser is considered a classical method that is often manipulated (Kandioller et al., 2022) by the efficiency of the compound combustion to be completed, thus we have provided the data of electrospray ionisation mass spectrometry (ES-MS) using liquid chromatography-mass spectrometry (LC-MS) that supported the purity of the synthesised complexes **IR1**–**IR4**. Detailed spectroscopic characterisation of each synthesised complex **IR1**–**IR4** was included in the subsequent discussion part.

Table 4.5

*The Elemental Analysis of the Synthesised Iridium(III) Complexes **IR1–IR4***

Compound (Molecular formula)	Composition Percentages, % (Found) (± percentage differences)		
	C	**H**	**N**
IR1	56.02	3.26	10.89
($IrC_{36}N_6F_2H_{25}$)	(56.05)	(3.69)	(10.17)
	(+0.03)	(+0.43)	(-0.72)
IR2	47.85	2.50	9.05
($IrC_{36}F_6N_6H_{21}.CH_2Cl_2$)	(48.23)	(2.59)	(9.14)
	(+0.38)	(+0.09)	(+0.09)
IR3	59.26	3.90	11.21
($IrC_{37}N_6H_{29}$)	(56.61)	(3.57)	(10.46)
	(-2.65)	(-0.33)	(-0.75)
IR4	50.33	3.00	9.27
($IrC_{37}N_6F4H_{25}.CH_2Cl_2$)	(51.26)	(3.87)	(7.95)
	(+0.93)	(+0.87)	(-1.32)

4.2.1 FT-IR Spectroscopic Characterisation of Complexes IR1–IR4

The IR spectra for all synthesised bis(phenylpyridine)(pyridinylformimidamide)iridium(III) complexes of **IR1–IR4** are shown in **Figure 4.4** for spectral comparison. In summary, all the spectra exhibit an almost similar pattern of the band stretching ν(C=N), ν(C=C), ν(C–N), ν(C–H) coming from the pyridine and phenyl aromatic ring. In addition, sharp ν(C–F) from aromatic ring observed at 983 cm^{-1} (**IR1**); 988 cm^{-1} (**IR2**); 1016 cm^{-1} (**IR4**) represents the structure of 2,4-difluorophenyl and 2,6-difluorobenzyl. Meanwhile, no ν(C–F) stretching band was observed in **IR3** as no fluorine atom was present in the molecular structure of complex **IR3**. In significant, the formation of the synthesised complexes **IR1–IR4** is proved by the presence of significant sharp bands stretching of ν(C≡N) that can be observed at each spectrum at 2218 cm^{-1} (**IR1**); 2220 cm^{-1} (**IR2**); 2223 cm^{-1} (**IR3**), and 2219 cm^{-1} (**IR4**) attributed to the nitrile functional group (Bahron et al., 2019; Zulkifli et al., 2023). **Figure 4.5** compares the starting dimer and starting ligand to the synthesised complex **IR2**. No ν(C≡N) band stretching appeared in the IR spectrum of the starting dimer precursor and starting ligand derivatives, indicating that the nitrile group only appears after the complexation process. This observation can be explained by the deprotonation of the starting triazole-based ligand: the first proton is removed to facilitate coordination with the iridium centre, while the second deprotonation promotes rearrangement to form a ν(C≡N) triple bond, leading to the formation of the acyclic formimidamide-type ligand. A more detailed mechanistic pathway for this transformation is proposed in **Subtopic 4.7**. In addition, this pattern also resembles the other complexes of **IR1**, **IR3**, and **IR4**, proving the consistency of

the formation of acyclic formimidamide-based ancillary ligands emerging from cyclic triazolium salts precursor.

Figure 4.4

*The IR spectra for complexes **IR1–IR4** with the labelling functional groups and the respective band stretching*

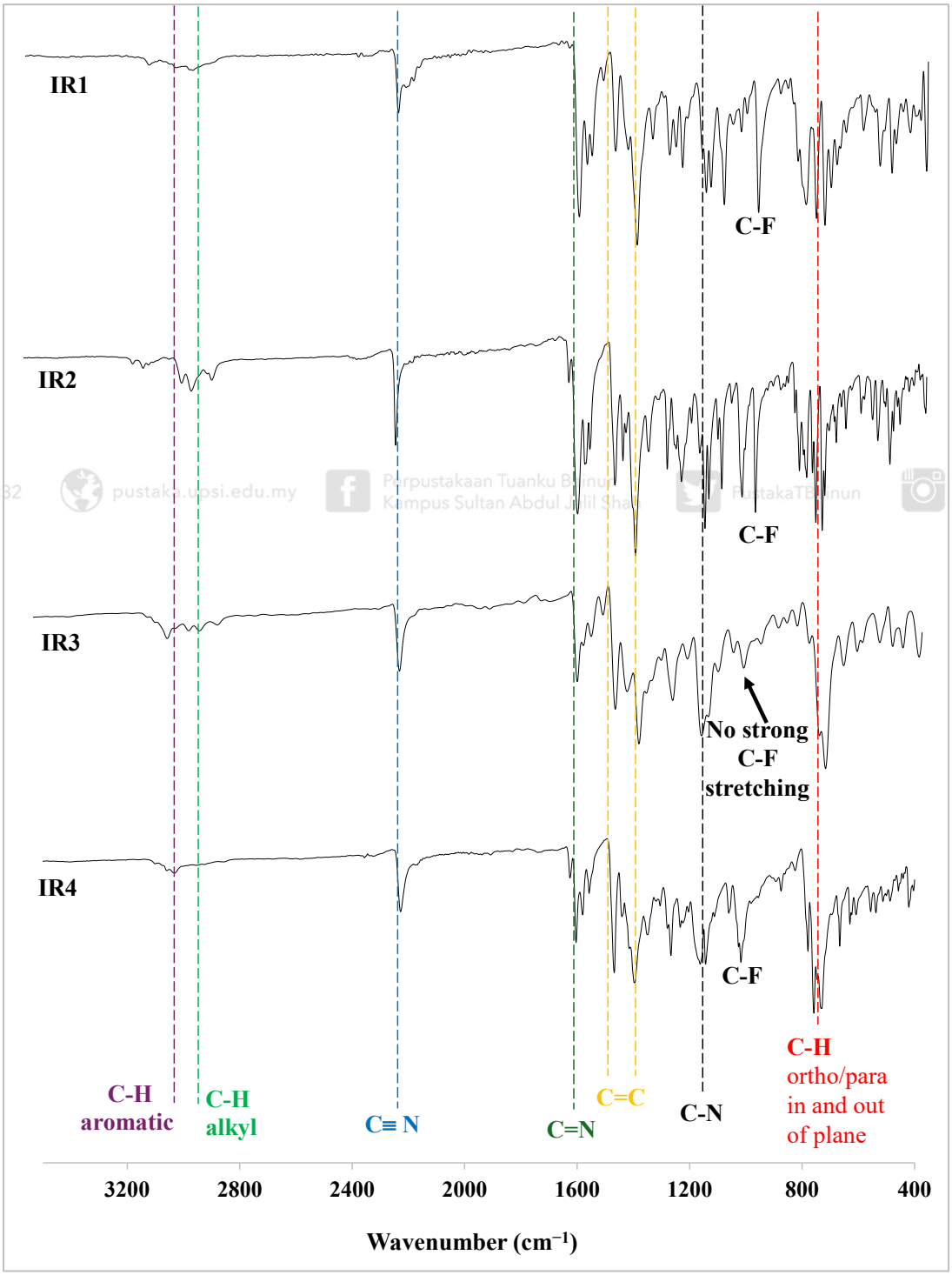

Figure 4.5

*Comparison of the IR spectrum between the synthesised iridium complex **IR2** with its respective starting ligand and dimer. The ν(C≡N) for nitrile is clearly shown in the spectrum of the complex*

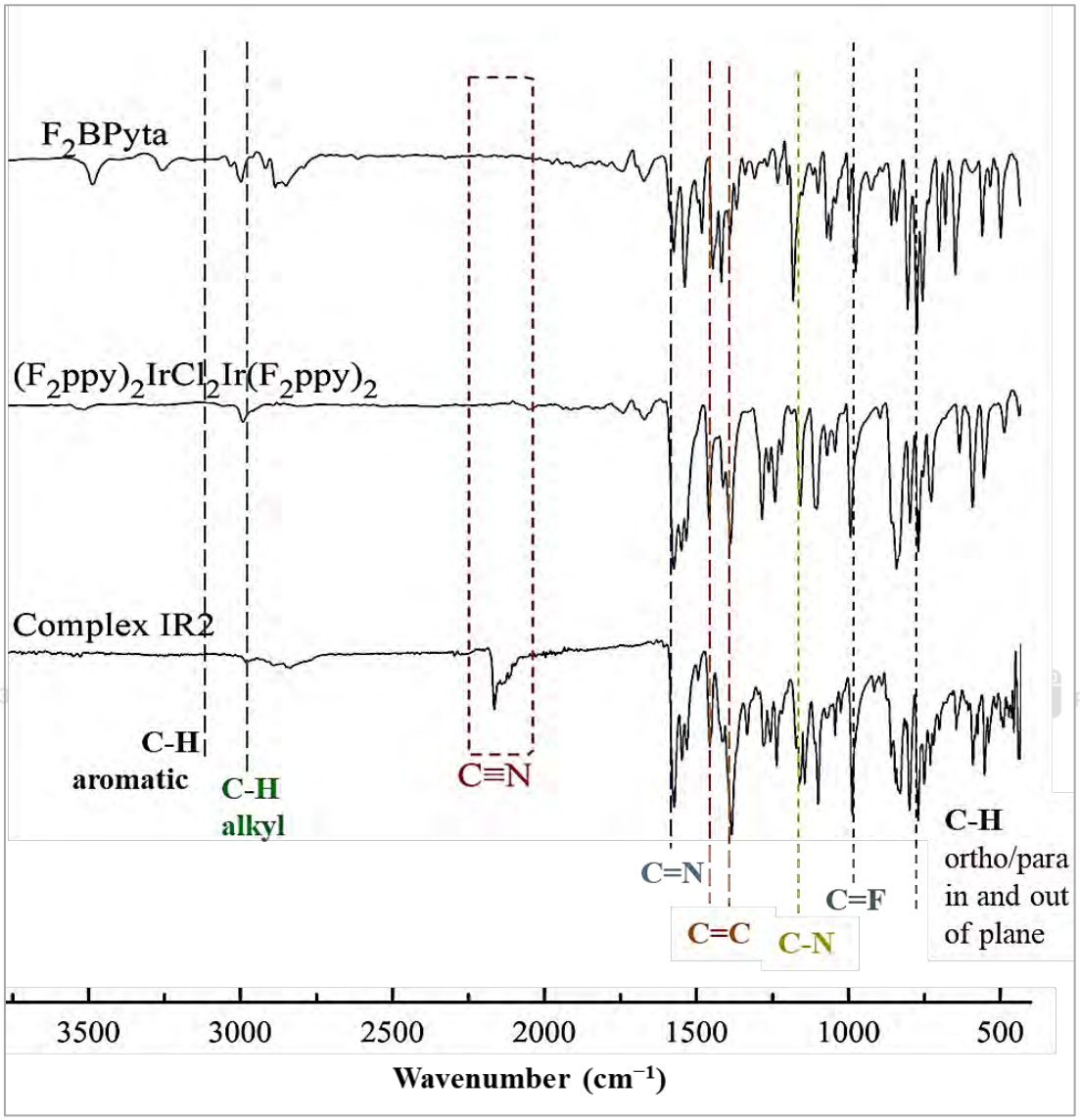

Table 4.6 summarises all the essential IR absorption bands of ν(C–H), ν(C–N), ν(C=H), and ν(C=N) that appeared in the IR spectra and confirmed the functionality of the molecular structure of complexes **IR1**–**IR4**. The C=N stretching bands appeared at 1599 cm^{-1} (**IR1**), 1600 cm^{-1} (**IR2**), 1604 cm^{-1} (**IR3**), and 1602 cm^{-1} (**IR4**) (Pavia et al., 2015). The common C=C aromatic stretching bands were observed

as two strong absorptions at 1474 and 1400 cm^{-1} (**IR1**); 1514 and 1467 cm^{-1} (**IR2**); 1468 and 1398 cm^{-1} (**IR3**); and 1468 and 1397 cm^{-1} (**IR4**) (Gokce et al., 2016) confirming the presence of aromatic rings from pyridine and phenyl moieties. The slight variations in the stretching frequencies among the complexes can be attributed to the electronic effects of different substituents on the ligand environments around the metal centre. For instance, the ν(C=N) band in **IR3** and **IR3** is among the highest among all complexes and is associated with the presence of a methyl ($-CH_3$) substituent, which is a mild electron-donating group that increases electron density and strengthens the C=N bond. Moreover, no fluorine atom in **IR3** has lower electron-withdrawing properties that can withdraw electron density from the ligand framework. In contrast, **IR1** and **IR2** show the lowest ν(C=N) stretching frequency (1599 cm^{-1} and 1600 cm^{-1} respectively), likely due to the presence of many fluoro (–F) substituent, a strong electron-withdrawing group that pulls electron density from the ligand framework, weakening the C=N bond (Pavia et al., 2015). In addition, the ν(C≡N) stretching bands show a similar trend: 2218 cm^{-1} (**IR1**), 2220 cm^{-1} (**IR2**), 2223 cm^{-1} (**IR3**), and 2219 cm^{-1} (**IR4**), with **IR3** again showing the highest frequency due to its electron-donating group environment that enhances the triple bond character of the nitrile. Conversely, the electron-withdrawing group effect of fluorine atoms in **IR1**, **IR2** and **IR3** leads to the lower ν(C≡N) stretching value (Pavia et al., 2015).

To conclude, these spectral shifts in **Table 4.6** highlight how subtle changes in ligand architecture, such as the introduction of electron-withdrawing fluorine or electron-donating methyl groups, can significantly influence the vibrational properties of the synthesised complexes. In conclusion, spectroscopic FT-IR analysis not only confirmed the presence of all expected functional groups in each synthesised complex

IR1–**IR4** but also demonstrated that the electronic nature of the substituents (EWG vs. EDG) can significantly affected the stretching frequencies observed in the IR spectra.

Table 4.6

*Experimental IR Vibrational Modes for Complex **IR1**–**IR4***

Vibrational modes	Wavenumber (cm^{-1})			
	IR1	**IR2**	**IR3**	**IR4**
ν(C–H) aromatic	3076	3092	3032	3079
ν(C–H) alkyl	2925	2928	2918	3000
ν(C≡N)	2218	2220	2223	2219
ν(C=N) pyridine	1599	1600	1602	1604
ν(C=C) aromatic	1474, 1400	1514, 1467	1468, 1398	1468, 1397
ν(C–N)	1243	1234	1264	1267
ν(C–F) aromatic	983	988	Not available	1016
ν(C–H) ortho/para out of plane (aromatic ring)	819, 783	780,759	758, 738	759, 731

4.2.2 Mass Spectrometry Characterisation of Complexes IR1–IR4

The calculated electrospray mass spectrometry (ES-MS) analysis is shown in **Table 4.7.** Their respective calculated spectra are attached as supplementary documents in **Appendices S1–S4**. The calculated result from ES-MS analysis confirmed the formation of major species of complex [Ir(ppy)$_2$(L^L)] + H], where L^L is a

ppyridinylformimidamide-based ancillary ligand. The term major species refers to the predominant ionic form observed in the mass spectrum, which corresponds to the protonated molecular ion of the synthesised complex (Shan, 2016). The observed pattern of the ES-MS spectra, which displayed a mass-to-charge ratio peak, m/z complemented the calculated theoretical molecular formula of all the species complexes **IR1–IR4**.

Table 4.7

*Expected and Experimental Mass-to-Charge Ratio (m/z) for Complex **IR1–IR4** with their Respective Molecular Formula and Significant Major Species*

Complexes	Calculated		Experimental data from ES-MS	
	Mass (m/z)	**Molecular formula**	**Mass (m/z)**	**Major species**
IR1	772.1	$IrC_{36}N_6F_2H_{25}$	773	$[Ir(ppy)_2(CNF_2BPyfa)] + H]$
IR2	844.1	$IrC_{36}F_6N_6H_{21}$	845	$[Ir(F_2ppy)_2(CNF_2BPyfa)] + H]$
IR3	750.2	$IrC_{36}N_6H_{29}$	751	$[Ir(ppy)_2(CNMBPyfa)] + H]$
IR4	822.1	$IrC_{37}N_6F4H_{25}$	823	$[Ir(F_2ppy)_2(CNMBPyfa)] + H]$

Notably, the ES-MS analysis presented in **Table 4.7** plays a crucial role in confirming the successful formation of the target iridium(III) complexes. For each complex, a prominent peak corresponding to the protonated molecular ion $[Ir(ppy)_2(L^L) + H]$ was observed as attached in **Appendices S1–S4**. The minimal deviations within ±1 m/z unit are attributed to the addition of a proton during ionisation, resulting in the formation of a positively charged species, which is typical in ES-MS analysis under positive ion mode. The excellent match between the calculated and

observed m/z values confirmed the formation of the intended major species in each iridium(III) complex. In addition, the detection of protonated molecular ions $[M + H]^+$ also rules out major impurities or ligand exchange, as even small structural changes can significantly alter the properties of a complex (Shan, 2016). Therefore, these ES-MS results, together with NMR and elemental analysis have successfully provided strong evidence for the successful synthesis and structural integrity of the **IR1–IR4** complexes.

4.2.3 NMR Spectroscopic Characterisation of Complexes IR1–IR4

4.2.3.1 ^{1}H NMR Spectroscopic Analysis of Complexes IR1–IR4

Assignments of proton resonances for **IR1–IR4** were made by comparison to their respective ^{1}H NMR spectra of the starting compound dichloro-bridged iridium(III) dimer and ancillary ligands. Then, the characterisation procedure was assisted by ^{13}C NMR spectra (**Appendices S5–S8**). Generally, there is no significant change in ^{1}H NMR spectral pattern between the starting dimer and the synthesised bis(phenylpyridine)(pyridinylformimidamide)iridium(III) complex **IR1–IR4**, indicating that the cleavage with both chloride bridges and substitution with 2-(1,2,4-triazole-1-yl)pyridine based ligand took placed without changing the octahedral geometry of the synthesised iridium(III) complexes (Nazeeruddin et al., 2003). To prove the occurrence of complexation, it is clearly shown in the spectral comparison of **Figure 4.6–4.9** that the singlet peaks of proton H13 and H14 in the starting ligand have disappeared in the complexes' spectra, indicating the deprotonation of both protons in the triazole ligand gives rise to complexes **IR1–IR4**. Protons of H13 and H14 with

singlet multiplicity are highly deshielded and hence are a reference peak in many studies. The singlet proton in triazole appeared highly deshielded in the higher chemical shift in the ^{1}H NMR spectrum (δ ~8–10 ppm) due to the electron-withdrawing effect of the three nitrogen atoms in the ring, which resembles the special spectroscopic characteristics of the N-heterocyclic carbene group (Ji Ram et al., 2019). Hence, the disappearance of this highly deshielded proton H13 and H14 is a benchmark of the successful complexation process.

On the other hand, the proton H19 and H20 corresponding to the methylene proton shifted to an upfield with a lower magnetic field in the complex spectra compared to its initial position in the ligand spectra due to the anisotropy of the induced field generated by the aromatic ring current (Welby et al., 2013). All the proton signals were in good agreement with the expected molecular structure, as the coupling constant values were consistent with the excellent proton coupling constant ranges (Friebolin, 2010). The presence of fluorine atoms and heterocyclic groups somehow widened the region of the aromatic ring from 5.00–10.00 ppm into 4.50–10.00 ppm. All the ^{13}C NMR spectra **(Appendices S5–S8)** are discussed in detail to support the ^{1}H NMR spectra, hence confirming the characterisation of all the synthesised complexes.

Figure 4.6

*The comparison between [1]H NMR spectrum of starting **F_2bpyta** ligand with its respective synthesised complexes of **IR1** clearly showing the disappearance of H13 and H14 label with red colour. ** is CD_2Cl_2 solvent peak, * is $CDCl_3$ solvent peak*

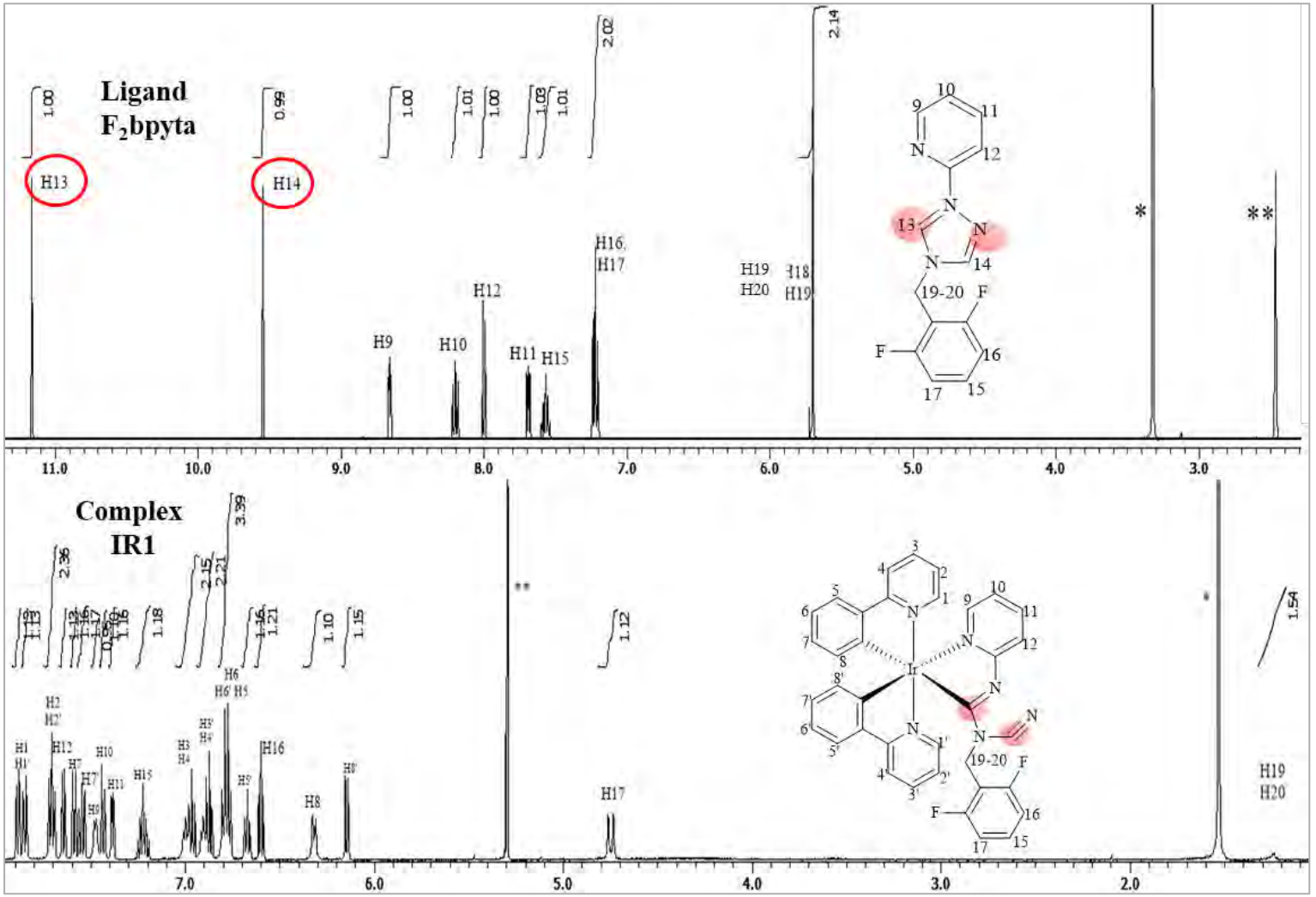

^{1}H-NMR of **IR1**
(500 MHz)
δ 7.89 (d, J = 8.0 Hz, 1H),
7.85 (d, J = 8.0 Hz, 1H),
7.71 (t, J = 7.7 Hz, 2H),
7.65 (d, J = 6.9 Hz, 1H),
7.59 (d, J = 8.0 Hz, 1H),
7.56-7.53 (m, 1H),
7.48 (d, J = 5.7 Hz, 1H),
7.44 (d, J = 8.0 Hz, 1H),
7.39 (d, J = 4.6 Hz, 1H),
7.25-7.19 (m, 1H),
7.01-6.95 (m, 2H),
6.92-6.86 (m, 2H),
6.81-6.76 (m, 3H),
6.67 (t, J = 8.0 Hz, 1H),
6.61-6.59 (m, 1H),
6.32 (d, J = 8.0 Hz, 1H),
6.15 (d, J = 7.4 Hz, 1H),
4.75 (d, J = 13.7 Hz, 1H),
1.24 (s, 2H)

Figure 4.7

*The comparison between [1]H NMR spectrum of starting **F_2bpyta** ligand with its respective synthesised complexes of **IR2** clearly showing the disappearance of H13 and H14 label with red colour. ** is CD_2Cl_2 solvent peak, * is $CDCl_3$ solvent peak*

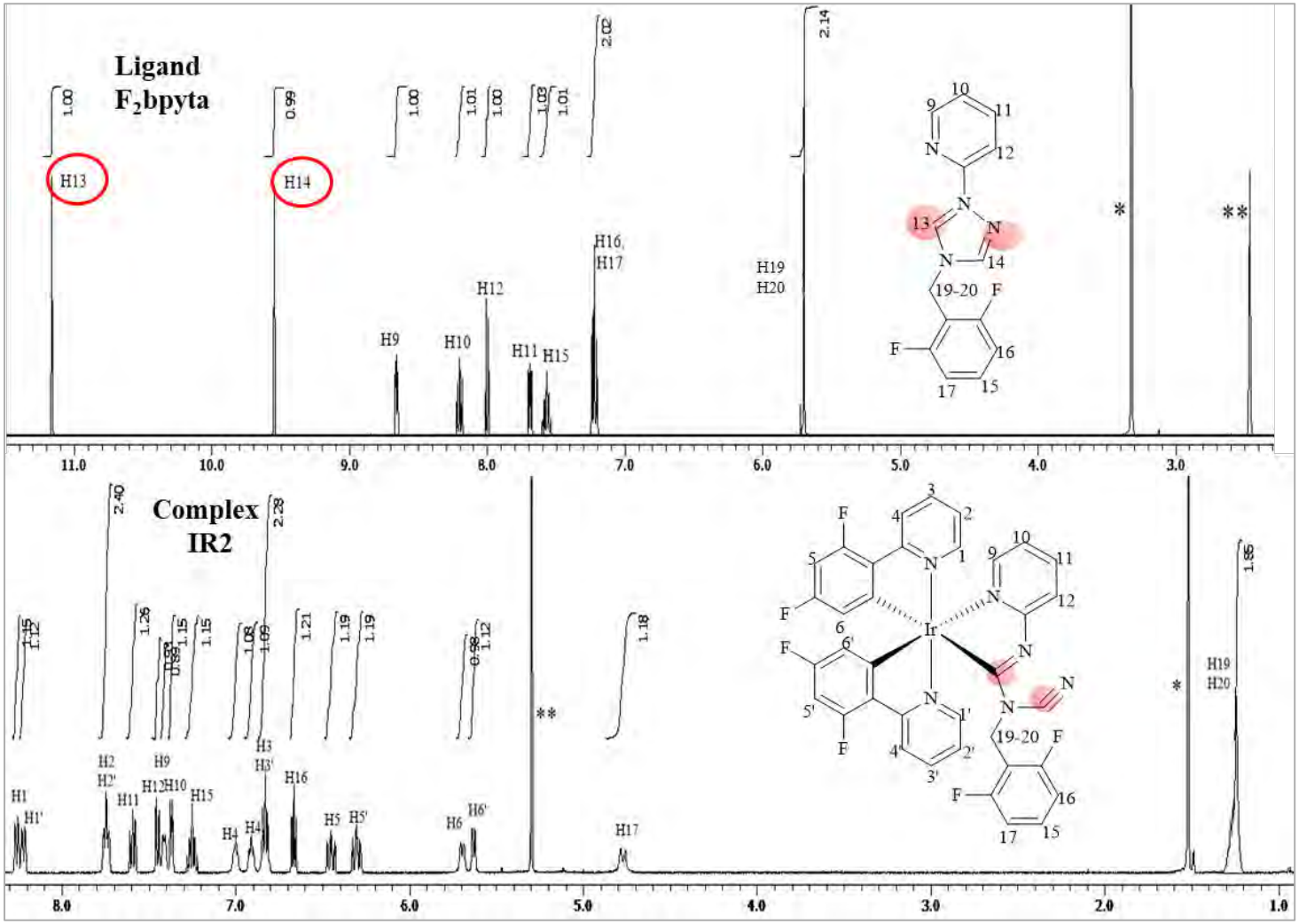

[1]H-NMR of **IR2** (500 MHz)
δ 8.26 (d, J = 8.6 Hz, 1H),
8.22 (d, J = 8.6 Hz, 1H),
7.75 (t, J = 7.7 Hz, 2H),
7.61-7.58 (m, 1H),
7.45 (d, J = 8.0 Hz, 1H),
7.41 (d, J = 5.2 Hz, 1H),
7.37 (d, J = 4.6 Hz, 1H),
7.28-7.22 (m, 1H),
7.00 (s, 1H),
6.91 (s, 1H),
6.83 (t, J = 8.0 Hz, 2H),
6.67 (t, J = 6.0 Hz, 1H),
6.47-6.43 (m, 1H),
6.30 (dd, J = 12.9, 9.5 Hz, 1H),
5.70 (d, J = 9.2 Hz, 1H),
5.63 (d, J = 9.7 Hz, 1H),
4.77 (d, J = 13.7 Hz, 1H),
1.24 (s, 2H)

Figure 4.8

*The comparison between [1]H NMR spectrum of starting **Mbpyta** ligand with its respective synthesised complexes of **IR3** clearly showing the disappearance of H13 and H14 label with red colour. ** is CD_2Cl_2 solvent peak, * is $CDCl_3$ solvent peak*

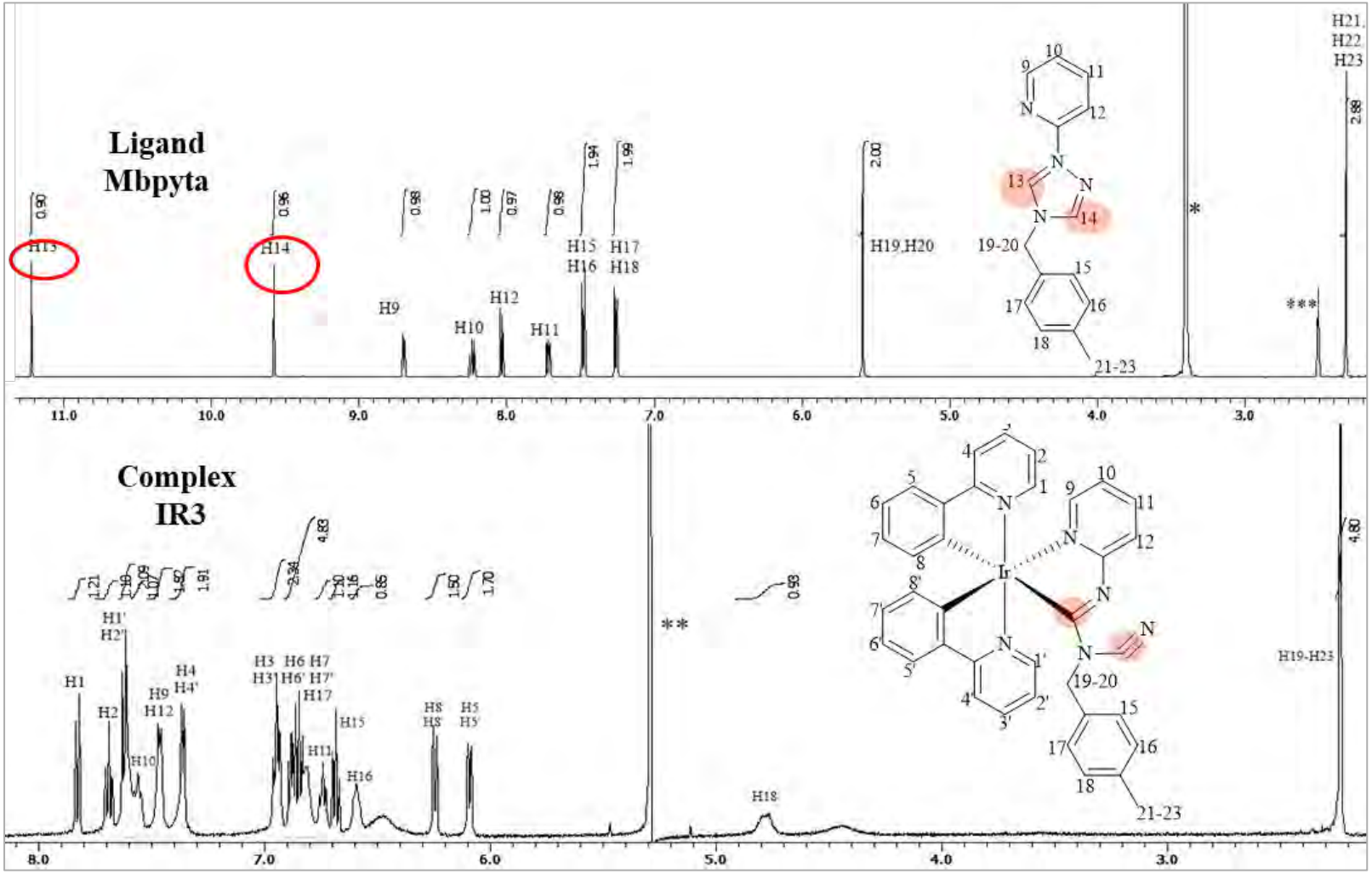

[1]H-NMR of **IR3** (500 MHz)
δ 7.83 (d, J = 8.0 Hz, 1H),
7.69 (t, J = 7.7 Hz, 1H),
7.63-7.58 (m, 2H),
7.57 (t, J = 7.4 Hz, 1H),
7.47 (d, J = 5.7 Hz, 2H),
7.37 (d, J = 5.2 Hz, 2H),
6.95 (t, J = 6.9 Hz, 2H),
6.90-6.82 (m, 5H),
6.75 (t, J = 7.2 Hz, 1H),
6.70-6.67 (m, 1H),
6.60 (d, J = 4.6 Hz, 1H),
6.25 (d, J = 7.4 Hz, 2H),
6.09 (d, J = 6.9 Hz, 2H),
4.78 (d, J = 16.6 Hz, 1H),
2.24 (s, 5H).

Figure 4.9

*The comparison between [1]H NMR spectrum of starting **Mbpyta** ligand with its respective synthesised complexes of **IR4** clearly showing the disappearance of H13 and H14 label with red colour. ** is CD_2Cl_2 solvent peak, * is $CDCl_3$ solvent peak*

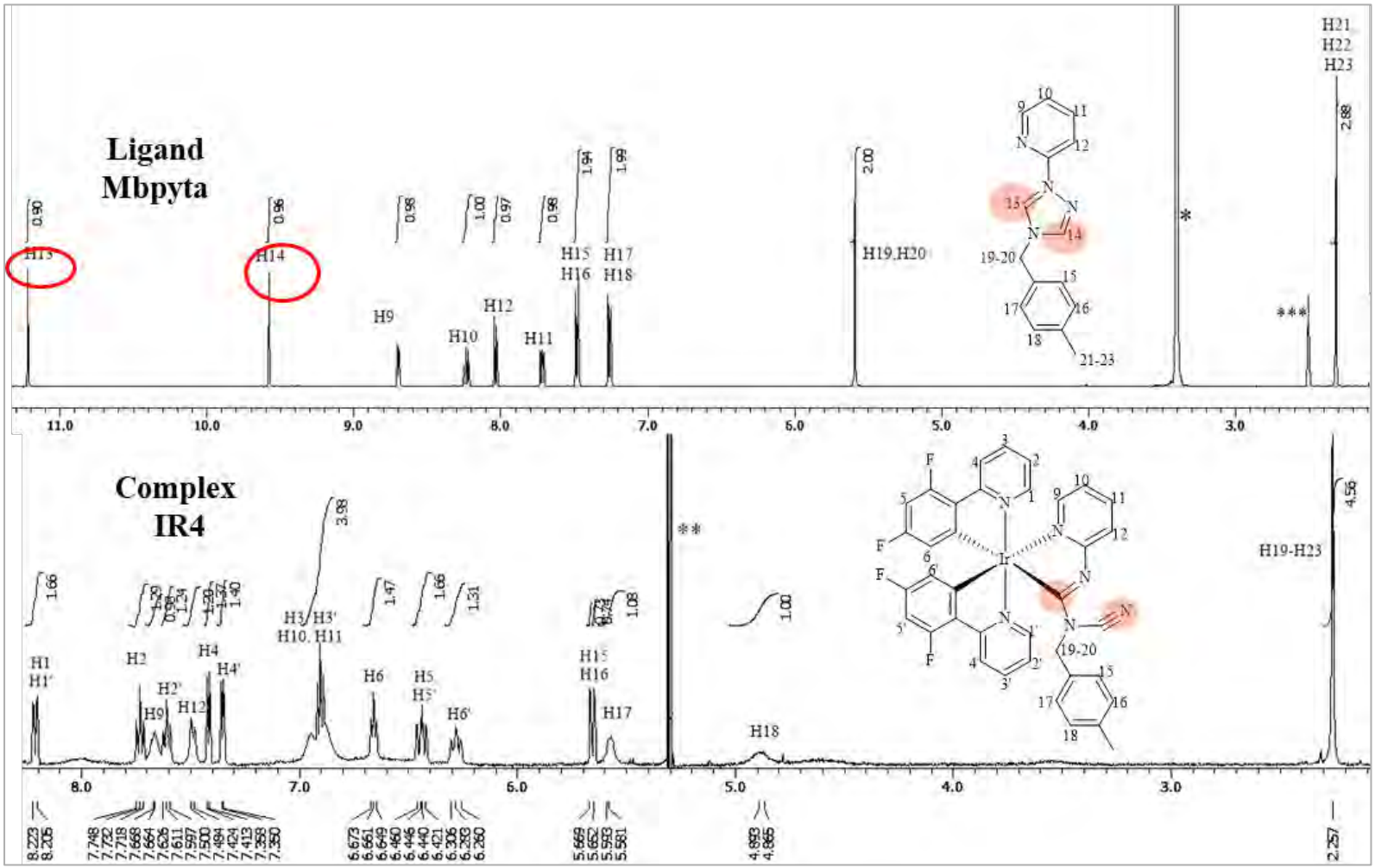

[1]H-NMR of **IR4**
(500 MHz)
δ8.21 (d, J = 8.6 Hz, 2H),
7.73 (t, J = 7.7 Hz, 1H),
7.67 (d, J = 2.3 Hz, 1H),
7.61 (t, J = 7.2 Hz, 1H),
7.49 (d, J = 8.0 Hz, 1H),
7.42 (d, J = 5.7 Hz, 1H),
7.35 (d, J = 4.0 Hz, 1H),
6.84-7.00 (4H),
6.66 (t, J = 6.0 Hz, 1H),
6.46-6.42 (m, 2H),
6.28 (t, J = 11.5 Hz, 1H),
5.67 (s, 1H),
5.65 (s, 1H),
5.59 (d, J = 6.3 Hz, 1H),
4.88 (d, J = 6.3 Hz, 1H),
2.25 (s, 5H)

Further analysis of the ^{1}H NMR spectral trends for all synthesised complexes **IR1**–**IR4** was carried out, with a focus on the aromatic region. A comparison between the spectra of complexes **IR1** and **IR2** is shown in **Figure 4.10**. In the aromatic region (δ 4.50–9.00 ppm), **IR1** displays 23 proton signals, whereas **IR2** shows 19 aromatic proton signals. These are attributed to protons from the phenylpyridine, pyridinylformimidamide, and 2,6-difluorobenzyl rings.

Notably, the ^{1}H NMR spectra of complexes **IR1** and **IR2** exhibit distinct differences in the aromatic region, primarily due to the presence of a fluorine substituent on the cyclometallating ligand in **IR2**. The downfield shifts observed in the overall spectrum of **IR2**, particularly the peaks at δ 8.22–8.26 ppm, indicate the increment of the deshielding effect of aromatic protons relative to **IR1**. This deshielding effect is attributed to the strong electron-withdrawing inductive effect (–*I*) of fluorine, which reduces the electron density on the aromatic ring and shifts adjacent proton signals downfield (Green & Yates, 2014). Additionally, the altered electronic distribution increases magnetic anisotropy, further influencing all the chemical shift values. In contrast, **IR1** lacks the fluorine substituent, resulting in a more electron-rich and shielded aromatic environment, with signals appearing upfield in the range of δ 6.15–7.89 ppm, which lower magnetic field than **IR2**. Overall, the presence of more fluorine atoms in **IR2** plays a significant role in altering the electronic environment of the aromatic system, leading to the observed spectral differences.

A similar trend is observed in the comparison between **IR3** and **IR4**, as shown in **Figure 4.11**. Complex **IR3,** which contains no fluorine atoms on both cyclometallating and ancillary moieties, displays broader and more overlapping

aromatic signals between δ 6.5–8.0 ppm. In contrast, **IR4**, which features fluorinated phenyl rings, shows distinct downfield shifts in several proton signals, particularly in the δ 7.2–7.8 ppm range (e.g., H2/H2′, H4/H4′, H10, H11). This deshielding is attributed to the strong electron-withdrawing inductive effect of fluorine, which lowering the local electron density and leads to pronounced chemical shift differences (Green & Yates, 2014).

In addition to inductive effects, fluorine also contributes to spin-orbit coupling due to its higher atomic mass, which is a phenomenon known as the heavy atom effect (Baranoff et al., 2012; Monti et al., 2021). This effect, while subtle, can alter local magnetic environments and influence the relaxation times of nearby nuclei. In metal-containing systems like iridium(III) complexes, such relativistic effects become more pronounced and can induce paramagnetic properties, making the NMR spectra less resolved (Chyba et al., 2023). Thus, the presence of fluorine in **IR4** not only causes classical deshielding but may also contribute to small but significant changes in spectral line shape and position due to enhanced magnetic anisotropy and spin-orbit interactions. To conclude, these combined effects confirm that fluorine substitution significantly modifies the aromatic region of ^{1}H NMR spectra, providing deeper insight into the electronic and structural environments of all the synthesised iridium(III) complexes **IR1–IR4**.

Figure 4.10

*Comparison of the ^{1}H NMR spectra of complexes **IR1** and **IR2** in the aromatic region*

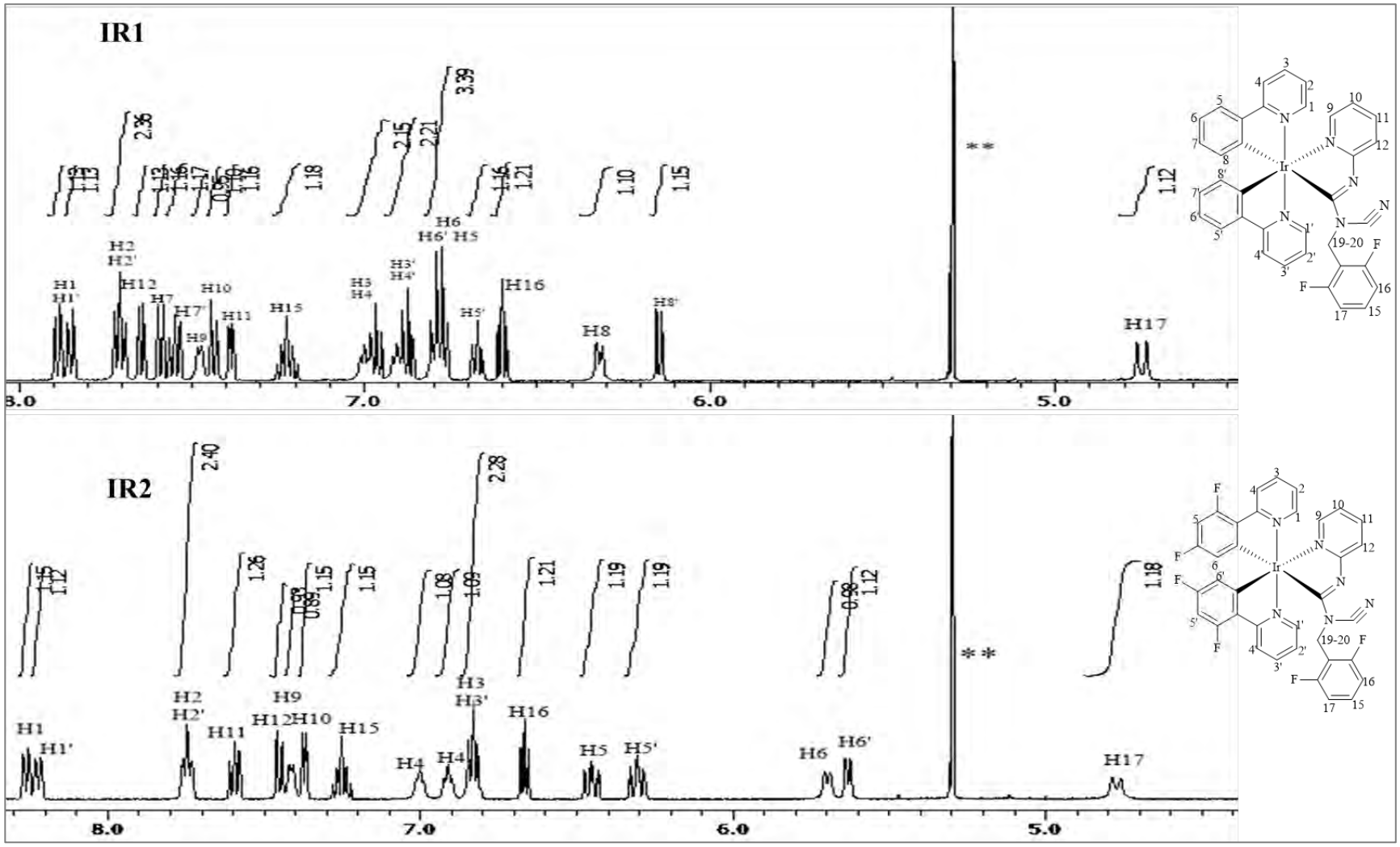

Figure 4.11

*Comparison of the ^{1}H NMR spectra of complexes **IR3** and **IR4** in the aromatic region*

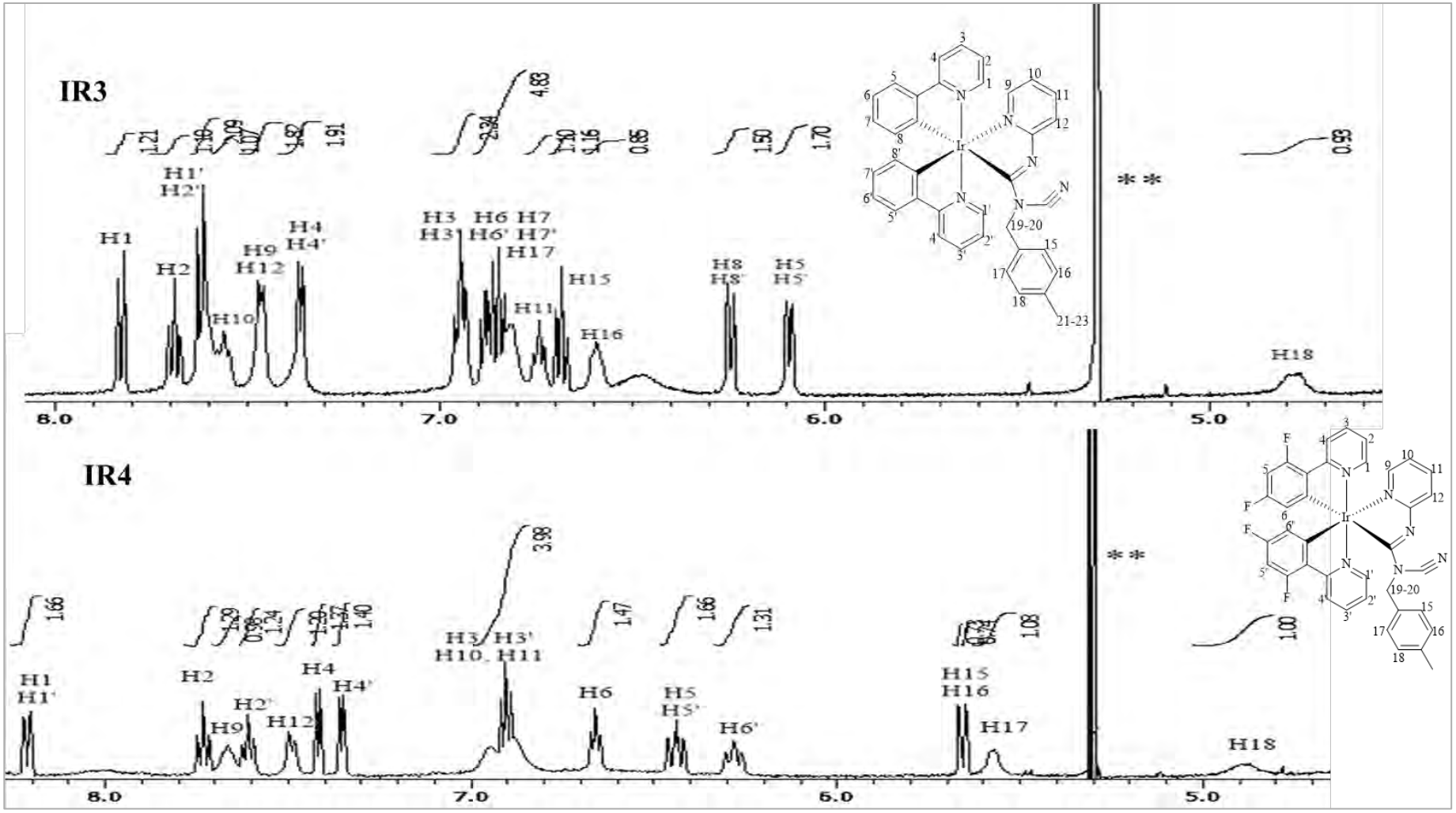

4.2.3.2 ^{13}C NMR Spectroscopic Analysis of Complexes IR1–IR4

The ^{13}C NMR spectra of complexes **IR1–IR4**, recorded in deuterated methylene chloride-d_2, reveal well-resolved carbon peaks corresponding to the number of carbon atoms in their respective molecular structures. Across all complexes, the spectra display signals for aromatic carbons in the range of 80–150 ppm and aliphatic carbons between 0–50 ppm, consistent with the expected chemical analysis. The presence of fluorine atoms and heterocyclic groups further influences the aromatic region, broadening it to approximately 70–200 ppm.

For complex **IR1** in **Appendix S5**, a total of 36 carbon signals were detected. The aromatic carbon attached to a nitrogen atom (ArCN) in the pyridine ring appears at chemical shifts higher than 150 ppm, consistent with typical ArCN environments. Aromatic carbons attached to fluorine atoms (ArCF) are observed between 90–110 ppm, with notable peaks at 111.2 ppm and 111.1 ppm. A C≡N peak at 129.6 ppm confirms the carbon associated with the nitrile functionality. In comparison, the specific signals at 111.2 ppm and 111.1 ppm indicate the successful attachment of the 2,6-difluorobenzyl group to the complex structure. Additionally, all 25 peaks related to sp^2 hybridised carbons in the aromatic and heteroatomic regions are between 110–170 ppm, further substantiating the molecular composition.

In the case of complex **IR2** in **Appendix S6**, 36 carbon signals are observed, similar to **IR1**. Aromatic carbons attached to a nitrogen atom (ArCN) in the pyridine ring are seen at 172.6 ppm, 171.9 ppm, 165.3 ppm, 164.9 ppm, 164.8 ppm, and 164.5 ppm, indicating a strong interaction within the ArCN environment. The aromatic carbons attached to fluorine atoms exhibit signals between 90–110 ppm, with distinct

peaks at 111.4, 111.2, 98.5, 98.1, 96.6, and 96.4 ppm. These shifts confirm the presence of the 2,4-difluorophenylpyridine group and the attachment of substituents to the complex structure. A C≡N peak at 127.0 ppm further validates the presence of the nitrile functionality. Moreover, all 21 sp^2 hybridised carbon peaks related to aromatic and heteroatomic regions are located within 110–170 ppm.

Complex **IR3** in **Appendix S7**, on the other hand, presents 37 carbon signals, with aromatic carbons attached to nitrogen atoms (ArCN) in the pyridine ring appearing at 172.6 ppm, 171.9 ppm, 165.3 ppm, 164.9 ppm, 164.8 ppm, and 164.5 ppm. This complex does not show aromatic carbons attached to fluorine atoms within the 90–110 ppm range, indicating the absence of fluorinated aromatic carbons. The presence of a C≡N peak at 127.0 ppm confirms the nitrile functionality within the structure. All 27 sp^2 hybridised carbon peaks associated with aromatic and heteroatomic carbons are located within the 110–170 ppm region, consistent with the expected molecular structure.

Lastly, complex **IR4** in **Appendix S8**, which also exhibits 37 carbon signals, shows aromatic carbons attached to nitrogen atoms (ArCN) in the pyridine ring at 172.0 ppm, 165.3 ppm, 165.3 ppm, 165.0 ppm, 164.9 ppm, and 164.5 ppm. Aromatic carbons attached to fluorine atoms are observed between 90-110 ppm, with specific signals at 112.7 ppm, 112.5 ppm, 98.4 ppm, and 96.3 ppm, confirming the presence of fluorinated aromatic groups. The C≡N peak at 128.9 ppm indicates the presence of nitrile functionality. All 23 sp^2 hybridised carbon peaks in the aromatic and heteroatomic regions are between 110–170 ppm.

In summary, the detailed analysis of the ^{13}C NMR spectra for complexes **IR1**–**IR4**, including the chemical shifts of carbon signals and their corresponding magnetic field values (ppm), has successfully supported the ^{1}H NMR spectroscopic characterisation of the molecular structures of these complexes. The consistent identification of key functional groups, such as ArCN, ArCF, and C≡N, across the spectra, along with the comparison of carbon peaks listed in **Appendices S5-S8**, provided essential insights into the molecular architecture of these compounds. This comprehensive data analysis has facilitated a deeper understanding of the structural features of these complexes, confirming their expected compositions and bonding environments.

In conclusion, detailed chemical analysis and spectroscopic investigations have confirmed a successful synthetic methodology development for forming a new class of iridium(III) complexes bearing formimidamide-based ancillary ligands. The successful synthesis of these complexes has furthered the study of luminescence and structural investigation.

4.3 X-ray Crystallography Analysis of Complexes IR1–IR4

The single crystal of each iridium(III) complex of **IR1–IR4** was successfully grown from the slow diffusion of hexane into a dichloromethane solution at room temperature. Despite the challenges of getting high-quality crystals, a single yellow crystal was chosen with the help of microscope instruments fitted at the Bruker D8 QUEST Single Crystal X-ray Diffractometer. The single crystal was then put on a glass fibre before data collection using the same instruments. The summary of crystallographic

refinement details is tabulated in **Table 4.8.** The crystallographic structure of complexes **IR1–IR4** was drawn with 50% probability displacement ellipsoids shown in **Figure 4.12–4.15**.

Figure 4.12

ORTEP diagram of the crystal structure Ir(ppy)$_2$(CNF$_2$bpyfa), ***IR1*** *complex draw with 50% probability ellipsoid*

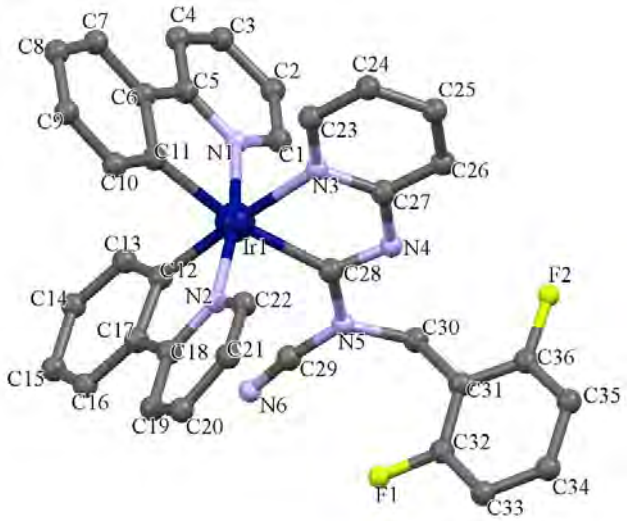

Figure 4.13

ORTEP diagram of the crystal structure Ir(F$_2$ppy)$_2$(CNF$_2$bpyfa), ***IR2*** *complex draw with 50% probability ellipsoid*

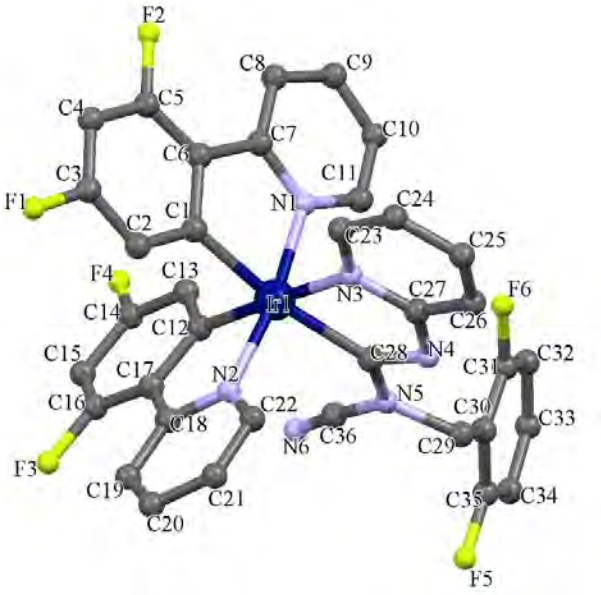

Figure 4.14

ORTEP diagram of the crystal structure Ir(ppy)$_2$(CNMbpyfa), ***IR3*** *complex draw with 50% probability ellipsoid*

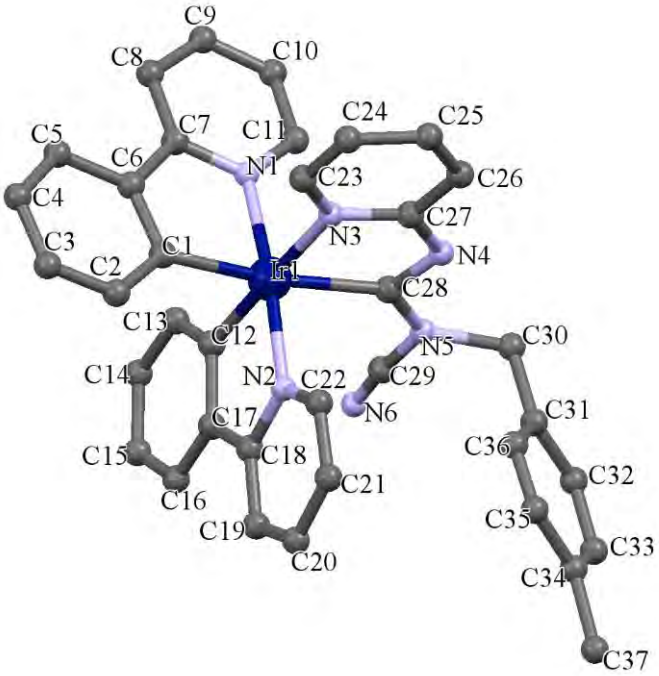

Figure 4.15

ORTEP diagram of the crystal structure Ir(F$_2$ppy)$_2$(CNMbpyfa), ***IR4*** *complex drawn with 50% probability ellipsoid, the dichloromethane solvate was omitted for clarity*

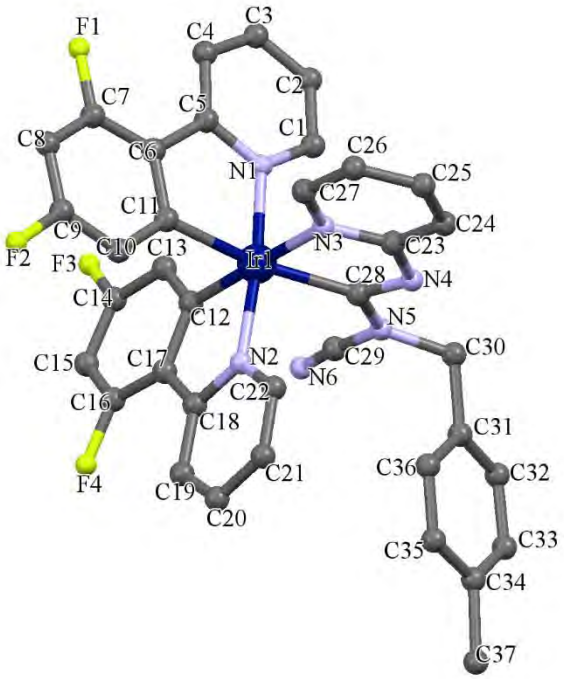

For all complexes, the single-crystal study significantly simulated the formation of acyclic formimidamide-based ligands in the complexes. As expected, the central iridium atom is six-coordinated by three carbon atoms and three nitrogen atoms, forming a distorted octahedral geometry due to the steric properties of the ligands (Sanner et al., 2019). Two phenylpyridine ligands are coordinated to the central iridium atom through their two pyridinyl nitrogen atoms and two phenylated carbon atoms. In contrast, one (pyridine-2-yl-)-formimidamide-based ligand is coordinated to the central iridium atom through its Nitrogen and Carbon atoms in a bidentate manner.

The single crystals of all complexes have a total reflection that is sufficient enough, and all the R internal values within the ranges are categorised as having good single-crystallographic properties. The term "sufficient total reflection" refers to both the high number of reflections collected during X-ray diffraction and the acceptable R internal values across the datasets. As shown in **Table 4.8**, the number of reflections collected ranges from 15,776 (**IR3**) to over 190,000 (**IR2** and **IR4**), demonstrating excellent data coverage. The corresponding R internal values ranging from 0.0105 (**IR3**) to 0.2043 (**IR1**) indicate good internal consistency, with values below 0.10 considered ideal and values below 0.20 still acceptable, particularly in heavy-metal systems like iridium (III) complexes (Mohammad Khaja Nazeeruddin et al., 2016). These values confirmed that all structures were refined with data of sufficient completeness and quality to yield reliable molecular geometries. All the complexes used Full-matrix least-squares on F^2 as a method of refinement.

Notably, complexes **IR1**, **IR2**, and **IR3** crystallised in the triclinic system in space group Pī, where three unequal axes intersect at oblique angles. In contrast,

complex **IR4** is crystallised in a monoclinic system (space group $P2_1/n$) with three unequal axes; two are inclined to one another, and the third is perpendicular. The molecular structures of all complexes were successfully solved, although there were special features of some which will now be discussed:-

Crystal of complex **IR3** crystallised with twin disordered properties, in which the lattices of all twin components coincide perfectly in both direct and reciprocal space (Nespolo, 2015). The occurrence of twin disorder has affected crystal's physical properties and hindered the refinement process of the crystal structure. In this study, the software then refined them as twins and merged them again as a single crystal; hence, only one output *hkl* file was successfully generated. The packing system of complex **IR3** is shown in **Figure 4.16**, which confirms the value of Z=2 (two molecules in one unit cell).

Figure 4.16

*Packing for the crystal of complex **IR3***

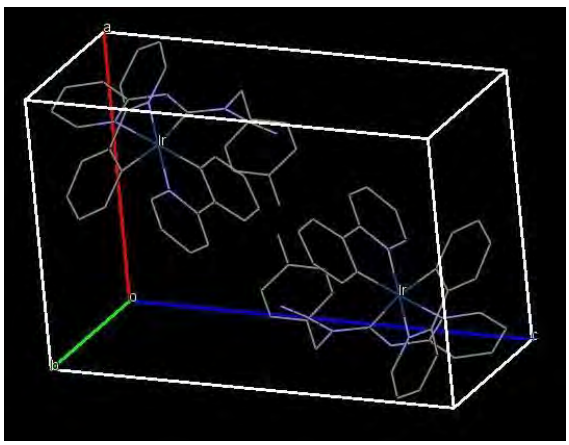

Crystal of complex **IR4** solvated with one molecule of dichloromethane. Several attempts have been made to solve the crystal by excluding this solvent. However, the density, absorption coefficient, thermal parameter, and F_{000} appeared incorrect. Hence, finally, the best estimate would include one molecule/unit of dichloromethane, and the best refinement data was extracted, as shown in **Table 4.8**. Dichloromethane was the residue of the slow diffusion process while the crystal was being prepared using the slow diffusion method.

In conclusion, the results of single-crystal molecular structures for all the complexes **IR1**–**IR4** have successfully assisted the chemical analysis, and the resulting structures agreed with their respective expected molecular structures.

Table 4.8

*Crystal Data and Refinement Parameters for Complexes **IR1–IR4***

Compound	**IR1**	**IR2**	**IR3**	**IR4**
Empirical Formula	$C_{36}H_{25}F_2IrN_6$	$C_{36}H_{21}F_6IrN_6$	$C_{37}H_{29}IrN_6$	$C_{38}H_{27}Cl_2F_4IrN_6$
Crystal system	Triclinic	Triclinic	Triclinic	Monoclinic
Space group	Pī	Pī	Pī	P $2_1/n$
Volume (Å^3)	1499.7	1874.0	1555.47	3638.3
Reflections collected	93294	190180	15776	190723
Independent Reflection	5285 R(int)=0.2043	9366 R(int)=0.0458	7727 R(int)=0.0105	9116 R(int)=0.1606
a/ Å	9.686	12.397	9.596	11.216
b/ Å	12.673	12.986	12.742	15.592
c/ Å	14.255	13.599	14.509	20.807
α/°	105.111	110.289	110.406	90.000
β/°	104.801	109.021	100.284	91.098
χ/°	107.639	96.805	102.915	90.002

4.3.1 Bond Angles and Bond Distances from Crystallographic Analysis

The bond angle and bond length were analysed. All the selected bond angles (°) and bond lengths (Å) for complexes **IR1–IR4** were summarised in **Table 4.9.** In an ideal octahedral geometry, the bond angles between adjacent (*cis*) ligands are 90°, and those between opposite (*trans*) ligands are 180°. These values are derived from the three-dimensional spatial arrangement of ligands, not from planar geometry; therefore, 60° angles do not apply. However, the experimental data for complexes **IR1**–**IR4** show clear deviations from these ideal values, indicating distortion. Notably, the *cis* angles such as N1–Ir–C11 and C12–Ir–N2 range from 79.7° to 82.0°, while the chelating angle C28–Ir–N3, associated with the formimidamide ligand, is consistently smaller at 74.9° to 76.7°, reflecting significant ring strain. The *trans* angles, including N1–Ir–N2, C12–Ir–N3, and C11–Ir–C28, fall short of the ideal 180°, typically ranging between 168.6° and 178.3°, confirming a distorted yet systematic octahedral coordination environment across the series.

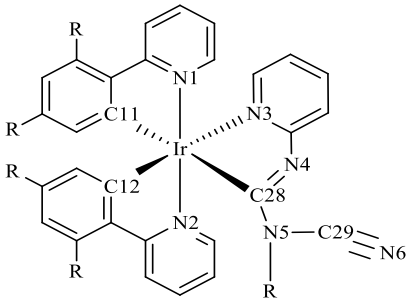

Table 4.9

*Selected Experimental Bond Angle (°) and Bond Length (Å) of Complexes **IR1–IR4***

Complex	Bond length (Å)			
	IR1	**IR2**	**IR3**	**IR4**
Ir–C11	2.059	2.053	2.023	2.058
Ir–C12	2.000	2.012	2.047	2.018
Ir–C28	2.109	2.090	2.104	2.072
Ir–N1	2.046	2.051	2.051	2.042
Ir–N2	2.053	2.044	2.071	2.046
Ir–N3	2.138	2.119	2.112	2.125
C28–N4	1.316	1.318	1.346	1.316
C28–N5	1.400	1.401	1.345	1.415
C29–N5	1.350	1.349	1.326	1.335
N6–C29	1.136	1.136	1.156	1.142
Complex	**Bond angle (°)**			
	IR1	**IR2**	**IR3**	**IR4**
N1 Ir C11	80.2	79.7	80.2	80.0
C12 Ir1 N2	80.2	80.4	82.0	80.2
C28 Ir1 N3	74.9	75.2	76.7	75.2
N1 Ir1 N2	170.6	171.1	174.7	173.3
C12 Ir1 N3	176.2	176.5	178.3	176.3
C11 Ir1 C28	168.6	168.9	170.0	168.8
N6 C29 N5	171.0	173.2	172.9	172.7

Substituent variations among the complexes appear to influence the degree of this angular distortion. **IR1** and **IR2** both possess a 2,6-difluorobenzyl group on the ancillary ligand, but **IR2** additionally features fluorine atoms on both phenyl rings of the cyclometallating ligands. This added electron-withdrawing effect in **IR2** leads to slightly more linear trans angles compared to **IR1**, suggesting increased rigidity and reduced angular strain. In contrast, **IR3** and **IR4** contain a 4-methylbenzyl substituent on the ancillary moiety, with **IR4** also incorporating fluorine atoms on the phenyl rings. Again, **IR4** exhibits a less improvement in trans-angle linearity relative to **IR3**, notably at N1–Ir–N2 (174.7°) and C12–Ir–N3 (178.3°). The most pronounced angular compression can be seen in the C28–Ir–N3 chelation angle across all complexes **IR1–IR4**, but shows subtle variation in **IR3** exhibits the widest angle (76.7°), while **IR1** is the most compressed (74.9°), indicating that ancillary ligand of pyridinylformimidamide have more steric effect that cyclometallating phenylpyridine ligand. Overall, these substituent-dependent differences support a difference in behaviour between ligand electronics in shaping the final geometry of the iridium(III) coordination sphere.

For the bond length analysis, bond lengths for C29–N6 were in the ranges of 1.13-1.16 Å suites the formation of a triple bond for nitrile in pyridinylformimidamide (Kaufmann et al., 2017) and the other essential bond length of C=C, C–C, C=N, and C–N are all in the normal ranges as expected which are ~1.33 Å, ~1.53 Å, ~1.38 Å and ~1.47 Å respectively which are similar to many analogous cyclometallated iridium(III) complexes (Idrees et al., 2017; You et al., 2021). The steric structure of the ligands once again plays a significant role in the complex's distorted nature in terms of the bond length deviation from the ideal iridium(III) complexes (Sanner et al., 2019).

One of the steps to achieve high-energy blue phosphorescent materials is changing the ancillary ligand's heterocyclic fragment with one with a higher triplet energy, such as carbene. The idea is that strong field ligands such as carbene are necessary to retard or eliminate non-radiative processes. While iridium complexes are in their triplet excited states, they may thermally populate a higher state known as the non-radiative (NR) state (Mingxing et al., 2021). A schematic representation of the emission and deactivating NR processes is given in **Figure 4.17**. For complete deactivation of NR at room temperature, the NR deactivating rate ($k_{nr}(T)$) must be significantly greater than the radiative rate (k_r) that the higher energy NR state is thermally accessible. From this NR state, they go through a non-radiative decay pathway and return to their ground state at a rate constant equal to $k_{nr}(T)$ instead of the K_{nr} pathway. Thus, a strong field ligand effectively eliminated the NR and fully activated the phosphorescence emission through K_{nr}.

Figure 4.17

Energy level scheme of the luminescence emission (K_{nr}) and non-radiative state (K_{nr} (T)). Figure reproduced from Lee & Han, 2020

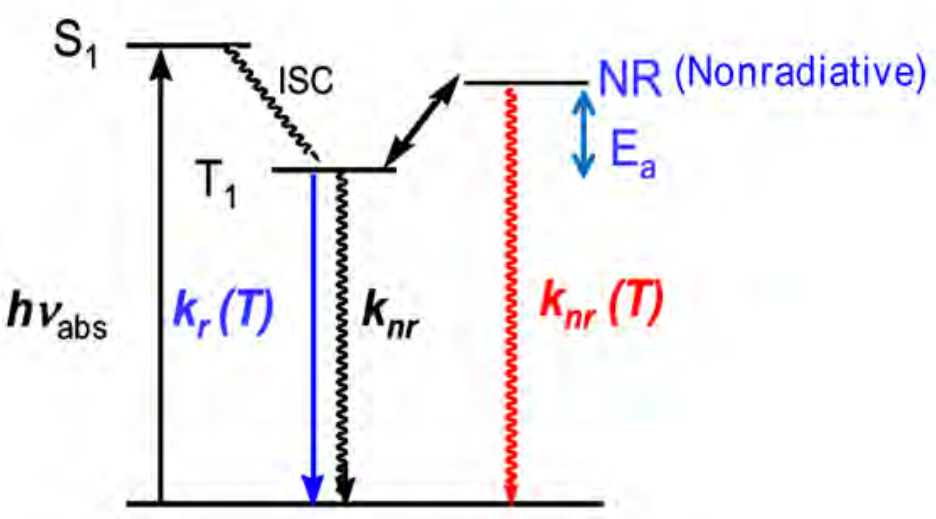

In the analysis of bond length between central metal iridium and the atoms of ligand for all complexes **IR1–IR4**, it can be seen that pyridinylformimidamide ancillary ligands exhibit weak field ligand coordination to iridium atom compared to the phenylpyridine cyclometallating counterparts. For all complexes, the average distances for Ir1–$N3_{formimidamide}$ (>2.10 Å) were significantly longer than the average Ir–$N_{pyridine}$ (between 2.00 and 2.10 Å). In addition, the bond distance for Ir1–$C28_{pyridinylformimidamide}$) was longer than the other averages of Ir-C_{phenyl} (Ir1–C11 and Ir1–C12). These elongated bond distances suggest the weaker coordination of the pyridinylformimidamide ancillary ligand with the central metal iridium atom, supporting the conclusion that pyridinylformimidamide is a type of weak field ligand (Donato et al., 2013).

The correlation between weak field ligands and weaker coordination lies in the ligand's electronic properties. Weak field ligands, according to crystal field theory, interact less strongly with the metal's *d* orbitals, leading to smaller splitting of the *d*-orbital energy levels. This weaker interaction results in longer metal-ligand bond distances and reduced overlap between ligand and metal orbitals, which in turn corresponds to lower overall bonding strength (Lee & Han, 2020). Therefore, the observed longer bond lengths in the Ir–N and Ir–C interactions with pyridinylformimidamide are consistent with its behaviour as a weak field ligand.

Initially, we hypothesised that using cyclic triazole carbene ancillary ligands would shorten the bond lengths and provide stronger ligand field strength through enhanced coordination with the iridium centre (Lee & Han, 2020; Sajoto et al., 2005). However, the properties exhibited by pyridinylformimidamide contradict this hypothesis, emphasising its character as a weak donor in the coordination environment

of these iridium complexes. Hence, it is interesting to find whether the phosphorescence quantum yield (PLQY) of the synthesised complexes **IR1–IR4** will be influenced by the weak field ligand properties of pyridinylformimidamide. All the PLQY were discussed in **Subtopic 4.4.**

4.4 Photophysical Properties of the Synthesised Iridium(III) Complexes IR1–IR4

4.4.1 Electronic Transition of UV/Vis Absorption Analysis

Table 4.10 compares UV/Vis absorption data, and **Figure 4.18** shows the absorption spectra of complexes **IR1–IR4** in dichloromethane solution at 298 K. As with most iridium(III) complexes, the absorption spectra can be divided into two regions. The first region is related to shorter wavelengths, which involves the electrons moving from bonding orbital to antibonding ($\pi \rightarrow \pi^*$) transitions of the ligand in the UV region. They tend to have molar absorptivity on the order of $\varepsilon \approx 20{,}000–55{,}000$ $M^{-1}cm^{-1}$. This transition is related to the ligand-centred, which is attributed to the electrons moving within the phenylpyridine ring and pyridinylformimidamide ring. The second region was related to the longer wavelength metal to ligand charge transfer (MLCT): $d\pi(M) \rightarrow \pi^*(L)$ transitions in or near the visible region, which is commonly weak, broad, and structureless. The peaks at 300–350 nm can be assigned to Ir($d\pi$)→phenylpyridine(π^*) MLCT transitions, which exhibit a predominant singlet spin multiplicity. In this singlet spin multiplicity state, all electron spins are paired, resulting in a total spin quantum number (S) of 0 and a spin multiplicity of 1, according to the formula $2S + 1$. Singlet states are typically the lowest energy excited states and

are often associated with short-lived lifetimes (Bai et al., 2020; S. Liu et al., 2011). This assignment is consistent with previous studies of $Ir(ppy)_3$ (Baranoff et al., 2011; Namdas et al., 2004; Smith et al., 2011). The peaks observed at >350 nm were MLCT transitions due to the strong intersystem crossing by the triplet (T_1) and singlet (S_1) excited states that are driven through the central metal of an iridium atom related to the $^{1/3}$MLCT transitions with a strong π→π* character with molar absorptivity, ε ≈ 5,000–6,600 $M^{-1}cm^{-1}$ (Ali et al., 2017; Würth et al., 2015).

Table 4.10

*Summary of UV/Vis Spectral Data for the Synthesised Iridium(III) Complexes **IR1–IR4** in Dichloromethane at 298 K*

Complex	Concentration (M)	λ_{abs} / nm (10^3 ε M^{-1} cm^{-1})
IR1	1.8 x 10^{-5}	269 (59), 356 (9.5), 392 (5.5)
IR2	4.1 x 10^{-5}	262 (31), 319 (10.6), 345 (8.1), 375 (5.9)
IR3	2.5 x 10^{-5}	269 (48), 355 (9.1), 385 (5.2)
IR4	3.9 x 10^{-5}	262 (27), 315 (9.7), 342 (7.8), 374 (5.4)

Figure 4.18

*Absorption spectra of complexes **IR1–IR4** in dichloromethane at 298 K with concentration stated in **Table 4.10***

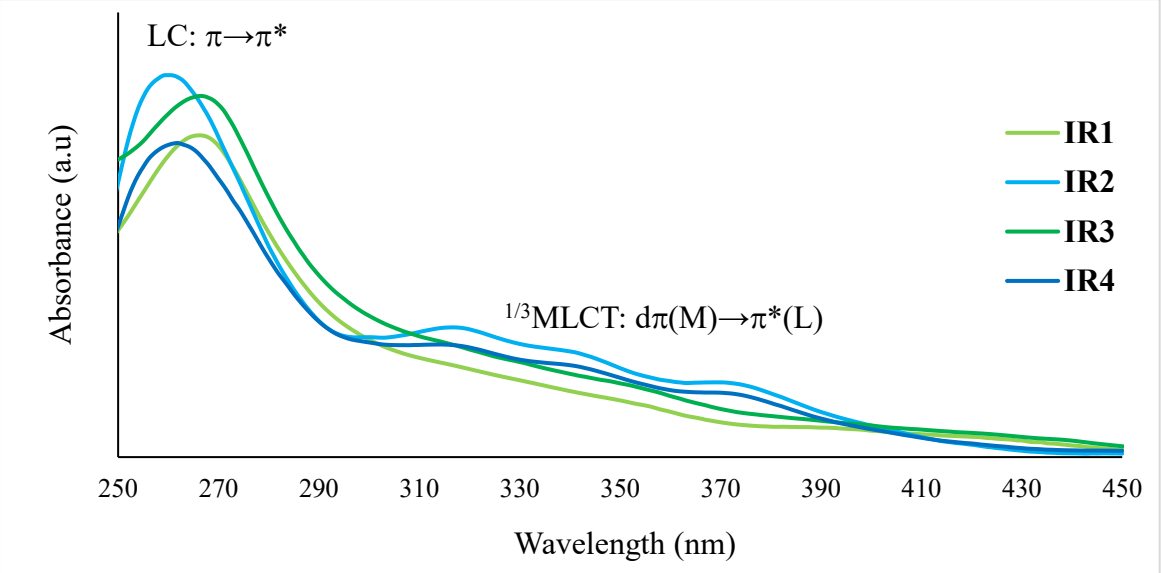

In general, the spectra of complexes **IR2** and **IR4** were found to be blue-shifted compared to absorption complexes **IR1** and **IR3**, as shown in **Figure 4.18**. These remarkable differences indicate that the fluorine atoms in cyclometallating moieties have caused the blue-shifted to occur and reduced the role of substituents on the ancillary moiety in shifting the peak to a shorter wavelength. In significance, the LC transition of complexes **IR2** and **IR4** (λ_{abs} = 262 nm) was a hypsochromic shift by 7 nm compared to complexes **IR1** and **IR4** (λ_{abs} = 269 nm). However, the low-lying wavelength of singlet and triplet MLCT shows a more remarkable spectral shift. Complex **IR1** (λ_{abs} = 392 nm) has a bathochromic shift of about 17 nm compared to complex **IR2** (λ_{abs} = 375 nm)**,** while complex **IR3** (λ_{abs} = 385 nm) has around an 11 nm bathochromic shift compared to complex **IR4** (λ_{abs} = 374 nm)**.** Overall analysis, complex **IR4** has superior absorption energy compared to other synthesised complexes with the presence of methyl-benzyl substituent on the ancillary moiety and fluorine atom on the cyclometallating moiety.

Another point that is worth highlighting in this discussion is the variation in preparing the concentration of complexes **IR1**–**IR4** during UV/Vis measurements, as shown in **Table 4.10**. This is primarily due to differences in their molar absorptivity (ε), solubility, and intrinsic optical properties, such as colour intensity (Würth et al., 2015). These complexes, which appeared light yellow in solution, absorb visible light due to metal-to-ligand charge transfer (MLCT) and ligand-centred (LC) transitions. Since the yellow colour indicates absorption in the violet-blue region, the precise absorption intensity depends on the electronic nature of the substituents on the ligands. Complexes with stronger absorption bands that have higher ε values, such as **IR2** and **IR3**, require more dilute solutions to keep absorbance within the linear and accurate range (typically

A ≈ 1.0) for UV/Vis spectrophotometry. Conversely, complexes with weaker absorptivity, such as **IR1**, require slightly higher concentrations to achieve detectable absorbance. Thus, the use of different concentrations is a standard experimental adjustment to optimise spectral clarity and ensure accurate comparison of spectral features across the series.

4.4.2 Steady-State Emission Analysis on Fluorescence Spectroscopy

The steady-state emission spectra of synthesised complexes **IR1–IR4** are shown in **Figure 4.19**. Spectra of complexes **IR2** and **IR4** exhibited two significant peaks with fine vibronic structure, which indicated that the emitting lowest triplet state has a predominantly ^{3}MLCT character with a minor ^{3}LC contribution (Lee & Han, 2020). On the other hand, the complexes **IR1** and **IR3** spectra exhibited only one peak with non-vibronic structures with a gaussian shape, indicating that the lowest triplet state is only predominantly ^{3}MLCT character.

Figure 4.19

*The emission spectra for complex **IR1–IR4** in air-equilibrated dichloromethane solution at 298K with the same concentration as **Table 4.10***

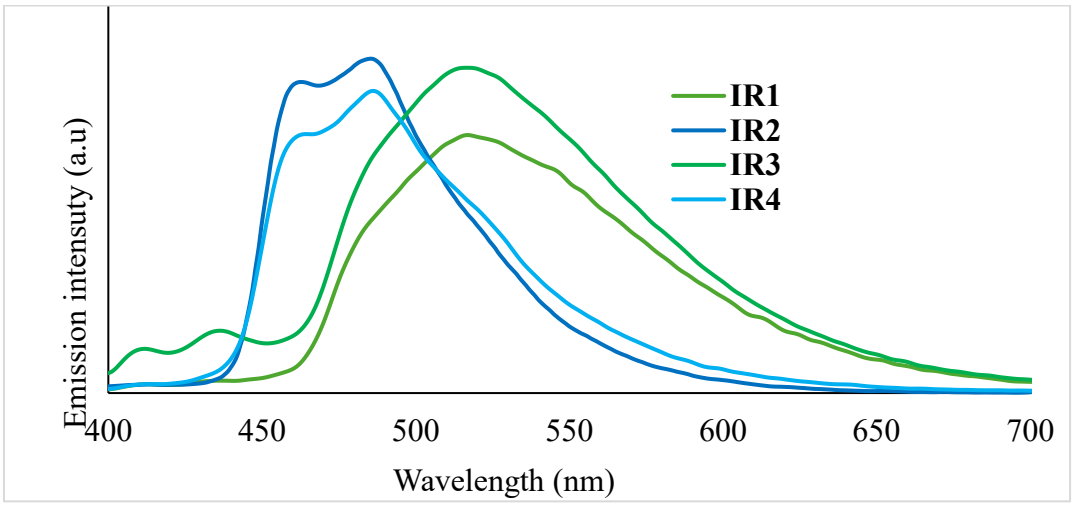

The summary of the luminescence peaks complexes **IR1–IR4** under the UV lamp is tabulated in **Table 4.11**. All complexes emitted light under the UV lamp, as shown in **Table 4.11**. For spectral comparison, fluorine atoms at the phenyl ring's 2- and 4-carbon positions contributed to electron-withdrawing (EWG) properties and shifted the emission energy of complexes **IR2** and **IR4** about ~50 nm compared to complexes **IR1** and **IR3**. The presence of EWG has contributed to HOMO stabilisation, lowered the HOMO-LUMO energy band gap, and shifted the spectrum into higher emission energy leading to almost blue colour emission of the complex under the UV lamp. These different energies have shown that the electron-withdrawing group is essential in the HOMO-LUMO band gap energy of heteroleptic species of iridium(III) complexes. Further TD-DFT studies were discussed in detail in the subsequent subtopic to compare the molecular orbitals of all the synthesised complexes. To summarise the emission spectrum study, complex **IR2** has a higher emission energy, which is hypsochromically shifted by 1 nm from complex **IR4** and 54 nm from complexes **IR1** and **IR3**, respectively.

Table 4.11

*The Summary of Phosphorescence Emission and Steady-state Emission Data for Complexes **IR1**–**IR4** in Dichloromethane Solution at 298 K*

Complexes	Emission, λ_{max} (nm)	Colour
IR1	517	 Yellowish green
IR2	463, 484	 Greenish-blue
IR3	517	 Yellowish-green
IR4	464, 486	 Greenish-blue

4.4.3 Phosphorescences Efficiencies

Phosphorescence efficiencies analysis aimed to study the potential application of the synthesised complexes **IR1–IR4**. All the efficiency data were summarised in **Table 4.12.**

Table 4.12

*The Summary of Phosphorescence Efficiencies Data for Complexes **IR1–IR4** in Dichloromethane Solution at Room Temperature. K_r = PLQY/τ, K_{nr} = [(1–PLQY)/τ]*

Complexes	Lifetime, τ (ns)	PLQY (%)	K_r (s^{-1})	K_{nr} (s^{-1})
IR1	34.73	48	1.38×10^6	1.50×10^6
IR2	1.61	44	27.32×10^6	34.78×10^6
IR3	78.82	49	0.62×10^6	0.65×10^6
IR4	29.51	37	12.5×10^6	21.35×10^6

The photoluminescence quantum yield (PLQY) was measured in dichloromethane at room temperature and using commercial $Ir(ppy)_3$ ($\Phi_{PLQY} = 0.5$) as references, owing to acceptable values of quantum yield. Notably, the most famous commercial iridium(III) complex was Bis[2-(4,6-difluorophenyl)pyridinato-C^2,N](picolinato)iridium(III), **FIrPic** which reported reaching 80% PLQY (Baranoff & Curchod, 2015; Cho, Kim, et al., 2017). Complex **IR3** was the most efficient among the synthesised complexes, with a 49% quantum yield and the longest excited lifetime at 78.82 ns. However, this complex only emitted a yellowish-green colour in the UV lamp instead of blue-emitting light. This experimental result can conclude that the

absence of fluorine-heavy atoms on both cyclometallating and the ancillary moiety of complex **IR3** has enhanced the PLQY and excited lifetime, but gave the lowest emission energy. In general, the excited decay lifetimes of the complexes **IR1–IR4** tabulated were among the shortest decay lifetimes reported compared to other cyclometallated iridium(III) complexes synthesised previously (Lee & Han, 2020; Suzuri et al., 2014; Thomassen et al., 2020). Most of the previously reported iridium(III) complexes have a longer decay lifetime in the range of μs due to the influence of the 5*d*-electron densities of the iridium centre on the HOMO. The complex **IR2** shows the shortest decay lifetime at 1.61 ns, with the presence of the highest number of fluorine atoms among the other complexes. The pattern that we can conclude is that the higher the number of fluorine atoms attached to the complex, the less efficient the phosphorescence properties are. Introducing fluorine into the ligand was among the promising factors to achieve HOMO stabilisation and hence contributed to blue emission luminescences complexes (He et al., 2016; Lee & Han, 2020). However, most of these synthesised complexes with fluorine substituents experienced low-efficiency phosphorescence due to the heavy atom effect triggered by the fluorine atom that introduces intrinsic drawbacks because the reactive C–F bonds are thermally and electrochemically unstable (He et al., 2016).

For all complexes, the rate constant for non-radiative values (K_{nr}) was higher than their rate constant for radiative values (K_r). Complex **IR2** and **IR4** show significant differences in values between the K_r and K_{nr}. The higher K_{nr} than K_r values were consistent with a high level of triplet MLCT character in the fine vibronic emission spectra of complex **IR2** and **IR4** in **Figure 4.19**. A similar correlation between the radiation rate and the degree of triplet MLCT character in the excited state can also be

observed for related iridium(III) complexes previously (Baranoff & Curchod, 2015; Monti et al., 2021; Shafikov et al., 2019).

To conclude, all the photophysical properties of complexes **IR1–IR4** were successfully studied using spectroscopic techniques of UV-Vis, Fluorescence, and Photoluminescence. All the complexes **IR1–IR4** show acceptable phosphorescence emission properties with different energies and different colours of emission. The hypothesis to synthesise deep blue phosphorescent iridium(III) complex is not accepted due to the low purity of the blue colour emission. However, the complexes **IR2** and **IR4** emitted almost blue colour emission with high emission energy and comparable phosphorescence quantum yield compared to previously reported iridium(III) complexes (Na et al., 2017; Tamayo et al., 2013; You et al., 2021; Zulkifli et al., 2023).

4.5 Theoretical Studies of the Synthesised Bis(phenylpyridine) (pyridinylformimidamide) Iridium(III) Complexes Using DFT

In practice, DFT has a great advantage in simulating the theoretical chemical analysis of transition metal complexes as it is better in the description of electron correlation effects due to the fitting of the exchange potential to high-accuracy calculations. In this subtopic, the DFT studies aimed to bridge the experimental data to the theoretical data. In significance, DFT has been proven as a reliable tool for semi-quantitative comparison between theoretical and experimental transition metal complexes. It is applicable to be used in the study of the theoretical chemical analysis related to the iridium(III) complexes **IR1–IR4**. All the synthesised complexes, **IR1**–**IR2,** were further analysed using spectroscopic DFT characterisation.

4.5.1 Molecular Geometrical Optimisation

The theoretical molecular structures of the synthesised complexes **IR1–IR4** were calculated using DFT to get the molecular geometrical optimisation. Since the experimental chemical analysis has shown a novel finding, the Crystallographic Integrated File (CiF) was avoided from being used in DFT to better compare experimental and theoretical studies. Hence, all the molecular structures were drawn from scratch and optimised in the software to get the minimum electronic energy. The complexes were drawn starting from optimising a small fragment of ligand **CNF_2Bpyfa**. After the ligand of **CNF_2Bpyfa** was successfully optimised, it became the starting fragment that expanded into the complex **IR1** and was optimised again. The process of expanding structure and optimisation was repeated until we got the completed optimised structure for all the complexes, **IR1–IR4**. The optimisation of small fragments and modification into big complexes has shortened the time needed for DFT calculation, leading to time efficiencies. The lack of imaginary frequencies confirmed that the geometries were successfully optimised. **Figures 4.20–4.23** show the optimised structures of complexes **IR1–IR4** resulting from DFT calculations.

Figure 4.20
The optimised structure of complex Ir(ppy)$_2$(CNF_2bpyfa), ***IR1***

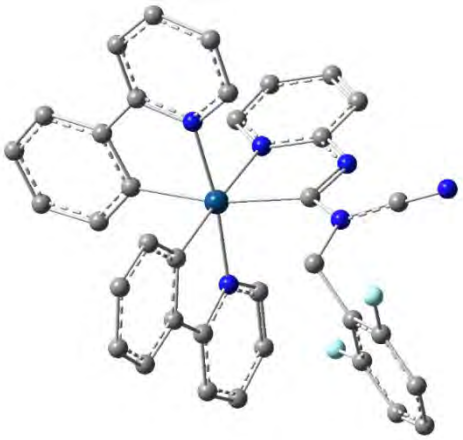

Figure 4.21

The optimised structure of complex Ir(F$_2$ppy)$_2$(CNF$_2$bpyfa), ***IR2***

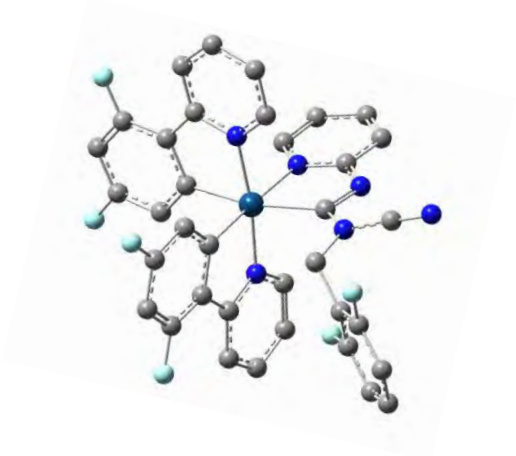

Figure 4.22

The optimised structure of complex Ir(ppy)$_2$(CNMbpyfa), ***IR3***

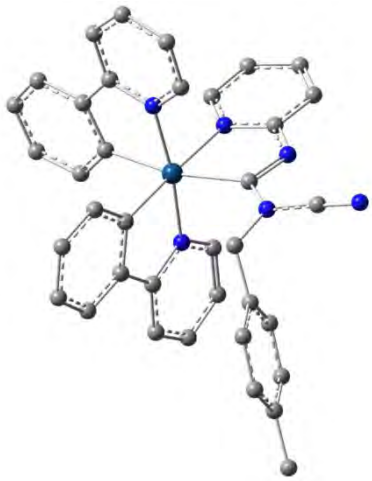

Figure 4.23

The optimised structure of complex Ir(F$_2$ppy)$_2$(CNMbpyfa), ***IR4***

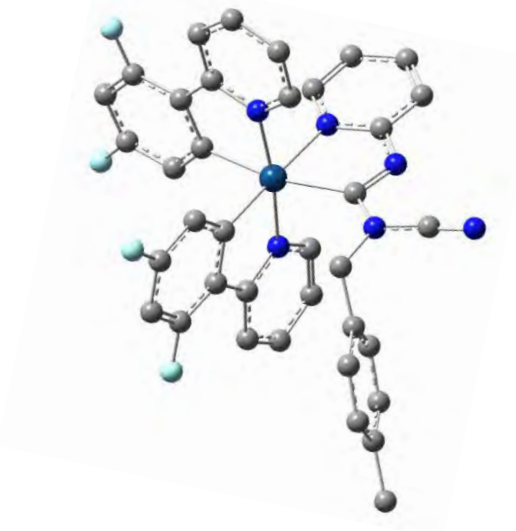

The optimised DFT structures of each complex **IR1–IR4** showed compatible results that were almost similar to their respective experimental crystallographic structures. The DFT structure has two phenylpyridine rings occupied by the cyclometallating moiety that are not planar to each other. However, the phenyl and the pyridine were in the planar position. Two phenylpyridine ligands occupied the coordination sphere in the axial position (N1/Ir1/N2), making the complexes coordinated in the trans-position of octahedral geometry. **Table 4.13** shows the selected bond angle and length for all the synthesised complexes **IR1–IR4**. All calculations have revealed data that is compatible with the experimental crystallographic analysis. Significantly, the bond length for N6–C29 shows correct ranges for the triple bond of the nitrile group for all complexes **IR1–IR4**.

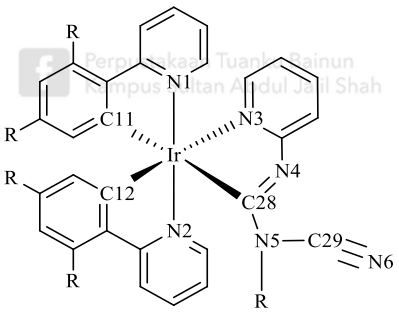

Table 4.13

DFT Calculation Data of the Selected Bond Angle (°) and Bond Length (Å)

Complex	Bond length (Å)			
	IR1	**IR2**	**IR3**	**IR4**
Ir-C11	2.070	2.068	2.069	2.067
Ir-C12	2.026	2.022	2.027	2.023
Ir-C28	2.147	2.143	2.149	2.147
Ir-N1	2.090	2.089	2.088	2.086
Ir-N2	2.069	2.069	2.071	2.070
Ir-N3	2.197	2.190	2.198	2.191
C28-N4	1.341	1.339	1.343	1.340
C28-N5	1.427	1.424	1.424	1.421
C29-N5	1.357	1.357	1.358	1.358
N6-C29	1.166	1.165	1.165	1.165

Complex	Bond angle (°)			
	IR1	IR2	IR3	IR4
N1-Ir-C11	79.4	79.4	79.4	79.4
C12 Ir1 N2	79.9	80.0	79.9	80.0
C28 Ir1 N3	74.4	74.5	74.4	74.5
N1 Ir1 N2	172.6	172.6	173.0	173.0
C12 Ir1 N3	176.4	176.6	176.5	176.6
C11 Ir1 C28	166.4	166.7	166.8	167.2
N6 C29 N5	174.6	174.6	174.8	174.7

4.5.2 Ground-State IR Spectra of Complex IR1–IR4

The optimised structures of all complex **IR1**–**IR4** were calculated in their ground states were successfully converged and hence used to calculate their vibrational frequencies. The IR spectra results show good agreement with the experimental data as the correlation coefficient (R) was in the range of 0.9–1.0, indicating a positive correlation, as shown in **Figures 4.24–4.27** with their respective R-value. An acceptable difference was found between them, but it was still in the absorption value ranges for each vibrational mode. This deviation was expected to be contributed by the differences in the structural behaviour discussed in **Subtopic 4.6.1**.

Figure 4.24

*Correlation between experimental and theoretical infrared absorption of complex **IR1***

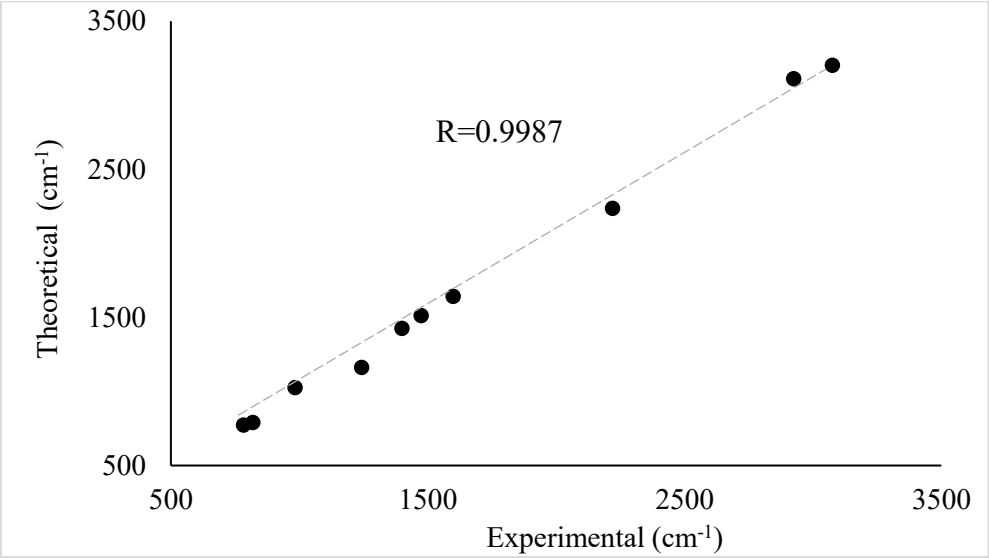

Figure 4.25

*Correlation between experimental and theoretical infrared absorption of complex **IR2***

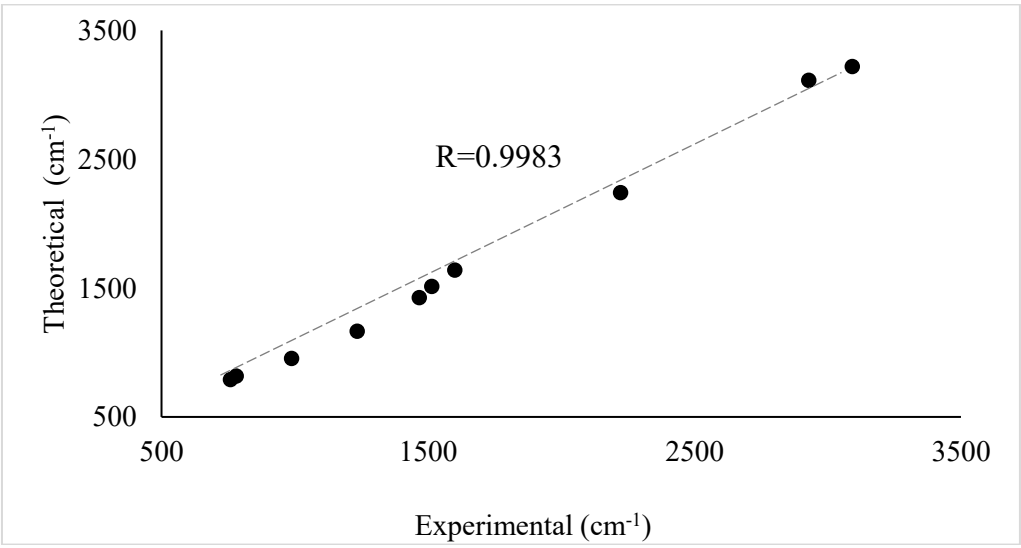

Figure 4.26

*Correlation between experimental and theoretical infrared absorption of complex **IR3***

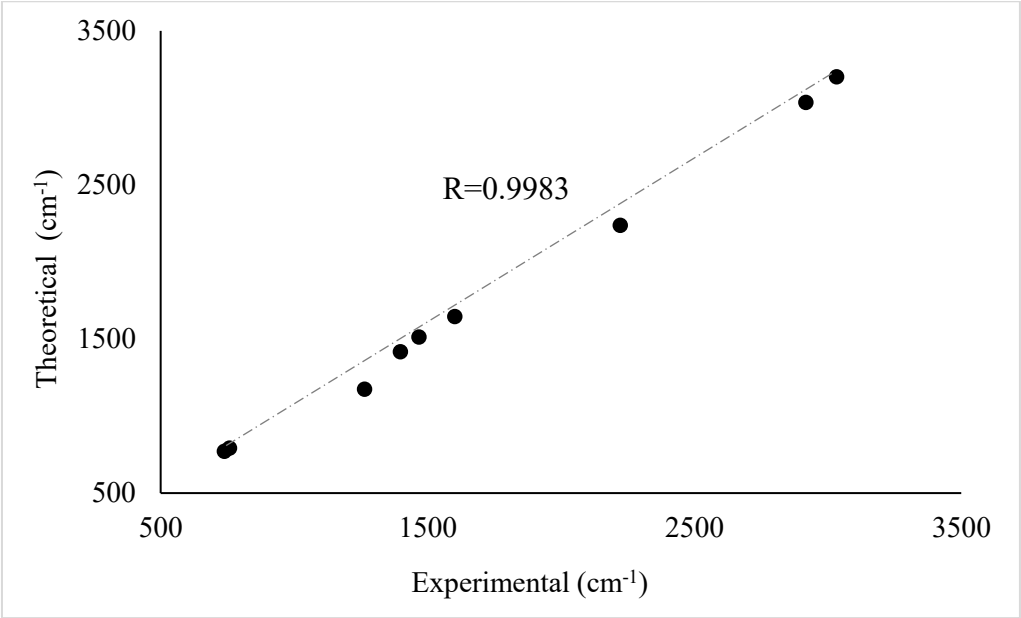

Figure 4.27

*Correlation between experimental and theoretical infrared absorption of complex **IR4***

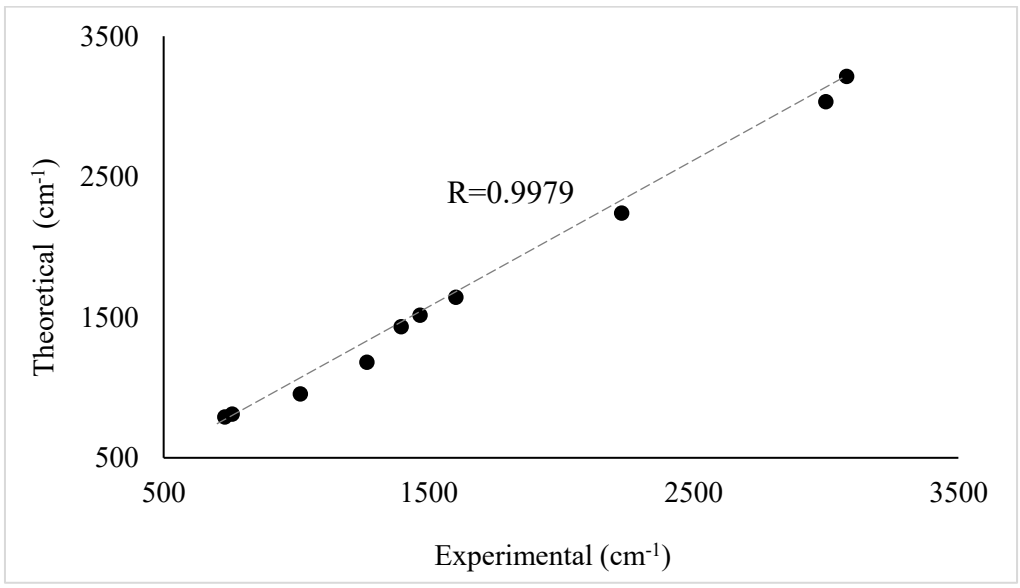

Table 4.14 shows the vibrational frequencies between experimental and DFT calculations for all complexes **IR1**–**IR4** and the data concluded that all the essential bands of infrared absorption were strongly correlated between experimental and theoretical values, showing that DFT supported the experimental IR spectra analysis. All complexes show the finest reproduction of the vibrational mode derived for ν(C≡N) with a ~10–19 cm^{-1} difference compared to their experimental value. Band of ν(C=N) stretching of complex **IR2** shows no differences between the experimental and calculated value at 1514 cm^{-1}. However, the stretching vibrations of ν(C–H) for alkyl and aromatic rings are underestimated with variations higher than 100 cm^{-1}. This large discrepancy is commonly attributed to limitations in DFT methods, particularly in modelling high-energy C–H stretching modes. These modes are sensitive to anharmonic effects and weak intermolecular interactions such as hydrogen bonding or dispersion forces, which are often not fully captured in standard harmonic DFT calculations (Pfeifer et al., 2016). Furthermore, ν(C–H) stretches are known to be influenced by subtle environmental effects (e.g., solvation or crystal packing), which are absent in gas-phase DFT simulations (Bernhammer et al., 2013). Other vibration modes are relatively well reproduced, with a distinction range of 10–90 cm^{-1} compared to their respective experimental vibrational bands. Notably, the vibrational data presented in **Table 4.14** also reflect important structural characteristics of the iridium(III) complexes. The ν(C≡N) stretching frequencies observed near 2220–2229 cm^{-1} in the experimental spectra, closely matched by the DFT-calculated values, confirmed the presence of the formimidamide-based ligand coordinated through a nitrile-like functionality. The consistent appearance of this band across all complexes, with only minor variation, indicates that the substitution on the ancillary or cyclometallating ligands does not significantly perturb the triple bond character of the

C≡N unit. In contrast, the ν(C=N) and ν(C=C) aromatic bands show broader variation (differences up to ~40–50 cm^{-1} between calculated and experimental values), reflecting the delocalised nature of these bonds and their sensitivity to electron-donating or -withdrawing substituents. For example, complexes **IR2** and **IR4**, which incorporate electron-withdrawing fluorine atoms on the cyclometallating ligands, show slightly higher calculated frequencies for ν(C=N) and ν(C=C), suggesting a strengthening of the double-bond character due to inductive effects (Pavia et al., 2015).

Overall, the correlation between experimental FT-IR and DFT not only validates the proposed molecular structures but also highlights how subtle modifications in ligand substitution can influence the vibrational and electronic properties of the metal complexes.

Table 4.14

*The Vibrational Frequencies Between Experimental and DFT Calculation for All Complexes **IR1**–**IR4***

Vibrational modes	Wavenumber (cm^{-1})							
	IR1		IR2		IR3		IR4	
	exp	calc	exp	calc	exp	calc	exp	calc
$\nu(C–H)_{aromatic}$	3076	3203	3092	3221	3032	3202	3079	3214
$\nu(C–H)_{alkyl}$	2925	3112	2928	3114	2918	3035	3000	3036
ν(C≡N)	2220	2237	2223	2242	2222	2238	2229	2242
ν(C=N)	1599	1642	1600	1641	1602	1646	1604	1644
$\nu(C=C)_{aromatic}$	1474	1513	1514	1514	1468	1512	1468	1516
	1400	1425	1467	1428	1398	1418	1397	1433

Vibrational modes	Wavenumber (cm^{-1})							
	IR1		IR2		IR3		IR4	
	exp	calc	exp	calc	exp	calc	exp	calc
ν(C–N)	1243	1163	1234	1167	1264	1175	1267	1180
$\nu(C–F)_{aromatic}$	983	1027	988	956	Not available		1016	956
$\nu(C–H)_{\text{out of plane}}$	819 783	791 774	780 759	817 790	758 738	791 772	759 731	812 791

4.5.3 Ground-State ^{1}H NMR Spectra Investigation

Like the ground state FT-IR spectroscopic, theoretical NMR spectra also correlated well with the experimental values. **Table 4.15** displays the observed and expected ^{1}H NMR chemical shifts of all synthesised complexes with their respective numbering scheme in **Figure 4.28.** The parameter used was TMS B3LYP/6-311+G(2d, p) GIAO. The comparison between observed and expected chemical shifts yielded a correlation coefficient (R) in the range of 0.8–0.9. R values do not achieve higher than 0.9, but still show a positive correlation since they did not give negative values. Each complex **IR1**–**IR4** obtained the most significant deviation of about ~3.5 ppm at proton H20 and H21, contributed by the methylene proton shown in **Table 4.15**. Other protons are relatively well reproduced, with a distinct range of 0–1.7 ppm compared to the experimental values.

Figure 4.28

*The numbering scheme of complexes **IR1**–**IR4** with respect to the proton NMR in **Table 4.15***

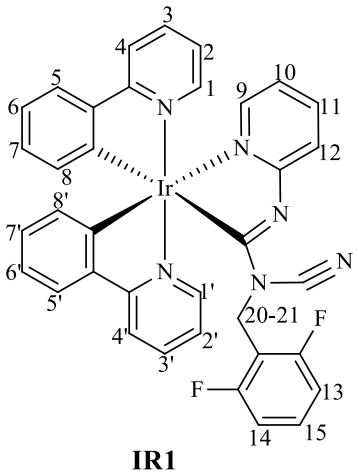

IR1

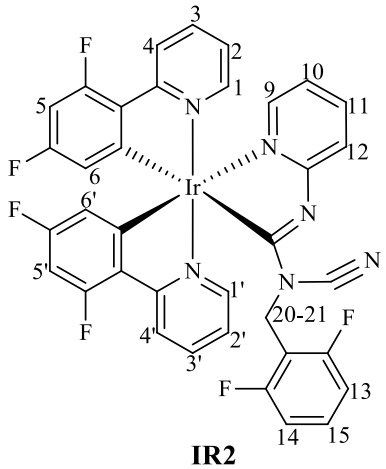

IR2

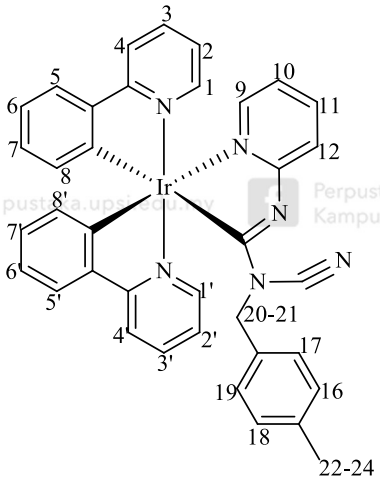

IR3

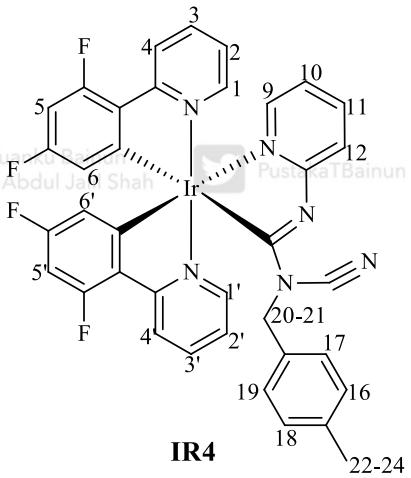

IR4

Table 4.15

Comparison of Experimental and Theoretical ^{1}H NMR Chemical Shift for Complexes ***IR1–IR4***

Proton	Chemical Shift (ppm)							
	IR1		IR2		IR3		IR4	
	Exp	Calc	Exp	Calc	Exp	Calc	Exp	Calc
H1	7.89	9.01	8.22	8.95	7.83	8.97	8.21	8.91
H2	7.71	7.18	7.75	7.22	7.69	7.11	7.73	7.18
H3	7.01	7.67	6.83	7.70	6.95	7.67	6.90	7.71
H4	7.00	7.92	7.00	8.54	7.37	7.93	7.42	8.55
H5	6.70	7.84	6.45	6.30	6.09	7.82	6.44	6.29
H6	6.70	7.03	5.70	6.30	6.90	7.00	6.66	6.29
H7	7.55	7.03	–	–	6.90	7.00	–	–
H8	6.32	6.93	–	–	6.25	6.93	–	–
H1'	7.85	8.19	8.26	8.12	7.60	8.27	8.21	8.19
H2'	7.65	7.03	7.75	7.10	7.60	7.11	7.61	7.11
H3'	6.90	7.77	6.83	7.82	6.95	7.67	6.90	7.76
H4'	6.90	8.06	6.91	8.63	7.37	7.82	7.35	8.41
H5'	6.70	7.84	6.30	6.17	6.10	7.56	6.44	6.07
H6'	6.67	6.85	5.63	6.58	6.90	6.76	6.28	6.55
H7'	7.48	7.03	–	–	6.90	7.00	–	–
H8'	6.15	7.31	–	–	6.25	7.22	–	–
H9	7.44	7.84	7.41	7.82	7.47	7.82	7.67	7.84
H10	7.22	6.46	7.37	6.58	7.57	6.49	6.90	6.55
H11	7.00	7.46	7.60	7.52	6.75	7.48	6.90	7.55
H12	7.59	7.40	7.45	7.39	7.47	7.48	7.49	7.49
H13	6.60	6.54	6.67	6.89	–	–	–	–
H14	4.75	6.85	4.77	6.58	–	–	–	–
H15	7.20	7.31	7.25	7.39	–	–	–	–
H16	–	–	–	–	6.60	6.85	5.65	6.88
H17	–	–	–	–	6.68	6.56	5.67	6.48
H18	–	–	–	–	4.78	7.11	4.88	7.18
H19	–	–	–	–	6.90	6.85	5.59	6.94
H20	1.54	5.01	1.24	4.87	2.24	5.58	2.25	5.46
H21	1.54	4.51	1.24	4.61	2.24	4.14	2.25	4.20
H22	–	–	–	–	2.24	2.54	2.25	2.55
H23	–	–	–	–	2.24	2.12	2.25	2.14
H24	–	–	–	–	2.24	2.00	2.25	2.05

Complex **IR1** shows relatively consistent deviations across most aromatic protons, particularly in protons H1–H6 and H1′–H6′, where most calculated values are higher than experimental by ~0.8–1.2 ppm, reflecting a typical overestimation trend in DFT-calculated shieldings (Alsaeedi, 2023). In complex **IR2**, although a similar trend is observed, the deviations at H4 and H4′ are more pronounced, exceeding 1.5 ppm, which could be attributed to the electronic effects of the additional fluorine substituents on the cyclometallating moiety that decreased the electron density within the complex (Pfeifer et al., 2016). Complex **IR3** displays smaller deviations in the aromatic region compared to **IR1** and **IR2**, suggesting a more balanced shielding environment, likely due to the presence of the electron-donating 4-methylbenzyl group. However, complex **IR3** also exhibits a significant shift discrepancy in the methylene and alkyl regions, especially at H20 and H21, supporting their strong environmental sensitivity. In complex **IR4**, similar to complex **IR3**, the largest differences also occur at the methylene protons (H20 and H21), but the presence of electron-withdrawing fluorines appears to stabilise some of the aromatic protons, leading to slightly improved agreement (e.g., H4 and H4′ with deviations below 1.2 ppm).

Another notable observation from **Table 4.15** is the distinct chemical shift patterns that help differentiate between complexes based on their ligand environments. In particular, the aromatic proton regions (H1–H12 and their counterparts H1′–H12′) provide consistent patterns that reflect the electronic nature of the ligands. For instance, downfield shifts in complexes **IR2** and **IR4** compared to complexes **IR1** and **IR3** were indicative of increased deshielding due to the presence of fluorine atoms as the contributor of electron-withdrawing properties on the cyclometallating rings. These electron-withdrawing groups draw electron density away from the aromatic system,

causing localised deshielding (Green & Yates, 2014). In contrast, the presence of electron-donating methyl groups in complexes **IR3** and **IR4** induces upfield shifts in some aromatic protons, confirming their electron-releasing influence (Green & Yates, 2014). Moreover, the diagnostic methylene protons (H20 and H21), which consistently show the highest deviations, act as sensitive reporters of structural flexibility and environmental changes. Their significant shift differences between calculated and experimental values may also suggest dynamic behaviour or conformational averaging in solution, especially near the flexible ancillary substituent (Alsaeedi, 2023). Thus, beyond general agreement, the NMR data not only validate the DFT-predicted geometries but also provide insight into how ligand electronics tune the local chemical environments. This highlights the utility of combining theoretical and experimental NMR data in characterising subtle structural and electronic differences among new synthesised metal complexes.

The correlation graph is shown in **Figure 4.29–4.32** for complexes **IR1–IR4** with the R-value of 0.81, 0.82, 0.87, and 0.88, respectively, which shows a positive correlation. This comparison is essential to validate the computational model and ensure it accurately reflects the experimental data. It confirms the structural assignments of the complexes and highlights subtle electronic effects not fully captured theoretically. Moreover, such comparisons help confirm the structural identity of newly synthesised complexes, particularly when spectroscopic techniques are the primary tools for characterising coordination environments. The discrepancies observed, such as the ~3.5 ppm deviation for protons H20 and H21, offer insight into the local electronic effects or conformational dynamics that may not be fully captured in the theoretical model (Younker & Dobbs, 2013). Despite some deviations, especially at

specific proton sites, the overall agreement supports the reliability of the computational approach.

Figure 4.29

*Correlation between experimental and theoretical ^{1}H NMR chemical shift of complex **IR1**, R=0.81*

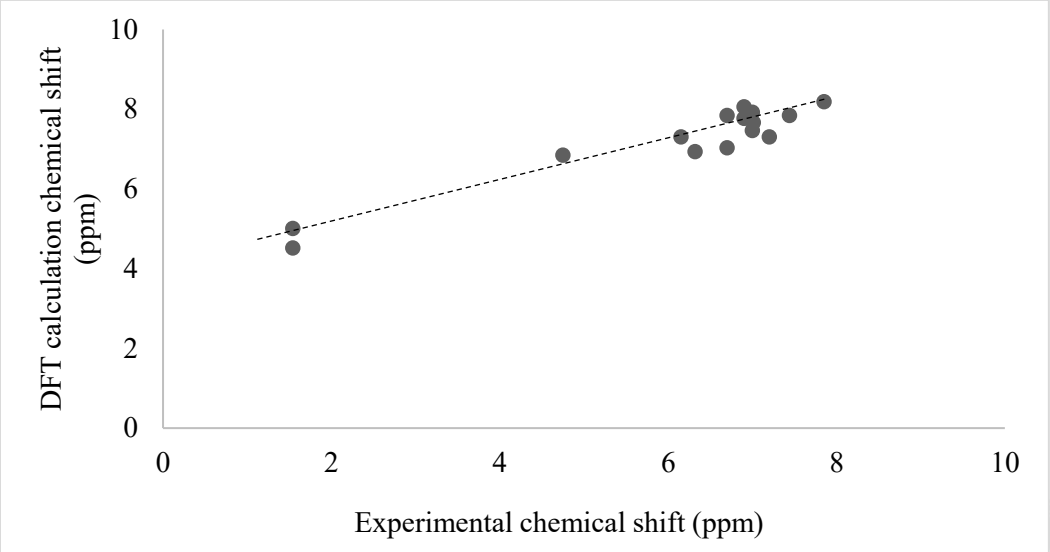

Figure 4.30

*Correlation between experimental and theoretical ^{1}H NMR chemical shift of complex **IR2**, R=0.82*

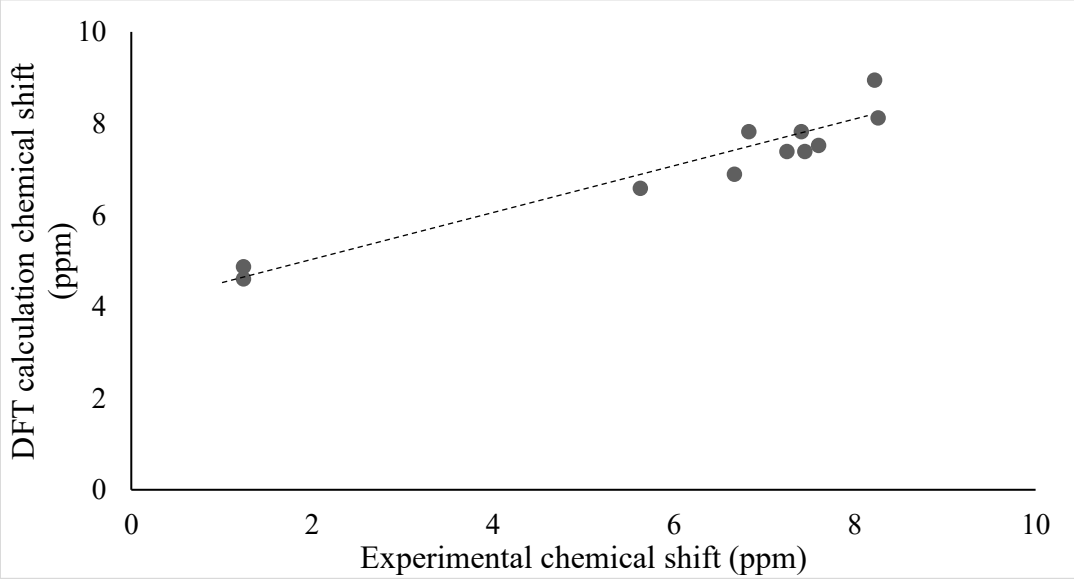

Figure 4.31

*Correlation between experimental and theoretical ^{1}H NMR chemical shift of complex **IR3**, R=0.87*

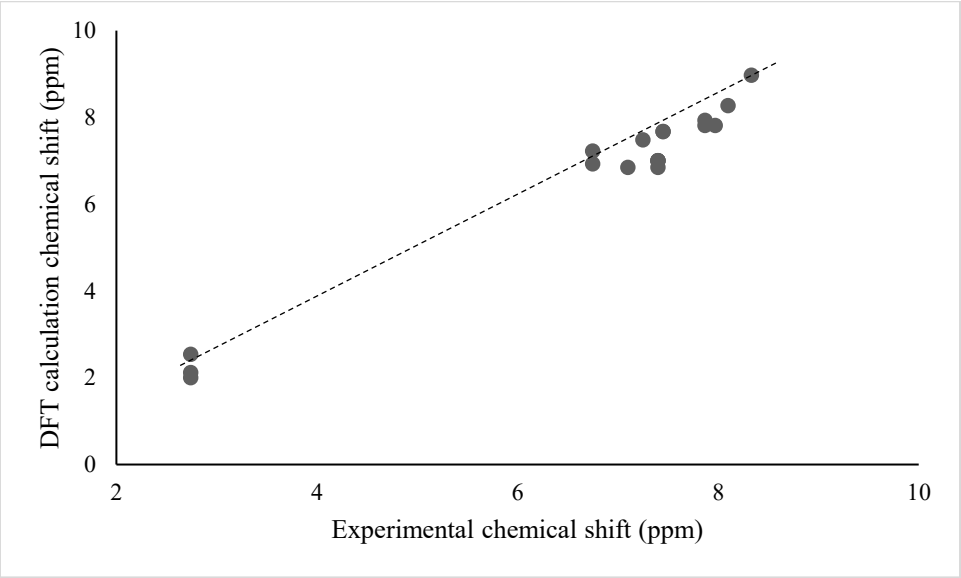

Figure 4.32

*Correlation between experimental and theoretical ^{1}H NMR chemical shift of complex **IR4**, R=0.88*

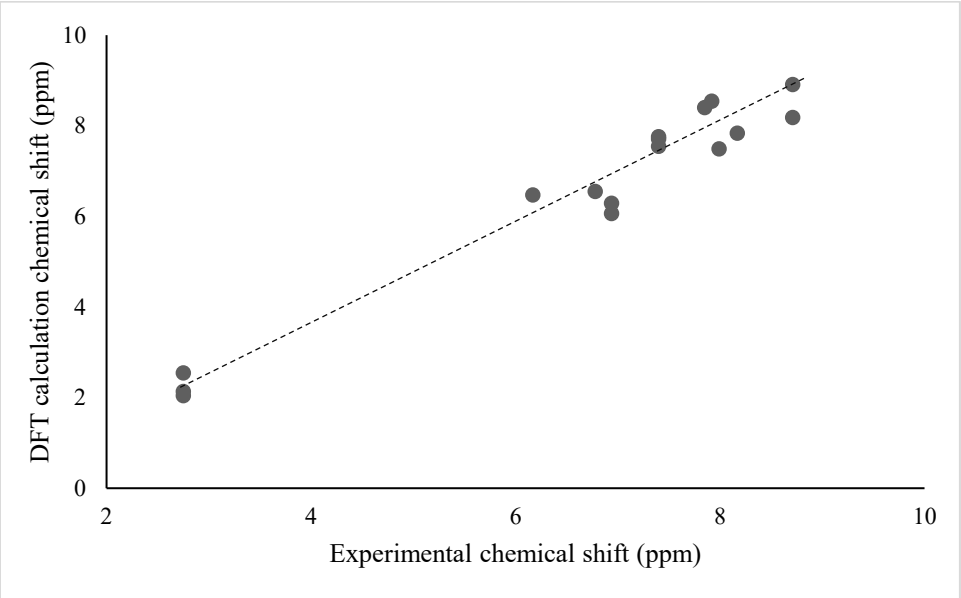

4.5.4 Ground-State TD-DFT Spectra Analysis

The TD-DFT calculations for the singlet ground state (S_0) have been performed using the geometry that was already minimised to the optimal electronic energy. Unlike FT-IR and NMR calculations that neglected the solvent effect, the Polarisable continuum model (PCM) was included in the absorption calculation with respective methylene chloride (DCM) constant to provide atom electrostatic interaction that is almost exactly like the experimental conditions.

Figure 4.33 shows the TD-DFT absorption spectra of complexes **IR1**–**IR4** in the ground state (S_0). Similar to the experimental absorption spectra, it can be observed that all complexes exhibited strong, intense peaks at the shorter wavelength of less than 300 nm and structureless broad peaks at higher wavelengths of 350 nm and above. Clearly, the TD-DFT spectra show a satisfying agreement with the experimental spectra. However, all the TD-DFT spectra of complexes **IR1**–**IR4** exhibited a bathochromic shift compared to their respective experimental absorption spectra. The significant differences owed by complexes **IR1** and **IR3** are that the experimental exhibited only three peaks in contrast to four peaks in their TD-DFT spectra shown in **Table 4.16**.

Table 4.16 summarises the electronic transition of complexes **IR1**–**IR4** with their respective experimental absorption values. The electronic energy and the oscillator strength resembling the absorption frequency (f) were included in **Table 4.16**. All compexes **IR1**–**IR4** showed strong intense bands associated with the $\pi \rightarrow \pi^*$ transition at 296 nm (f = 0.068), 286 nm (f = 0.068), 300 nm (f = 0.038), and 290 nm (f = 0.081),

respectively. The difference between the computational and experimental values was in the range of 27–31 nm. Among all the complexes, complex **IR2** is the bluest-shifted, while complex **IR3** is the most red-shifted. This indicated that fluorine atoms had an electron-withdrawing effect that significantly altered the ligand-centred (LC) transition associated with this π→π* transition (He et al., 2016; Nazeeruddin et al., 2016).

Figure 4.33

*Calculated TD-DFT spectrum for the complex **IR1–IR4** in the ground singlet state (S_0). Inset: the experimental UV-Vis absorption of complexes **IR1–IR4** for comparison*

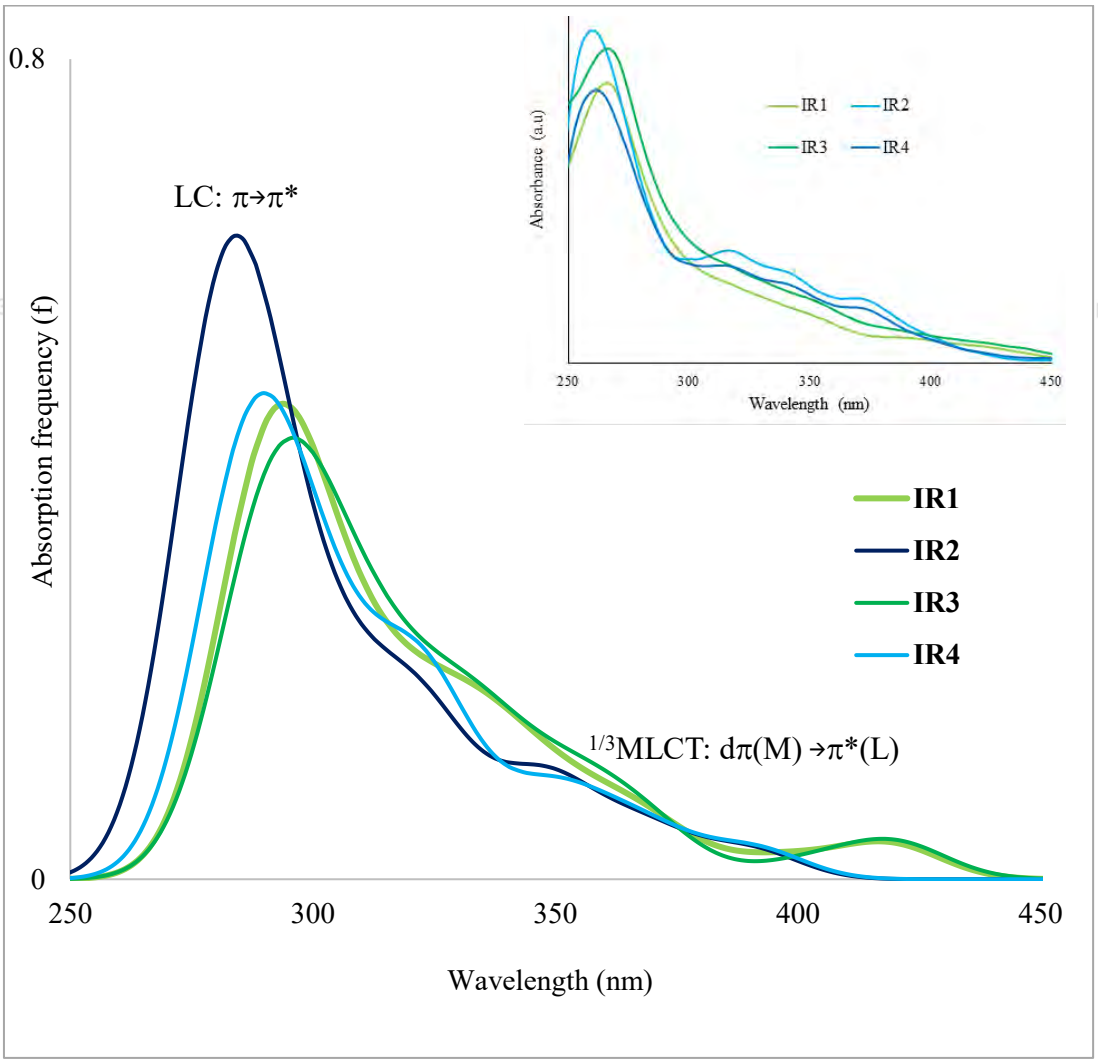

In addition, TD-DFT calculations have shown that the energy trend for LC transitions is **IR2** > **IR4** > **IR1** > **IR3**, confirming that the higher the number of fluorine atoms, the higher the absorption energy of the LC electronic transition. The LC transition showed highest contribution in complex **IR3** at 77% which consisted of HOMO-5→LUMO+1 (65%), HOMO-6→LUMO (5%), HOMO-7→LUMO+1(4%), and HOMO-8→LUMO+1 (3%). On the other hand, the smallest contribution of the LC electronic transition was 57% owed to complex **IR4**, which was attributed to HOMO-5→LUMO (48%), HOMO-6→LUMO+2 (2%), and HOMO-2→LUMO+3 (7%).

Consequently, the wavelength above 300 nm showed the involvement of three transitions for all complexes **IR1**–**IR4**. All the transitions were mainly contributed by the MLCT from Ir *d* orbitals to phenyl pyridine ligands, and some minor contributions were made to the π-π* transition. However, the longest wavelength peak of the complexes **IR1**–**IR4** complexes was the singlet-singlet absorptions located at 419 nm (f = 0.034), 391 nm (f = 0.027), 420 nm (f = 0.035), and 392 nm (f = 0.027), respectively. These values were agreed with the experimental wavelengths of 392 nm, 375 nm, 385 nm, and 374 nm for complexes **IR1**–**IR4**, respectively. The highest deviation was 35 nm, shown by complex **IR3**, revealing that TD-DFT has values that red-shifted the MLCT transition energy to a longer wavelength. Similar to the LC transition, the trend of the energy for MLCT transitions was concluded to be **IR2** > **IR4** > **IR1** > **IR3**, which once again correlated to the early experimental hypotheses. The longer the absorption wavelength led to the higher the absorption energy trend (**IR2**= 3.18 eV > **IR4**= 3.16 eV > **IR1**= 2.96 eV > **IR3**= 2.95 eV).

For all complexes, the lowest-lying singlet-singlet absorptions were the major contributor to the electronic transition at 96–97% which corresponded to HOMO→LUMO meaning that this lowest-lying MLCT transition strongly influenced the absorptivity of complexes **IR1**–**IR4**. Other molecular orbital (MO) contributions were summarised in **Table 4.16** for a clear comparison.

Since the TD-DFT absorbtivity graph only explained the role of fluorine at the cyclometallating moieties, further investigations were done using Frontier Molecular Orbital (FMO) on the TD-DFT calculations to study whether the substituents on the ancillary ligand have a contribution towards the electronic transition of all the synthesised complexes.

05-4506832 pustaka.upsi.edu.my Perpustakaan Tuanku Bainun Kampus Sultan Abdul Jalil Shah PustakaTBainun ptbupsi

Table 4.16
*The Summary of Experimental and TD-DFT UV-Vis Spectral Data for Complexes **IR1–IR4***

Complex	Experimental	TD-DFT Calculation			
	Abs (nm) $\varepsilon((10^3/M^{-1}cm^{-1}))$	λ_{abs} (nm)	Major Contribution (%)	Energy (eV)	Frequency (f)
IR1	269 (59) 356 (9.5) 392 (5.5)	295.9	H-5→L+1 (44%), H-5→L (3%), H-5→L+2 (7%), H-3→L+2 (3%), H-2→L+2 (3%)	4.19	0.068
		329.4	H-3→L+1 (43%), H-2→L+1(19%), H-2→L+2 (9%), H1→L+2 (4%),	3.76	0.044
		358.8	H-1→L+1 (33%), H-1→L+2 (55%)	3.46	0.028
		418.7	H→L (97%)	2.96	0.034
IR2	262 (31) 319 (10.6) 345 (8.1) 375 (5.9)	286.0	H-3→L+2 (19%), H-4→L+2 (29%), H-5→L+1(18%), H-5→L+2 (4%)	4.34	0.068
		323.8	H-1→L+1 (66%), H-2→L+2(4%), H→L+1 (2%)	3.83	0.068
		349.0	H-2→L+2 (36%), H-3→L+3 (7%), H-3→L+1 (2%), H-1→L+2 (7%)	3.55	0.067
		390.5	H→L (96%)	3.18	0.027

Complex	Experimental		TD-DFT Calculation		
	Abs (nm) $\varepsilon((10^3/M^{-1}cm^{-1}))$	λ_{abs} (nm)	Major Contribution (%)	Energy (eV)	Frequency (f)
IR3	269 (48) 355 (9.1) 385 (5.2)	299.8	H-5→L+1 (65%), H-6→L (5%), H-7→L+1(4%), H-8→L+1 (3%)	4.14	0.038
		334.1	H-3→L (24%), H-5→L+2(4%)	3.71	0.054
		368.7	H-4→L (2%), H-1→L (90%)	3.36	0.046
		420.0	H→L (97%)	2.95	0.035
IR4	262 (27) 315 (9.7) 342 (7.8) 374 (5.4)	290.01	H-5→L (48%), H-6→L+2 (2%), H-2→L+3(7%)	4.28	0.081
		322.7	H-2→L+1 (56%), H-6→L (9%), H-3→L (4%), H-2→L+2(10%)	3.84	0.021
		351.8	H-1→L+1 (85%), H-1→L+2(5%)	3.52	0.050
		391.8	H→L (97%)	3.16	0.027

4.5.5 Frontier Molecular Orbital (FMO) Analysis

The hypothesis highlighted at the beginning is that the ancillary ligands in complexes **IR1** and **IR2** with electron-withdrawing substituents (–F) would destabilise the LUMO energy, hence wider the HOMO-LUMO band gap energy. In contrast, the ancillary ligand in complexes **IR3** and **IR4** with electron-donating substituents ($–CH_3$) will stabilise the LUMO, lowering the HOMO-LUMO band gap energy. The bigger the band-gap energy will subsequently provide a blue-emission phosphorescent colour. Thus, the FMO study has revealed the HOMO-LUMO band gap energy for all the synthesised complexes, as shown in **Figure 4.34**. Complex **IR4** has the biggest band gap value at 3.880 eV, followed by complex **IR2** at 3.878 eV, with a very tiny difference of 0.002 eV. Both emitted an almost blue colour. On the other hand, the smallest band-gap energy is owed to complex **IR3** at 3.641 eV, which has a greenish-yellow emission colour.

Focusing on the trend for LUMO energy, the trend for LUMO destabilisation was concluded to be **IR3** > **IR1** > **IR4** > **IR2**. Complex **IR3** and **IR1** have the most LUMO destabilisation energy, and surprisingly, their LUMO surface plot shows that their molecular orbital contribution was not attributed to the ancillary ligand. Significantly, their π* major contribution was only related to π*(ppy) from cyclometallating moieties. On the other hand, complex **IR2** and **IR4** have the minor contribution of π*(pyridinylformimidamide) without the substituent's involvement, and these contributions have stabilised the LUMO energy. To conclude, the 4-methylbenzyl and 2,6-difluorobenzyl substituents on the ancillary ligand did not play a significant role in the LUMO destabilisation of complex **IR1** and **IR3**. Hence, the MLCT

electronic transition of all complexes **IR1**–**IR4** was not strongly influenced by the substituents on the ancillary ligand.

On the other perspective, the trend for HOMO stabilisation was **IR4** > **IR2** > **IR3** > **IR1**. For all cases, the surface plot of HOMO shows a major contribution from the *d* orbital of iridium metal as well as a minor contribution from the π(phenylpyridine) and π(pyridine of the pyfa). Following the HOMO surfaces plot, the fluorine on the cyclometallating phenylpyridine (ppy) ligand has provided the EWG properties that significantly lowered the HOMO energy of complexes **IR2** and **IR4** agrees with previously discussed in the experimental spectroscopic part.

Complex **IR4** has a more significant band gap energy compared to the commercial complex of $Ir(ppy)_3$, as shown in **Figure 4.35** (Karmis et al., 2019; Tamayo et al., 2013). Greater HOMO and LUMO stabilisation shown in complex **IR4** compared to $Ir(ppy)_3$ can be seen from the energy level diagram. No effect of LUMO destabilisation can be seen when the ancillary moiety changes to a formimidamide-based ligand. However, all complexes show a very significant LUMO stabilisation compared to the -1.26 eV of $Ir(ppy)_3$ related to the presence of nitrile in all ancillary moieties that lowered the LUMO energy by 0.30 eV due to the strong EWG properties and strong field ligand properties of the nitrile group. Theoretically, the explanation of tailoring the HOMO-LUMO band gap energy mechanism using EWG and EDG is simplified in **Figure 4.36**. Significantly, complex **IR2** contained fluorine and nitrile while simultaneously possessing the lowest LUMO energy among all the synthesised complexes. Hence, the enlargement of the band gap energy of complex **IR2** has led to the almost blue colour emission that is critically needed for OLED applications.

Figure 4.34

*The B3LYP TD-DFT with LANL2DZ basis set calculated frontier molecular orbital energy diagram including HOMO-LUMO gaps and surface plots of the HOMO and LUMO contribution for complexes **IR1–IR4**. Dichloromethane solvent correction is included with single-print SCRF*

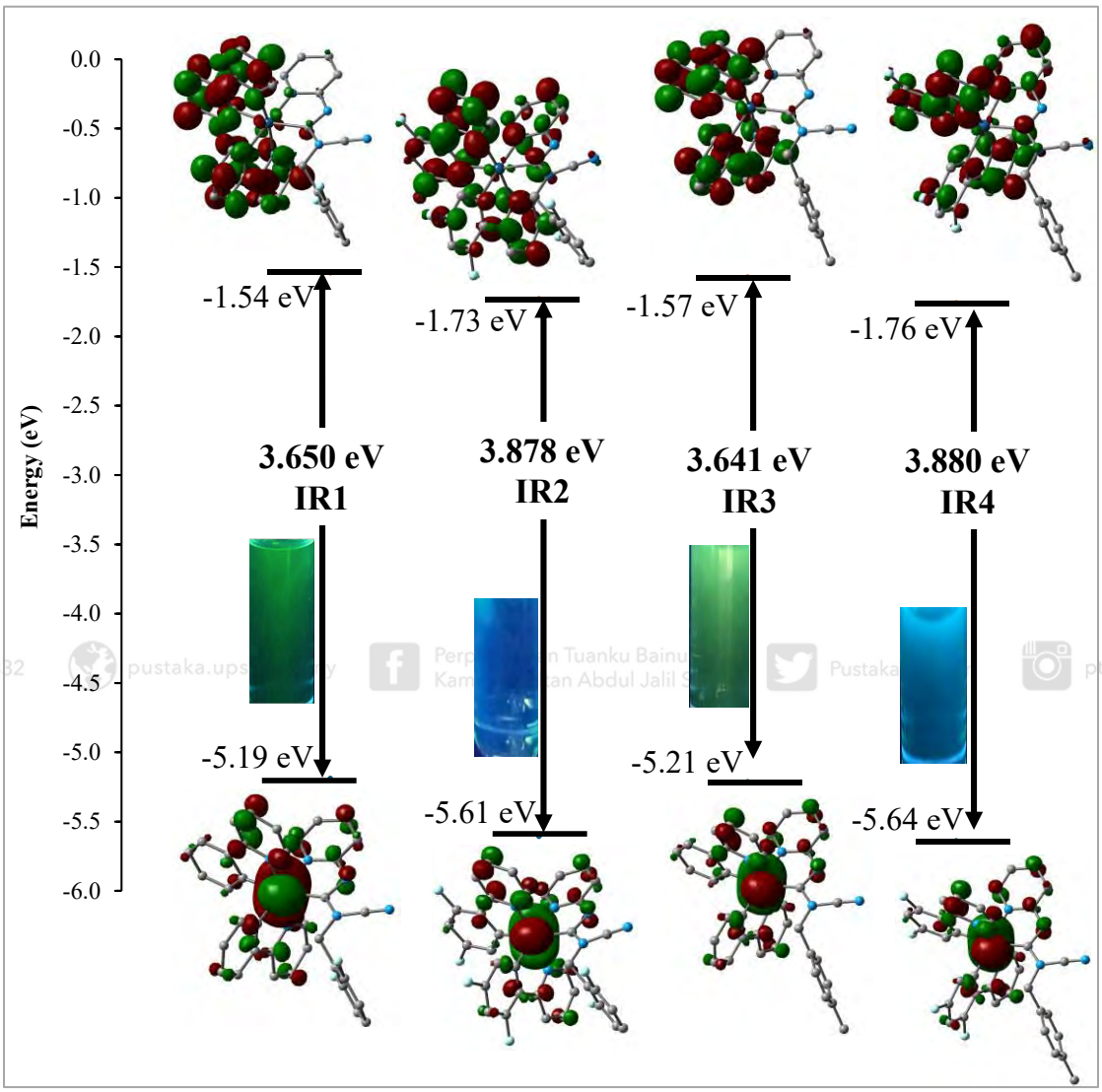

Figure 4.35

*Comparison of the energy level diagram of complex **IR4** with the previous synthesised complex Ir(ppy)$_3$. Inset: the photograph of the emission colour under a UV lamp (Karmis et al., 2019; Omae, 2016; Tamayo et al., 2013)*

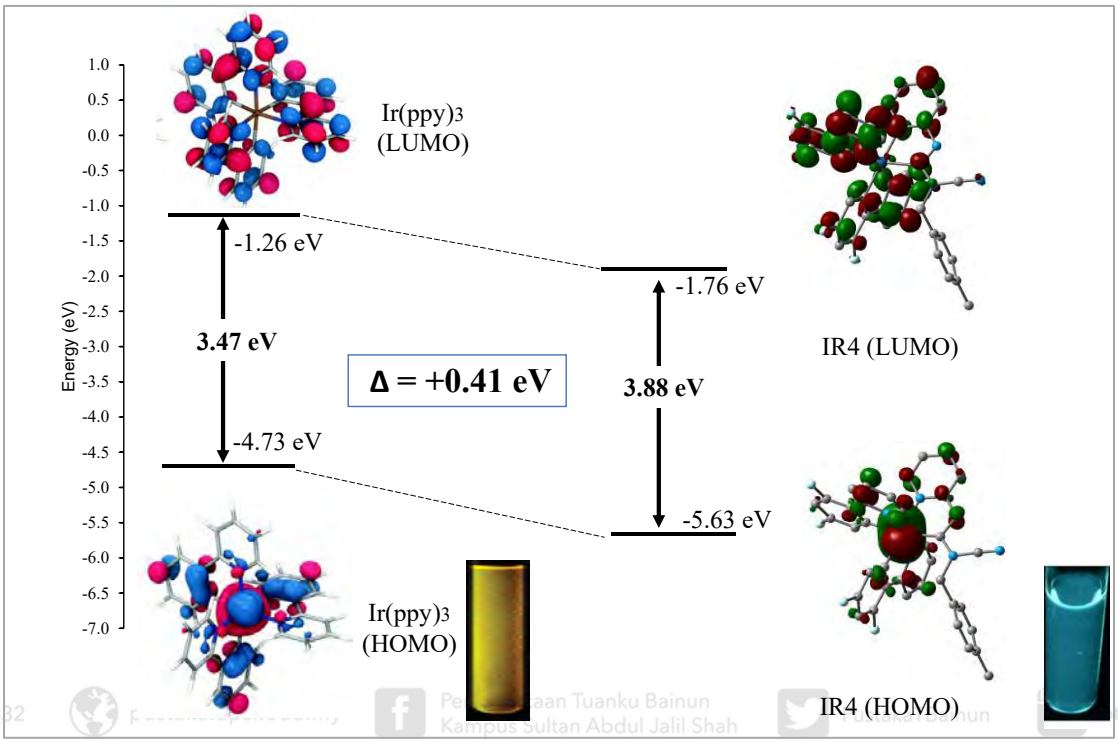

Figure 4.36

*Simplified strategies for emission colour tuning of cyclometallated iridium complexes (Alsaeedi, 2023). For ancillary moiety properties, EWG was contributed by nitrile for all complexes. In addition, complex **IR2** has EWG properties from the fluorine atom, while complex **IR4** has EDG properties from the methyl substituent.*

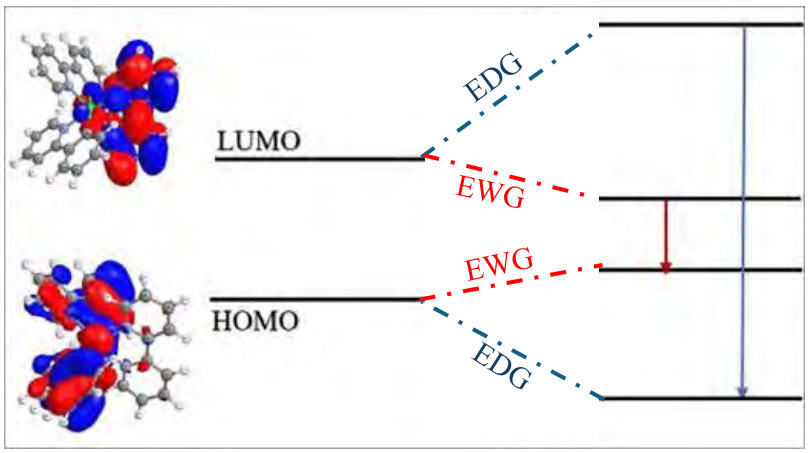

Approximately, **Figures 4.34** and **4.35** only discussed the major ^{1}MLCT transition at lowest-lying singlet-singlet absorptions, and all the discussions confirmed that the ancillary ligand did not contribute towards the HOMO-LUMO surfaces plot. Hence, detailed comparisons were made on FMO to find the contribution of ancillary ligands to the other electronic transitions, rather than only focusing on the lowest-lying ^{1}MLCT transition. Complex **IR1** is compared to complex **IR3,** while at the same time, complex **IR2** is compared to complex **IR4** to keep all other variables constant. As a result, only substituents on the ancillary ligand become the manipulation variables in each discussion.

4.5.5.1 Detailed Comparison of Molecular Orbital Contribution of Complexes IR1 and IR3

Tables **4.17**–**4.19** show the detailed orbital distribution for all the transitions involved in complexes **IR1** and **IR3**. The ancillary ligands in complexes **IR1** and **IR3** only show a small contribution to the HOMO and LUMO. Detailed explanations were discussed as below: -

Table 4.17 shows that ancillary ligands have contributed to the electronic properties of complexes **IR1** and **IR3.** Both substituents, 2,6-difluorobenzyl and 4-methylbenzyl, gave almost similar percentage contributions towards the Intra-Ligand Charge Transfer (ILCT) and Ligand to Ligand Charge Transfer (LLCT). However, the biggest percentage of H-5→L+1 (**IR1**: 44%, **IR3**: 65%) only shows a contribution of 2,6-difluorobenzyl at the HOMO orbital of complex **IR1**. No ancillary ligand involvement is demonstrated in this H-5→L+1 of complex **IR3**.

Table 4.18 shows that the most significant percentage contribution of the electronic transition of complexes **IR1** (43%) and **IR3** (24%) was at H-3→L transition. Both orbitals show a significant ancillary ligand contribution at HOMO orbitals without their respective substituents' involvement, and these transitions are attributed to LLCT. On the contrary, **Table 4.19** shows that ancillary ligands only contributed to complex **IR1**. Both complexes **IR1** and **IR3** were related to MLCT transition, indicating that ancillary ligands have contributed to MLCT transition at a wavelength of 359 nm for complex **IR1**.

To conclude, the percentage of ancillary ligand contribution is more significant in complex **IR1** compared to its counterpart in complex **IR3**. This leads to the conclusion that the substituent of 2,6-difluorobenzyl affected the electronic properties more than the 4-methylbenzyl substituent. However, this substituent's factor only dramatically impacts the LLCT and ILCT compared to the MLCT electronic properties.

Table 4.17

*Detailed Orbital Distribution for the Intense Peak at the Lowest Wavelength of Less than 300 nm Related to **IR1** and **IR3***

IR1			IR3		
λ_{abs} (nm)	**Contribution (%)**	**Transition Description**	**λ_{abs} (nm)**	**Contribution (%)**	**Transition Description**
296	H-5→L+1 (44%)	**ILCT, LLCT:** π(ppy) + π(F_2B)→ π*(ppy) 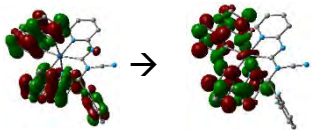	300	H-5→L+1 (65%)	**ILCT, LLCT:** π(ppy) →π*(ppy) 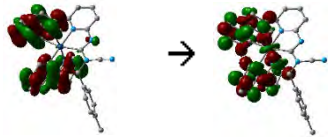
	H-5→L (3%)	**ILCT, LLCT:** π(ppy) + π(F_2B)→π*(ppy) + π*(Fa) 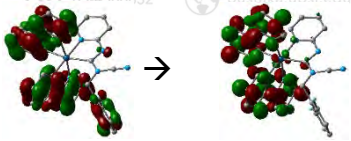		H-5→L (5%)	**ILCT, LLCT:** π(ppy) → π*(ppy) 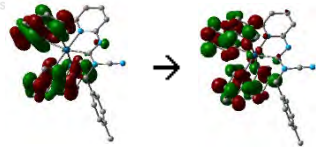
	H-5→L+2 (7%)	**ILCT, LLCT:** π(ppy) + π(F_2B)→ π*(ppy) + π*(PyFa) 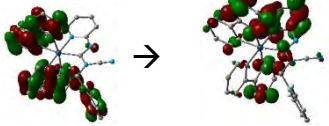		H-7→L (4%)	**ILCT, LLCT:** π(phenyl)(MBPyFa)→ π*(ppy) 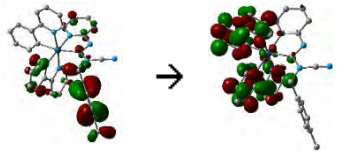
	H-3→L+2 (3%)	**ILCT, LLCT:** π(PyFa)→ π*(ppy) + π*(PyFa) 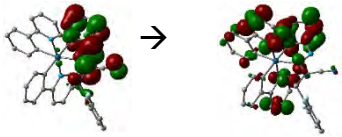		H-7→L+1 (3%)	**LLCT:** π(phenyl)(MBPyFa) → π*(ppy) 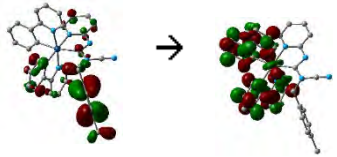

ppy= phenylpyridine, pyfa=pyridinylformimidamide, F_2B= difluorobenzyl, MB= methylbenzyl, H= HOMO, L= LUMO

Table 4.18

*Detailed Orbital Distribution for the Shoulder Peak Above 300 nm Related to **IR1** and **IR3***

IR1			IR3		
λ_{abs} (nm)	**Contribution (%)**	**Transition Description**	**λ_{abs} (nm)**	**Contribution (%)**	**Transition Description**
329	H-3→L (43%)	**LLCT:** π(PyFa) →π*(ppy)(Fa) 	334	H-3→L (24%)	**LLCT:** π(CNPyFa) →π*(ppy) 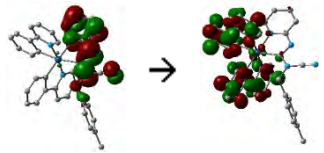
	H-2→L+1 (19%)	**MLCT:** d(Ir) + π(ppy)(Fa) → π*(ppy) 			
	H-2→L+2 (9%)	**MLCT:** d(Ir) + π(ppy)(Fa) → π*(ppy) + π*(PyFa) 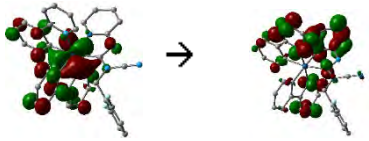		H-5→L+2 (4%)	**ILCT, LLCT:** π(ppy) → π*(ppy) + π*(CNpyfa) 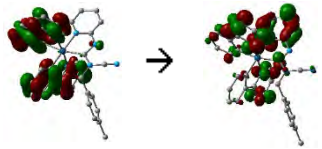
	H-1→L+2 (4%)	**MLCT:** d(Ir) + π(ppy)(PyFa) →π*(ppy) + π*(PyFa) 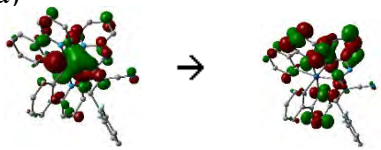			

ppy= phenylpyridine, pyfa=pyridinylformimidamide, F_2B= difluorobenzyl, MB= methylbenzyl, H= HOMO, L= LUMO

Table 4.19

*Detailed Orbital Distribution for the Structureless Peak at the Lowest Lying Wavelength Related to **IR1** and **IR3***

IR1			IR3		
λ_{abs} (nm)	**Contribution (%)**	**Transition Description**	**λ_{abs} (nm)**	**Contribution (%)**	**Transition Description**
359	H-1→L+1 (33%)	**MLCT:** d(Ir) + π(ppy)(PyFa) → π*(ppy) 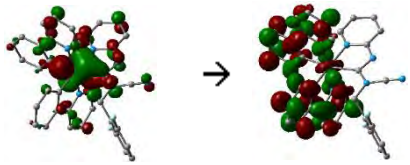	369	H-4→L (2%)	**MLCT:** d(Ir) + π(phenyl)(CNPyFa) → π*(ppy) 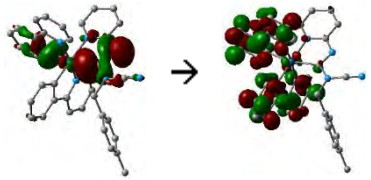
	H-1→L+2 (55%)	**MLCT:** d(Ir) + π(ppy)(PyFa) →π*(ppy) + π*(PyFa) 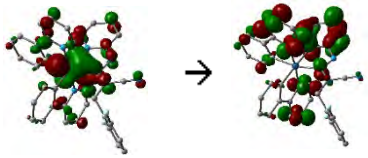		H-1→L (90%)	**MLCT:** d(Ir) + π(ppy)(CNPyFa) →π*(ppy) 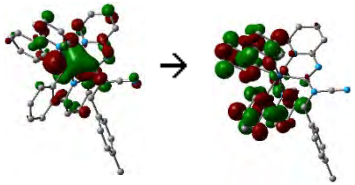

ppy= phenylpyridine, pyfa=pyridinylformimidamide, F_2B= difluorobenzyl, MB= methylbenzyl, H= HOMO, L= LUMO

4.5.5.2 The Detail Comparison of Molecular Orbital Contribution of Complexes IR2 and IR4

Table 4.20–4.22 shows the detailed orbital distribution for all the transitions involved in complexes **IR2** and **IR4**. As previously discussed, ancillary ligands in complexes **IR2** and **IR4** did not destabilise the LUMO orbital in the longest wavelength of the ground state (S_0). The FMO analysis shows that the ancillary ligand contributed to the HOMO and LUMO of all the transitions of LLCT, ILCT, and MLCT, as shown in **Table 4.20–4.22**. By differing the substituent of 2,6-difluorobenzyl and methylbenzyl, the percentages of MO contribution in all transitions of ILCT, LLCT, and MLCT were higher in complex **IR4** compared to complex **IR2** for all the electronic transitions presented in **Tables 4.20–4.22**.

To conclude the FMO analysis, ancillary ligands contribute to the electronic properties of all the synthesised complexes **IR1**–**IR4**. However, the role of the ancillary ligand is to stabilise the LUMO orbitals rather than destabilise them. The substituents on the ancillary ligand did not show significant properties of EWG and EDG effect towards the synthesised complexes **IR1**–**IR4**. Finally, the significant band gap energy of complexes **IR2** and **IR4** was attributed to the MLCT transition at the highest wavelength of absorptivity and strongly correlated to the presence of a fluorine atom at the cyclometallating ligand.

Table 4.20

*Detail Orbital Distribution for the Intense Peak at the Lowest Wavelength of Less than 300 nm Related to **IR2** and **IR4***

IR2			IR4		
λ_{abs} (nm)	**Contribution (%)**	**Transition Description**	**λ_{abs} (nm)**	**Contribution (%)**	**Transition Description**
	H-3→L+2 (19%)	**LLCT:** π(CNPyFa) → π*(F_2ppy) + π*(Pyridine of PyFa) 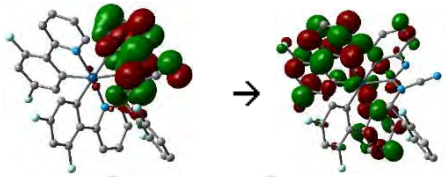		H-5→L (48%)	**ILCT, LLCT:** π(F_2ppy) → π*(F_2ppy) + π*(F_2ppy) (CNPyfa) 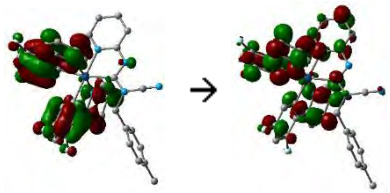
286	H-5→L+2 (29%)	**ILCT, LLCT:** π(F_2ppy) → π*(F_2ppy) + π*(Pyridine of PyFa) 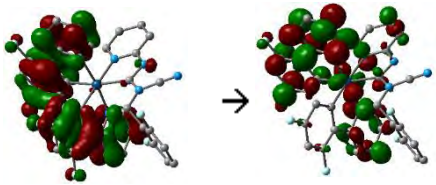	290	H-6→L+2 (2%)	**ILCT, LLCT:** d(Ir) + π(F_2ppy) → π*(F_2ppy) (MB & Pyridine of Pyfa) 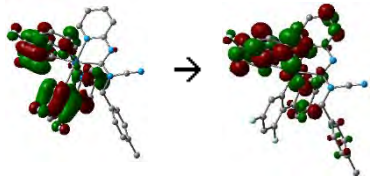
	H-5→L+1 (18%)	**ILCT, LLCT:** π(F_2ppy) → π*(F_2ppy) + π*(Pyridine of PyFa) 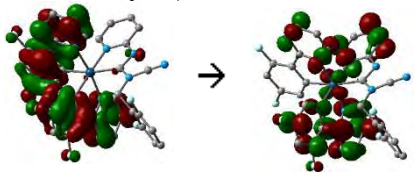		H-3→L+3 (7%)	**MLCT:** d(Ir) + π(F_2ppy) (Fa) → π*(F_2ppy) + π*(F_2ppy) (MB) 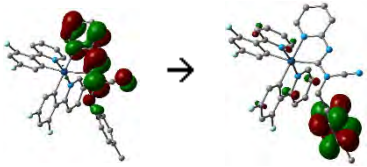

F_2ppy= 2,6-difluorophenylpyridine, pyfa=pyridinylformimidamide, F_2B= difluorobenzyl, MB= methylbenzyl, H= HOMO, L= LUMO

Table 4.21

*Detail Orbital Distribution for the Shoulder Peak above 300 nm Related to **IR2** and **IR4***

IR2			IR4		
λ_{abs} (nm)	**Contribution (%)**	**Transition Description**	**λ_{abs} (nm)**	**Contribution (%)**	**Transition Description**
324	H-2→L+2 (36%)	**MLCT:** d(Ir) + π(F_2ppy) (Fa) → π*(F_2ppy) + π*(Pyridine of PyFa) 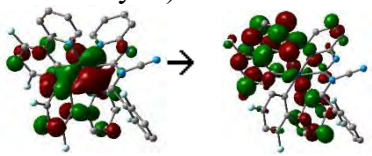	323	H-2→L+1 (56%)	**LLCT:** d(Ir) + π(F_2ppy) (Fa) → π*(F_2ppy) (MB & Pyridine of Pyfa) 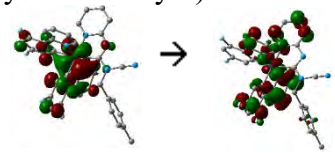
	H-3→L+3 (7%)	**LLCT:** π(CNPyFa) →π*(pyridine)(Fa) 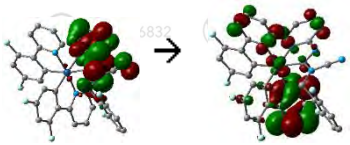		H-6→L (9%)	**LLCT:** d(Ir) + π(F_2ppy) → π*(F_2ppy) + π*(F_2ppy) (CNPyfa) 
	H-3→L+1 (2%)	**LLCT:** π(CNPyFa) → π*(F_2ppy) + π*(Pyridine of PyFa) 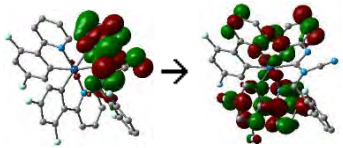		H-3→L (4%)	**MLCT, LLCT:** π(CNPyFa)→ π*(F_2ppy) + π*(F_2ppy) (CNPyfa) 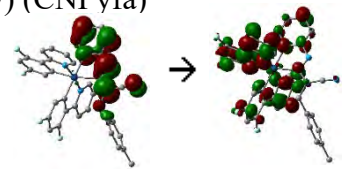
	H-1→L+2 (7%)	**MLCT, LLCT:** d(Ir) + π(F_2ppy) (CNPyFa) → π*(F_2ppy) + π*(Pyridine of PyFa) 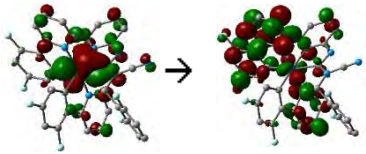		H-2→L+2 (10%)	**MLCT, LLCT:** d(Ir) + π(F_2ppy) (Fa) → π*(F_2ppy) (MB & Pyridine of Pyfa) 

F_2ppy= 2,6-difluorophenylpyridine, pyfa=pyridinylformimidamide, F_2B= difluorobenzyl, MB= methylbenzyl, H= HOMO, L= LUMO

Table 4.22

*Detail Orbital Distribution for the Structureless Peak at the Lowest Lying Wavelength Related to **IR2** and **IR4***

IR2			IR4		
λ_{abs} (nm)	**Contribution (%)**	**Transition Description**	**λ_{abs} (nm)**	**Contribution (%)**	**Transition Description**
349	H-1→L+1 (66%)	**MLCT, LLCT:** d(Ir) + π(F_2ppy) (CNPyFa) → π*(F_2ppy) + π*(Pyridine of PyFa) 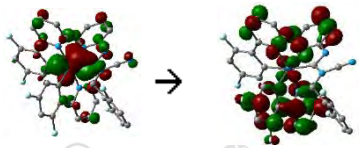	352	H-1→L+1 (85%)	**MLCT, LLCT:** d(Ir) + π(F_2ppy) (Fa) → π*(F_2ppy) (MB & Pyridine of Pyfa) 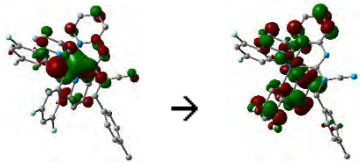
	H-2→L+2 (4%)	**MLCT, LLCT:** d(Ir) + π(F_2ppy) (Fa) → π*(F_2ppy) + π*(Pyridine of PyFa) 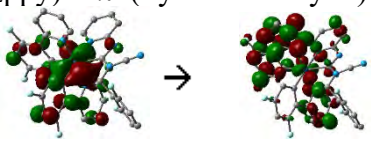		H-1→L+2 (5%)	**MLCT, LLCT:** d(Ir) + π(F_2ppy) (Fa) → π*(F_2ppy) (MB & Pyridine of Pyfa) 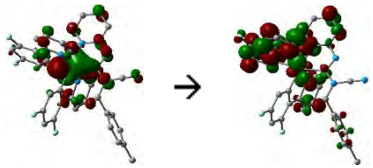
	H→L+1 (2%)	**MLCT, LLCT:** d(Ir) + π(F_2ppy) (PyFa) →π*(F_2ppy) + π*(Pyridine of PyFa) 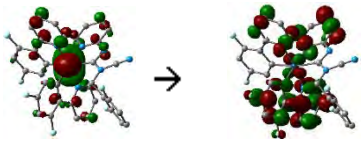			

F_2ppy= 2,6-difluorophenylpyridine, pyfa=pyridinylformimidamide, F_2B= difluorobenzyl, MB= methylbenzyl, H= HOMO, L= LUMO

4.6 Structural Properties: Comparison Between Single-Crystallographic and Theoretical DFT Study

Structural properties play an essential role in investigating newly synthesised inorganic compounds, especially in defining their potential applications. In this subchapter, the investigation aimed to bridge the experimental and theoretical data related to molecular structure variables such as bond distances and bond angles. The experimental data extracted from the single crystallographic XRD analysis have been compared to the theoretical data from the Density Functional Theory (DFT) calculation. Since the complexes studied in this research are a new class of iridium(III) complexes, it is important to have a comparison discussion between the experimental and theoretical data to have an insightful view of how these complexes behave in their structural aspects.

4.6.1 Behaviour of Molecular Structure between Experimental and Theoretical Data

Figures 4.37–4.40 show the comparison of the molecular structure between single crystallographic and their respective optimised structures from the DFT calculations. For the comparison perspectives, the optimised DFT structures of each complex **IR1**–**IR4** showed compatible results that were almost similar to their respective experimental crystallographic structures. Both crystal structures and DFT have two phenylpyridine rings occupied by the cyclometallating moiety that are not planar to each other. However, the phenyl and the pyridine were in the planar position. Two phenylpyridine ligands occupied the coordination sphere in the axial position (N1/Ir1/N2), making the complexes coordinated in the *trans*-position of octahedral geometry (**Figure 4.41**). However, significant differences in the *trans*-behaviour of two phenylpyridines can be

obviously seen. Each complex has a different way of how two phenylpyridine ligands have occupied the cyclometallating moiety, and the differences are simplified in **Table 4.23** by showing different types of bonds to visualise the behaviour into or out of the plane.

Figure 4.37

Left: *ORTEP diagram of the crystal structure Ir(ppy)$_2$(CNF$_2$BPyfa),* ***IR1*** *complex drawn with 50% probability ellipsoid.* ***Right;*** *the optimised calculated structure for Ir(ppy)$_2$(CNF$_2$BPyfa),* ***IR1*** *complex using DFT*

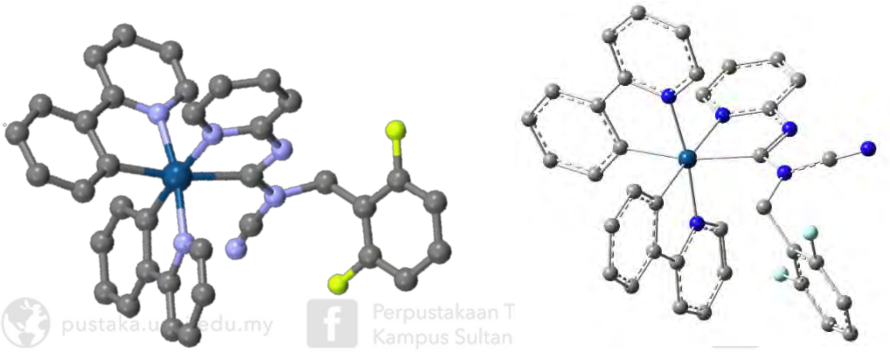

Figure 4.38

Left: *ORTEP diagram of the crystal structure Ir(F$_2$ppy)$_2$(CNF$_2$BPyfa),* ***IR2*** *complex drawn with 50% probability ellipsoid.* ***Right;*** *the optimised calculated structure for Ir(F$_2$ppy)$_2$(CNF$_2$BPyfa),* ***IR2*** *complex using DFT*

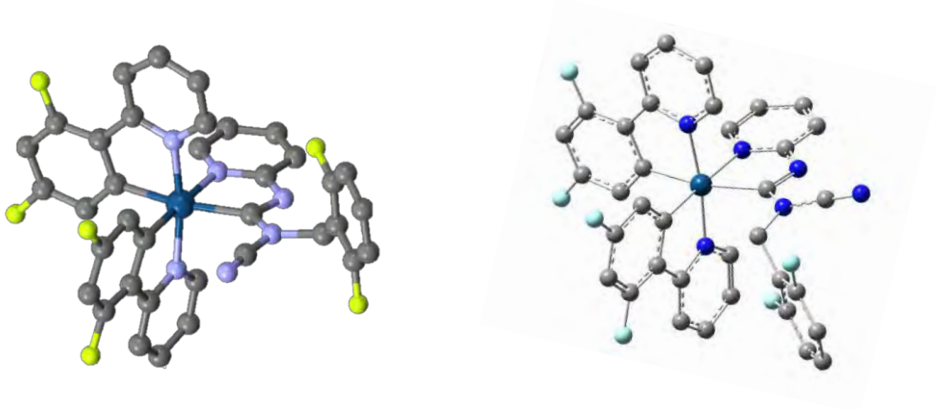

Figure 4.39

Left: *ORTEP diagram of the crystal structure Ir(ppy)$_2$(CNMBPyfa),* ***IR3*** *complex drawn with 50% probability ellipsoid.* ***Right;*** *the optimised calculated structure for Ir(ppy)$_2$(CNMBPyfa),* ***IR3*** *complex using DFT*

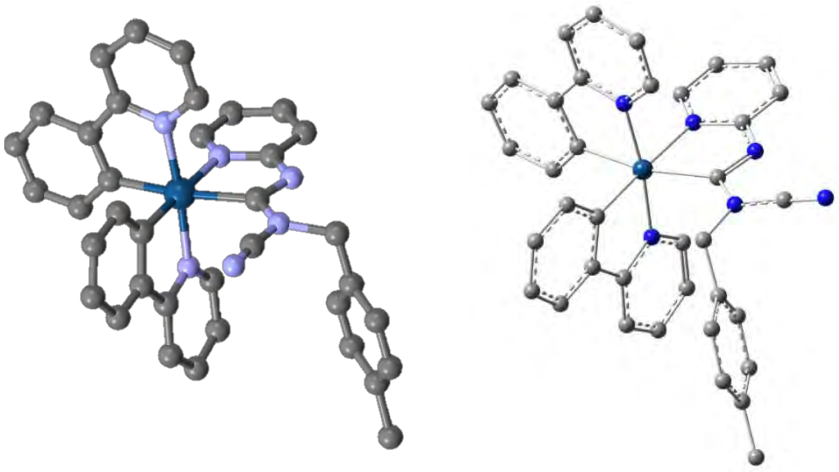

Figure 4.40

Left: *ORTEP diagram of the crystal structure Ir(F$_2$ppy)$_2$(CNMBPyfa),* ***IR4*** *complex drawn with 50% probability ellipsoid; the dichloromethane solvate was omitted for clarity.* ***Right;*** *the optimised calculated structure for Ir(F$_2$ppy)$_2$(CNMBPyfa),* ***IR4*** *complex using DFT*

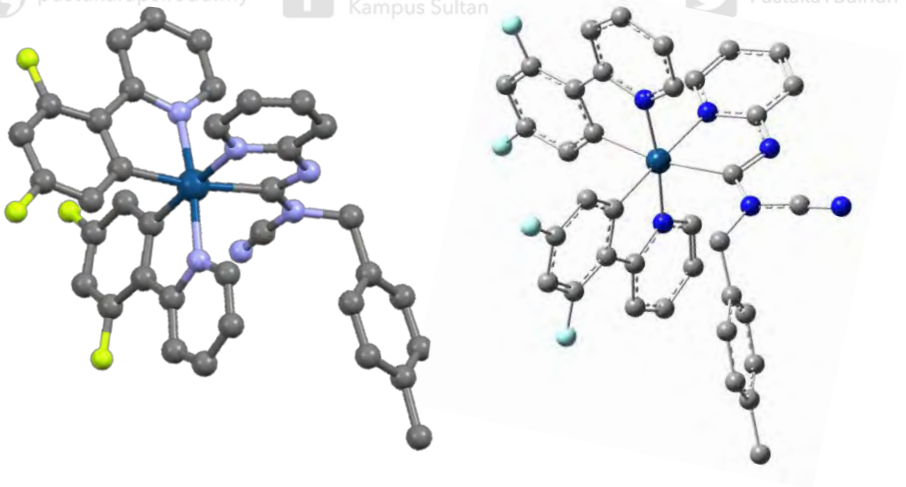

In addition, the position of nitrile C29≡N6 (**Figure 4.41**) in all complexes **IR1**–**IR4** has very significant differences between the experimental and theoretical positions. It can be seen that C29≡N6 in a single crystal has a bigger angle deviation compared to the starting ligand and the optimised DFT structure. This deviation is

already expected to happen due to the neglect of the solvation effect in the computational calculation for time efficiency purposes.

Table 4.23

Comparison of Different Orientations of Phenylpyridine Moiety Between Single Crystal and DFT Optimisation Structures
(C^N= ppy cyclometallating ligand, L^X= pyfa ancillary ligand)

Complexes	Single crystal	DFT
IR1	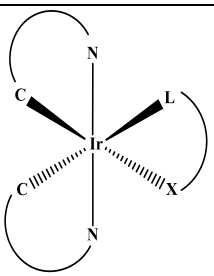	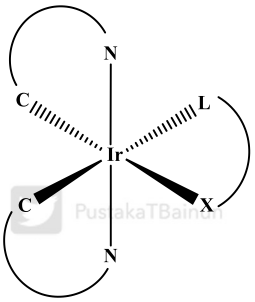
IR2		
IR3	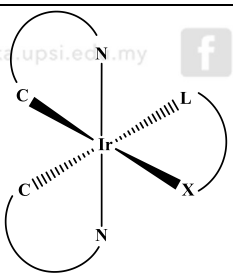	
IR4		

Figure 4.41

The simplified drawing of all complexes with schematic numbering. The different behaviour of substituents attached to formimidamide-based ancillary ligands between the crystal and the DFT structures was drawn for better comparison

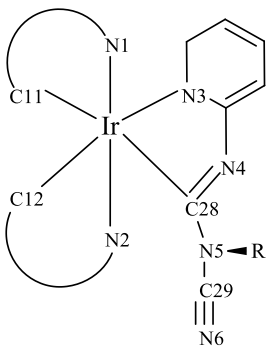

Simplified crystal structures

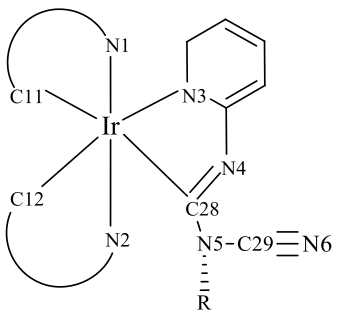

Simplified DFT structures

To better understand the occurrence of this behaviour, detailed structural optimisation has been calculated in DFT using complex **IR2** to study the electronic energy of each designed geometry complex formation. This electronic energy investigation was designed to answer the question of why the angle of N5–C29–N6) behaves differently between experimental and theoretical. A series of complex **IR2** was designed and drawn as **IR2(a)**, **IR2(b)** and **IR2(c)**. The CiF file of complex **IR2** was successfully optimised, and the output file was used to design complexes **IR(b)** and **IR(c).** The design of the ancillary ligand differed in the nitrile arrangement to confirm that the angle of N6–C4≡N5 (**Figure 4.42**) deviates wider, approaching 180° in the synthesised complex. All the geometries were successfully optimised and all the xyz coordinates are attached in the **Appendices S12–S14**.

Figure 4.42

*Optimised DFT structures of complex **IR2** with differences like nitrile position in the ancillary ligand*

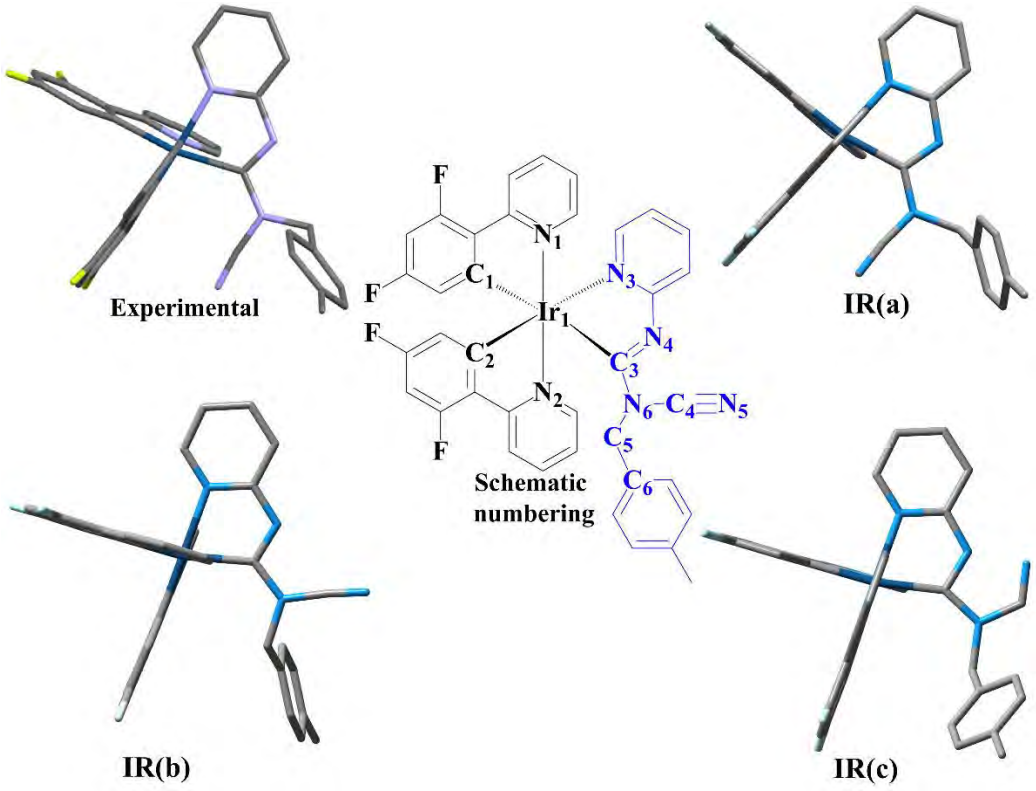

Table 4.24

Geometrical optimisation parameters

Complex	IR(a)	IR(b)	IR(c)
Electronic energy (Kcal mol^{-1})	-1416541	-1416535	-1416497
Dipole moment (Debye)	8.80	3.57	4.66
Polarizability, α (a.u.)	487.76	477.81	480.86

The geometrical optimisation structure, together with the numbering scheme shown in **Figure 4.42,** reveals that all complexes adopt a trans-octahedral orientation, with N1/Ir1/N2 positioned along the same axial line, and the two 2,4-difluorophenylpyridine ligands are not co-planar. **Table 4.24** shows complex **IR(a)** has the lowest energy at -1,416,541 kcal mol^{-1}, while complex **IR(c)** has a 44 kcal mol^{-1} higher energy, at -1,416,497 kcal mol^{-1}. The minimum electronic energy of **IR(a)** represents the most stable state of the complex, assuming no external forces or thermal effects (Zulkarnaen et al., 2025). This aligns with experimental observations, as complex **IR(a)** most closely resembles the experimental crystallographic structure, maintaining the same N6–C4≡N5 position, with the benzyl substituent positioned out of the plane through carbon C5. Hence, this geometrical optimisation supported the structural properties of why C4≡N5 did not maintain the cyclic position, such as complex **IR(c)**.

Another significant outcome from this calculation is that complex **IR(b)**, which has a similar N6–C4≡N5 bond angle, shows only a 6 kcal mol^{-1} higher energy than complex **IR(a)**. The optimised structure of **IR(b)**, obtained from a raw-drawn geometry, deviates only slightly from the experimental single-crystal structure of **IR(a)**. This

small difference in electronic energy supports the validity of all DFT calculations conducted in this study. This result strongly supports the decision to use raw, idealised geometries as the starting point for DFT calculations rather than coordinates derived from CIF files. This approach avoids biasing the theoretical optimisation toward the experimental crystal structure, which may be influenced by packing forces, solvent interactions, or crystal-field distortions, none of which are present in the gas-phase environment assumed in DFT. By constructing the geometry manually, any structural deviations observed during optimisation reflect the molecule's true electronic and steric preferences, rather than adaptations to the solid-state environment (X. Li et al., 2011; Mitani et al., 2020). This strategy is particularly relevant in this work, as the complexes feature a new class of ancillary ligands whose flexible coordination and spatial conformations may be restricted in the crystal but are more freely expressed under vacuum conditions in DFT. As a result, the comparison between DFT-optimised and experimental geometries becomes more meaningful and provides clearer insights into the behaviour of the ligands in isolated conditions.

4.6.2 Comparison of Bond Angles and Bond Distances between the Experimental and Theoretical Data

The bond angle and bond length of the experimental and computational were analysed. All the selected bond angles (°) and bond lengths (Å) for complexes **IR1**–**IR4** were summarised in **Table 4.25.** The results complied with each other with tiny differences, except, as mentioned in the previous **subtopic 4.6.1,** that related to the bond angle of nitrile C29≡N6 in ancillary moieties.

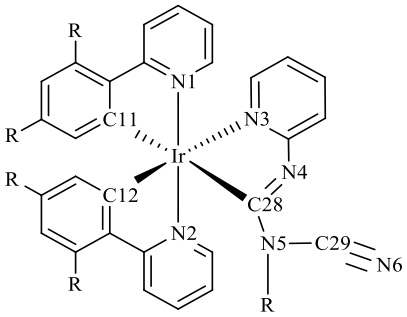

Table 4.25

Comparison of Experimental and Theoretical Data for Selected Bond Angle (°) and Bond Length (Å)

Complex	Bond length (Å)							
	IR1		IR2		IR3		IR4	
	Exp	Calc	Exp	Calc	Exp	Calc	Exp	Calc
Ir–C11	2.059	2.070	2.053	2.068	2.023	2.069	2.058	2.067
Ir–C12	2.000	2.026	2.012	2.022	2.047	2.027	2.018	2.023
Ir–C28	2.109	2.147	2.090	2.143	2.104	2.149	2.072	2.147
Ir–N1	2.046	2.090	2.051	2.089	2.051	2.088	2.042	2.086
Ir–N2	2.053	2.069	2.044	2.069	2.071	2.071	2.046	2.070
Ir–N3	2.138	2.197	2.119	2.190	2.112	2.198	2.125	2.191
C28–N4	1.316	1.341	1.318	1.339	1.346	1.343	1.316	1.340
C28–N5	1.400	1.427	1.401	1.424	1.345	1.424	1.415	1.421
C29–N5	1.350	1.357	1.349	1.357	1.326	1.358	1.335	1.358
N6–C29	1.136	1.166	1.136	1.165	1.156	1.165	1.142	1.165
Complex	**Bond Angle (°)**							
	IR1		IR2		IR3		IR4	
	Exp	Calc	Exp	Calc	Exp	Calc	Exp	Calc
N1 Ir C11	80.2	79.4	79.7	79.4	80.2	79.4	80.0	79.4
C12 Ir1 N2	80.2	79.9	80.4	80.0	82.0	79.9	80.2	80.0
C28 Ir1 N3	74.9	74.4	75.2	74.5	76.7	74.4	75.2	74.5
N1 Ir1 N2	170.6	172.6	171.1	172.6	174.7	173.0	173.3	173.0
C12 Ir1 N3	176.2	176.4	176.4	176.6	178.3	176.5	176.3	176.6
C11 Ir1 C28	168.6	166.4	168.9	166.7	170.0	166.8	168.8	167.2
N6 C29 N5	171.0	174.6	173.2	174.6	172.9	174.8	172.7	174.7

It can be said that DFT calculations supported the experimental data without any significant deviation from the experimental structural properties. All bond lengths also complied with the types of bonds in the crystallographic and optimised structures of **IR1**–**IR4**. The coefficient correlation graph between the experimental and DFT of bond length and bond angle for complex **IR1** is shown in **Figures 4.43** and **4.44.** The other complexes, **IR2**–**IR4,** resemble the positive correlation graph similar to complex **IR1**, as shown in **Figures 4.43** and **4.44**. The R values for all synthesised complexes approach ~1.0 (R for bond length; **IR2**= 0.99, **IR3**= 0.99 and **IR4**= 0.98, while R for bond angle; **IR2**= 0.97, **IR3**= 0.97 and **IR4**= 0.98).

Figure 4.43

*Correlation between experimental and theoretical **bond length** of complex **IR1**, R=0.99*

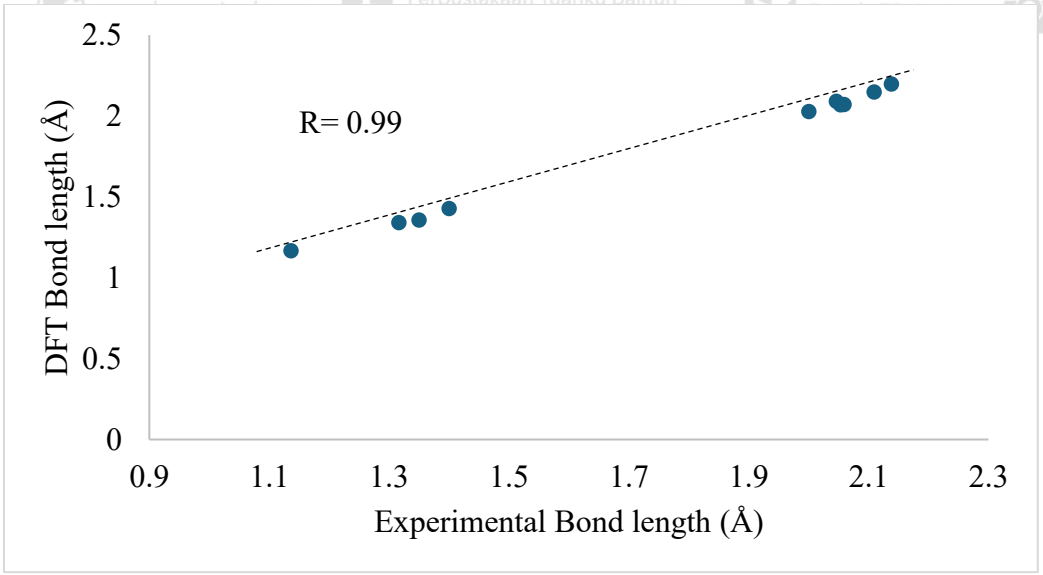

Figure 4.44

Correlation between experimental and theoretical ***bond angle*** *of complex* ***IR1****, R=0.97*

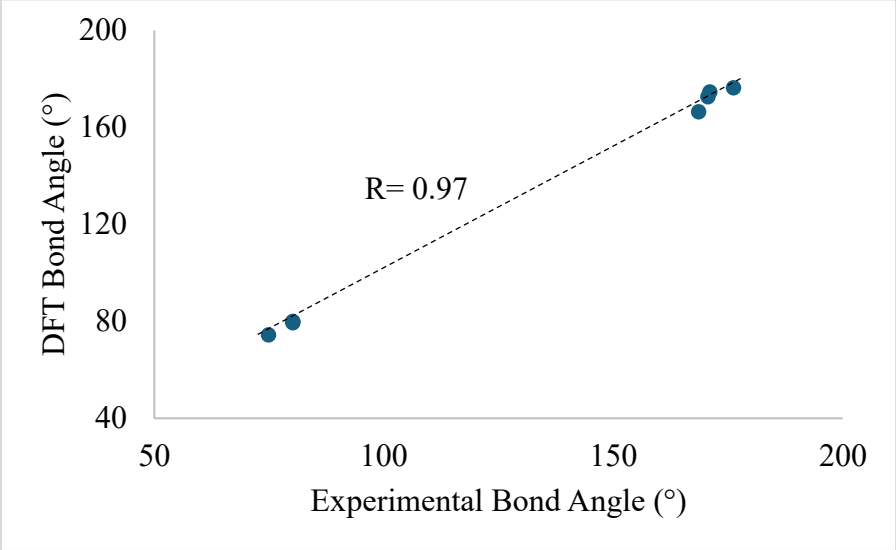

The influence of various substituents is evident in some minor but consistent variations in bond lengths and angles across **IR1**–**IR4**. Complexes **IR2** and **IR4**, which both incorporate electron-withdrawing fluorine atoms on the cyclometallating phenyl rings, exhibit slightly shorter Ir–C and Ir–N bond distances and narrower bond angles involving these donor atoms. This trend once again reflects the inductive effect of fluorine, pulling electron density away from the metal centre and causing a subtle tightening of the coordination geometry (He et al., 2016). In contrast, complex **IR3** and **IR4**, which feature a 4-methylbenzyl group on the ancillary ligand, show marginally wider angles such as C12–Ir–N2 and C11–Ir–C28 compared to their fluorinated counterparts, likely due to increased steric bulk from the methyl substituent pushing ligands further apart.

Another notable observation from **Table 4.25** is the consistent elongation and linearity of the nitrile moiety, particularly in the N6–C29 bond and the N6–C29–N5 bond angle. Across all four complexes, the N6–C29 bond length remains nearly identical between experimental (1.136–1.156 Å) and theoretical (1.165 Å) values, confirming the strong triple bond character regardless of substitution. Hence confirmed that the complexation between the iridium atom and the anchillary ligand occurred successfully. Additionally, the N6–C29–N5 bond angle shows excellent agreement with calculated values, ranging from 171.0° to 173.2° experimentally and 174.6° to 174.8° computationally. This suggests that the linear geometry of the nitrile group is preserved in all complexes, and only minimally affected by either electron-withdrawing fluorine atoms (**IR2**, **IR4**) or electron-donating methyl groups (**IR3**, **IR4**). Such results indicate that the nitrile group behaves as a rigid structural motif in the ancillary ligand and is electronically insulated from peripheral substituents, thereby maintaining its geometry across different environments.

In addition to the effects discussed, the consistently compressed C28–Ir–N3 bite angles (~74.4–76.7°) across **IR1**–**IR4** highlight the geometric strain imposed by the bidentate formimidamide ligand. The widest angle observed in **IR3** suggests a slight relaxation due to the electron-donating nature of the 4-methylbenzyl group and the absence of fluorine atoms, supporting the role of substituent flexibility in modulating chelation strain. Lastly, the deviations in *trans* angles, such as N1–Ir–N2 and C12–Ir–N3, reflect the varying trans influence across complexes. The more linear geometry in **IR3** and **IR4** may arise from the reduced electron-withdrawing character of methyl versus fluorine substituents, allowing a more relaxed coordination axis.

4.7 Reaction Mechanism Investigations of a Synthetic Pathway of the Complex

As the chemical analysis and spectroscopic studies have successfully proved the development of a novel iridium(III) complex with pyridinylformimidamide-based ancillary ligand, the reaction mechanism investigation has been conducted to study the way of binding mechanism between the starting ligand and the dimer precursor. Since all complexes have almost similar chemical analyses, only complex **IR4** was selected to further investigate using DFT for time efficiencies, as the results will resemble the other synthesised complexes **IR1**–**IR3**. In the beginning, triazole was chosen to manipulate the electrochemical and spectroscopic properties of this iridium (III) complex towards higher emission energy (Ahn et al., 2011; Khomenko et al., 2015; Omae, 2016), thus making related triazolium salts be used as precursors to *N*-heterocyclic carbenes (NHC) ligands (K. Lin et al., 2014; Strassner et al., 2013). However, the previous spectroscopic analysis supported by X-ray crystallographic study on a single crystal showed that the starting NHC-based ancillary ligand of (2-(4-methylbenzyl)-1*H*-1,2,4-triazol-1-yl)pyridine, (**Mbpyta**), had become an acyclic formimidamide ligand (**CNMbpyfa**) when cleaving bidentately to iridium in the complex formation. In this paper, we report a comprehensive mechanistic study to explain the reaction mechanisms behind this phenomenon, as no high-level computations have yet been performed to determine the mechanism of formimidamide intermediates formation emerging from triazolium salt precursor in iridium complex formation. To the best of our knowledge, the previous studies only report the mechanistic study involving imidazolium salt (Mitani et al., 2020; Vellé et al., 2017; X. Zhang et al., 2019), such as the formation of iridium (III) complexes involving imidazole ligands typically taking place through a transmetallation route, as shown in **Scheme 4.4**.

Scheme 4.4

General schematic of the transmetallation route in the presence of metal oxide (M_2O) for the formation of metal complex

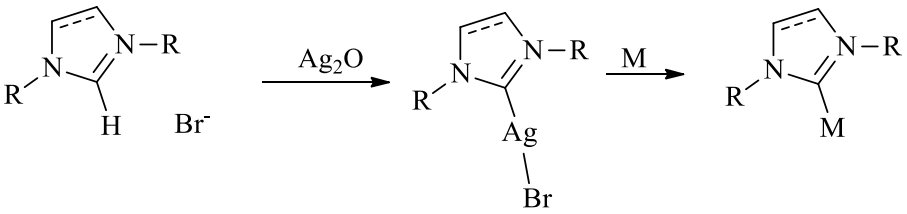

In the case of five-membered rings of a heterocyclic compound such as 1*H*-1,2,4-triazolium salt, the presence of silver(I) oxide (Ag_2O) provides favourable conditions in the experimental synthesis stage, encouraging both carbons in the triazole ring to deprotonate, forming a silver-formimidamide intermediate complex as depicted in **Scheme 4.5**. This condition was contradicted by the imidazole ring that can only deprotonate at one carbon atom (**Scheme 4.4**) (Martynova et al., 2021).

Scheme 4.5

*A schematic pathway for the synthesis of complex **IR4** with the formation of the silver-formimidamide intermediate complex*

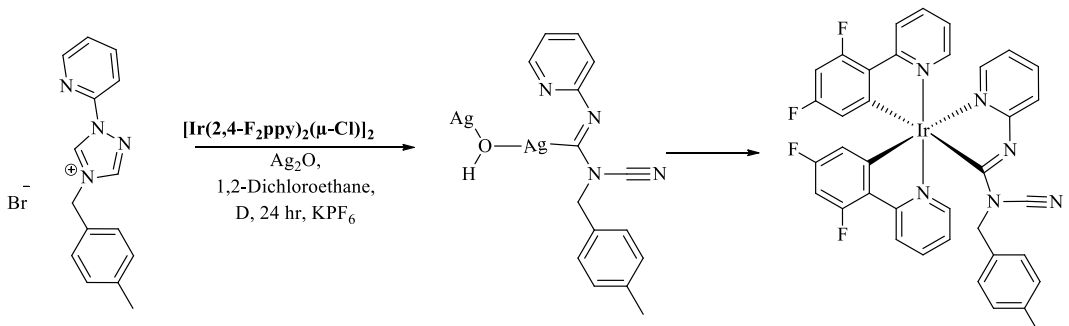

2-(4-methylbenzyl-1,2,4-triazol-1-yl)pyridine , **Mbpyta**

silver-formimidamide intermediate complex.

Complex IR4
Yield = 69%

4.7.1 Proposed Reaction Mechanism for Complex IR4

In the hypothesis, the formation of the silver-formimidamide intermediate complex is proposed in **Figure 4.45** through deprotonation in two stages. The pyridine and triazole rings are co-planar and have resonance properties as their electrons are delocalized to achieve molecular stability. These resonance properties cause an increase in their electron-withdrawing properties, hence facilitating the deprotonation to occur at both carbons of the *1H*-1,2,4-triazolium salt. Consequently, the presence of Ag_2O in the experimental protocol resulted in the strong resonance properties of the pyridine and benzene moieties in Mbpyta, forming an adduct with the Ag_2O (**Figure 4.45(b)**). Thus, electron delocalisation continued in the unsaturated 1*H*-1,2,4-triazolium ring. The positively charged nitrogen of the triazole ring is covalently linked to the pyridine C2, which is electron-deficient. Deprotonation of C3–H was accompanied by the formation of a new π bond between C3–N2 as shown in **Figure 4.45(c)**. The released proton and bromide anion react with the silver oxide to precipitate silver bromide and silver hydroxide, forming another bond with silver and bromide anion and eventually completing the formation of a silver-formimidamide intermediate complex. To confirm these proposed mechanisms, DFT calculations were performed using the ωB97X-D3 functional (Y. S. Lin et al., 2013) and def2-TZVPP basis set (Weigend & Ahlrichs, 2005) implemented in the Q-Chem 5.4 package (Epifanovsky et al., 2021) to provide a theoretical mechanistic study of the role of silver oxide, Ag_2O, in the synthesis of complex **IR4.**

Figure 4.45

A proposed mechanism for the formation of silver-formimidamide intermediate complex affected by the resonance of benzene and pyridine substituents on N1 and N4 of the 1H-1,2,4-triazolium in the presence of Ag_2O

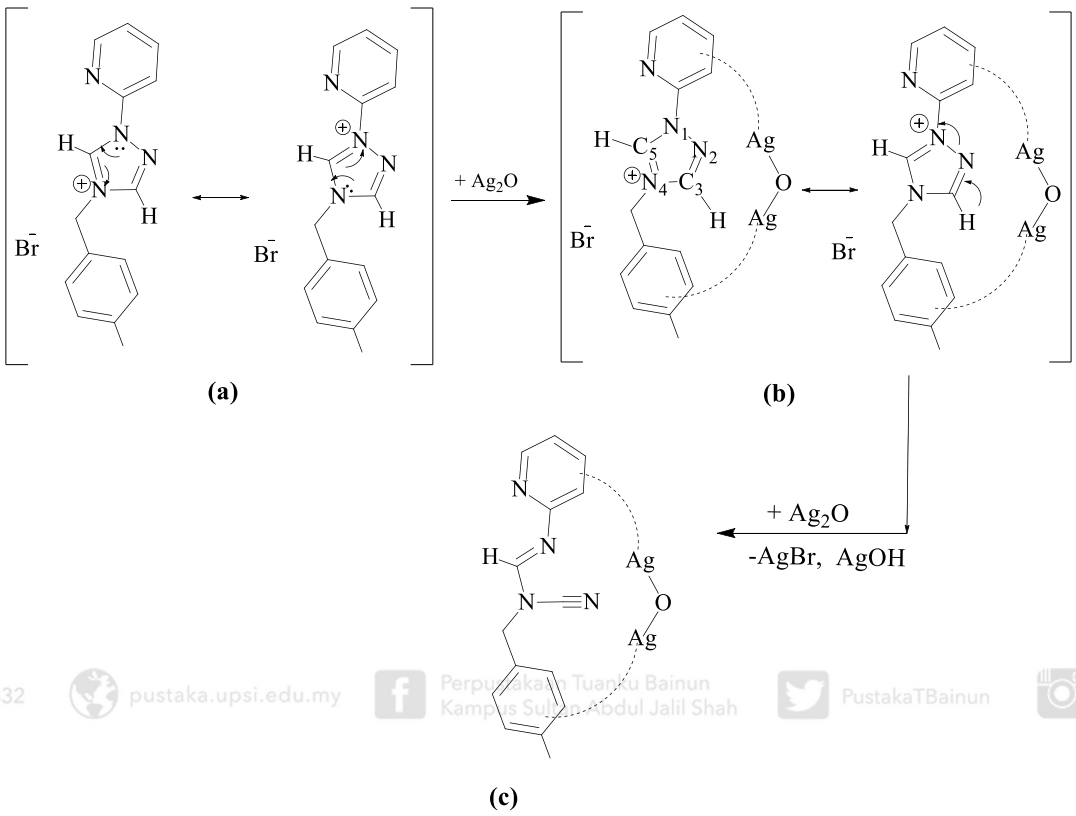

4.7.2 Molecular Electrostatic Potential (MEP) Analysis of Starting Ancillary Ligands

Since the proposed mechanism stated that the resonance properties of the pyridine and benzyl ring of the **Mbpyta** have a big influence on the deprotonation of both carbonic in the triazole ring, DFT calculations have been executed to calculate the Molecular Electrostatic Potential (MEP) of both ligands **Mbpyta** and **F_2bpyta**. The results shown in **Figure 4.46** confirmed that the pyridine ring has the highest electron density, contributing to resonance properties that become one of the factors of why the triazole ring undergoes two stages of deprotonation and hence breaks into pyridine-formimidamide ancillary ligand.

Figure 4.46

The Molecular Electrostatic Potential (MEP) mapped surface studies of starting ligand ***F$_2$bpyta*** *and* ***Mbpyta*** *using DFT calculation*

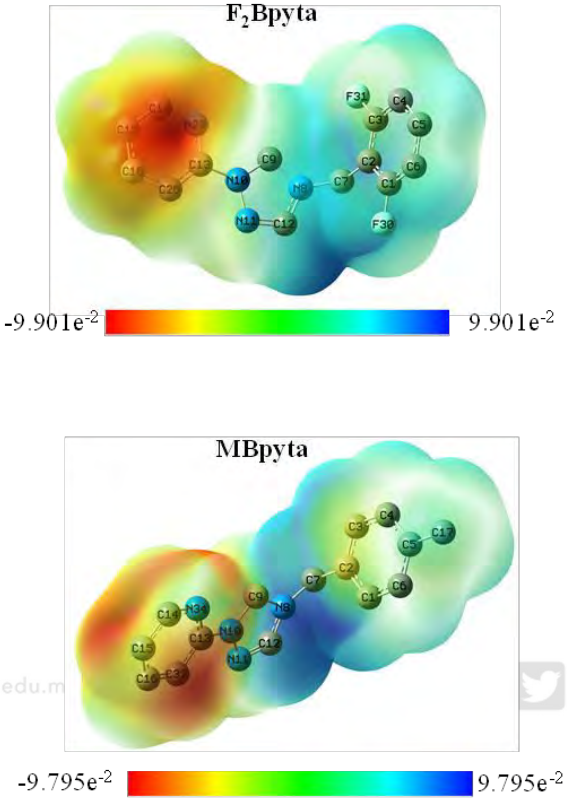

4.7.3 Mechanistic Reaction Mechanism Using Density Functional Theory (DFT) Calculation

To properly analyse the proposed mechanism, a higher level of mechanistic study was employed using DFT to provide a theoretical mechanistic study of the role of silver oxide, Ag_2O, in the synthesis of complex **IR4**. All the calculations. The DFT calculation was compatible with the proposed mechanism, where the presence of Ag_2O as a reactant led to the formation of an acyclic ancillary ligand from the starting cyclic triazole ligand.

Figure 4.47 shows the Gibbs free energy profile diagram with reasonable ranges of calculated energy for optimised intermediates, transition states, product geometry, and critical parameters in the reaction mechanism pathway leading to the silver-formimidamide intermediate complex. The optimised intermediates and transition state structures, together with the key structural parameters on the potential energy surfaces of the title reaction, are detailed in **Figure 4.48** and **Table 4.26**. The zero imaginary frequencies correspond to a local minimum, confirming that the geometries were successfully optimised and all the *xyz* coordinates are attached in the **Appendix S9–S15**. An adduct **(I)** is formed between the starting reactants of ligand MBpyta and Ag_2O, with Ag_2O coordinating across the molecule initially. Upon formation of the first transition state, the aromatic benzyl ring has strong resonance properties that affect the first deprotonation at the transition state ‡**I**, where the ligands **Mbpyta** and Ag_2O form a cyclic structure and lead to a coordinated intermediate **I**. The C4–H1 bond length in transition state ‡**I** was calculated to be 1.287 Å, significantly longer than the typical C–H bond. This elongation reflects the unstable nature of transition state ‡**I**, in which the weak C–H bond interaction facilitated deprotonation of H1 from the triazole ring, as further supported by the formation of intermediate **I**. This intermediate **I** lies above the reactive adduct energy and is highly reactive with unstable properties, leading to the immediate formation of transferring iridium metal to the ligand (Martynova et al., 2021; Scattolin & Nolan, 2020). However, the resonance property of the other pyridyl ring and the presence of another carbon in the triazolium ring prevented the direct cleavage between iridium and the silver-carbene intermediate from occurring. The second transition state ‡**II** emerged as an alternative, where the N4–N5 bond breaks and the electron moves to the neighbouring bond to form a new π bond. As a result, the second intermediate **(**Intermediate **II)**, with a newly formed C4≡N5 bond, has a relative energy

of -31.0 kcal mol^{-1}. The DFT calculation has proved the formation of C4≡N5 **(**Intermediate **II)** from C4=N5 **(**Intermediate **I)** as the bond length decreases from 1.32 Å **(**Intermediate **I)** to 1.15 Å **(**Intermediate **II)**. Concurrently, the N6–C4≡N5 bond angle increases markedly from 107.8° to 175.4°, indicating a geometric reorganisation from the cyclic triazolium structure to an acyclic formimidamide configuration. The near-linear alignment of the C≡N moiety also suggests a substantial out-of-plane displacement relative to its original orientation. Furthermore, the conversion of transition state ‡**II** into intermediate **II** is corroborated by a reduction in the N5–Ag1 bond length, from 2.255 Å to 2.104 Å, which closely aligns with typical N–Ag bond lengths, further supporting the structural assignment of intermediate **II**. Finally, the Br^- counterion substituted one of the Ag–O bonding, implicated one molecule of AgOH to leave the intermediate **II** (the energy of the Br– ion was added to balance the total energy).

Figure 4.47

Energy profile diagram for the silver-formimidamide intermediate complex's reaction mechanism from the silver oxide and ligand ***Mbpyta*** *reactant*

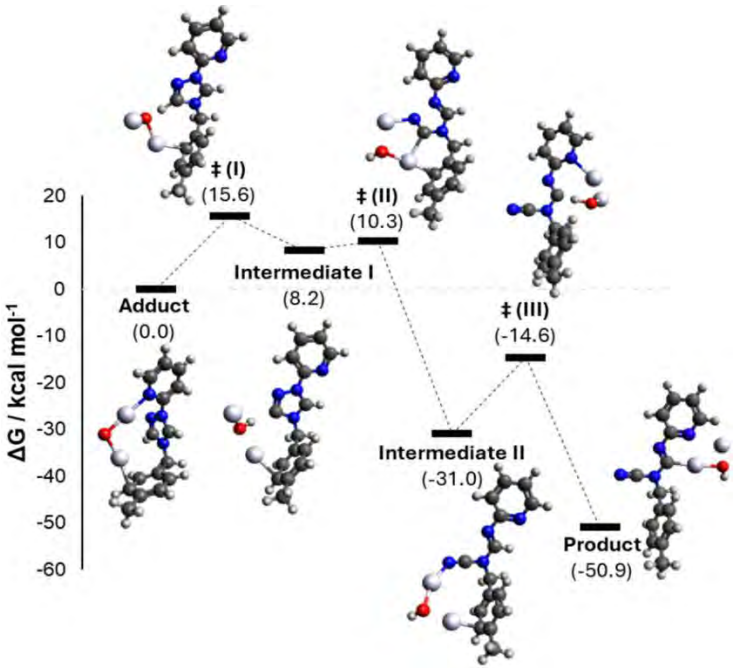

In the final stage, the bond length of C3–H2 was calculated to be 1.352 Å, which is an unusual value for a typical C–H bond, confirming the presence of transition state ‡**III**. Then, a product of the silver-formimidamide intermediate complex has been synthesised from the transition state ‡**III**. This transition state describes the second deprotonation, which occurs at a different carbon atom (C3–H2) of the formimidamide ligand, leading to the cleavage between the ligand and the di-silver hydroxide (Ag_2OH). This step suggests that the same silver species involved in the initial steps continues to participate in the second deprotonation. This interpretation is supported by the experimental conditions, where 0.25 equivalents of Mbpyta ligand and only 0.21 equivalents of Ag_2O were used, yet a 69% yield of the final product was achieved (**Scheme 4.5**), hence implying that a single Ag_2O unit may re-coordinate and function in both deprotonation events. In a broader comparison, the theoretical study by Hayes et al. (2007) demonstrates similar behaviour, in which Ag_2O acts as a bifunctional base capable of promoting two deprotonation events via reactive Ag^+ species (Hayes et al., 2007). Although their model involves separate ligands, the same principle applies here: Ag_2O mediates C–H activation and deprotonation through coordination. The formation of the product silver-formimidamide intermediate has $\Delta_{reac}G$ = -50.9 kcal mol^{-1} relative to the reactants, indicating that the product is thermodynamically favoured and likely to form under experimental conditions. Furthermore, there is no significant difference between the bond length and angle between intermediate **II** and the final product of intermediate, indicating that the second stage of deprotonation did not alter the geometrical structure of the formimidamide-based ligand towards another geometry. The formation of AgOH or Ag_2OH as leaving groups supports the chemical consumption of silver, thereby justifying the effective use of sub-stoichiometric Ag_2O for complete ligand deprotonation (Hayes et al., 2007).

In conclusion, a detailed computational study estimates the DFT level for forming silver-formimidamide intermediates in the synthetic route of the complex $Ir(F_2ppy)_2(CNMbpyfa)$. The DFT calculation was compatible with the proposed mechanism in which the presence of Ag_2O as the reactant strongly affects the formation of acyclic ancillary ligands from the starting cyclic triazole ligand.

Figure 4.48

Molecular structure of adduct, intermediates and transition state, together with a numbering scheme compatible with ***Table 4.26***

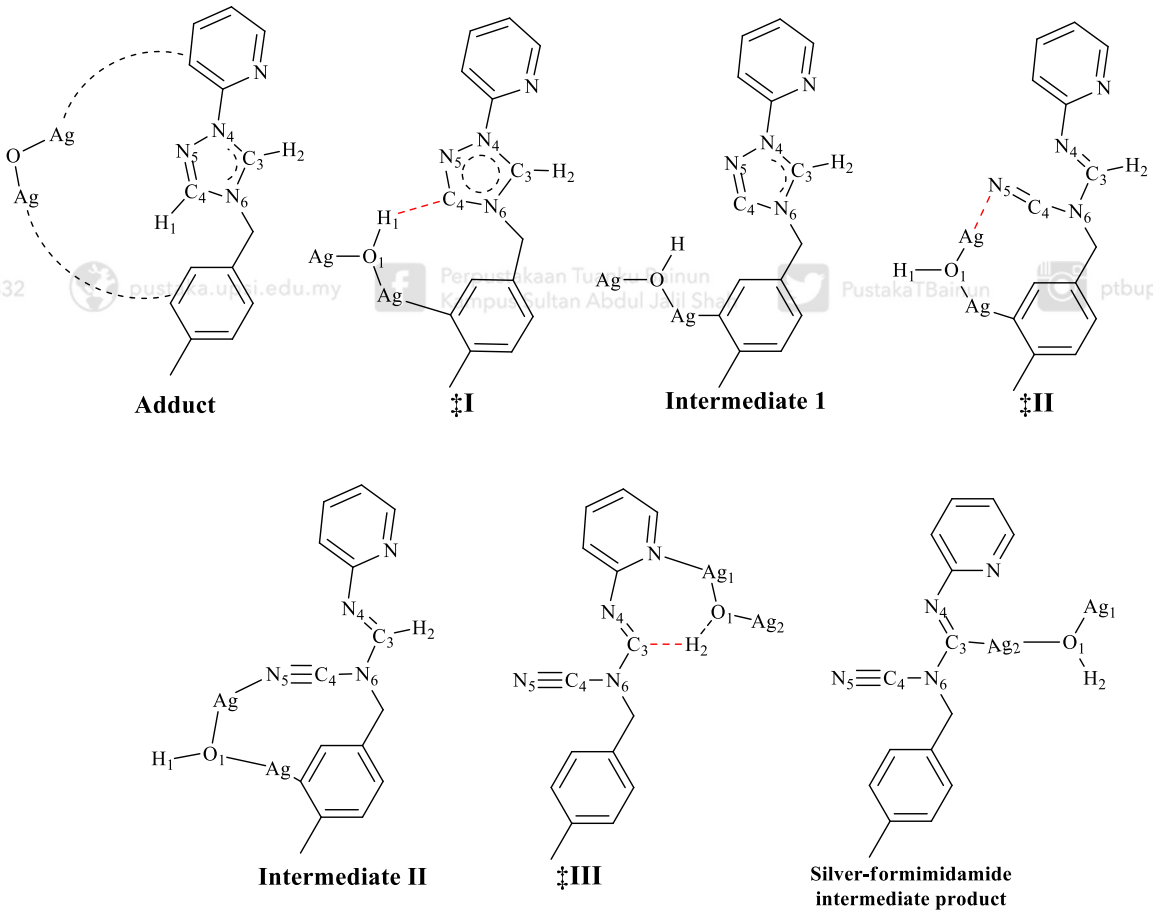

Table 4.26

Bond lengths for all structures involved in the energy profile diagram
*(Each imaginary bonding of transition state ‡I, ‡II and ‡III marked as **)*

Bond stretching	Bond length (Å)						
	Adduct	**‡I**	**Intermediate 1**	**‡II**	**Intermediate 2**	**‡III**	**Product**
N4–C3	1.318	1.316	1.315	1.269	1.259	1.284	1.284
C3–N6	1.328	1.326	1.324	1.370	1.395	1.401	1.412
N6–C4	1.365	1.389	1.407	1.354	1.318	1.334	1.333
C4–N5	1.297	1.308	1.320	1.224	1.153	1.154	1.154
N5–N4	1.354	1.360	1.375	–	–	–	–
C3–H2	1.079	1.077	1.076	1.083	1.088	1.352**	–
C4–H1	1.078	1.287**	–	–	–	–	–
H1–O1	–	1.318	0.982	0.957	0.958	–	–
O1–Ag1	1.992	2.066	2.109	2.180	2.106	2.136	2.129
O1–Ag2	2.013	2.075	2.117	2.168	2.132	2.048	2.109
N5–Ag1	–	–	–	2.255**	2.104	–	–
H2–O1	–	–	–	–	–	1.261	0.958
Imaginary frequency compatible with the stretching/bending marked with ** (cm^{-1})							
	-1130.28		-406.42		-1411.71		

CHAPTER 5

CONCLUSION AND RECOMMENDATION

5.1 Conclusion

In conclusion, a new class of octahedral heteroleptic iridium(III) complexes bearing one bidentate pyidinylformimidamide-based ancillary ligand moiety were successfully synthesised and characterised with spectroscopic and chemical analysis. Four complexes; bis(phenylpyridine)(2,6-difluorobenzylpyridinylformimidamide) iridium(III) (**IR1**), bis(2,4-difluorophenylpyridine)(2,6-difluorobenzylpyridinylformimidamide)iridium(III) (**IR2**), bis(phenylpyridine)(4-methylbenzylpyridinylformimidamide)iridium(III) (**IR3**) and bis(2,4-difluorophenylpyridine)(4-methylbenzylpyridinylformimidamide)iridium(III) (**IR4**)

varied by their substituents have shown different colour emission and photophysical behaviour. An interesting finding has been revealed in this research where the starting cyclic triazole-based ligand of (2-(2,6-difluorobenzyl)-*1H*-1,2,4-triazol-1-yl)pyridine (F_2bpyta) and 2-(4-methylbenzyl)-(1,2,4-triazol-1-yl)pyridine **(**Mbpyta) have converted into acyclic formimidamide based ligand of CNF2pyfa; (E)-N-cyano-N-(2,6-difluorobenzyl)-N'-(pyridin-2-yl)formimidamide and CNMBpyfa; (E)-N-cyano-N-(methylbenzyl)-N'-(pyridin-2-yl)formimidamide respectively when undergoes complexation with iridium atom. This result contradicted the hypothesis of having a product of iridium(III) carbene complexes. However, this result has successfully opened a new discussion on the reaction mechanism of how the complexation process between iridium(III) dimer precursor with the triazole-based ligand took place in two stages of deprotonation with the presence of silver(I) oxide using DFT investigation.

In addition, this research has successfully bridged the experimental data of a new class of iridium(III) complexes bearing with pyridinylformimidamide ancillary ligand into a DFT computational study. The experimental data had good replication of the DFT calculations with good correlation analysis, proving that DFT is a reliable method for studying the new class of complexes. In particular, DFT has successfully analysed the FMO analysis of the synthesised complexes **IR1**–**IR4** to better understand the potential application of these novel complexes.

For the photophysical analysis of complexes **IR1**–**IR4**, all complexes show acceptable phosphorescence emission properties with different energies and different colours of emission. The hypothesis to synthesise deep blue phosphorescent iridium(III) complex is not accepted due to the low purity of the blue colour emission. However, complex **IR2** (λ_{em}=463 nm) and **IR4** (λ_{em}=464 nm) emitted almost blue colour emission

with high emission energy, which was blue-shifted compared to the green light of **IR1** and **IR3** (λ_{em}=518 nm). For instance, DFT and TD–DFT calculation have supported the emission of almost blue colour by the calculation of FMO on the complex **IR2** (3.878 eV) and **IR4** (3.880 eV), where they reveal more significant HOMO-LUMO band gap energy compared to complexes **IR1** (3.650 eV) and **IR3** (3.641 eV). On the other hand, complex **IR3** show the most excellent phosphorescence efficiency by having the highest quantum yield at 49% and the longest lifetime at 78.82 ns compared to complexes **IR1**, **IR2** and **IR4**.

Finally, this study has successfully proved that EWG and EDG properties of the substituent attached to the ancillary ligand do not significantly affect the destabilisation of LUMO energy for complexes **IR1**–**IR4**. However, they still have a smaller contribution to the HOMO energy of complexes **IR1**–**IR4**. In significance, fluorine substituents on the cyclometallating ligand have an immense contribution towards the HOMO and LUMO energy compared to the role of ancillary ligands. Hence, the MLCT electronic transition of all complexes **IR1**–**IR4** was not significantly influenced by the substituents on the ancillary ligand.

5.2 Recommendations

Given the promising photophysical properties of the synthesised iridium(III) complexes, particularly the high quantum yield and long emission lifetime of **IR3**, future research should focus on their incorporation into OLED devices. These complexes can serve as phosphorescent emitters in the emissive layer of OLEDs, where their strong spin–orbit coupling and efficient triplet emission are highly advantageous. Device fabrication should involve a multilayer OLED architecture with suitable host

materials to evaluate electroluminescence performance, including key parameters such as external quantum efficiency (EQE), luminance, and operational stability. This approach would provide practical insights into the suitability of these complexes for OLED display and lighting technologies.

In addition, future work is recommended to explore the bioactivity potential of the synthesised iridium(III) complexes. Iridium complexes are known for their applications in anticancer therapy, photodynamic therapy, and cellular imaging due to their luminescence and structural stability. The good emission properties and tunable ligands of complexes **IR1**–**IR4**, particularly **IR3** with its high quantum yield, make them promising candidates for such applications. Future studies should include cytotoxicity assays, Reactive Oxygen Species (ROS) generation analysis, and cellular imaging tests. These investigations could broaden the functional scope of the synthesised complexes and support their development as multifunctional agents in biomedical applications.

Additionally, further computational validation using more advanced DFT and TD-DFT methods, including the incorporation of solvent effects, excited-state dynamics, and vibronic coupling, could enhance the predictive accuracy for future ligand design and photophysical behaviour. To broaden the chemical scope, the coordination of similar ligand frameworks with alternative metal centers such as Pt(II), Ru(II), or Os(II) is also recommended. This would help determine whether the observed ligand transformations and photophysical characteristics are retained across different metals, thereby deepening the understanding of metal–ligand coordination chemistry in related systems.

REFERENCES

Adeloye, A. O., Mphahlele, M. J., Adekunle, A. S., Rhyman, L., & Ramasami, P. (2017). Spectroscopic, electrochemical and DFT studies of phosphorescent homoleptic cyclometalated iridium(III) complexes based on substituted 4-fluorophenylvinyl and 4-methoxyphenylvinylquinolines. *Materials*, *10*(10).

Ahn, S. Y., Lee, H. S., & Ha, Y. (2011). New blue phosphorescent iridium complexes containing phenylpyridine and triazole ligands: Synthesis and luminescence studies. *Journal of Nanoscience and Nanotechnology*, *11*(5), 4414–4418.

Ali, N. M., Ward, M. D., Hashim, N., & Daud, N. (2017). Synthesis and photophysical properties of bis(phenylpyridine) iridium(III) dicyanide complexes. *Materials Research Innovations*, *8917*, 1–6.

Alsaeedi, M. S. (2023). A theoretical study on the electronic structures and phosphorescence properties of light-emitting electrochemical cell champions reported in early 2022. *Polyhedron*, 242, 116490.

Altinolcek, N., Battal, A., Tavasli, M., Cameron, J., Peveler, W. J., Yu, H. A., & Skabara, P. J. (2020). Yellowish-orange and red emitting quinoline-based iridium(III) complexes: Synthesis, thermal, optical and electrochemical properties and OLED application. *Synthetic Metals*, 268, 116504.

Bahron, H., Khaidir, S. S., Tajuddin, A. M., Ramasamy, K., & Yamin, B. M. (2019). Synthesis, characterization and anticancer activity of mono- and dinuclear Ni(II) and Co(II) complexes of a schiff base derived from *o*-vanillin. *Polyhedron*, 161(ii), 84–92.

Bai, R., Meng, X., Wang, X., & He, L. (2020). Blue-Emitting iridium(III) complexes for light-emitting electrochemical cells: advances, challenges, and future prospects. *Advanced Functional Materials*, 1907169, 1–28

Bain, N. H. A. S., Ali, N. M., Juahir, Y., Hashim, N., Isa, I. M., Mohamed, A., Kamari, A., Anouar, E. H., Yamin, B. M., Tajuddin, A. M., & Baharudin, M. H. (2020). Synthesis, crystal structure, photophysical properties, DFT studies and Hirshfeld surface analysis of a phosphorescent 1,2,4-triazole-based iridium(III) complex. *Polyhedron*, *188*, 114690.

Balci, M. (2005). Basic ^{1}H- and ^{13}C-NMR Spectroscopy. *Elsevier.*

Baranoff, E., & Curchod, B. F. E. (2015). FIrPic: Archetypal blue phosphorescent emitter for electroluminescence. *Dalton Transactions*, *44*(18), 8318–8329.

Baranoff, E., Curchod, B. F. E., Monti, F., Steimer, F., Accorsi, G., Tavernelli, I., Rothlisberger, U., Scopelliti, R., Grätzel, M., & Nazeeruddin, M. K. (2012). Influence of halogen atoms on a homologous series of bis-cyclometalated iridium(III) complexes. *Inorganic Chemistry*, *51*(2), 799–811.

Baranoff, E., Fantacci, S., De Angelis, F., Zhang, X., Scopelliti, R., Grettzel, M., & Nazeeruddin, M. K. (2011). Cyclometalated iridium(III) complexes based on phenyl-imidazole ligand. *Inorganic Chemistry*, *50*(2), 451–462.

Barbante, G. J., Doeven, E. H., Francis, P. S., Stringer, B. D., Hogan, C. F., Kheradmand, P. R., Wilson, D. J. D., & Barnard, P. J. (2015). Iridium(III) N-heterocyclic carbene complexes: an experimental and theoretical study of structural, spectroscopic, electrochemical and electrogenerated chemiluminescence properties. *Dalton Transactions*, *44*, 8564–8576.

Barbante, G. J., Francis, P. S., Hogan, C. F., Kheradmand, P. R., Wilson, D. J. D., Barnard, P. J., Barbante GJ, Francis PS, H. C., Kheradmand, P. R., Wilson, D. J. D., Barnard, P. J., Barbante, G. J., Francis, P. S., Hogan, C. F., Kheradmand, P. R., Wilson, D. J. D., & Barnard, P. J. (2013). Electrochemiluminescent ruthenium(II) N-heterocyclic carbene complexes: A combined experimental and theoretical study. *Inorganic Chemistry*, *52*(13), 7448–7459.

Bernhammer, J. C., Frison, G., & Huynh, H. V. (2013). Electronic structure trends in N-heterocyclic carbenes (NHCs) with varying number of nitrogen atoms and NHC-transition metal bond properties. *Chemistry - A European Journal*, *19*(38), 12892–12905.

Beucher, H., Kumar, S., Kumar, R., Merino, E., Hu, W. H., Stemmler, G., Cuesta-Galisteo, S., González, J. A., Bezinge, L., Jagielski, J., Shih, C. J., & Nevado, C. (2020). Phosphorescent K^3-(N^C^C)-Gold(III) Complexes: Synthesis, Photophysics, Computational Studies and Application to Solution-Processable OLEDs. *Chemistry - A European Journal*, *26*(72), 17604–17612.

Brulatti, P. (2010). New luminescent iridium (III) complexes containing NCN cyclometallated ligands: synthesis, photophysical properties and emission tuning. *Durman E-Theses*.

Buil, M. L., Esteruelas, M. A., & López, A. M. (2021). Recent Advances in Synthesis of Molecular Heteroleptic Osmium and Iridium Phosphorescent Emitters. *European Journal of Inorganic Chemistry*, *2021*(46), 4731–4761.

Chan, K. T., Tong, G. S. M., To, W. P., Yang, C., Du, L., Phillips, D. L., & Che, C. M. (2017). The interplay between fluorescence and phosphorescence with luminescent gold(I) and gold(III) complexes bearing heterocyclic arylacetylide ligands. *Chemical Science*, *8*(3), 2352–2364.

Chen, Z., Suramitr, S., Zhu, N., Ho, C. L., Hannongbua, S., Chen, S., & Wong, W. Y. (2020). Tetrafluorinated phenylpyridine based heteroleptic iridium(III) complexes for efficient sky blue phosphorescent organic light-emitting diodes. *Journal of Materials Chemistry C*, *8*(7), 2551–2557.

Cheng, W., Sheng, R., Liu, Y., Wang, S., Chen, P., & Tong, B. (2021). Dinuclear iridium complexes with non-conjugated bis-terdentate cyclometallating ligands and their electroluminescence properties. *Inorganic Chemistry Communications*, *129*(April), 108667.

Chiu, Y. C., Hung, J. Y., Chi, Y., Chen, C. C., Chang, C. H., Wu, C. C., Cheng, Y. M., Yu, Y. C., Lee, G. H., & Chou, P. T. (2009). En route to high external quantum efficiency (∼12%), organic true-blue-light-emitting diodes employing novel design of iridium(III) phosphors. *Advanced Materials*, *21*(21), 2221–2225.

Cho, H., Lee, J., Lee, J. I., Cho, N. S., Park, J. H., Lee, J. Y., & Kang, Y. (2016). Phenylimidazole-based homoleptic iridium(III) compounds for blue phosphorescent organic light-emitting diodes with high efficiency and long lifetime. *Organic Electronics*, *34*, 91–96.

Cho, Kim, S. Y., Kim, J. H., Lee, J., Cho, D. W., Yi, S., Son, H. J., Han, W. S., & Kang, S. O. (2017). Probing photophysical properties of isomeric N-heterocyclic carbene Ir(III) complexes and their applications to deep-blue phosphorescent organic light-emitting diodes. *Journal of Materials Chemistry C*, *5*(7), 1651–1659.

Cho, KimJin-Hyoung, K. S.-Y., Dounglas, W. C., Mu-Hyun, B., Jiwon, L., Chul, H. K., Ho-Jin, S., Won-Sik, H., & Sang Ook, K. (2017). Important role of ancillary ligand in the emission behaviours of blue-emitting heteroleptic Ir(III) complexes. *Journal of Materials Chemistry C*, *5*(18), 4480–4487.

Chyba, J., Hruzíková, A., Knor, M., Pikulová, P., Marková, K., Novotný, J., & Marek, R. (2023). Nature of NMR Shifts in Paramagnetic Octahedral Ru(III) Complexes with Axial Pyridine-Based Ligands. *Inorganic Chemistry*, *62*(8), 3381–3394.

Szafrański, P. W., Patryk Kasza, Mariusz Kępczyński, & Marek T. Cegła. (2015). Fluorescent 1,2,3-triazole derivative of 3′-deoxy-3-azidothymidine : synthesis and absorption / emission spectra. *Heterocyclic Communications*, *21*(5), 263–267.

Cortés-Arriagada, D., Sanhueza, L., González, I., Dreyse, P., & Toro-Labbé, A. (2015). About the electronic and photophysical properties of iridium(III)-pyrazino[2,3-F][1,10]-phenanthroline based complexes for use in electroluminescent devices. *Phys. Chem. Chem. Phys.*, 15–17.

Costa, R. D., Orti, E., Bolink, H. J., Monti, F., Accorsi, G., & Armaroli, N. (2012). Luminescent ionic transition-metal complexes for light-emitting electrochemical cells. *Angewandte Chemie - International Edition*, 51(33), 8178–8211.

De Angelis, F., Fantacci, S., Evans, N., Klein, C., Zakeeruddin, S. M., Moser, J. E., Kalyanasundaram, K., Bolink, H. J., Grätzel, M., & Nazeeruddin, M. K. (2007). Controlling phosphorescence color and quantum yields in cationic iridium complexes: A combined experimental and theoretical study. *Inorganic Chemistry*, *46*(15), 5989–6001.

Donato, L., Abel, P., & Zysman-Colman, E. (2013). Cationic iridium(III) complexes bearing a bis(triazole) ancillary ligand. *Dalton Transactions*, *42*(23), 8402–8412.

Dong, Y. S., Yang, F., Liu, W. C., Wang, X. D., Xing, Y., & Xiu, Z. L. (2019). Separation and purification of wortmannilactone analogues by three-liquid-phase salting-out extraction coupled with column chromatography. *Separation and Purification Technology*, *224*(April), 397–404.

Eremina, A. A., Kinzhalov, M. A., Katlenok, E. A., Smirnov, A. S., Andrusenko, E. V., Pidko, E. A., Suslonov, V. V., & Luzyanin, K. V. (2020). Phosphorescent Iridium(III) Complexes with Acyclic Diaminocarbene Ligands as Chemosensors for Mercury. *Inorganic Chemistry*, *59*(4), 2209–2222.

Epifanovsky, E., Gilbert, A. T. B., Feng, X., Lee, J., Mao, Y., Mardirossian, N., Pokhilko, P., White, A. F., Coons, M. P., Dempwolff, A. L., Gan, Z., Hait, D., Horn, P. R., Jacobson, L. D., Kaliman, I., Kussmann, J., Lange, A. W., Lao, K. U., Levine, D., Krylov, A. I. (2021). Software for the frontiers of quantum chemistry: An overview of developments in the Q-Chem 5 package. *Journal of Chemical Physics*, *155*(8).

Escudero, D. (2016). Quantitative prediction of photoluminescence quantum yields of phosphors from first principles. *Chemical Science*, *7*(2), 1262–1267.

Fan, C., Li, Y., Yang, C., Wu, H., Qin, J., & Cao, Y. (2012). Phosphoryl/Sulfonyl-substituted iridium complexes as blue phosphorescent emitters for single-layer blue and white organic light-emitting diodes by solution process. *Chemistry of Materials*, *24*, 4581–4587.

Fan, Quan, K., Han, Z., Han, F., Li, Z., Liu, J., & Liu, X. (2023). Recovery and purification of iridium from secondary resources: A review. *Journal of Sustainable Metallurgy*, *9*(3), 909–926.

Ferreira, V. F., Da Rocha, D. R., Da Silva, F. C., Ferreira, P. G., Boechat, N. A., & Magalhães, J. L. (2013). Novel *1H*-1,2,3-, *2H*-1,2,3-, *1H*-1,2,4- and *4H*-1,2,4-triazole derivatives: A patent review (2008-2011). *Expert Opinion on Therapeutic Patents*, *23*(3), 319–331.

Flifel, I. A., & Hlail, A. N. (2017). Preparation, spectra characterization of new 1,2,4-triazole derivatives and its complexities with some transition metal ions. *International Journal of Applied Engineering Research*, *12*(24), 14878–14881.

Fu, Y., Liu, H., Tang, B. Z., & Zhao, Z. (2023). Realizing efficient blue and deep-blue delayed fluorescence materials with record-beating electroluminescence efficiencies of 43.4%. *Nature Communications*, *14*(1).

Fuertes, S., Chueca, A. J., Arnal, L., Martín, A., Giovanella, U., Botta, C., & Sicilia, V. (2017). Heteroleptic cycloplatinated N-heterocyclic carbene complexes: A new approach to highly efficient blue-light emitters. *Inorganic Chemistry*, *56*(9), 4829–4839.

Fulmer, G. R., Miller, A. J. M., Sherden, N. H., Gottlieb, H. E., Nudelman, A., Stoltz, B. M., Bercaw, J. E., & Goldberg, K. I. (2010). NMR chemical shifts of trace impurities: Common laboratory solvents, organics, and gases in deuterated solvents relevant to the organometallic chemist. *Organometallics*, *29*(9), 2176–2179.

Glory, D. C. M., Madivanane, R., & Sambathkumar, K. (2015). Electronic Structure Investigations of 3- and 5- Diamino-1,2,4-triazole by UV-Visible , NMR Spectral Studies and HOMO-LUMO analysis by AB Initio and DFT Calculations.

Gökce, H., Akyildirim, O., Bahçeli, S., Yüksek, H., & Kol, Ö. G. (2014). The 1-acetyl-3-methyl-4-[3-methoxy-4-(4-methylbenzoxy)benzylidenamino]-4,5-dihydro-*1H*-1,2,4-triazol-5-one molecule investigated by a joint spectroscopic and quantum chemical calculations. *Journal of Molecular Structure*, *1056–1057*(1), 273–284.

Gokce, H., Ozturk, N., Tasąn, M., Alpaslan, Y. B., & Alpaslan, G. (2016). Spectroscopic characterization and quantum chemical computations of the 5-(4-pyridyl)-*1H*-1,2,4-triazole-3-thiol molecule. *Spectroscopy Letters*, *49*(3), 167–179.

Green, T. F. G., & Yates, J. R. (2014). Relativistic nuclear magnetic resonance J-coupling with ultrasoft pseudopotentials and the zero-order regular approximation. *Journal of Chemical Physics*, *140*(23).

Guijie, L., Xiangdong, Z., Fleetham, T., Qidong, C., Feng, Z., Jianbing, Z., Yang, Y. F., Lou, W., Yang, Y., Fang, K., Shao, Z., Zhang, Q., & She, Y. (2020). Tetradentate Platinum(II) Complexes for Highly Efficient Phosphorescent Emitters and Sky Blue OLEDs. *Chemistry of Materials*, *32*(1), 537–548.

Haghighatbin, M. A., Laird, S. E., & Hogan, C. F. (2018). Electrochemiluminescence of cyclometalated iridium (III) complexes. In *Current Opinion in Electrochemistry* (Vol. 7, pp. 216–223). Elsevier B.V.

Han, J., Chun, Y. K., Chan, S. L., Cheng, S. C., Yiu, S. M., & Ko, C. C. (2022). Development of Dual Phosphorescent Materials Based on Multiple Stimuli-Responsive Ir(III) Acyclic Carbene Complexes. *CCS Chemistry*, *4*(7), 2354–2368.

Haneder, S., Da Como, E., Feldmann, J., Lupton, J. M., Lennartz, C., Erk, P., Fuchs, E., Molt, O., Münster, I., Schildknecht, C., & Wagenblast, G. (2008). Controlling the radiative rate of deep-blue electrophosphorescent organometallic complexes by singlet-triplet gap engineering. *Advanced Materials*, *20*(17), 3325–3330.

Hayes, J. M., Peris, E., & Ujaque, G. (2007). Mechanism of Formation of Silver N -Heterocyclic Carbenes Using Silver Oxide : A Theoretical Study. *Organometallics*, *26*(25), 6170–6183.

He, L., Wang, Z., Duan, L., Yang, C., Tang, R., Song, X., & Pan, C. (2016). Toward fluorine-free blue-emitting cationic iridium complexes: To generate emission from the cyclometalating ligands with enhanced triplet energy. *Dalton Transactions,* 45 (13).

Henwood, A. F., Bansal, A. K., Cordes, D. B., Slawin, A. M. Z., Samuel, I. D. W., & Zysman-Colman, E. (2016). Solubilised bright blue-emitting iridium complexes for solution processed OLEDs. *J. Mater. Chem. C*, *4*, 3726–3737.

Henwood, A. F., & Zysman-Colman, E. (2017). Lessons learned in tuning the optoelectronic properties of phosphorescent iridium(iii) complexes. *Chemical Communications*, *53*(5), 807–826.

Henwood, A. F., & Zysman, E. (2016). Luminescent Iridium Complexes Used in Light-Emitting Electrochemical Cells (LEECs). *Topics in Current Chemistry*, *374*(4), 1–41.

Herrmann, W. a. (2015). N-Heterocyclic Carbenes: A New Concept in Organometallic Catalysis13. *Angewandte Chemie International Edition*, *41*(8), 1290–1309.

Hong, G., Gan, X., Leonhardt, C., Zhang, Z., Seibert, J., Busch, J. M., & Bräse, S. (2021). A Brief History of OLEDs Emitter Development and Industry Milestones. *Advanced Materials*, *33*(9).

Hopkinson, M. N., Richter, C., Schedler, M., & Glorius, F. (2014). An overview of N-heterocyclic carbenes. *Nature*, *510*(7506), 485–496.

Hopmann, K. H. (2016). How accurate is DFT for iridium-mediated chemistry? *Organometallics*, *35*(22), 3795–3807.

Hsiang, E. L., Yang, Z., Yang, Q., Lan, Y. F., & Wu, S. T. (2021). Prospects and challenges of mini-LED, OLED, and micro-LED displays. *Journal of the Society for Information Display*, *29*(6), 446–465.

Ibrahim-Ouali, M., & Dumur, F. (2019). Recent advances on metal-based near-infrared and infrared emitting OLEDs. *Molecules*, 24(7).

Idrees, K. B., Astashkin, A. V., & Rajaseelan, E. (2017). [μ-1,4-Bis(diphenylphosphanyl)butane-κ^2P: P′]bis{(4-benzyl-2-neopentyl-1,2,4-triazol-3-ylidene)[(1,2,5,6-η)-cycloocta-1,5-diene]iridium(I)}bis(tetrafluoroborate) dichloromethane disolvate . *IUCrData*, *2*(7).

Ito, A., Hiokawa, T., Sakuda, E., & Kitamura, N. (2011). Bright green-phosphorescence from metal-to-boron charge transfer excited state of a novel cyclometalated iridium(III) complex. *Chemistry Letters*, *40*(1), 34–36.

Jansson, E., Minaev, B., Schrader, S., & Ågren, H. (2007). Time-dependent density functional calculations of phosphorescence parameters for *fac*-tris(2-phenylpyridine) iridium. *Chemical Physics*, *333*(2–3), 157–167.

Ji Ram, V., Sethi, A., Nath, M., & Pratap, R. (2019). Five-Membered Heterocycles. In *The Chemistry of Heterocycles* (pp. 149–478).

Kajjam, A. B., & Vaidyanathan, S. (2018). Structural Mimics of Phenyl Pyridine (ppy) Substituted, Phosphorescent Cyclometalated Homo and Heteroleptic Iridium(III) Complexes for Organic Light Emitting Diodes – An Overview. *Chemical Record*, *18*(3), 293–349.

Kaklamanos, G., Aprea, E., & Theodoridis, G. (2015). Mass Spectrometry: Principles and Instrumentation. In *Encyclopedia of Food and Health* (1st ed.). Elsevier Ltd.

Kandioller, W., Theiner, J., Keppler, B. K., & Kowol, C. R. (2022). Elemental analysis: An important purity control but prone to manipulations. *Inorganic Chemistry Frontiers*, *9*(3), 412–416.

Karatsu, T., Takahashi, M., Yagai, S., & Kitamura, A. (2013). Photophysical properties of substituted homoleptic and heteroleptic phenylimidazolinato Ir(III) complexes as a blue phosphorescent material. *Inorganic Chemistry*, *52*(21), 12338–12350.

Karmis, R. E., Carrara, S., Baxter, A. A., Hogan, C. F., Hulett, M. D., & Barnard, P. J. (2019). Luminescent iridium(III) complexes of N-heterocyclic carbene ligands prepared using the 'click reaction'. *Dalton Transactions*, *48*(27), 9998–10010.

Kaufmann, S., Schäfer, S., Gamer, M. T., & Roesky, P. W. (2017). Reactivity studies of silylene [PhC(N: *T*Bu)$_2$](C$_5$Me$_5$)Si-reactions with [M(COD)Cl]$_2$ (M = Rh(I), Ir(I)), S, Se, Te, and BH$_3$. *Dalton Transactions*, *46*(27), 8861–8867.

Khomenko, D. M., Doroschuk, R. O., & Lampeka, R. D. (2015). Synthesis, characterization and luminescent properties of palladium complexes with 3-(2-pyridyl)-*1H*-1,2,4-triazole-5-acetic acid ethyl ester. *Polyhedron*.

Kinzhalov, M. A., Eremina, A. A., Smirnov, A. S., Suslonov, V. V., Kukushkin, V. Y., & Luzyanin, K. V. (2019). Cleavage of acyclic diaminocarbene ligands at an iridium(iii) center. Recognition of a new reactivity mode for carbene ligands. *Dalton Transactions*, *48*(22), 7571–7582.

Kinzhalov, M. A., & Luzyanin, K. V. (2019). Reactivity of acyclic diaminocarbene ligands. *Coordination Chemistry Reviews*, *399*, 213014.

Klubek, K. P. (2014). Investigation of blue phosphorescent organic light-emitting diode. *e-theses University of Rochester.*

Kwon, Y., Han, S. H., Yu, S., Lee, J. Y., & Lee, K. M. (2018). Functionalized phenylimidazole-based: *Facial*-homoleptic iridium(III) complexes and their excellent performance in blue phosphorescent organic light-emitting diodes. *Journal of Materials Chemistry C*, *6*(16), 4565–4572.

Lakshmanan, R., Shivaprakash, N. C., & Sindhu, S. (2018). Orange Fluorescent Ru(III) Complexes Based on 4′-Aryl Substituted 2,2′:6′,2″-Terpyridine for OLEDs Application. *Journal of Fluorescence*, *28*(1), 173–182.

Lee, S., & Han, W. S. (2020). Cyclometalated Ir(III) complexes towards blue-emissive dopant for organic light-emitting diodes: Fundamentals of photophysics and designing strategies. *Inorganic Chemistry Frontiers*, *7*(12), 2396–2422.

Li, G., Congrave, D. G., Zhu, D., Su, Z., & Bryce, M. R. (2018). Recent advances in luminescent dinuclear iridium(III) complexes and their application in organic electroluminescent devices. *Polyhedron*, *140*(iii), 146–157.

Li, H., Yin, Y. M., Cao, H. T., Sun, H. Z., Wang, L., Shan, G. G., Zhu, D. X., Su, Z. M., & Xie, W. F. (2014). Efficient greenish-blue phosphorescent iridium(III) complexes containing carbene and triazole chromophores for organic light-emitting diodes. *Journal of Organometallic Chemistry*, *753*(iii), 55–62.

Li, T. Y., Liang, X., Zhou, L., Wu, C., Zhang, S., Liu, X., Lu, G. Z., Xue, L. S., Zheng, Y. X., & Zuo, J. L. (2015). N-heterocyclic carbenes: Versatile second cyclometalated ligands for neutral iridium(III) heteroleptic complexes. *Inorganic Chemistry*, *54*(1), 161–173.

Li, T. Y., Wu, J., Wu, Z. G., Zheng, Y. X., Zuo, J. L., & Pan, Y. (2018). Rational design of phosphorescent iridium(III) complexes for emission color tunability and their applications in OLEDs. In *Coordination Chemistry Reviews* (Vol. 374, pp. 55–92). Elsevier B.V.

Li, X., Minaev, B., Ågren, H., & Tian, H. (2011). Theoretical study of phosphorescence of iridium complexes with fluorine-substituted phenylpyridine ligands. *European Journal of Inorganic Chemistry*, *16*, 2517–2524.

Lin, K., Chile, L. E., Zhen, S. C., Boyd, P. D. W., Ware, D. C., & Brothers, P. J. (2014). Pyrrole pincers containing imidazole, pyrazole and 1,2,4-triazole groups. *Inorganica Chimica Acta*, *422*, 95–101.

Lin, Y. S., Li, G. De, Mao, S. P., & Chai, J. Da. (2013). Long-range corrected hybrid density functionals with improved dispersion corrections. *Journal of Chemical Theory and Computation*, *9*(1), 263–272.

Liu, S., Müller, P., Takase, M. K., & Swager, T. M. (2011). 'Click' synthesis of heteroleptic tris-cyclometalated iridium(III) complexes: Cu(I) triazolide intermediates as transmetalating reagents. *Inorganic Chemistry*, *50*(16), 7598–7609.

Liu, Z., Zhang, S., Zhang, M., Wu, C., Li, W., & Wu, Y. (2021). Highly Efficient Phosphorescent Blue-Emitting (3+2+1) Coordinated Iridium (III) Complex for OLED Application. *Frontiers in Chemistry*, *9*:758357.

Lo, S. C., Bera, R. N., Hording, R. E., Burn, P. L., & Samuel, I. D. W. (2008). Solution-processible phosphorescent blue dendrimers based on biphenyl-dendrons and fac-tris(phenyltriazolyl)iridium(III) cores. *Advanced Functional Materials*, *18*(19), 3080–3090.

Lu, Z., Shangguan, M., Jiang, X., Xu, P., Hou, L., & Wang, T. (2019). A water-soluble cyclometalated iridium(III) complex with fluorescent sensing capability for hypochlorite. *Dyes and Pigments*, 171,107715.

Lynch, I. (1987). Software Reference Manual. In *Electronic Systems News* (Vol. 1987, Issue 1, p. 43).

Maroń, A. M., & Małecki, J. G. (2014). Spectroscopic characterization of chloride and pseudohalide ruthenium(II) complexes with 4-(4-nitrobenzyl)pyridine. *Transition Metal Chemistry*, *39*(7), 831–841.

Martynova, E. A., Tzouras, N. V., Pisanò, G., Cazin, C. S. J., & Nolan, S. P. (2021). The "weak base route" leading to transition metal-N-heterocyclic carbene complexes. *Chemical Communications*, *57*(32), 3836–3856.

Mathias Mydlak, Claudia Bizzarri, David Hartmann, Wiebke Sarfert, Gunter Schmid, and L. D. C. (2010). Positively Charged Iridium(III) Triazole Derivatives as Blue Emitters for Light-Emitting Electrochemical Cells. *Advanced Functional Materials*, *20*(iii), 1812–1820.

Matteucci, E., Monti, F., Mazzoni, R., Baschieri, A., Bizzarri, C., & Sambri, L. (2018). Click-derived triazolylidenes as chelating ligands: achievement of a neutral and luminescent iridium(III)-triazolide complex. *Inorganic Chemistry*, 57(18), 11673–11686

Minaev, B., Minaeva, V., & Ågren, H. (2009). Theoretical study of the cyclometalated iridium(III) complexes used as chromophores for organic light-emitting diodes. *J. Phys. Chem. A*, *113*, 726–735.

Mingxing, Yu, R., Chen, M., & He, L. (2021). Fluorine-free, blue-emitting cationic iridium complexes with a phenyl-triazole type cyclometalating ligand: Synthesis, characterizations and their use for efficient organic light-emitting diodes. *Dyes and Pigments*, *193*, 109477.

Mitani, R., Yamamoto, H., & Sumimoto, M. (2020). Theoretical study on the reaction mechanism of imidazole-catalyzed phenol-epoxy ring-opening reaction and the evaluation of catalyst performance. *Chemical Physics Letters*, *742*, 137143.

Mohammad Khaja Nazeeruddin;, Aghazada;, S., Huckaba;, A. J., & An- tonio Pertegas Ojeda; Azin Babaei; Giulia Grancini; Iwan Zimmermann; Henk Bolink. (2016). Molecular Engineering of Iridium Blue Emitters Using Aryl N-Heterocyclic Carbene Ligands. *European Journal of Inorganic Chemistry*.

Mohd Yusoff, A. R. Bin, Huckaba, A. J., & Nazeeruddin, M. K. (2017). Phosphorescent Neutral Iridium(III) Complexes for Organic Light-Emitting Diodes. *Topics in Current Chemistry*, *375*(2), 111–112.

Monti, F., Baschieri, A., Sambri, L., & Armaroli, N. (2021). Excited-State Engineering in Heteroleptic Ionic Iridium(III) Complexes. *Accounts of Chemical Research*, *54*(6), 1492–1505.

Monti, F., Kessler, F., Delgado, M., Frey, J., Bazzanini, F., Accorsi, G., Armaroli, N., Bolink, H. J., Ort, E., Scopelliti, R., Nazeeruddin, K., & Baranoff, E. (2013). Charged bis-cyclometalated iridium(III) complexes with carbene-based ancillary ligands. *Inorganic Chemistry*, 52, 10292–10305.

Na, H., Maity, A., Morshed, R., & Teets, T. S. (2017). Bis-Cyclometalated Iridium Complexes with Chelating Dicarbene Ancillary Ligands. *Organometallics*, *36*(15), 2965–2972.

Na, H., & Teets, T. S. (2018). Highly Luminescent Cyclometalated Iridium Complexes Generated by Nucleophilic Addition to Coordinated Isocyanides. *Journal of the American Chemical Society*, *140*(20), 6353–6360.

Nakorchevsky, A., & Yates, J. R. (2012). Mass spectrometry. In *Comprehensive Biophysics* (Vol. 1).

Namdas, E. B., Ruseckas, A., Samuel, I. D. W., Lo, S. C., & Burn, P. L. (2004). Photophysics of fac-tris(2-phenylpyridine) iridium(III) cored electroluminescent dendrimers in solution and films. *Journal of Physical Chemistry B*, *108*(5), 1570–1577.

Navarro, M., Smith, C. A., & Albrecht, M. (2017). Enhanced Catalytic Activity of Iridium(III) Complexes by Facile Modification of C,N-Bidentate Chelating Pyridylideneamide Ligands. *Inorganic Chemistry*, *56*(19), 11688–11701.

Nazeeruddin, M. K., Humphry-Baker, R., Berner, S., Rivier, S., Zuppiroli, L., & Graetzel, M. (2003). Highly Phosphorescence Iridium Complexes and Their Application in Organic Light-Emitting Devices. *J. Am. Chem. Soc.*, *125*(29), 8790–8797.

Nespolo, M. (2015). Tips and traps on crystal twinning: How to fully describe your twin. *Crystal Research and Technology*, *50*(5), 362–371.

Novotny, J., Komorovsky, S., & Marek, R. (2024). Paramagnetic Effects in NMR Spectroscopy of Transition-Metal Complexes: Principles and Chemical Concepts. *Accounts of Chemical Research*, *57*(10), 1467–1477.

Omae, I. (2016). Application of the five-membered ring blue light-emitting iridium products of cyclometalation reactions as OLEDs. *Coordination Chemistry Reviews*, *310*, 154–169.

Omar, S. A. E., Scattergood, P. A., McKenzie, L. K., Jones, C., Patmore, N. J., Meijer, A. J. H. M., Weinstein, J. A., Rice, C. R., Bryant, H. E., & Elliott, P. I. P. (2018). Photophysical and Cellular Imaging Studies of Brightly Luminescent Osmium(II) Pyridyltriazole Complexes. *Inorganic Chemistry*, *57*(21), 13201–13212.

Omidyan, R., Abbasi, M., & Azimi, G. (2019). Photophysical and optoelectronic properties of a platinum(II) complex and its derivatives, designed as a highly efficient OLED emitter: A theoretical study. *International Journal of Quantum Chemistry*, *119*(3), 1–12.

Park, H. J., Kim, J. N., Yoo, H. J., Wee, K. R., Kang, S. O., Cho, D. W., & Yoon, U. C. (2013). Rational design, synthesis, and characterization of deep blue phosphorescent Ir(III) complexes containing (4′-Substituted-2′- pyridyl)-1,2,4-triazole ancillary ligands. *Journal of Organic Chemistry*, *78*(16), 8054–8064.

Parker, S. F. (2019). Characterisation of *fac*-tris[2-phenylpyridinato-c^2, n]iridium(III) by inelastic neutron scattering spectroscopy and periodic density functional theory. *Journal of Physics Communications*, *3*(6).

Pavia, D. L., Lampman, G. M., Kriz, G. S. and Vyvyan, J. R. (2015). Introduction to spectroscopy. *Cengage Learning 200 First Stamford Place,* Stamford, USA. Fifth Edition: pp. 14-329.

Peng, Q., Shi, Q., Niu, Y., Yi, Y., Sun, S., Li, W., & Shuai, Z. (2016). Understanding the efficiency drooping of the deep blue organometallic phosphors: A computational study of radiative and non-radiative decay rates for triplets. *Journal of Materials Chemistry C*, *4*(28), 6829–6838.

Pfeifer, V., Jones, T. E., Velasco Vélez, J. J., Massué, C., Arrigo, R., Teschner, D., Girgsdies, F., Scherzer, M., Greiner, M. T., Allan, J., Hashagen, M., Weinberg, G., Piccinin, S., Hävecker, M., Knop-Gericke, A., & Schlögl, R. (2016). The electronic structure of iridium and its oxides. *Surface and Interface Analysis*, *48*(5), 261–273.

Qu, X., Liu, Y., Si, Y., Wu, X., & Wu, Z. (2014). A theoretical study on supramolecularly-caged positively charged iridium(III) 2-pyridyl azolate derivatives as blue emitters for light-emitting electrochemical cells. *Dalton Transactions*, *43*(3), 1246–1260.

Robert, M. S., Francis, X. W. and David, J. K. (200 5). Spectrometric identification of organic compounds. *John Wiley & Sons, Inc.,* New York. Seventh Edition: pp. 72-204

Rocha, F. S., Gomes, A. J., Lunardi, C. N., Kaliaguine, S., & Patience, G. S. (2018). Experimental methods in chemical engineering: Ultraviolet visible spectroscopy, UV-Vis. *Canadian Journal of Chemical Engineering*, *96*(12), 2512–2517.

Ryu, C. H., Lim, J., Kim, M. B., Lee, J. H., Hwang, H., Lee, J. Y., & Lee, K. M. (2021). Tris(5-phenyl-*1H*-1,2,4-triazolyl)iridium(III) Complex and Its Use in Blue Phosphorescent Organic Light-Emitting Diodes to Provide an External Quantum Efficiency of up to 27.8%. *Advanced Optical Materials*, *9*(7), 1–7.

Sajoto, T., Djurovich, P. I., Tamayo, A. B., Oxgaard, J., Iii, W. A. G., & Thompson, M. E. (2009). Temperature Dependence of Blue Phosphorescent Cyclometalated Ir(III) Complexes. *Journal of American Chemical Society*, *12*, 9813–9822.

Sajoto, T., Djurovich, P. I., Tamayo, A., Yousufuddin, M., Bau, R., Thompson, M. E., Holmes, R. J., & Forrest, S. R. (2005). Blue and near-UV phosphorescence from iridium complexes with cyclometalated pyrazolyl or N-heterocyclic carbene ligands. *Inorganic Chemistry*, *44*(22), 7992–8003.

Sanner, R. D., Cherepy, N. J., Martinez, H. P., Pham, H. Q., & Young, V. G. (2019). Highly efficient phosphorescence from cyclometallated iridium(III) compounds: Improved syntheses of picolinate complexes and quantum chemical studies of their electronic structures. *Inorganica Chimica Acta*, *496*(July), 119040.

Sanner, R. D., Cherepy, N. J., & Young, V. G. (2016). Blue light emission from cyclometallated iridium(III) cyano complexes: Syntheses, crystal structures, and photophysical properties. *Inorganica Chimica Acta*, *440*(Iii), 165–171.

Sarada, G., Maheshwaran, A., Cho, W., Lee, T., Hyun, S., Yeob, J., & Jin, S. (2018). Pure blue phosphorescence by new N-heterocyclic carbene-based Ir(III) complexes for organic light-emitting diode application. *Dyes and Pigments*, *150*, 1–8.

Savka, R., & Plenio, H. (2014). Facile synthesis of [(NHC)MX(COD)] and [(NHC)MCl(CO)$_2$] (M = Rh, Ir; X = Cl, I) complexes. *Dalton Transactions*, *44*(3), 891–893.

Scattolin, T., & Nolan, S. P. (2020). Synthetic Routes to Late Transition Metal–NHC Complexes. *Trends in Chemistry*, *2*(8), 721–736.

Schuster, O., Yang, L., Raubenheimer, H. G., & Albrecht, M. (2009). Beyond Conventional N -Heterocyclic Carbenes : Abnormal, Remote, and other Classes of NHC Ligands with Reduced Heteroatom Stabilization. *American Chemical Society*, *109*(8).

Shafikov, M. Z., Daniels, R., Pander, P., Dias, F. B., Williams, J. A. G., & Kozhevnikov, V. N. (2019). Dinuclear Design of a Pt(II) Complex Affording Highly Efficient Red Emission: Photophysical Properties and Application in Solution-Processible OLEDs. *Applied Materials and Interfaces*, *11*(8), 8182–8193

Shan, Y. (2016). Isolation and Structural Identification of Flavonoids From Citrus. In *Comprehensive Utilization of Citrus By-Products* (pp. 59–64).

Sicilia, V., Arnal, L., Chueca, A. J., Fuertes, S., Babaei, A., Muñoz, A. M. I., Sessolo, M., & Bolink, H. J. (2020). Highly Photoluminescent Blue Ionic Platinum-Based Emitters. *Inorganic Chemistry*, *59*(2), 1145–1152.

Smith, A. R. G., Riley, M. J., Burn, P. L., Gentle, I. R., & Powell, B. J. (2012). Effects of Fluorination on Iridium(III) Complex Phosphorescence: Magnetic Circular Dichroism and Relativistic Time-Dependent Density Functional Theory. *Inorganic Chemistry*, *51*, 2821–2831.

Smith, Arthur R.G., Burn, P. L., & Powell, B. J. (2011). Spin-orbit coupling in phosphorescent iridium(III) complexes. *ChemPhysChem*, *12*(13), 2429–2438.

Smith, Arthur R.G., Burn, P. L., & Powell, B. J. (2016). Exact exchange and the density functional theory of metal-to-ligand charge-transfer in fac-Ir(ppy)$_3$. *Organic Electronics*, *33*, 110–115.

Srivastava, R., & Joshi, L. R. (2014). The effect of substituted 1,2,4-triazole moiety on the emission, phosphorescent properties of the blue emitting heteroleptic iridium(III) complexes and the OLED performance: A theoretical study. *Physical Chemistry Chemical Physics*, *16*(32), 17284–17294.

Stanitska, M., Volyniuk, D., Minaev, B., Agren, H., & Grazulevicius, J. V. (2024). Molecular design, synthesis, properties, and applications of organic triplet emitters exhibiting blue, green, red and white room-temperature phosphorescence. In *Journal of Materials Chemistry C*,12(8), 2662–2698.

Strassner, T., Unger, Y., Meyer, D., Molt, O., Munster, I., & Wagenblast, G. (2013). The 'enders Triazole': A well known molecule, but still a new ligand!! *Inorganic Chemistry Communications*, *30*, 39–41.

Suzuri, Y., Oshiyama, T., Ito, H., Hiyama, K., & Kita, H. (2014). Phosphorescent cyclometalated complexes for efficient blue organic light-emitting diodes. *Science and Technology of Advanced Materials*, *15*(5).

Tamayo, A. B., Alleyne, B. D., Djurovich, P. I., Lamansky, S., Tsyba, I., Ho, N. N., Bau, R., & Thompson, M. E. (2013). Synthesis and Characterization of Facial and Meridional Tris-cyclometalated Iridium(III) Complexes. *Journal of American Chemical Society*, *125*, 7377–7387.

Tang, M. C., Chan, A. K. W., Chan, M. Y., & Yam, V. W. W. (2016). Platinum and Gold Complexes for OLEDs. *Topics in Current Chemistry*, *374*(4), 67–68.

Tang, M. C., Chan, M. Y., & Yam, V. W. W. (2021). Molecular Design of Luminescent Gold(III) Emitters as Thermally Evaporable and Solution-Processable Organic Light-Emitting Device (OLED) Materials. *Chemical Reviews*, *121*(13), 7249–7279.

Tao, P., Zhang, Y., Wang, J., Wei, L., Li, H., Li, X., Zhao, Q., Zhang, X., Liu, S., Wang, H., & Huang, W. (2017). Highly efficient blue phosphorescent iridium(III) complexes with various ancillary ligands for partially solution-processed organic light-emitting diodes. *Journal of Materials Chemistry C*, *5*(36), 9306–9314.

Tatarin, S. V., Kalle, P., Taydakov, I. V., Varaksina, E. A., Korshunov, V. M., & Bezzubov, S. I. (2021). Sterically Hindered Phenanthroimidazole Ligands Drive the Structural Flexibility and Facile Ligand Exchange in Cyclometalated Iridium(III) Complexes. *Dalton Transactions*, *50*(20), 6889–6900.

Thomassen, I. K., McCormick-McPherson, L. J., Borisov, S. M., & Ghosh, A. (2020). Iridium Corroles Exhibit Weak Near-Infrared Phosphorescence but Efficiently Sensitize Singlet Oxygen Formation. *Scientific Reports*, *10*(1), 1–9.

Thompson, M. (2008). A TECHNICAL BRIEF: CHNS Elemental Analyser. In *Royal Society of Chemistry* (Issue 1).

Tian, M., Yu, R., Chen, M., & He, L. (2021). Fluorine-free, blue-emitting cationic iridium complexes with a phenyl-triazole type cyclometalating ligand: Synthesis, characterizations and their use for efficient organic light-emitting diodes. *Dyes and Pigments*, 193, 109477.

Vellé, A., Cebollada, A., Macías, R., Iglesias, M., Gil-Moles, M., & Sanz Miguel, P. J. (2017). From Imidazole toward Imidazolium Salts and N-Heterocyclic Carbene Ligands: Electronic and Geometrical Redistribution. *Omega*, *2*(4), 1392–1399.

Walden, M. T., Pander, P., Yufit, D. S., Dias, F. B., & Williams, G. J. A. (2019). Homoleptic platinum(ii) complexes with pyridyltriazole ligands: Excimer-forming phosphorescent emitters for solution-processed OLEDs. *Journal of Materials Chemistry C*, *7*(22), 6592–6606.

Wang, D., Cheng, C., Tsuboi, T., & Zhang, Q. (2020). Degradation mechanisms in blue organic light-emitting diodes. *CCS Chemistry*, *2*(4), 1278–1296.

Wang, X., Wang, S., Pan, F., He, L., & Duan, L. (2019). Cationic Iridium Complexes with 5-Phenyl-1 H-1,2,4-triazole Type Cyclometalating Ligands: Toward Blue-Shifted Emission. *Inorganic Chemistry*, *58*(18), 12132–12145.

Wang, Yafei, Sun, N., Curchod, B. F. E., Male, L., Ma, D., Fan, J., Liu, Y., Zhu, W., & Baranoff, E. (2016). Tuning the oxidation potential of 2-phenylpyridine-based iridium complexes to improve the performance of bluish and white OLEDs. *Journal of Materials Chemistry C*, *4*(17), 3738–3746.

Wang, Yang, Lu, Y., Gao, B., Wang, S., Ding, J., Wang, L., Jing, X., & Wang, F. (2016). Self-Host Blue-Emitting Iridium Dendrimer Containing Bipolar Dendrons for Nondoped Electrophosphorescent Devices with Superior High-Brightness Performance. *Applied Materials and Interfaces*, *8*(43), 29600–29607.

Wang, Z., He, L., Duan, L., Yan, J., Tang, R., Pan, C., & Song, X. (2015). Blue-green emitting cationic iridium complexes with 1,3,4-oxadiazole cyclometallating ligands: synthesis, photophysical and electrochemical properties, theoretical investigation and electroluminescent devices. *Dalton Transactions*, 44(36).

Weigend, F., & Ahlrichs, R. (2005). Balanced basis sets of split valence, triple zeta valence and quadruple zeta valence quality for H to Rn: Design and assessment of accuracy. *Phys. Chem. Chem. Phys.*, *7*, 3297–3305.

Welby, C. E., Gilmartin, L., Marriot, R. R., Zahid, A., Rice, C. R., Gibson, E. A., & Elliott, P. I. P. (2013). Luminescent biscyclometalated arylpyridine iridium(III) complexes with 4,4'-bi-1,2,3-triazolyl ancillary ligands. *Dalton Transactions*, *42*(207890), 13527–13536.

Werle, S., Ziółkowski, Ł., Tomescu, C., & Rusu, V. (2017). Use of the FTIR-ATR Technique for Testing Heavy Metal Contaminated Energy Crops. *11*(2), 4–7.

Wiśniewski, J. R. (2019). Filter Aided Sample Preparation – A tutorial. *Analytica Chimica Acta*, *1090*, 23–30.

Wong, M., Xie, G., Tourbillion, C., Sandroni, M., Cordes, D. B., & Slawin, A. M. Z. (2015). Formylated Chloro-Bridged Iridium(III) Dimers as OLED Materials: Opening Up New Possibilities. *Royal Society of Chemistry*, *1*, 38–42.

Wu, Y., Wen, Z., Wu, J. I. C., & Teets, T. S. (2020). Efficient Deep Blue Platinum Acetylide Phosphors with Acyclic Diaminocarbene Ligands. *Chemistry - A European Journal*, *26*(68), 16028–16035.

Würth, C., Geißler, D., Behnke, T., Kaiser, M., & Resch-Genger, U. (2015). Critical review of the determination of photoluminescence quantum yields of luminescent reporters. *Analytical and Bioanalytical Chemistry*, *407*(1), 59–78.

Xu, S., Wang, J., Xia, H., Zhao, F., & Wang, Y. (2015). Computational prediction for emission energy of iridium(III) complexes based on TD-DFT calculations using exchange-correlation functionals containing various HF exchange percentages. *Journal of Molecular Modeling*, *21*(2), 1–7.

Xun, S., Zhang, J., Li, X., Ma, D., & Wang, Z. Y. (2008). Synthesis and near-infrared luminescent properties of some ruthenium complexes. *Synthetic Metals*, *158*(12), 484–488.

Yao, J., Dong, S. C., Tam, B. S. T., & Tang, C. W. (2023). Lifetime Enhancement and Degradation Study of Blue OLEDs Using Deuterated Materials. *Applied Materials and Interfaces*, *15*(5), 7255–7262.

Yin, C., Zhang, Y., Huang, T., Liu, Z., Duan, L., & Zhang, D. (2022). Highly efficient and nearly roll-off–free electrofluorescent devices via multiple sensitizations. *Science Advances*, *8*(30).

You, C., Wang, X. Q., Zhou, X., Yuan, Y., Liao, L. S., Liao, Y. C., Chou, P. T., & Chi, Y. (2021). Homoleptic Ir(III) Phosphors with 2-Phenyl-1,2,4-triazol-3-ylidene Chelates for Efficient Blue Organic Light-Emitting Diodes. *Applied Materials and Interfaces*, *13*(49), 59023–59034.

You, Y., & Nam, W. (2012). Photofunctional triplet excited states of cyclometalated Ir(III) complexes: Beyond electroluminescence. *Chemical Society Reviews,* 41(21), 7061–7084.

Younker, J. M., & Dobbs, K. D. (2013). Correlating experimental photophysical properties of iridium(III) complexes to spin-orbit coupled TDDFT predictions. *Journal of Physical Chemistry C*, *117*(48), 25714–25723.

Zhang, Q., Li, B., Huang, S., Nomura, H., Tanaka, H., & Adachi, C. (2014). Efficient blue organic light-emitting diodes employing thermally activated delayed fluorescence. *Nature Photonics*, *8*(March), 1–7.

Zhang, X., Wu, X., & Lei, Y. (2019). Theoretical study on reaction mechanism of synthesis of iridium complexes having cyclometalated acyclic diaminocarbene ancillary ligands. *Journal of Molecular Modeling*, *25*(9).

Zhou, X., Burn, P. L., & Powell, B. J. (2016). Bond Fission and Non-Radiative Decay in Iridium(III) Complexes. *Inorganic Chemistry*, *55*(11), 5266–5273.

Zhu, W., Liu, S., Wang, Z., Shi, C., Zhang, Q., Wu, Z., Li, G., & Zhu, D. (2023). An AIE Metal Iridium Complex: Photophysical Properties and Singlet Oxygen Generation Capacity. *Molecules*, *28*(23).

Zulkarnaen, N. K., Ali, N. M., Mustafar, S., Kamari, A., & Bain, N. H. A. S. (2025). Synthesis and characterisation of cationic iridium(III) complex with phenanthroline-based ancillary ligand. *Malaysian Journal of Analytical Sciences*, *29*(1), 1–10.

Zulkifli, N., Ali, N. M., Bain, N. H. A. S., Juahir, Y., Mustafar, S., Hashim, N., Yusof, M. S. M., El-Sawaf, A. K., & Anouar, E. H. (2023). Synthesis, spectroscopic characterizations, photophysical properties and DFT studies of a novel iridium(III) complex containing 2-(2-butoxy-4-fluorophenyl)pyridine ligand. *Inorganica Chimica Acta*, 558(121757).

APPENDICES

Appendix S1

The mass spectrometry profile of the synthesised complex **IR1**

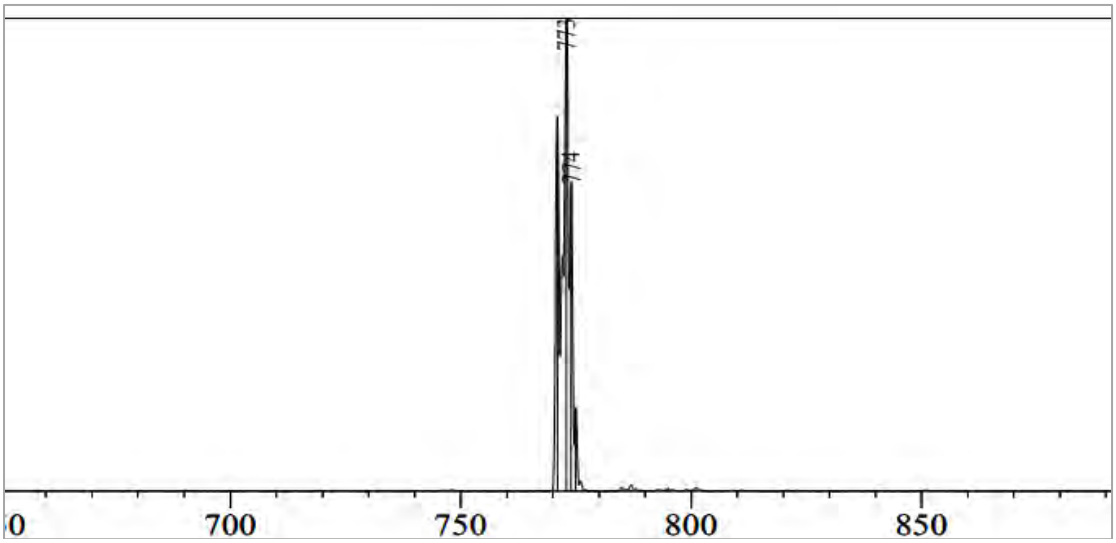

Appendix S2

The mass spectrometry profile of the synthesised complex **IR2**

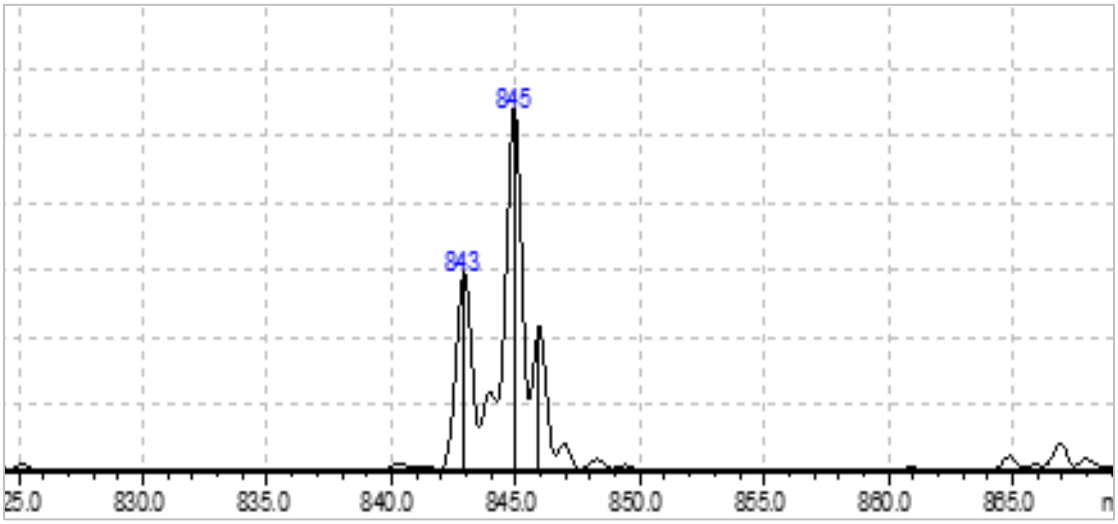

Appendix S3

The mass spectrometry profile of the synthesised complex **IR3**

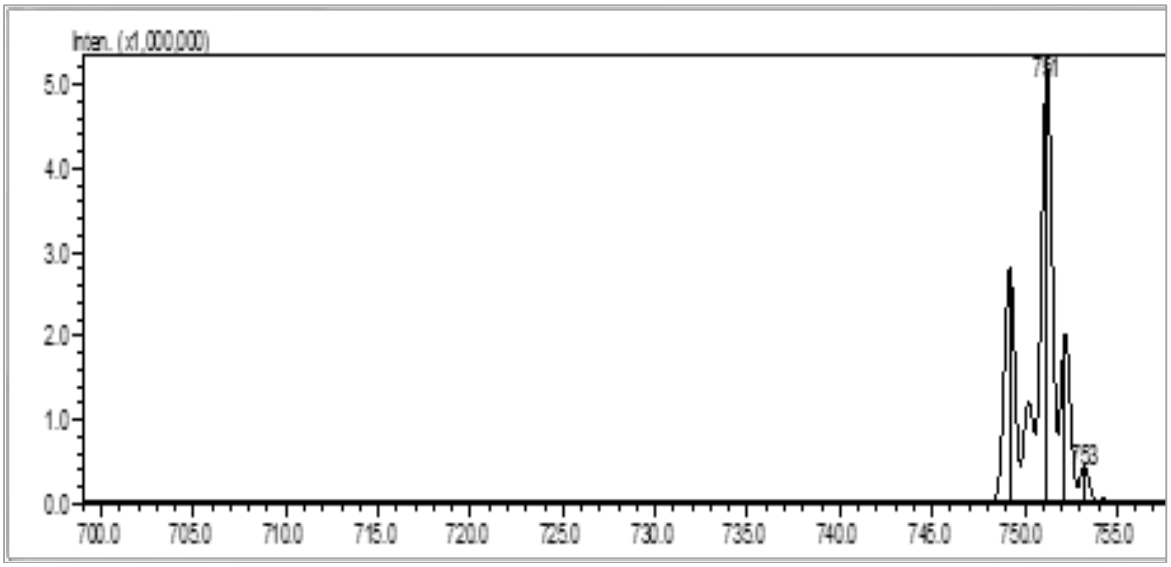

Appendix S4

The mass spectrometry profile of the synthesised complex **IR4**

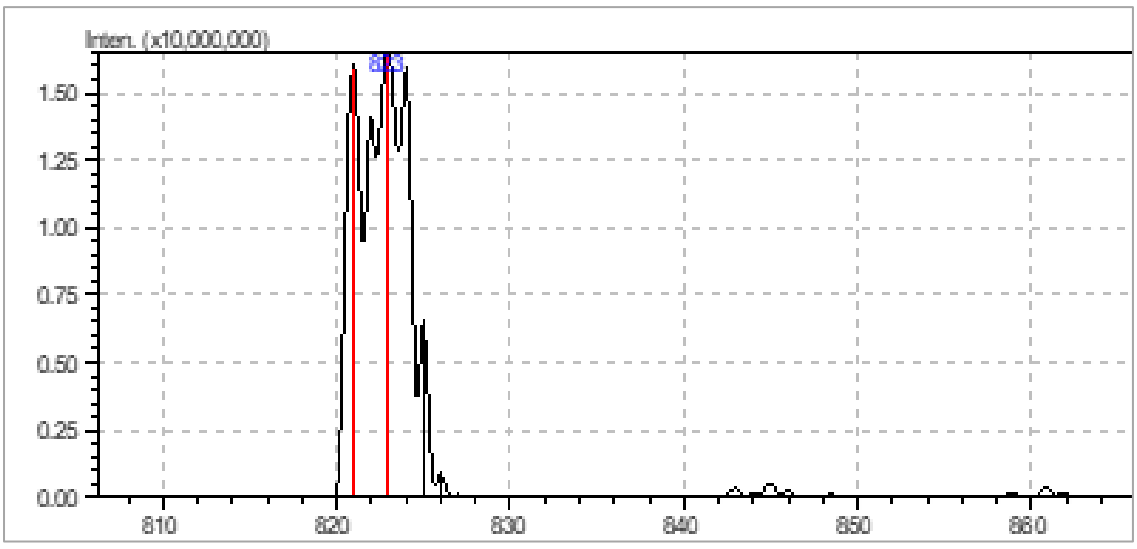

Appendix S5

Spectrum of ^{13}C NMR for recorded **IR1** in deuterated dichloromethane with their labelling peak

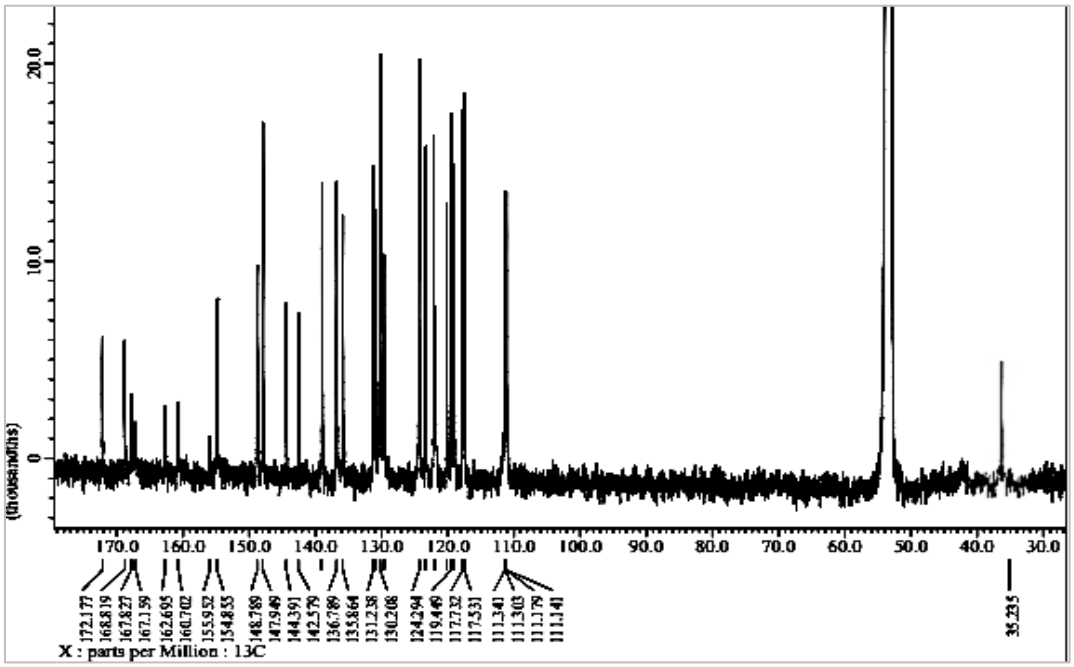

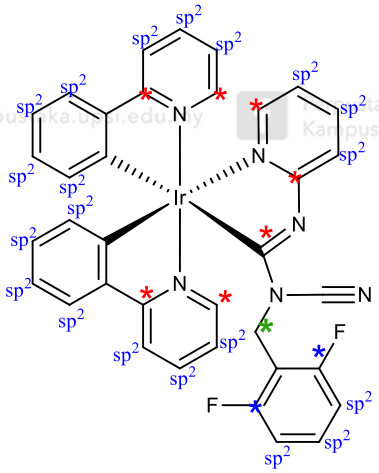

* : $C_{methylene}$

* : C-$N_{aromatic}$, C=$N_{aromatic}$

* : C-$F_{aromatic}$

sp^2 : $C_{aromatic}$, $C_{quarternary\ in\ aromatic}$

^{13}C-NMR (126 MHz, Methylene-Chloride) δ 172.2 (C-$N_{pyridine}$), 168.8 (C-$N_{pyridine}$), 167.8(C-$N_{pyridine}$), 167.2(C-$N_{pyridine}$), 162.7(C-$N_{pyridine}$), 160.8(C-$N_{pyridine}$), 160.7(C-$N_{formimidamide}$), 155.9 (C sp^2), 154.9 (C sp^2), 148.8 (C sp^2), 147.9 (C sp^2), 144.4 (C sp^2), 142.6 (C sp^2), 139.1 (C sp^2), 136.8 (C sp^2), 135.9 (C sp^2), 131.2 (C sp^2), 131.0 (C sp^2), 130.9 (C sp^2), 130.2 (C sp^2), 129.6 (C≡$N_{nitrile}$), 124.4 (C sp^2), 124.3 (C sp^2), 123.3 (C sp^2), 122.1 (C sp^2), 121.9 (C sp^2), 120.1 (C sp^2), 119.4 (C sp^2), 119.0 (C sp^2), 117.7 (C sp^2), 117.5 (C sp^2), 111.3 (C sp^2), 111.3 (C sp^2), 111.2 (C–F), 111.1 (C–F), 35.2 (–CH_2).

Appendix S6

Spectrum of ^{13}C NMR for recorded **IR2** in deuterated dichloromethane with their labelling peak

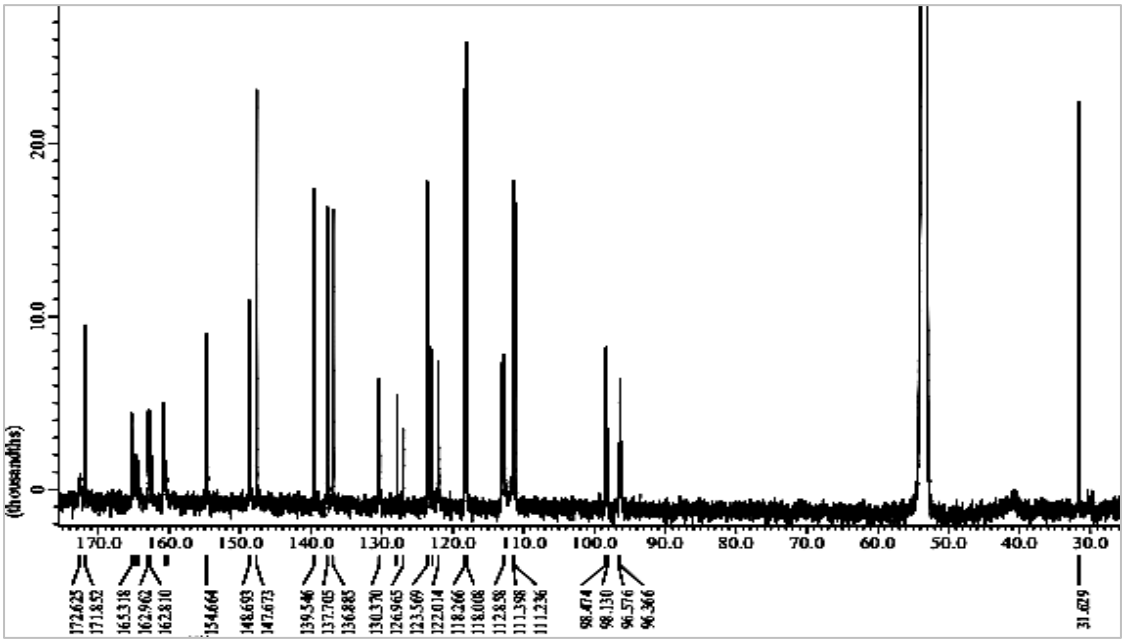

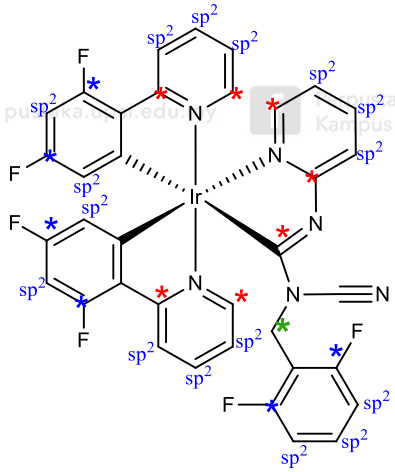

* : $C_{methylene}$

* : C-$N_{aromatic}$, C=$N_{aromatic}$

* : C-$F_{aromatic}$

sp^2: $C_{aromatic}$, $C_{quarternary\ in\ aromatic}$

^{13}C NMR (126 MHz, Methylene-Chloride) δ 172.6 (C-$N_{pyridine}$), 171.9 (C-$N_{pyridine}$), 165.3 (C-$N_{pyridine}$), 164.9 (C-$N_{pyridine}$), 164.8 (C-$N_{pyridine}$), 164.5 (C-$N_{pyridine}$), 164.3 (C-$N_{formimidamide}$), 163.0 (C sp^2), 162.8 (C sp^2), 162.6 (C sp^2), 160.6 (C sp^2), 160.3 (C sp^2), 154.7 (C sp^2), 148.7 (C sp^2), 147.7 (C sp^2), 139.5 (C sp^2), 137.7 (C sp^2), 136.9 (C sp^2), 130.4 (C sp^2), 128.0 (C≡$N_{nitrile}$), 127.0 (C sp^2), 123.6 (C sp^2), 122.9 (C sp^2), 122.0 (C sp^2), 118.3 (C sp^2), 118.0 (C sp^2), 112.9 (C sp^2), 112.8 (C sp^2), 112.6 (C sp^2), 111.4 (C–F), 111.2 (C–F), 98.5 (C–F), 98.1 (C–F), 96.6 (C–F), 96.4 (C–F), 31.6(–CH_2).

Appendix S7

Spectrum of ^{13}C NMR for recorded **IR3** in deuterated dichloromethane with their labelling peak

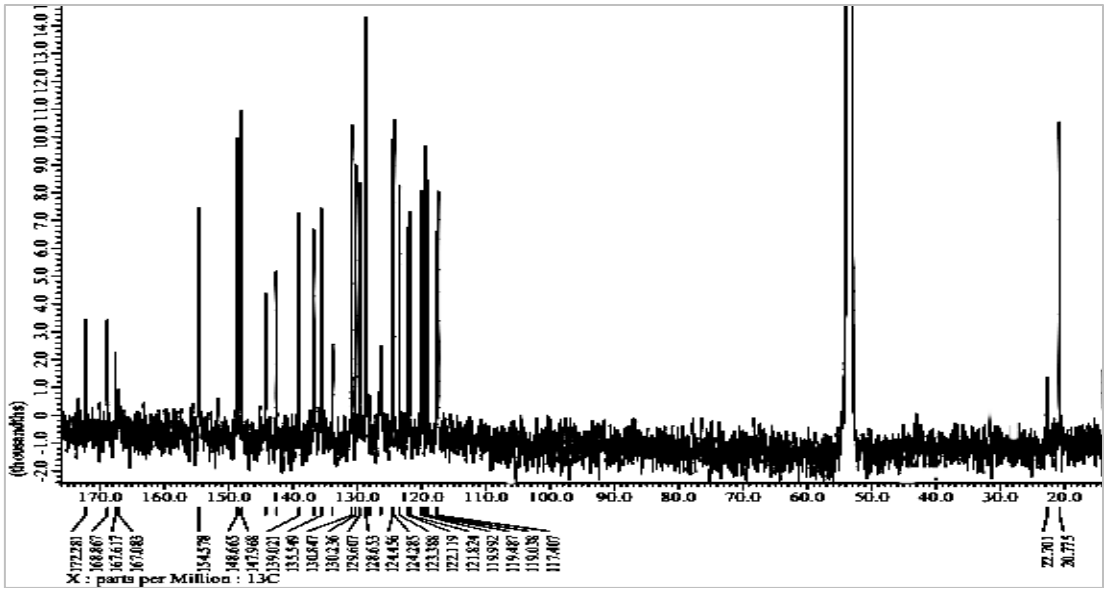

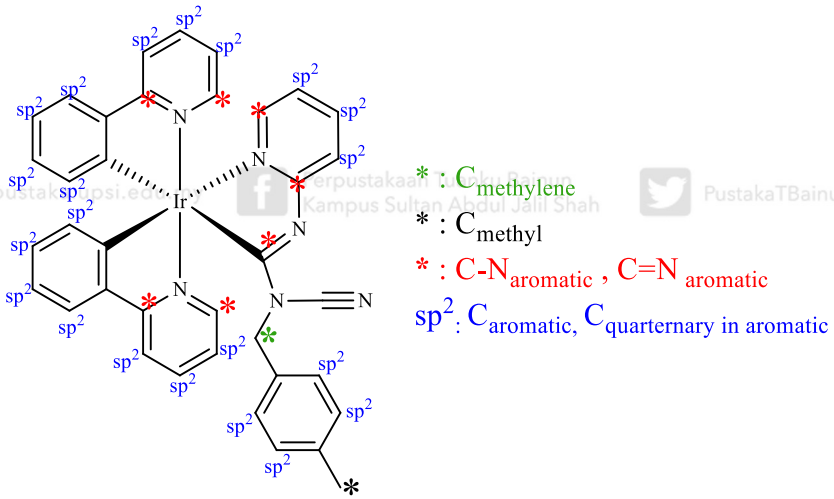

^{13}CNMR (126 MHz, Methylene-Chloride) δ 172.3 (C-$N_{pyridine}$), 172.2 (C-$N_{pyridine}$), 168.9 (C-$N_{pyridine}$), 168.8 (C-$N_{pyridine}$), 167.6 (C-$N_{pyridine}$), 167.5 (C-$N_{pyridine}$), 167.2(C-$N_{formimidamide}$), 167.1 (C sp^2), 154.6 (C sp^2), 148.7 (C sp^2), 148.0 (C sp^2), 144.3 (C sp^2), 142.6 (C sp^2), 139.0 (C sp^2), 136.8 (C sp^2), 136.7 (C sp^2), 135.5 (C sp^2), 133.8 (C sp^2), 130.9 (C sp^2), 130.8 (C sp^2), 130.2 (C sp^2), 129.6 (C sp^2), 128.7 (C sp^2), 128.1 (-C≡N $_{nitrile}$), 126.3 (C sp^2), 124.5 (C sp^2), 124.3 (C sp^2), 123.4 (C sp^2), 122.1 (C sp^2), 121.8 (C sp^2), 120.0 (C sp^2), 119.5 (C sp^2), 119.0 (C sp^2), 117.6 (C sp^2), 117.4 (C sp^2), 22.7 (–CH_2), 20.8 (–CH_3).

Appendix S8

Spectrum of ^{13}C NMR for recorded **IR4** in deuterated dichloromethane with their labelling peak

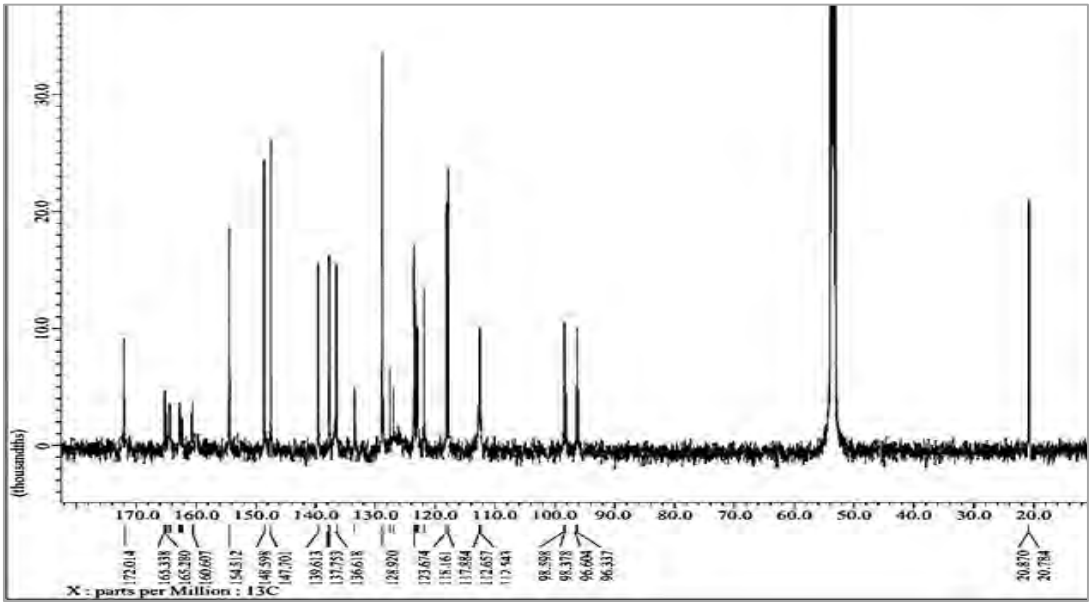

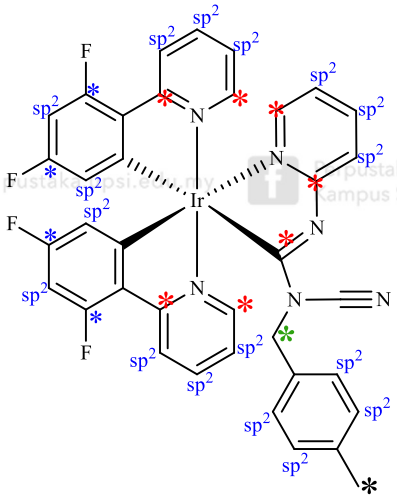

* : $C_{methylene}$

* : C_{methyl}

* : C-$N_{aromatic}$, C=$N_{aromatic}$

* : C-$F_{aromatic}$

sp^2: $C_{aromatic}$, $C_{quarternary\ in\ aromatic}$

^{13}CNMR (126 MHz, Methylene-Chloride) δ 172.0 (C-$N_{pyridine}$), 165.3 (C-$N_{pyridine}$), 165.3 (C-$N_{pyridine}$), 165.0 (C-$N_{pyridine}$), 164.9 (C-$N_{pyridine}$), 164.5 (C-$N_{pyridine}$), 164.4 (C-$N_{formimidamide}$), 162.9 (C sp^2), 162.8 (C sp^2), 162.5 (C sp^2), 162.4 (C sp^2), 160.7 (C sp^2), 160.6 (C sp^2), 154.5 (C sp^2), 148.6 (C sp^2), 147.7 (C sp^2), 139.6 (C sp^2), 137.8 (C sp^2), 136.6 (C sp^2), 133.6 (C sp^2), 128.9 (C≡$N_{nitrile}$), 127.7 (C sp^2), 127.0 (C sp^2), 123.7 (C sp^2), 123.6 (C sp^2), 123.4 (C sp^2), 123.1 (C sp^2), 123.0 (C sp^2), 122.0 (C sp^2), 118.2 (C sp^2), 117.9 (C sp^2), 112.7 (C–F), 112.5 (C–F), 98.4 (C–F), 96.3 (C–F), 20.9(–CH_2), 20.8(–CH_3)

Appendix S9

Cartesian coordinates of Adduct
ωB97X-D3/def2-TZVPP
opt E=-1168.86298693191kcal/mol, zero imaginary frequencies

C	-0.17604	5.010972	0.811734
C	0.957382	4.262467	1.178581
C	2.160822	4.525192	0.557986
C	2.257279	5.497851	-0.43892
C	1.156027	6.237725	-0.82639
C	-0.07448	5.992573	-0.17712
C	0.853074	3.195843	2.23354
N	0.328896	1.931202	1.679521
C	0.933155	1.148727	0.793529
N	0.108606	0.151158	0.5442
N	-1.04012	0.267057	1.25177
C	-0.88323	1.358747	1.935158
C	0.295323	-0.91145	-0.40046
C	0.902049	-2.0767	-0.0003
C	1.05948	-3.07302	-0.95447
C	0.60345	-2.84631	-2.23876
C	0.00273	-1.6345	-2.5393
N	-0.15262	-0.66957	-1.63019
C	1.250389	7.310742	-1.87042
Ag	-0.98766	4.14181	-1.2686
Ag	-1.07179	1.208276	-2.13336
O	-1.85517	2.964698	-2.6523
H	-0.36455	-1.42035	-3.53344
H	0.708943	-3.59404	-3.01189
H	1.532197	-4.00892	-0.689
H	1.236908	-2.19533	1.020361
H	1.906528	1.294665	0.351829
H	-1.60322	1.771961	2.622681
H	1.823127	2.977639	2.674271
H	0.167208	3.480101	3.028209
H	3.045376	3.968554	0.845254
H	3.214535	5.677971	-0.91235
H	-0.9124	6.655383	-0.36476
H	-1.09853	4.903732	1.371609
H	1.106057	8.29378	-1.41816
H	0.476881	7.18211	-2.62804
H	2.221961	7.299082	-2.3607

Appendix S10

Cartesian coordinates of TS1

ωB97X-D3/def2-TZVPP

opt TS E=-1168.83075912810 kcal/mol v= -1130.28 cm^{-1}

C	2.514693	-3.11204	-0.6197
C	1.612136	-3.9672	-1.23044
C	0.308848	-3.53189	-1.41194
C	-0.05205	-2.26558	-0.98162
C	0.939586	-1.50831	-0.38673
N	2.185327	-1.89272	-0.20064
N	0.646556	-0.19369	0.086707
C	1.475105	0.63303	0.688701
N	0.78793	1.735423	0.956018
C	-0.50906	1.559171	0.492221
N	-0.58541	0.368237	-0.04309
C	1.334666	2.906851	1.648446
C	1.148721	4.174137	0.854791
C	1.540915	4.266618	-0.4708
C	1.274672	5.41084	-1.21458
C	0.611901	6.498016	-0.65817
C	0.24744	6.42777	0.698648
C	0.531268	5.279685	1.451484
C	0.339733	7.741576	-1.45357
H	3.543497	-3.41092	-0.45728
H	1.927522	-4.94907	-1.55475
H	-0.42572	-4.17023	-1.88518
H	-1.05322	-1.87958	-1.09835
H	2.509668	0.440628	0.915945
H	-1.51132	2.366043	0.47333
H	2.389286	2.701475	1.827694
H	0.837674	2.986166	2.613384
H	2.031577	3.425999	-0.94775
H	1.578286	5.450594	-2.2537
H	-0.17467	7.299024	1.18699
H	0.297595	5.259548	2.509987
H	1.134812	8.472311	-1.29085
H	-0.59867	8.203783	-1.14947
H	0.296032	7.525928	-2.51996
O	-2.58259	3.124543	0.358693
Ag	-1.66431	4.976533	0.542605
Ag	-3.2152	3.117609	-1.59762

Appendix S11
Cartesian coordinate of Intermediate I
ωB97X-D3/def2-TZVPP
opt E=-1168.84440142412 kcal/mol, zero imaginary frequencies

C	2.549623	-2.99508	-0.82551
C	1.619093	-3.85853	-1.37872
C	0.291619	-3.45996	-1.4149
C	-0.06166	-2.22363	-0.90175
C	0.958051	-1.45035	-0.3741
N	2.228092	-1.80338	-0.32762
N	0.667534	-0.17019	0.172589
C	1.518475	0.669823	0.720189
N	0.816763	1.729136	1.092421
C	-0.53826	1.544352	0.76304
N	-0.60187	0.356677	0.191671
C	1.377937	2.908067	1.747696
C	1.19197	4.152369	0.916607
C	1.662059	4.227892	-0.38503
C	1.411913	5.345274	-1.17332
C	0.685218	6.425684	-0.68858
C	0.233875	6.373055	0.643448
C	0.504177	5.250725	1.442991
C	0.439874	7.646314	-1.52689
H	3.59814	-3.26528	-0.77678
H	1.931805	-4.81679	-1.76957
H	-0.46707	-4.10545	-1.83809
H	-1.08008	-1.86665	-0.90475
H	2.57647	0.51084	0.839404
H	-2.20851	2.613645	0.544501
H	2.434447	2.711272	1.927377
H	0.887042	3.02114	2.71246
H	2.208333	3.392887	-0.8085
H	1.7844	5.37116	-2.1902
H	-0.23243	7.246386	1.086539
H	0.207959	5.250957	2.486028
H	1.177544	8.416351	-1.29159
H	-0.5469	8.06621	-1.33458
H	0.522728	7.41749	-2.58815
O	-2.90897	3.25585	0.29528
Ag	-1.63792	4.943694	0.419403
Ag	-3.52825	2.638366	-1.62357

Appendix S12
Cartesian coordinate of TS2
ωB97X-D3/def2-TZVPP
opt TS E= -1168.83711326154 kcal/mol v=-406.42 cm^{-1}

C	2.32715	-3.29985	-0.88587
C	1.284951	-4.20446	-1.00838
C	-0.00653	-3.75683	-0.77436
C	-0.20543	-2.43319	-0.42543
C	0.911367	-1.61434	-0.32753
N	2.152427	-2.02199	-0.55631
N	0.712697	-0.26812	0.020569
C	1.591389	0.541752	0.448375
N	1.149641	1.821362	0.659294
C	-0.16495	1.919056	0.350992
N	-0.79299	0.950686	-0.05596
C	1.973533	2.897604	1.241185
C	1.555498	4.23989	0.710203
C	2.137028	4.788098	-0.41645
C	1.674151	5.993999	-0.94348
C	0.611004	6.671674	-0.37092
C	0.027306	6.129292	0.787205
C	0.501621	4.934322	1.331214
C	0.10096	7.965787	-0.93464
H	3.35072	-3.60944	-1.06511
H	1.485288	-5.23109	-1.28235
H	-0.84972	-4.4299	-0.8613
H	-1.19002	-2.03249	-0.22821
H	2.628043	0.306404	0.653771
H	-3.86493	3.824108	-0.85963
H	3.007984	2.682606	0.981906
H	1.87239	2.863664	2.326051
H	2.956007	4.271594	-0.90294
H	2.150138	6.403364	-1.82617
H	-0.74472	6.684211	1.308128
H	0.113864	4.582369	2.281816
H	0.230075	8.774972	-0.21394
H	-0.96428	7.895292	-1.15928
H	0.629128	8.233539	-1.84805
O	-3.01719	3.539039	-1.19886
Ag	-1.34903	4.127656	0.054579
Ag	-2.70317	1.381545	-1.17363

Appendix S13
Cartesian coordinates of Intermediate II
ωB97X-D3/def2-TZVPP
opt E=-1168.90535428009 kcal/mol, zero imaginary frequencies

C	3.01217	-2.57815	-1.38146
C	2.43869	-3.82806	-1.54288
C	1.120557	-4.00065	-1.14569
C	0.436481	-2.9264	-0.60815
C	1.106514	-1.71443	-0.4766
N	2.365814	-1.53644	-0.86181
N	0.39189	-0.62706	0.067229
C	1.04038	0.302948	0.614568
N	0.370988	1.416205	1.124371
C	-0.93204	1.519646	0.953025
N	-2.06528	1.695256	0.838142
C	1.070232	2.57085	1.728397
C	0.93019	3.827017	0.903726
C	1.293424	3.839924	-0.44642
C	1.193218	4.989544	-1.20064
C	0.76089	6.197167	-0.63106
C	0.38369	6.184002	0.723175
C	0.458862	4.994817	1.4757
C	0.828614	7.476817	-1.4168
H	4.037212	-2.399	-1.68764
H	3.008462	-4.63867	-1.97594
H	0.630255	-4.95958	-1.25653
H	-0.5936	-3.00585	-0.28897
H	2.119528	0.344403	0.745337
H	-4.34891	5.603656	-0.04886
H	2.114801	2.273951	1.811907
H	0.683432	2.721685	2.734661
H	1.66291	2.934015	-0.91313
H	1.487679	4.97445	-2.24286
H	0.166447	7.119932	1.229305
H	0.179717	5.014532	2.522417
H	1.873268	7.764846	-1.54853
H	0.315538	8.289964	-0.906
H	0.394825	7.354212	-2.40878
O	-3.6967	5.205479	-0.62688
Ag	-1.74302	5.851001	-0.06968
Ag	-3.21574	3.270166	0.049813

Appendix S14
Cartesian coordinate of TS III
ωB97X-D3/def2-TZVPP
opt TS E=-1168.35977805141 kcal/mol, v=-1411.71 cm^{-1}

C	2.840527	-2.66532	-1.34623
C	2.125926	-3.83732	-1.31178
C	0.895439	-3.83104	-0.65709
C	0.435765	-2.6605	-0.10551
C	1.213462	-1.49306	-0.18071
N	2.413786	-1.51701	-0.78905
N	0.634655	-0.32995	0.285505
C	1.208589	0.586643	0.977392
N	0.397898	1.699379	1.237832
C	-0.8493	1.759618	0.768067
N	-1.93347	1.843408	0.382992
C	0.905993	2.875958	1.959646
C	0.952386	4.104013	1.08691
C	1.723777	4.119585	-0.07167
C	1.755372	5.242648	-0.88161
C	1.021671	6.383638	-0.55949
C	0.26021	6.364872	0.604507
C	0.222406	5.238438	1.414931
C	1.029653	7.590304	-1.45742
H	3.803289	-2.619	-1.84015
H	2.518733	-4.72852	-1.7802
H	0.299988	-4.73348	-0.59637
H	-0.52611	-2.60432	0.384833
H	2.448854	0.788279	1.475726
H	1.904948	2.598637	2.295347
H	0.280542	3.053852	2.834732
H	2.302197	3.243157	-0.34438
H	2.360689	5.23616	-1.78109
H	-0.31736	7.240209	0.880107
H	-0.38366	5.242267	2.313989
H	1.010186	8.513874	-0.87848
H	0.150586	7.592664	-2.10592
H	1.912835	7.601769	-2.09558
O	3.644048	1.095992	1.7356
Ag	4.407529	0.029365	3.308046
Ag	3.932319	-0.1318	0.012276

Appendix S15
Cartesian coordinates of Product
ωB97X-D3/def2-TZVPP
opt E=-1168.42011271981 kcal/mol, zero imaginary frequencies

C	2.958975	-2.48398	-1.08341
C	2.397692	-3.74525	-1.09072
C	1.066755	-3.86522	-0.70163
C	0.372353	-2.73502	-0.32844
C	1.026717	-1.49697	-0.33833
N	2.299681	-1.38044	-0.72229
N	0.293779	-0.37017	0.031244
C	0.870929	0.568981	0.68954
N	0.030106	1.668538	0.966594
C	-1.21674	1.69282	0.49569
N	-2.30173	1.75533	0.107668
C	0.459073	2.830468	1.745476
C	0.630898	4.083234	0.922555
C	1.312338	4.0622	-0.29093
C	1.492518	5.227462	-1.01745
C	1.001014	6.44827	-0.55691
C	0.323408	6.462361	0.657379
C	0.136746	5.295134	1.385431
C	1.173099	7.704178	-1.36593
H	3.990607	-2.33898	-1.38821
H	2.978564	-4.60344	-1.40015
H	0.578476	-4.83207	-0.69438
H	-0.66461	-2.77927	-0.02345
H	5.132789	1.229055	2.390585
H	1.404218	2.539325	2.206565
H	-0.25805	3.004603	2.54838
H	1.703522	3.126519	-0.67485
H	2.026774	5.190716	-1.96026
H	-0.07003	7.397581	1.039735
H	-0.40112	5.329047	2.326349
H	1.157252	8.589711	-0.73089
H	0.366633	7.807861	-2.09548
H	2.113134	7.692061	-1.91769
O	4.918167	0.499233	1.808242
Ag	4.81399	-1.27138	2.985266
Ag	2.886426	0.590896	1.250424

LIST OF CONFERENCES

1. Oral Presenter at IUPAC 2025, 50th World Chemistry Congress (50WCC), Kuala Lumpur Convention Centre (KLCC), Kuala Lumpur. Date: 14th–19th July 2025. Title: New iridium(III) complex bearing with (E)-N-cyano-N-(2,6-difluorobenzyl)-N'- (pyridin-2-yl)formimidamide ancillary ligand.

2. Oral Presenter at 5th International Conference on Chemistry and Material Sciences 2023 (IC2MS), Malang, Indonesia. Date: 11st−12nd October 2023. Title: Phosphorescent Cyclometallated Iridium(III) Complex with (E)-Ncyano-N-(4-methylbenzyl)-N'-(pyridin-2-yl)formimidamide Ancillary Ligand: Synthesis, Spectroscopic and Theoretical Studies.

3. Oral Presenter at International Congress on Pure & Applied Chemistry Kota Kinabalu, 2022 (ICPACKK2022), Sabah, Malaysia. Date: 22nd−27th November 2022. Title: Spectroscopic and Theoretical Studies on Reaction Mechanism of Iridium Complex with Pyridine-Formimidamide Ancillary Ligand.

4. Oral Presenter at 9th International Postgraduate Conference on Science and Mathematics 2021 (IPCSM2021), Perak, Malaysia. Date: 7th August 2021. Title: Phosphorescent Cyclometallated 1,2,4-Triazolepyridyl-Based Iridium(III) Complex: Synthesis, Crystal Structure and Photophysical Studies

LIST OF WORKSHOPS, SEMINARS AND TRAINING

1. Systematic Literature Review Workshop, Institut Pengajian Siswazah, Universiti Pendidikan Sultan Idris, 2025.
2. International Workshop on Computational Chemistry, Faculty of Sciences, UTM Skudai and Universitas Negeri Malang, 2023.
3. Comprehensive Training on NMR Spectroscopy, JEOL JNM-ECA500, 2022.
4. Webinar of Computational Modelling in Chemistry, Universiti Malaysia Terengganu, 2022.
5. Webinar on Photoluminescence and UV-VIS-NIR: Fundamental and Data Interpretation, 2022.
6. Workshop on DFT Molecular Modelling, Atta-ur-Rahman Institute for Natural Product Discovery, Universiti Teknologi MARA, 2021.
7. Bengkel Asas Keselamatan Makmal & Tempat Kerja, Universiti Pendidikan Sultan Idris, 2021.